

Computational Developments and Applications for Cryo-Electron Tomography

Inauguraldissertation

Zur Erlangung der Würde eines Doktors der Philosophie

vorgelegt der

Philosophisch – Naturwissenschaftlichen Fakultät der Universität Basel

von

Stefano Scaramuzza

2021

Genehmigt von der Philosophisch-Naturwissenschaftlichen Fakultät auf Antrag von

Prof. Dr. Henning Stahlberg
Dr. Daniel Castaño-Díez
Prof. Dr. Jan Pieter Abrahams
Prof. Dr. Benoît Zuber

Basel, den 16.12.2020

Prof. Dr. Martin Spiess,
Dekan

Acknowledgements

I express my sincere gratitude to the following people, without whom the completion of my doctoral thesis would not have been possible:

My first supervisor Prof. Henning Stahlberg who offered me a position in his diverse and skilled lab. I particularly thank him for his support and freedom he gave me to conduct my research.

My co-first supervisor Dr. Daniel Castaño-Díez, with whom I worked on almost all my projects. I specially thank him for being a great mentor in electron tomography and for assisting me in countless opportunities to connect with the scientific community through collaborations, lab visits, and the numerous *Dynamo* workshops.

My second supervisor Prof. Jan Pieter Abrahams as well as the chair of my PhD committee Dr. Thomas Braun for their valuable scientific advice.

Prof. Benoît Zuber for kindly accepting to co-referee this thesis.

Dr. Paula Pérez-Navarro, with whom I collaborated on various *Dynamo* related projects.

Dr. Aitor Hierro from CIC bioGUNE and his lab members Dr. Carlos López-Robles, Dr. Adriana Rojas and Dr. Soledad Baños-Mateos for the collaboration on the SNX-BAR project.

Dr. Amanda Lewis for the collaboration on the TDP-43 project.

Dr. Giulia Zanetti and Dr. Joshua Hutchings from Birkbeck College and Assoc. Prof. Alex De Marco from Monash University for welcoming me to their labs for research visits.

Researchers in the cryo-EM community for the scientific exchange: Dr. Misha Kudryashov, Dr. Alex Noble, Justin Morado, Asst. Prof. Florian Schur, Dmitry Tegunov, Alister Burt, Dr. Jasenko Živanov, Dr. Lauren Ann Metskas and the countless people I met during workshops and conferences.

My colleagues and friends at C-CINA and the Biozentrum for the fruitful discussions

and for creating a great working atmosphere: Anastasia, Ricardo R., Ricardo A., Inay, Ricardo G., Kai, Paolo, Luca, Claudio, Max, Thorsten, Ashraf, Nadia, Dong, Carola, Philippe, Raphael, Andrej and Đorđe. Lubomir, Mohammed, Kenny, Ariane, Daniel C.B. and Frank for reliably managing the lab and the microscopes. Martin Fox, Martin Jacquot and their teams for providing an excellent computing environment. Karen Bergmann for the administrative support.

I finally thank my parents Gianantonio and Giuliana and my brother Roberto, as well as Maurizio, Laura and all my relatives including my friends for their constant support throughout my career and for always believing in me.

Abstract

Cellular organelles and biological macromolecules such as proteins play a fundamental role in almost all life sciences. Structural biology studies the molecular structure of these particles to gain information about their morphology and function. A quickly evolving technique in this field is cryo electron-tomography (cryo-ET). Its big advantage is the ability to determine the three dimensional structure of particles in their native environment. A powerful method for image analysis in cryo-ET is subtomogram averaging (STA), where repetitions of the same particle of interest within a tomogram are computationally extracted, aligned to a common reference and averaged. This procedure significantly increases the signal of the underlying structure.

A main bottleneck in cryo-ET and STA is the low throughput in sample preparation, data acquisition and image processing. With the goal to overcome this challenge, we developed computational methods to automate and streamline key steps in image processing. Two projects were designed for this purpose: In the first project, we streamlined the complete processing pipeline of STA and minimized the manual user interaction. In the second project we developed a new algorithm to fully automate the alignment of tomographic tilt series. We further developed a range of specialized tools for STA. We applied them on biological samples in combination with our established methods for increased throughput. Thereby we determined the architecture of protein coats involved in membrane trafficking and shed light on the underlying mechanics. With our new methods we successfully reduced processing times for STA, answered biological questions and laid the foundation for further developments.

Contents

Acknowledgements	3
Abstract	5
1. Introduction	9
1.1. The importance of structural biology	9
1.2. Transmission electron microscopy for structural biology	11
1.3. Cryo-electron tomography	14
1.4. Sub-tomogram averaging	18
1.5. The <i>Dynamo</i> software for sub-tomogram averaging	21
2. Motivation and Aim of this Thesis	23
3. Subtomogram Averaging from Cryo-Electron Tomograms	25
3.1. Comment	25
3.2. Abstract	26
3.3. Introduction	27
3.4. Sample preparation for cryo-ET	30
3.5. Aspects of data collection for subtomogram averaging	32
3.6. Generation of tomograms for StA	35
3.7. Subtomogram averaging	48
3.8. Dealing with heterogeneity	54
3.9. Software packages for subtomogram averaging	58
3.10. Future opportunities and challenges	60
4. Protocols for Subtomogram Averaging of Virus-Like Particles with <i>Dynamo</i>	63
4.1. Comment	63
4.2. Abstract	64
4.3. Introduction	65
4.4. Materials and equipment	67
4.5. Procedure	69
4.6. Conclusion	87

5. Automated Alignment of Tilt Series for Cryo-Electron Tomography in <i>Dynamo</i>	89
5.1. Comment	89
5.2. Abstract	90
5.3. Introduction	91
5.4. Algorithm	95
5.5. Software package	107
5.6. Conclusion and outlook	112
6. Molecular architecture of the SNX-BAR membrane coat for endosomal sorting	113
6.1. Comment	113
6.2. Abstract	115
6.3. Introduction	116
6.4. Results	119
6.5. Conclusion	133
6.6. Methods for cryo-electron tomography and subtomogram averaging . . .	135
7. Conclusion and outlook	143
8. Summary of my PhD	147
Appendix A. Supplementary material: "Automated Alignment of Tilt Series"	149
Appendix B. Supplementary material: "Molecular Architecture of the SNX-BAR Membrane Coat"	151
B.1. Automatic computation of helix parameters	161
B.2. Automatic outlier exclusion	163
Appendix C. Supplementary material: "Protocols for STA of VLPs"	167
List of Abbreviations	183
List of Figures	187
List of Tables	191
Bibliography	193
Curriculum Vitae	215

1. Introduction

1.1. The importance of structural biology

Cells are the fundamental building blocks of every living organism [Alberts et al. 2018]. In simple terms, they are compartments defined by a cell membrane containing the genetic information of the organism. There are two types of cells: Prokaryotic and eukaryotic. Prokaryotic cells contain the genetic information directly in the cytoplasm while in eukaryotic cells the DNA is protected by the nucleus. The nucleus is one of the many specialized entities called organelles, that are found in eukaryotic cells. Other important organelles include the endoplasmic reticulum, the Golgi apparatus, mitochondria, ribosomes and vesicles. Prokaryotes, such as bacteria and archaea, are unicellular organisms while eukaryotes, such as animals, plants and fungi, are multicellular organisms.

Proteins are macromolecules making up the machinery that performs a large amount of essential functions of cells and thus of all living organism [Branden et al. 2012]. Their functions include the catalysis of chemical reactions, DNA replication, signaling, enforcing structure and transportation of cargo. Proteins are further found in viruses, for example in their protein coat.

Because of their fundamental role in biology, the understanding of the processes within cells – in particular of the function of proteins – is central to almost all life science disciplines. It is of special interest in pharmacology, since many proteins are potential drug targets [Renaud 2020].

Among the many research fields dealing with answering questions related to cellular processes and protein functions, the field of structural biology focuses mainly on determining the three-dimensional (3D) structure – and the resulting implications on the function – of the cellular content, with a strong focus on proteins. The gained information ranges from contextual information at low resolution, e.g. interactions between cellular organelles or large protein complexes, to high-resolution 3D maps that enable to determine the coordinate of every single atom of small proteins (molecular structure). This structural knowledge can help to determine function and dynamics of different organelles and proteins. It allows to visualize their interactions and different conformations or to make quantitative statements. It can also lead to discoveries of binding sites of

proteins for specific drug targets or it may confirm and complement observations made by other assessments [Renaud 2020].

There are three main techniques in structural biology for high-resolution structure determination. Briefly summarized, they are:

- *X-ray crystallography*: In X-ray crystallography, or X-ray diffraction (XRD), focused monochromatic X-rays (usually produced in synchrotron accelerators) are aimed at crystallized protein samples. The resulting diffraction patterns – in combination with complementary methods for phase determination – allow to reconstruct the protein structure at high resolution [Branden et al. 2012]. XRD is the oldest and most common technique in structural biology and many concepts from it have been adapted to other techniques such as transmission electron microscopy. While the technique is very mature and imposes almost no limits on protein size, its main limitation is the dependency on the crystallization of proteins. This can be very difficult or impossible to obtain and, once achieved, does not necessarily fully represent a physiological state of the protein due to modifications on the proteins that are often needed to achieve crystallization in the first place.
- *Nuclear magnetic resonance*: In Nuclear magnetic resonance (NMR) spectroscopy, isolated proteins are exposed to a strong constant magnetic field and then perturbed by a weaker oscillating magnetic field (radio frequency pulses). This results in an electromagnetic signal emitted by the nuclei with non-zero magnetic spin of the atoms in the protein. The frequency of the emitted signal depends on the magnetic field around each of the nuclei. Based on the known protein sequence and the obtained NMR spectra, it is possible to derive pairwise distances between atoms in the protein and therefore its structure [Branden et al. 2012]. While NMR spectroscopy is as also a mature technique and it can provide structural information of different conformations of the same molecule, it is limited by the size of the protein, as it is mainly optimized for small molecules.
- *Transmission electron microscopy*: In transmission electron microscopy (TEM), a thin biological sample is imaged using an electron beam, resulting in a 2D projection of the specimen that can be further processed. TEM is the main technique used in this thesis and therefore the full following section is dedicated to it (see Section 1.2).

While each technique has its advantages and disadvantages, the true power of structural biology lies in the combination of all these techniques [Cerofolini et al. 2019; Rout et al. 2019; Ward et al. 2013]. This so called integrative approach is not limited by the aforementioned techniques but may also include other techniques that provide lower resolution or partial structural information such as mass spectrometry (proteomics), atomic force microscopy (AFM), fluorescence resonance energy transfer (FRET), electron paramagnetic resonance (EPR), bio-informatics and many others.

1.2. Transmission electron microscopy for structural biology

Transmission electron microscopy is an imaging technique in high-resolution structural biology with the particular feature to depict the biological sample in direct space. The major difference to conventional light microscopy is that – instead of photons – electrons are used as a probe. Electrons at energies commonly used in TEM have significantly shorter wavelengths than light. This drastically reduces the theoretical resolution limit of an electron microscope.

TEM was originally developed for material sciences and was soon extended to structural biology. Recent technical advancements in all major aspects of TEM – especially in sample preparation, detectors and image processing – made it a fast growing major player among the high-resolution structural biology techniques [Kühlbrandt 2014a,b; Nogales 2016] and also boosted the integrative approaches [Cerofolini et al. 2019; Rout et al. 2019].

A typical TEM setup for structural biology can briefly be described as follows: Electrons are first emitted by an electron gun. They are then focused by a system of electromagnetic lenses into a coherent beam that is transmitted through the sample. Because electrons interact strongly with matter, the inside of a TEM needs to be vacuumed and the sample needs to be thin enough for the electrons to be transmitted. The detector records an image which is formed by interference of scattered and unscattered electrons, representing the projection of the coulomb potential of the exposed biological structure. TEM setups can further be extended by building in additional modules such as energy filters, spherical aberration correctors or phase plates¹ to increase the image quality. A complete and detailed overview of TEM can be found in the books by Reimer 2013 and Pennycook et al. 2010.

The recorded micrographs are either directly used for interpretation or further processed to generate 3D maps of the sample. The 3D reconstruction from 2D micrographs is based on the following fundamental concepts [Frank 2006]:

- *Weak phase object approximation*: The weak phase object approximation (WPOA) assumes that the sample is a weak scatterer, i.e., the amplitude contrast is neglectable compared to phase contrast. The phase shift induced by the sample is further assumed to be small enough so that the exit wave can be described by the first order Taylor expansion only. This assumptions facilitate the image processing, including CTF-correction (more details in Section 1.3) and Wiener filtering [Sindelar et al. 2012; Vulović et al. 2014].

¹Unleashing the full potential of phase plates remains yet a challenge [Buijsse et al. 2020].

- *Central slice theorem*: The central slice theorem states that the Fourier transformation of the 2D projection of an object is equivalent to a central slice in the Fourier space of the actual 3D object [Ronald N Bracewell 1956]. This allows to reconstruct a 3D volume based on projections only. This theorem is of great importance, since micrographs acquired in TEM are projections.
- *Big datasets and iterative processes*: Key to all 3D reconstruction methods is to acquire a dataset that contains projections from enough different angles of the object of interest to allow full coverage of its Fourier space. The initially unknown orientations of the central slices in Fourier space are iteratively determined and refined until convergence, resulting in the final 3D map of the structure.

To preserve the structure of biological samples in the vacuum of a TEM, they need to be fixated. Common fixation methods are chemical fixation, resin embedding, negative staining with heavy metal salts, vitrification (cryofixation) or combinations of these techniques [Winey et al. 2014]. The highest resolution reconstructions are currently achieved by vitrification of the sample (more details in Section 1.3), because it perfectly conserves high-resolution features of the specimen [Dobro et al. 2010]. TEM using vitrified samples is known as cryo-EM.

High-resolution structures in TEM are almost exclusively achieved by cryo-EM, which is currently a very fast growing field [Cheng, Glaeser, et al. 2017]. One reason for the popularity of cryo-EM is its potential to analyse structures under more physiological conditions. Depending on the technique this includes isolated proteins and protein complexes over a broad range of sizes, membrane proteins reconstituted in liposomes, proteins or proteins complexes in interaction with their native environment and even proteins and organelles within their cellular context.

There are three major cryo-EM modalities. Briefly summarized, they are:

- *2D electron crystallography*: In 2D electron crystallography, proteins (mainly membrane proteins) are arranged in a 2D lattice or crystal. The TEM is operated in diffraction mode to produce diffraction patterns (similar to XRD) at different orientations [Abeyrathne et al. 2012]. Together with the phases – that are retrieved by real space imaging – the 3D structure of the protein can be computationally determined using various algorithms that also deal with bending of the lattice and local defects [Arheit et al. 2013; Righetto et al. 2019; Stahlberg et al. 2015]. Recently, the related 3D electron diffraction method has become of interest [Gemmi et al. 2019].
- *Single particle analysis*: In single particle analysis (SPA), multiple copies of the protein of interest (usually isolated and in solution) are imaged at random orientations. The individual proteins are then computationally identified in the micrographs and their relative orientations are determined to perform a 3D reconstruc-

tion and classification. Numerous computational methods exist for those tasks [Cheng, Grigorieff, et al. 2015; Frank 2006]. For particle alignment this includes maximum-likelihood and Bayesian approaches [Scheres 2012; Sigworth et al. 2010]. For classification this includes methods based on multivariate statistical analysis (MSA) [Heel, R. Portugal, et al. 2006], maximum-likelihood [Lyumkis et al. 2013; Scheres, Valle, et al. 2005], Bayesian statistics [Scheres 2012] and stochastic gradient descent (SGD) [Punjani et al. 2017]. SPA is currently the most popular cryo-EM technique.

- *Cryo-electron tomography*: In cryo-electron tomography (Cryo-ET), a 3D reconstruction of the sample is generated by combining images of the same area of interest that were acquired from different viewing angles. This allows to generate 3D visualizations of large and complex biological structures. Cryo-ET is the main modality used in this thesis and is therefore explained in more detail in the following section (Section 1.3).

1.3. Cryo-electron tomography

In cryo-electron tomography², a full 3D reconstruction of a region of a biological sample is generated. This is done by first imaging the same area of interest at a range of different angles relative to the electron beam by tilting the microscope stage. The resulting tilt series of micrographs is then used to computationally reconstruct the 3D volume, or tomogram, which can be further processed [Frank 2013].

The ability to reconstruct complete regions of a sample enables cryo-ET to go beyond the imaging of isolated or crystallized proteins. It allows to image structures in their native or near-native context such as membrane proteins reconstructed in vesicles or tubules, particles such as viruses and organelles in interaction with their environment or even complete parts of cells and tissue leading to the imaging of proteins, organelles and viruses *in situ* [Asano, Benjamin D. Engel, et al. 2016; Briggs 2013].

Depending on the sample properties, different methods of vitrification may be required. An important factor for each technique is the resulting sample thickness. As previously mentioned (Section 1.2), the specimen needs to be thin enough for the electron beam to be transmitted. Thicknesses below 300 nm are usually preferred. There are three main methods for sample preparation in cryo-ET:

- *Plunge freezing*, as it is also used in SPA, in which the sample is rapidly immersed in a cryogen such as liquid ethane (see Section 3.4.1).
- *High pressure freezing and sectioning*, where the sample is frozen under high pressure and then cut to produce thin sections of the specimen (see Section 3.4.2).
- *Focused ion beam (FIB) milling*, in which an already vitrified sample is further thinned using a FIB (see Section 3.4.3).

The data acquisition is usually done by tilting the microscope stage along one axis in constant angular steps and acquiring an image at each tilt. The resulting tilt series usually consist of 40-60 micrographs with a total accumulated dose of approximately 80-100 $e^-/\text{\AA}^2$. It has been proven to be beneficial to expose low tilt angles first and to distribute the dose evenly between positive and negative tilt angles (Section 3.5.2 and [Hagen et al. 2017]).

A series of image processing steps are needed to generate a tomogram based on the raw tilt series data. The steps of the tomographic reconstruction pipeline are:

²I co-authored a review paper on cryo-ET and subtomogram averaging presented in Chapter 3. This section and the following ones therefore occasionally refer to said chapter for more detailed explanations and additional literature references.

1. *Pre-processing*: Depending on the type and settings of the used detector, pre-processing includes binning (Fourier cropping [Penczek, Fang, et al. 2014]) of the raw micrographs and drift correction (if movie-mode was used). The micrographs are usually also dose weighted to reduce high-resolution noise caused by radiation damage (see Section 3.6.1).
2. *Contrast transfer function (CTF) determination and correction*: The mathematical formulation of the imaging process of any optical system includes the convolution with a point spread function (PSF). In Fourier space this corresponds to a frequency dependent amplitude modulation and contrast reversal, which in cryo-EM is described by the so called CTF. Micrographs can be partially corrected for the CTF. There are cryo-ET specific methods for CTF determination and correction that are described in more detail in Section 3.6.4 and 3.6.5.
3. *Tilt series alignment*: Tilt series alignment corrects the micrographs in a tilt series for shifts caused by mechanical inaccuracies of the stage or beam induced motion. This is an important step as it directly impacts the quality of the reconstructed tomogram. Fiducial markers or high contrast features are used for the alignment (see Section 3.6.2).
4. *Tomographic reconstruction*: The final tomogram is reconstructed based on the aligned tilt series. The most popular method is the weighted back projection (WBP). Various other reconstruction algorithms exist and are explained in more detail in Section 3.6.3.

The generated tomograms are either directly used for interpretation or are further processed. The two most common tomogram analysis techniques are:

- *Segmentation*: In segmentation, the different components and structures inside the tomogram, such as membranes, organelles or filaments, are identified and rendered into independent 3D objects. This allows for an accurate visualization and interpretation of the 3D scene inside a tomogram. Segmentation is either done manually or automatically, depending on the sample complexity and the used software. A good introduction to tomographic segmentation is given by Sandberg 2007 and J.-J. Fernández 2012. Recent segmentation approaches also include machine learning algorithms [M. Chen, Dai, et al. 2017].
- *Subtomogram averaging*: In subtomogram averaging (STA) multiple copies of a structure that are present in the sample are individually extracted from the tomogram, aligned to each other and averaged to generate a high-resolution reconstruction. STA often depends on prior segmentation of the tomogram for particle localization (particle picking). STA is the main technique used in this thesis and is therefore described in more detail in the next section (Section 1.4).

Cryo-ET is less mature compared other cryo-EM techniques and poses many interesting challenges. Currently, the main general challenges in cryo-ET are:

- *Low dose and radiation damage:* Due to the strong interaction of electrons with matter, radiation damage in cryo-EM is a serious issue. Measurable damage to high-resolution features occurs already starting from an accumulated dose of $20 e^-/\text{\AA}$ [Grant et al. 2015b]. The consequence is that generally low electron doses have to be applied, resulting in low signal to noise ratios (SNR) of micrographs³. In tomography, the maximum accumulated dose that a sample can take needs to be divided among all tilts, resulting in an even lower SNR. Dose weighting [Grant et al. 2015b], denoising algorithms [Bepler et al. 2019; Tegunov and Cramer 2019] or alternative reconstruction methods such as SIRT algorithms [M. Chen, Bell, et al. 2019] are a few common methods used to increase the contrast in tomograms on the computational level. With low SNR being a main challenge in cryo-EM in general, many more computational methods as well as hardware applications exist that tackle this problem and a lot of research is still done on that topic [Grant et al. 2015b].
- *Sample movement:* Beam induced sample motion may lead to distortions in the tomograms. Advanced algorithms may partially correct the issue [J.-J. Fernández, Sam Li, and Agard 2019; Tegunov and Cramer 2019].
- *Missing wedge:* Currently, standard stages of TEMs are only capable of covering a tilt range of 120° - 140° . This leads to missing information in a tomogram, also called the missing wedge due to the shape of the missing information in Fourier. The missing information leads to distortions in the tomogram.
- *Tilt series alignment:* The quality of the tilt series alignment directly impacts the quality of tomogram. Local deformations and lack of fiducial markers or other high contrast features can severely deteriorate the alignment quality. Solutions to this problem pose advanced alignment algorithms (see Chapter 5) or algorithms not directly depending on classic tilt series alignment [M. Chen, Bell, et al. 2019; Himes et al. 2018].
- *Throughput:* Cryo-ET – compared to other Cryo-EM techniques such as SPA – is more time consuming. The main bottlenecks are the sample preparation (e.g. FIB milling), data acquisition (about 45 min. per tomogram) and image processing that still requires extensive user interventions, e.g., for tilt series alignment or segmentation. Processing times are further generally slower because operations on large volumes are computationally intensive. Research is done to improve all aspects such as sample preparation [Gorelick et al. 2019], data acquisition [Chreifi et

³It should be noted that contrast is already generally low for TEM when generating phase-contrast by defocus [Sigworth 2016].

al. 2019], tilt series alignment (see Chapter 5) and image processing (see previously mentioned automatic segmentation).

Cryo-ET is a beautiful example to demonstrate the strength of integrative approaches in structural biology. While some sample types and preparation techniques can lead to high-resolution structures [Schur, Obr, et al. 2016], others are still limited in this regard (e.g. *in situ* tomography). However, they do still provide the valuable information about the cellular context and interactions with the native environment of the structure of interest. Complementing this information with high-resolution information gained by other structural biology techniques can lead to invaluable insights and contribute to the completion of the biological picture. Successful examples of such integrative approaches are presented by Hutchings et al. 2018, Kovtun et al. 2018 and Hurt et al. 2015.

1.4. Sub-tomogram averaging

Sub-tomogram averaging is one of the most powerful image analysis techniques in cryo-ET. It is also the main technique used in this thesis. Similar to SPA, it takes advantage of the presence of multiple copies of the structure of interest inside the sample. The main goal of STA is to obtain a 3D electron density map of this structure by first detecting its copies in the tomograms, extracting them into so called subtomograms, aligning them to a common reference and finally average them. Averaging multiple subtomograms significantly increases the SNR and the information content in Fourier space. This is why STA is currently the main technique in cryo-ET for high-resolution 3D reconstruction. A great overview of subtomogram averaging can be found in various books and reviews [Castaño-Díez and Zanetti 2019; Danev, Yanagisawa, et al. 2019; Frank 2013; Jesus G. Galaz-Montoya et al. 2017; W. Wan and Briggs 2016] and in the review Leigh et al. 2019 shown in Chapter 3.

The STA pipeline consists of the following steps (each step is explained in more detail in Section 3.7):

1. *Particle picking*: The coordinates of the particle of interest inside the tomogram are determined. Depending on the sample and number of particles, this is done manually or automatically. Subvolumes are extracted from the tomograms at each coordinate and initial orientations are imposed (e.g., normal to a membrane surface).
2. *Iterative alignment*: Each subtomogram is aligned to an initially generated reference by rotating and shifting the subtomogram within user defined limits and by finding the orientation that optimizes an algorithm dependent similarity measurement between subtomogram and reference [Jesús G Galaz-Montoya et al. 2016]. The aligned subtomograms are averaged, resulting in a new reference. This procedure is iterated until convergence (Figure 1.1). To optimize the similarity measurements, alignment masks and missing wedge compensations are used. Overfitting, i.e., mistakingly generating signal by aligning noise, is minimized by using adaptive lowpass filters and the gold standard refinement method [Scheres and S. Chen 2012].
3. *Optional improvements*: Structures can be improved by classification, in which low quality particles are removed from the dataset or different conformations are identified. Subboxing, on the other hand, is used to improve selected subregions of the structure by performing localized alignments.
4. *Resolution estimation*: The current scientific consensus for resolution estimation of a structure is to first split the particle dataset into two half-datasets that are processed independently. The Fourier shell correlation (FSC) is then computed

using the resulting two halfmaps [Harauz et al. 1986] and the final resolution of the structure is finally determined using a threshold criteria on the FSC curve [Penczek 2010; Rosenthal et al. 2003; Van Heel et al. 2005]. Resolution estimation through computation of this so called gold standard FSC also serves to minimize overfitting. After the resolution estimation, the two halfmaps are merged and ready for post-processing.

5. *Post-processing*: In post-processing, the final map is usually globally or locally sharpened [Rosenthal et al. 2003] and lowpass filtered to the estimated resolution.

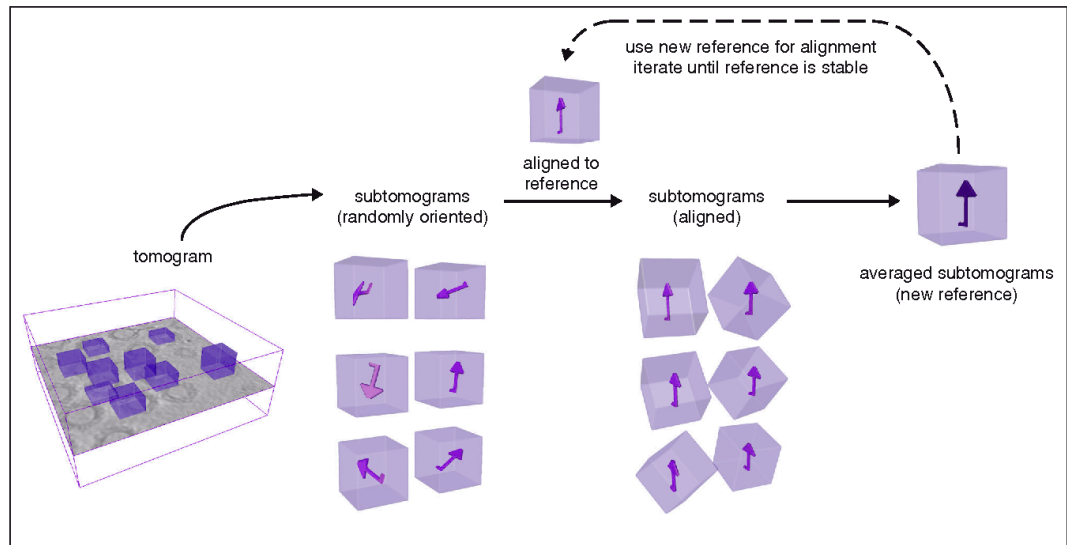


Figure 1.1.: **Illustration of the STA workflow.** Subtomograms are defined and extracted from the tomogram. They are aligned to a reference and averaged, resulting in a new reference. This procedure is iterated until convergence. (Figure adapted from W. Wan and Briggs 2016)

Different software packages and processing algorithms exist for STA. The most prominent are *Dynamo* [Castaño-Díez, Kudryashev, Arheit, et al. 2012; Castaño-Díez, Kudryashev, and Stahlberg 2017], RELION [Bharat, Russo, et al. 2015], PEET [Heumann et al. 2011], Jsubtomo [Huisken et al. 2014], EMAN2 [Jesús G. Galaz-Montoya et al. 2015], PyTom [Hrabe et al. 2012], emClarity [Himes et al. 2018] and M [Tegunov, Xue, et al. 2020]. An extensive overview of all packages related to STA is shown in Section 3.9. In this thesis, mainly the *Dynamo* software for subtomogram averaging was used. The software is therefore presented in more detail in the next section (Section 1.5).

While STA is a great technique for high-resolution cryo-ET, its main limitation is the low throughput (see challenges in cryo-ET in Section 1.3). It also requires hundreds, sometimes thousands of particles in random orientations to achieve a 3D reconstruction. Depending on the sample it is however hard to obtain this number of particles within a reasonable amount of time, as there might be only a few particles present per tomogram (e.g., secretion systems). Also, due to sample dependent complex geometries, a one-

fits-it-all approach for processing does not exist and time consuming manual work (e.g., particle picking) is still needed.

1.5. The *Dynamo* software for sub-tomogram averaging

The main software package used in this thesis is the *Dynamo* software for STA [Castaño-Díez, Kudryashev, Arheit, et al. 2012; Castaño-Díez, Kudryashev, and Stahlberg 2017]. It is being developed in-house and it was created for high-performance STA. It belongs to the most popular softwares for STA due to its broad range of features, user friendliness and flexibility. The *Dynamo* processing pipeline was recently extended to include all steps used for STA, ranging from the tilt series alignment (see Chapter 5) to the computation of the final average. Only the pre- and post-processing remains dependent on third party softwares.

Dynamo is mainly written in MATLAB (MathWorks⁴) and only performance and graphics processing unit (GPU) related tasks are written in CUDA and C++. It runs either in the native MATLAB environment or as an independent standalone version. It is supported by Linux, Windows and MacOS. Many tools, in particular visualisation tools, are compatible with third party softwares such as Chimera UCSF [Pettersen et al. 2004], EMAN2 [Tang et al. 2007] and IMOD [Mastronarde and Held 2017].

Subtomogram alignment and averaging form the core of the *Dynamo* pipeline. The subtomogram alignment is done by rotating and shifting the reference within a user defined parameter space relative to the subtomogram in order to search the orientation that optimizes the Roseman correlation [Roseman 2003] between subtomogram and reference (modulated by the missing wedge corresponding to the subtomogram). *Dynamo* provides various tools for the creation of masks and references and for setting up the alignment parameters. The averaging of the aligned subtomograms is done using a Fourier compensation method that re-weights overrepresented Fourier components. Subtomogram alignment and averaging are both optimized for GPU and CPU clusters and can be set up and monitored through various graphical user interfaces (GUIs).

Other important components of *Dynamo* are listed in the following:

- *Tilt series alignment*: The alignment of tomographic tilt series can be done automatically. This is explained in more detail in Chapter 5.
- *Geometry models*: The geometry models are 3D objects describing the content inside a tomogram. They are defined manually or semi-automatically and are used to assist the definition of coordinates for subtomogram extraction.
- *Catalog*: The catalog is a database system that manages all tomograms of a project and keeps track of the relevant meta data and in particular of the geometry models.

⁴www.mathworks.com

- *Classification*: 3D classification can be done using multi reference alignment (MRA) or Principal component analysis (PCA).
- *Visualization and analysis tools*: A broad range of tools is provided to visualize and analyze 2D and 3D objects such as tomograms, subtomograms, masks, references, averages, alignment results and tilt series.
- *Independent functions*: Every function used in the processing and data analysis can be independently called. This enables users to create and customize their own tools and processing pipelines.

STA projects often deal with unique and complex geometries that can vary considerably depending on the sample. This is why the philosophy of *Dynamo* is to provide both, a complete streamlined processing workflow as well as a highly flexible and customizable toolbox for STA. This is achieved by providing user friendly GUIs for every main task and at the same time offering the option to design user specific procedures by creating project specific scripts and functions through combinations of independent *Dynamo* functions and normal MATLAB commands. The fact that MATLAB is a popular, user friendly and well documented scripting language is a great advantage for this type of tasks and also a main reason why *Dynamo* is written in this language.

Dynamo has successfully been used on a broad range of data sets to retrieve high-resolution cryo-ET structures [Hutchings et al. 2018; Kovtun et al. 2018; Kudryashev, Castaño-Díez, Deluz, et al. 2016; Schur, Obr, et al. 2016; J. Wang et al. 2017].

2. Motivation and Aim of this Thesis

The main goal of this thesis is to advance the field of STA in cryo-ET by improving dedicated computational methods. The motivation to push research in this direction lies in the fact that STA is the leading method for high-resolution structure determination in cryo-ET, a highly complex and challenging technique with extreme potential for the future and a strong influence in structural biology.

The choice of conducting the research with the *Dynamo* software for STA was based on the fact that it is currently one of the leading softwares for STA. It further serves the main goal of this thesis because of its high versatility and its direct in-house access.

With throughput being the main bottleneck in STA and cryo-ET (see Section 1.4), two projects were designed to address this specific problem:

- *Protocols for STA of virus like particles*: To streamline, simplify and automate the image processing in STA, a complete command line based STA pipeline was established. This project is presented in Chapter 4 in the form of a protocol paper to be submitted.
- *Automatic tilt series alignment*: A fully automatic and fast tilt series alignment, including various tools to simplify data management and visualisation, was added to the *Dynamo* processing pipeline. This project is presented in Chapter 5 as a manuscript to be submitted.

To put in use the established command line based processing pipeline and to identify potential areas for development, STA was performed on a complex biological sample in the form of the following collaboration:

- *Architecture of the SNX-BAR membrane coat*: The processing pipeline was extended with a range of specialized tools to determine the architecture of the SNX-BAR membrane coat on tubules. This project is presented in Chapter 6 as a manuscript to be submitted.

Additionally, a review paper about STA for cryo-ET was written and is presented in

Chapter 3. A summary and conclusion of the thesis is made in Chapter 7, including an outlook to what the near and far future of STA in general is expected to bring.

3. Subtomogram Averaging from Cryo-Electron Tomograms

3.1. Comment

In this chapter, a review paper is presented that covers all aspects of subtomogram averaging in cryo-ET, ranging from sample preparation, data acquisition, tomographic reconstruction, image processing pipelines and software packages. My main contributions as third author were writing parts and creating figures related to the mechanics of subtomogram averaging, plus editing and revising text and figures of all sections. For this thesis, I added a few more relevant references. This review paper was published as a chapter in the book Muller-Reichert et al. 2019 with the title:

Subtomogram averaging from cryo-electron tomograms

Kendra E. Leigh^{1,2}, Paula P. Navarro³, **Stefano Scaramuzza**³, Wenbo Chen^{1,2}, Yingyi Zhang^{1,2}, Daniel Castaño-Díez^{3,4*}, Misha Kudryashev^{1,2*}

¹ *Max Planck Institute for Biophysics, Frankfurt am Main, Germany*

² *Buchmann Institute for Molecular Life Sciences, Goethe University of Frankfurt, Frankfurt am Main, Germany*

³ *Center for Cellular Imaging and Nano-Analytics (C-CINA), Biozentrum, University of Basel, Basel, Switzerland*

⁴ *BioEM Lab, Center for Cellular Imaging and Nano-Analytics (C-CINA), Biozentrum, University of Basel, Basel, Switzerland*

*Correspondence to: daniel.castano@unibas.ch, misha.kudryashev@biophys.mpg.de

Published in: *Methods in Cell Biology*, vol. 152, pp. 217-259. Academic Press, 2019.
doi: 10.1016/bs.mcb.2019.04.003

3.2. Abstract

Cryo-electron tomography (cryo-ET) allows three-dimensional (3D) visualization of frozen-hydrated biological samples, such as protein complexes and cell organelles, in near-native environments at nanometer scale. Protein complexes that are present in multiple copies in a set of tomograms can be extracted, mutually aligned, and averaged to yield a signal-enhanced 3D structure up to sub-nanometer or even near-atomic resolution. This technique, called subtomogram averaging (StA), is powered by improvements in EM hardware and image processing software. Importantly, StA provides unique biological insights into the structure and function of cellular machinery in close-to-native contexts. In this chapter, we describe the principles and key steps of StA. We briefly cover sample preparation and data collection with an emphasis on image processing procedures related to tomographic reconstruction, subtomogram alignment, averaging, and classification. We conclude by summarizing current limitations and future directions of this technique with a focus on high-resolution StA.

3.3. Introduction

3.3.1. General considerations on cryo-ET

Cryo-electron microscopy (cryo-EM) has revolutionized the field of structural biology due to its ability to determine high-resolution structures over a broad scale range, from purified proteins to large macromolecular complexes and cell organelles (Figure 1). The two major structural techniques in cryo-EM are: (i) single particle analysis (SPA), and (ii) cryo-electron tomography (cryo-ET) combined with subtomogram averaging (StA). SPA determines high-resolution structures of purified proteins and protein complexes in solution by exploiting their random orientation in vitreous ice to collect two-dimensional (2D) views of the target from multiple angles. These 2D views are then used to computationally reconstruct a three-dimensional (3D) structure of the macromolecule of interest. On the other hand, in cryo-ET, the microscope stage is progressively tilted to acquire a set of micrographs, called a tilt series, from multiple angles. The tilt series is then used for a computational *3D reconstruction*, which results in a 3D volume (*tomogram*) of the entire region of interest. StA can be used when multiple copies of a target macromolecule are contained in one or more tomograms. These copies can be extracted from the tomogram(s) as so called *subtomograms*, which are then computationally aligned to each other and averaged to retrieve the 3D structure of the macromolecule.

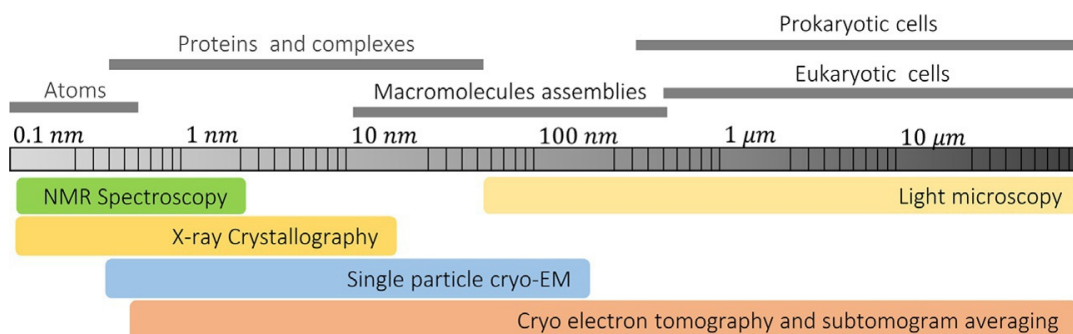


Figure 3.1.: **Scales and techniques in molecular and cell biology.** The scale ranges covered by different imaging approaches in molecular and cellular biology from atoms to cells.

In cryo-EM, the interaction between electrons and the sample generates contrast, but this interaction also damages the sample, imposing a limit on the total number of electrons that can be tolerated before features in the sample become too degraded (the *electron dose*). In cryo-ET, the imaging target area must be exposed multiple times to generate the *tilt series*. The total electron dose of approximately $100 e^-/\text{\AA}$ for an entire tilt series, generally composed of 40 to 60 images, is only 1-3 times the electron dose used for a single image in SPA. As a result, the electron dose per image is much lower, and therefore, individual cryo-ET images are much noisier than SPA images. After acquisition, this tilt series is computationally aligned and corrected for distortions. The aligned tilt series

is then used to calculate a 3D tomographic reconstruction, which can then be used for StA. StA requires that the 3D coordinates of each protein complex of interest are identified within each tomogram in a process known as *particle picking*. *Subtomograms* containing the protein complexes (the *particles*) are extracted and iteratively aligned to a common reference. Aligned subtomograms may be grouped into classes first, but are finally averaged to reinforce common signal, resulting in 3D structures with higher resolution than present in individual subtomograms. Importantly, cryo-ET and StA are capable of visualizing protein complexes *in situ* in different conformational states, bound to interaction partners, and in the context of other macromolecules and cell organelles.

3.3.2. Applications of high-resolution StA

Cryo-ET and StA have been used to unravel the molecular mechanisms involved in fundamental biological processes, including virus maturation, bacterial survival, and protein trafficking. An example of the power of this technique is the pioneering research on the HIV capsid from the Briggs group, which has set the standard for high-resolution cryo-ET and StA. The first HIV capsid structure in native virions yielded 8.8 Å resolution using conventional CCD cameras [Schur, Hagen, Rumlová, et al. 2015]. However, with the advent of direct electron detectors, the group was able to improve the resolution to 3.9 Å [Schur, Obr, et al. 2016]. Later, application of a 3D-CTF-correction algorithm to this dataset improved the resolution even further to 3.4 Å [Turoňová et al. 2017]. These improvements in resolution revealed crucial molecular interactions for the native assembly of immature HIV-1 virions.

Wan and colleagues applied StA to the study of the nucleocapsid of Ebola virus [W. Wan, Kolesnikova, et al. 2017]. Ebola virus has an RNA genome that is encapsulated by a set of viral proteins, which condense to form the helically ordered nucleocapsid. StA was applied to determine the viral nucleocapsid structure within intact virions and nucleocapsid-like structures derived from virus-like-particles and purified nucleoprotein. The highest resolution structure reached 6.6 Å, allowing unambiguous identification of alpha-helices. The resulting StA reconstructions were of sufficiently high resolution to permit fitting of available atomic models into the densities, revealing the molecular basis of nucleocapsid formation.

Cryo-ET has also been instrumental in uncovering fundamental aspects of microbiology through the imaging of intact bacterial cells, and by combining StA with high-resolution information obtained using other structural techniques (reviewed in Cyrklaff et al. 2017 and Oikonomou et al. 2016). Notably, Bharat and colleagues applied a hybrid approach to study the protective surface layer (S-layer) composed of repeating surface layer proteins (SLPs) encapsulating bacteria. They solved the structure of the S-layer monomer using X-ray crystallography and fitted it into the *in situ* structure of the oligomer, determined from cell stalks and solved by StA to a resolution of 7.4 Å [Bharat, Kureisaite-

Ciziene, et al. 2017]. This combined model showed an S-layer organization with multiple gaps of varying size, and this study is an example of how cryo-ET and StA can be integrated with other structural approaches to study native molecular arrangements over a range of size scales (Figure 3.1).

StA has also been applied to study the organization of membrane-assembled protein complexes to advance the understanding of protein-lipid interactions. StA analysis by Pfeffer and colleagues of the ribosome-Sec61 complex in native endoplasmic reticulum-derived vesicles resulted in a structure that locally reached sub-nanometer resolution. This native “idle” complex structure revealed Sec61 in a laterally open conformation, a conformation previously thought to only exist transiently during the “inserting state” based on previous cryo-EM structures of detergent solubilized complex [Pfeffer et al. 2015]. Recently, StA has also been applied to *in vitro* reconstituted components of the protein trafficking machinery. Kovtun and colleagues determined the structure of membrane-assembled retromer associated with the sorting nexin protein (Vps5) to a resolution range of 8.7 to 9.4 Å [Kovtun et al. 2018], and Hutchings and colleagues reported the structure of *in vitro*-reconstituted, membrane-bound, inner COPII coat at a resolution of 4.9 Å. This 4.9 Å resolution allowed visualization of a membrane-embedded Sar1 amphipathic helix that imparts membrane curvature, and which is absent in the X-ray structure [Hutchings et al. 2018].

The examples highlighted above demonstrate that biological context is critical to protein function. Tomography naturally includes information on the spatial environment, such as the relative orientation of protein complexes within a cell, for example. StA extracts high-resolution structural information (Figure 3.2, blue line) from this contextual data, and gives these structures functional meaning.

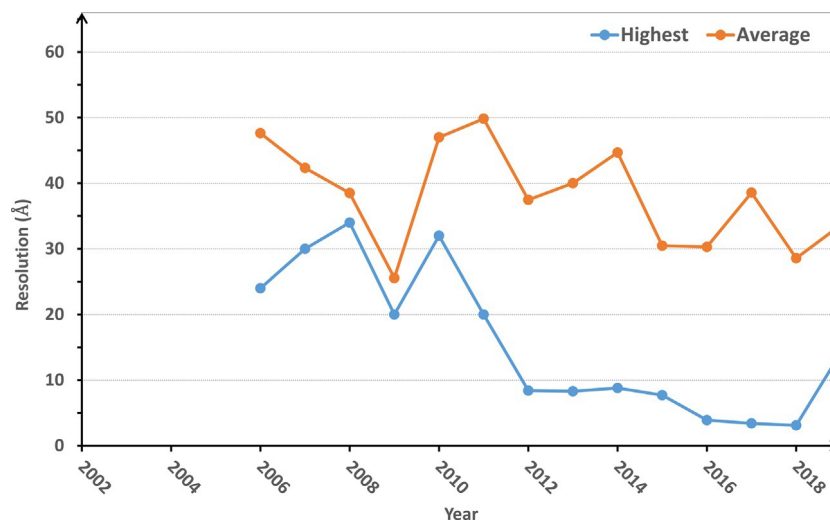


Figure 3.2.: **Resolution trends for subtomogram averaging.** The minimum (blue) and average (red) resolution deposited to the Electron Microscopy Data Bank (statistics available at www.ebi.ac.uk/pdbe/emdb) as of the end of March 2019.

3.4. Sample preparation for cryo-ET

StA can be successfully performed using tomograms of purified protein complexes, vesicles, viruses [Schur, Obr, et al. 2016; W. Wan, Kolesnikova, et al. 2017], purified organelles [Davies et al. 2011; Kosinski et al. 2016], or even intact bacteria and eukaryotic cells [Kudryashev, Stenta, et al. 2013; Nans et al. 2015]. However, the primary factor for consideration when preparing a sample for cryo-ET is sample thickness. The mean free path of an electron accelerated at 300 kV is on the order of 300 nm [Rice et al. 2018], and thicker samples have an increased likelihood of multiple and inelastic scattering events as the electrons pass through the sample, leading to deterioration of image quality. Furthermore, as the sample is tilted for tomography, the effective electron path increases proportionally to $1/\cos(\theta)$, where θ is the tilting angle. The method selected for sample preparation must not only consider how sample thickness will affect vitrification, but must also include steps to thin the sample if necessary. To-date, high-resolution StA structures, such as those outlined in Section 3.3, were all obtained from thin-ice samples prepared by plunge freezing. In the case of thicker samples, e.g., eukaryotic cells, high-pressure freezing followed by cryo-sectioning [Al-Amoudi et al. 2004] or cryo-focused ion beam (cryo-FIB) milling may be used to produce thinner samples for imaging [Villa et al. 2013], both of which are discussed in greater depth below.

3.4.1. Plunge freezing

For specimens thinner than 300-500 nm, conventional plunge freezing, in which the liquid sample is rapidly vitrified in a cryogen [Dubochet and McDowell 1981; Villa et al. 2013], has been shown to be successful for the imaging of biological samples by electron microscopy (reviewed in Dubochet, Adrian, et al. 1988). Advantageously, as the sample for plunge freezing is usually applied to the grid in liquid form, gold fiducials may be easily added to the sample for later use in tilt series alignment (see Section 3.6.2). Recently, increasing attention has been focused in the SPA field on how sample preparation by plunge freezing may result in interaction of the protein sample with the air-water interface, leading to partial or complete protein denaturation [Noble, Venkata P. Dandey, et al. 2018]. A number of approaches have been proposed to limit the effect of the air-water interface including the use of surfactants or grids with a continuous carbon or affinity-based back-support (reviewed in Glaeser 2018 and Glaeser and B.-G. Han 2017), or even faster plunging times [Noble, Wei, et al. 2018]. Preparation of some types of cryo-ET samples could potentially also benefit from these approaches and gain similar advantages to those observed with SPA samples.

3.4.2. High-pressure freezing and cryo-sectioning

This combination of techniques is commonly used for structural preservation of cell cultures and tissues. The sample is first vitrified under high-pressure in the presence of a cryoprotectant. The use of high-pressure increases the thickness of the specimen which can be vitrified from approximately 10 μm to hundreds of microns (reviewed in Dahl et al. 1989 and Moor 1987). The frozen sample is then sectioned into 50 nm to 150 nm sections with a diamond knife at cryogenic temperatures keeping the sample vitreous and thin enough to be observed in cryo-EM [Al-Amoudi et al. 2004; Matias et al. 2003]. High pressure freezing and cryo-sectioning can be combined with cryo-ET and StA [Al-Amoudi et al. 2007; Cai et al. 2018]; however, it is not always possible to incorporate gold fiducials into these samples, necessitating the use of markerless tilt series alignment (see Section 3.6.2). Common drawbacks of the technique are the cutting artefacts that appear on the ice surface during cryo-sectioning and the associated compression of the sample in the direction of cutting.

3.4.3. Cryo-focused ion beam (FIB) milling

Cryo-FIB milling is used to prepare thin samples either vitrified directly on EM grids or cut from high-pressure-frozen samples. A gallium ion beam is used to mill unnecessary layers of sample in a target region, leaving 200-400 nm-thick lamellae that can be subsequently imaged by cryo-EM [Marko et al. 2007]. Cryo-FIB-milling (reviewed in Rigort et al. 2015 and Mahamid et al. 2015) overcomes the sample thickness limit, enabling cryo-ET on eukaryotic cell cytoplasm and tissue [Mahamid et al. 2015].

3.5. Aspects of data collection for subtomogram averaging

For methods on automated data collection, the reader is referred to G. Resch (Software for automated acquisition of electron tomography tilt series, this volume). Here, we briefly describe the major data collection considerations for StA.

3.5.1. Data quality

Assuming optimal microscope alignments, data quality can be further improved by minimizing sample drift due to stage tilting with the incorporation of stage settling time during acquisition, by optimizing ice quality and thickness through manipulation of blotting conditions and sample composition, and by enhancing contrast through the use of a precisely tuned energy filter. Data quality can also be affected by the choice of imaging magnification as currently even high-end microscopes have magnification anisotropy, which results in pixel size variation across different areas of the image [Grant et al. 2015a]. At intermediate magnifications, this variation can be as high as 2.7%, resulting in distortions up to tens of pixels for a 4k micrograph. Higher magnifications have reduced anisotropic magnification [Grant et al. 2015a]. Furthermore, high resolution information is better preserved at higher magnifications due to transfer of the same physical frequency with higher intensity than at lower magnifications [G. McMullan et al. 2009]. For these reasons, high-resolution structural analyses are typically performed at higher nominal magnifications, to avoid magnification anisotropy altogether. Alternatively, magnification distortion should be measured and corrected [Grant et al. 2015a]. The impact of magnification choice on throughput is discussed further in Section 3.5.3.

3.5.2. Dose distribution

Due to radiation damage of the sample by the electron exposure, high resolution information is concentrated in the early image frames and at lower angles of tilting where the sample is thinner [Bartesaghi, Lecumberry, et al. 2012; Bharat, Russo, et al. 2015; Grant et al. 2015b]. This time-dependent loss of signal means that the distribution of the limited electron dose (typically 80-150 e^-) across the tilt series is a significant factor for consideration. A classical approach is to apply higher electron dose when acquiring at higher tilt angles [Grimm et al. 1998] to compensate for the increased sample thickness. However, if higher tilts are exposed to more of the fixed total dose, then less dose is available for acquisition of the low-tilt micrographs, which contain more high-resolution information. A balance must be reached between distributing more dose to the low-tilt

images earlier in the acquisition sequence and ensuring high-tilt images have sufficient signal and frequency information to contribute to the reconstruction. Commonly used data collection strategies are:

- a) A *bi-directional* tilt scheme starting from 0° with recording of a half-dataset in increments until the maximum tilt is reached, e.g., 0° to 60° , followed by a return to 0° , and acquisition of the second half-dataset to the opposing symmetric tilt maximum, e.g., -3° to -60° . A drawback of acquiring tilt series as two non-continuous halves is that beam-induced sample movement accumulates between recording of the low-tilt images in the first half and recording of the low-tilt images in the second half. This gradual image deformation results in a significant “jump” in the positions of the sample and fiducial markers in the tilt images on either side of 0° . This “jump” makes it difficult to accurately align the two halves of the tilt series, which negatively affects the quality of the resulting reconstruction.
- b) A bi-directional tilt scheme starting at moderately low tilt, e.g., 20° - 30° with recording at increments through 0° to the maximum negative tilt angle, e.g., -60° , before returning to the starting tilt angle and acquiring the remaining missing positive angles [Pfeffer et al. 2015]. This scheme suffers from the same drawback as (A) but advantageously allows all the low tilt angles to be imaged earlier in the acquisition sequence, when the sample has less accumulated radiation damage.
- c) A *dose symmetric* scheme that begins at 0° and alternates between positive and negative tilt angles allows the low-tilt images to be recorded first without recording halves of data, thus avoiding the associated beam-induced “jump” [J.-J. Fernández, Sam Li, and Agard 2019]. It should be noted that this scheme requires large angular changes in stage tilt when alternating between positive and negative angles, which can result in greater stage-movement-induced drift that must be accounted for through a combination of stage settling time and post-processing (i.e., motion correction).
- d) Finally, any of the above tilt schemes can be modified by recording an un-tilted (0°) image with a higher electron dose of $\sim 30 e^-/\text{\AA}^2$. This approach has been previously shown to yield higher resolution after the application of customized image processing routines [K. Song et al. 2018].

Most of the reported high-resolution StA structures have typically been recorded with a dose-symmetric tilt scheme ([J.-J. Fernández, Sam Li, and Agard 2019], approach C discussed above) using a constant electron dose for each tilt, favouring the preservation of high-resolution signal in the low-tilt images.

3.5.3. High throughput

Large numbers of particles are required to obtain high-resolution structures or to perform classification of particles into several functional states. Therefore, the number of tomograms that can be acquired per microscope session and the number of particles present in each tomogram are important considerations for the resolution of the final reconstruction. Reducing the microscope magnification increases the field of view and typically results in a larger number of particles per tomogram. However, using a lower magnification results in lower data quality (see section 3.5.1). On the other hand, at higher magnification the field of view is limited, resulting in reduced total particle number, which could potentially limit the resolution of the StA structure. The choice of magnification for data collection should balance throughput and quality, and should be designated based on target resolution, particle abundance, and expected molecular heterogeneity.

Automated data collection includes focusing and position tracking steps (X-Y) in order to keep the region of interest in the field of view, and the mechanical drift that occurs after incrementing the stage tilt must be monitored. Stage drift is tracked at a pre-selected focusing location, so that micrographs are only acquired after the drift rate has dropped below a pre-set threshold [J.-J. Fernández, Sam Li, and Agard 2019]. Drift monitoring and/or autofocusing more frequently than necessary adds non-productive time to the data collection routine. As drift monitoring and autofocusing are currently needed due to mechanical limitations in stage stability, the next generation of microscope hardware could help reduce the duration of non-data-collection steps. Currently, high-throughput tomography approaches requiring only 13-20 minutes per tilt series have been successfully implemented [Henderson et al. 2018; Morado et al. 2016]; however, these approaches have not yet yielded high-resolution subtomogram averages. The reported high-resolution structures that have been produced to-date prioritized data quality over throughput.

3.6. Generation of tomograms for StA

Once the tilt series have been acquired, these must be processed and used to computationally reconstruct 3D volumes known as tomograms. The resolution of cryo-electron tomograms is limited by factors from a number of sources:

1. Acquisition geometry (e.g., angular sampling, the missing wedge).
2. Low signal-to-noise originating from the limited electron dose.
3. Microscope optics (e.g., microscope misalignment and lens aberrations, limited precision of CTF correction).
4. Processing and reconstruction imperfections (e.g., tilt series alignment).

StA efficiently compensates for the limited electron dose and the geometric factors; however, sub-optimally generated tomograms will limit the quality of the resulting StA structures. A more detailed overview on the factors affecting the resolution of tomograms and StA structures can be found elsewhere [Kudryashev 2018].

Tomographic reconstruction involves four major steps: pre-processing of the tilt series, including drift correction of each tilt image to compensate for sample movement; CTF correction to recover high-resolution information; tilt series alignment; and 3D reconstruction.

3.6.1. Pre-processing: Motion correction and dose weighting

As the sample is being imaged, it experiences movement from two major sources: stage drift after each mechanical rotation and beam-induced motion of the vitreous material. Dose-fractionated movies recorded on direct electron detectors allow efficient measurement and correction of the movement related to global drift [Brilot et al. 2012; X. Li et al. 2013]. However, beam-induced motion [Bai et al. 2013; Brilot et al. 2012; Glaeser 2016; X. Li et al. 2013] can result in complex sample movement that is more difficult to account for during pre-processing. This beam-induced motion may not only result in lateral motion of particles in the field of view, but can also result in particle rotation and z-axis movement, which in turn affects particle defocus [Brilot et al. 2012]. Sample motion is initially rapid over the first few electrons applied to the sample, but slows as the electron dose accumulates.

Several software packages have been developed, originally for single-particle applications, which correct motion globally, such as Unblur [Grant et al. 2015b], and/or “locally” in

sub-divided tiles of the whole frame, such as MotionCor2 [S. Q. Zheng, Palovcak, et al. 2017], which originates from MotionCorr [X. Li et al. 2013]. In cryo-ET, the electron dose per tilt of $1\text{-}3\ e^-/\text{\AA}^2$ is much lower than the $30\text{-}60\ e^-/\text{\AA}^2$ used for SPA cryo-EM exposures. Due to this low electron dose, generally only a few image frames are recorded per tilt, to ensure sufficient signal is present in each image frame for the implemented algorithms to successfully align the frames to each other. It should be noted that the local movements occurring during the short exposure lengths of each tilt image are potentially very small. Therefore, it is not known if performing “local” motion correction of these images is necessary for resolution improvement during the subsequent StA.

Motion-correction algorithms are currently not able to completely eliminate the effects of sample motion. This has led to the development of other technical approaches to minimize sample motion from the outset. Use of commercially available gold grids have been shown to significantly minimize beam-induced motion [Russo et al. 2016]. This reduction in motion resulted in improved resolution for StA: hepatitis B capsid structures by Bharat and colleagues gained resolution, going from $9.7\ \text{\AA}$ to $8.1\ \text{\AA}$ through the use of gold grids over carbon ones [Bharat, Russo, et al. 2015]. Future progress in minimizing beam-induced motion through developments in sample preparation, data collection, and motion-correction will be beneficial for the resolutions attainable by StA.

As discussed in Section 3.5.2], radiation damage results in the gradual loss of high-resolution signal as the applied electron dose accumulates during imaging. Dose weighting can be applied to account for dose-dependent resolution decay by down-weighting high frequencies in the individual tilt images. The images recorded later in the tilt series acquisition sequence have higher accumulated electron doses and face stronger down-weighting of high frequencies. Dose weighting, also called *exposure filtering*, can be done in combination with motion correction and results in reduced noise [Grant et al. 2015b]. Unblur, MotionCor2, and other packages that perform motion correction are also able to do dose-weighting.

3.6.2. Tilt series alignment

The tomographic reconstruction of an object from a tilt series requires an accurate determination of the relationship between the microscope tilt axis, the tilt axes of each 2D projection and the internal coordinate system of the specimen [Lawrence 1992; Penczek, Marko, et al. 1995]. This process, called *tilt series alignment*, determines shifts, rotations, magnifications and sample deformations between each tilt image in the tilt series. These alignment parameters define the projection model used for tilt series alignment prior to tomographic reconstruction. Hence, tilt series alignment has a direct impact on the quality of the 3D reconstruction and therefore, on the attainable resolution in StA [Amat, Castaño-Díez, et al. 2010].

To accurately determine the alignment parameters for the tilt series in high-resolution cryo-ET experiments, fiducial markers are used [W. Wan and Briggs 2016]. Spherical gold beads are the most common fiducial marker, as gold scatters electrons more strongly than biological material and the projections of these spheres appear as high-contrast circles in the images, regardless of tilt angle [Amat, Castaño-Díez, et al. 2010]. Since these colloidal gold fiducials are commonly added to the specimen during cryo-ET sample preparation (see Section 3.4.1), the appropriate concentration and size of the gold beads must be determined ahead of time, based on the nature of the biological sample, the purpose of the experiment, and the planned magnification of the microscope. Commonly used gold fiducials are 5-10 nm in diameter.

Automated *location* of gold fiducials is possible by using peak-searching algorithms [Amat, Moussavi, et al. 2008; Brandt et al. 2001; Mastronarde and Held 2017]. However, automated *tracking* of gold fiducial positions through the tilt series remains a challenge for current software packages. Often, manual intervention is required to identify well-behaved gold fiducials that contribute to an accurate calculation of the alignment parameters. Manual intervention also helps to discern gold fiducial trajectories when they cluster or overlap in some images within the tilt series. Although recent developments in alignment algorithms have allowed automated tilt series alignment [Amat, Moussavi, et al. 2008; Mastronarde and Held 2017], manual intervention is still essential for high-resolution cryo-ET [Hutchings et al. 2018; Kovtun et al. 2018; Schur, Obr, et al. 2016]. This suggests that automated tilt series alignment remains a bottleneck in the field and therefore, research on automated marker detection and tracking is crucial for high-throughput cryo-ET and StA.

Before computing the alignment parameters, a projection model needs to be formulated. The projection model defines the geometric relationship between the positions of the gold beads in the tilt series and their 3D position in the sample. At its most basic formulation, the movement of the sample is assumed to be determined by a rotation of known magnitude θ_t around an unknown axis of rotation ψ that remains fixed during the acquisition of the tilt series, followed by an in-plane translation $(x, y)_t$ of unknown magnitude, where t represents each tilt. Solving this basic model involves finding values for the parameters $(x, y)_t$ and ψ that minimize the residuals, i.e., distances between the experimentally determined positions of the fiducials in the micrographs and the re-projection positions predicted by the model. The solution of this particular parameter-fitting problem can be easily computed by a linear least squares regression for each possible value of ψ . When the model is enriched with additional parameters, such as correction of the initial tilt angles, perturbation of the orientation of the tilt axis for each tilt, or consideration of possible electron beam tilt, the minimization problem needs to be solved by approximation, frequently using the solution of the most basic model as starting point. While the parameters described so far represent only rigid body transformations (combinations of rotations and translations), transformations involving image deformation may also be considered, e.g., local magnifications or anisotropic sample deformation [J.-J. Fernández, Sam Li, and Agard 2019; J.-J. Fernández, Sam Li, Bharat, et al. 2018].

The extension of the projection model with additional parameters necessarily improves the merit figure (given by the mean residual) of the alignment. However, this does not necessarily imply superior quality of the extended projection model: inclusion of parameters that do not model mechanisms actually in operation will result in overfitting, which may compromise the quality of the alignment. Besides physical considerations about the suitability of modelling different effects (caused by characteristics of the sample or the quality of the microscope), mathematical considerations can guide the choice of parameters entering the model. When gold beads are sparse, are unevenly distributed, or are missing in a large number of micrographs, a conservative approach based on the determination of the basic set of parameters ($(x, y)_t$ and ψ) is recommended. A large number of fiducial markers can also be advantageous as it allows the physical meaningfulness of parameter sets to be tested by solving the model using a subset of markers and observing the behaviour of residuals in a validation set of markers not used in the fitting.

Markerless alignment methods substitute the use of physical fiducial markers with computational analysis of the projection images of the sample. They are therefore the method of choice when inclusion of gold beads in the specimen is not feasible (for example, in cryo-FIB milled samples). Additionally, markerless alignment represents the motion of the sample directly, instead of characterizing the movement of fiducials. In spite of this, markerless alignment is often less accurate than marker-based alignment. The projection of the 3D center of any given gold bead can be located with high precision on each micrograph where it appears, due to the spherical shape and the intense contrast of its appearance in the projection image. In contrast, biological structures project as different noisy views in each tilted image, making the geometric relationship between two views of the same feature non-obvious *a priori* without further computation. Thus, the performance of markerless alignment is bound to show a high degree of dependence on the characteristics of the sample. Further, the quality of image features decreases for high tilts, as the increasing sample thickness decreases the signal-to-noise ratio and the tilting of the sample itself favours occlusion effects. In addition, use of dose-symmetric tilt schemes results in accumulated radiation damage at high tilts as outlined in Section 3.5.2 of this chapter [J.-J. Fernández, Sam Li, and Agard 2019], further reducing the precision of alignment.

All the principles for alignment model determination and the general workflow outlined in Figure 3.3 also apply for markerless alignment. Markerless alignment methods fall into one of two categories: feature-based alignment and alignment based on reprojections of a 3D-model. Alignator is an example of feature-based markerless alignment where biological features are treated as markers to determine the projection model [Castaño-Díez, Scheffer, et al. 2010]. *Protomo* is an example of projection matching of tilted images to a 3D model [Winkler 2007]. Here, the whole image or region of interest can be considered for an alignment cycle. Each alignment cycle consists of aligning tilted images to a reference 3D reconstruction, starting with the untilted image and adding consecutive higher tilted images until the entire tilt series is aligned. The initial

reference is determined by re-projecting a preliminary back-projection map, which is based on coarse-aligned images in the tilt series [Winkler and Taylor 2006]. Several alignment cycles are generally required to refine tilt series alignment until the alignment parameters converge, and the deviations between the model and the experimental data are minimized.

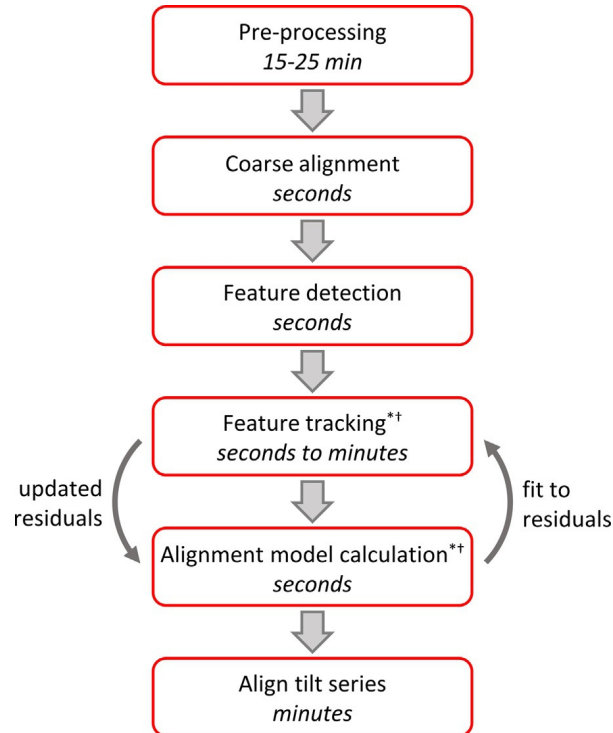


Figure 3.3.: **Tilt series alignment workflow.** After pre-processing the tilt images are ready for alignment. From coarse alignment onwards, all the steps are integrated in different software packages for tilt series alignment. Coarse alignment pre-aligns tilt images to create a stack on which feature detection and tracking is performed. Coarse alignment helps to assess tilt series quality. After that, an alignment model is determined together with the residuals of each feature. Feature positions can be manually corrected to obtain a new alignment model. Subpixel root mean square (RMS) residual values are often required when pursuing high-resolution STA projects, although values up to 2 Å may be sufficient. After pre-processing: in addition to the RMS values, quality check the tilt series by exploring the CTF at tilt 0° and tilt 30°. Thon rings to the expected resolution should be detectable by eye. *Manual detection of gold beads can make this step more time-consuming. †Manual intervention to fit residuals can make this step more time-consuming.

A summary of commonly used software packages for marker-based and marker-less alignment are listed in Table 3.1. A typical tilt series alignment workflow, as implemented fully or partially in different software packages is described in Figure 3.3. IMOD, the most popular software for tilt series alignment [Kremer et al. 1996], offers marker-based and markerless alignment. First, a coarse alignment is performed by cross-correlation of the tilt images to facilitate feature detection. In marker-based mode, a peak-searching

algorithm detects potential marker features in the 0° tilt image, while in markerless mode, the micrograph is divided semi-automatically into smaller sub-areas known as patches. Inaccuracies in identification of marker centers, selection of false fiducials, and identification of patch areas may all require manual intervention. It is convenient to ensure that selected features are distinguishable and evenly spread throughout the tilt series to facilitate unsupervised feature tracking. The identified gold fiducials or patches are then tracked across the tilt series, and their corresponding trajectories are computed. To obtain an accurate projection model, marker positions with high residuals are manually fixed in an iterative manner until an optimal root-mean-square (RMS) value is achieved. The RMS value is used in IMOD and other software packages to measure the imperfection of the 3D feature model with respect to the 2D positions of these features in the tilt series. Ten to fifty gold bead trajectories are often used to guarantee good accuracy, although in some cases as few as five fiducial trajectories may be sufficient. For high-resolution StA projects, the RMS value should be in the range of 0.1-1.3 pixels [Hutchings et al. 2018], which in the case of Hutchings et al., corresponded to a 0.13 to 1.7 Å error, and resulted in an StA structure with 4.9 Å resolution. However, it must be mentioned that in marker-based alignment, the RMS describes the quality of the fit with respect to the fiducial markers alone, and thus, motion of the biological sample itself may not be optimally modelled. In this case, manual intervention is necessary to correct feature trajectories, guided either by their residuals or by manually correcting inaccurate feature positions, generally occurring due to clustering and occlusion.

Table 3.1.: Software packages for tilt series alignment.

Software package	Alignment	Pipeline	Batching system	Time per tilt series	Comments	References
IMOD	Marker-based Patch tracking	eTomo GUI Command line	Yes	15–30min	Part of a complete pipeline Well-documented Easy installation Control of alignment parameters	Kremer et al. (1996) , Mastronarde (2005, 2008) , Mastronarde and Held (2017)
AuTom	Marker-based Markerless	GUI	No	5–10min	Complete pipeline Easy Installation No possibility for manual intervention	Han et al. (2017)
Protomo	Markerless	Webpage	Yes	Hours to days	Integrated in Appion Expertise required for installation	Noble and Stagg (2015) , Winkler and Taylor (2006)
Alignator	Markerless	GUI Command line	Yes	Minutes to hours	GPU accelerated Robust	Castaño-Díez et al. (2010)
RAPTOR	Marker-based	eTomo GUI	Through eTomo	15–30min	Same as IMOD	Amat et al. (2008) , Mastronarde and Held (2017)
TomoJ	Markerless	GUI Command line	Through ImageJ	minutes	Plug-in of ImageJ	Schneider, Rasband, and Eliceiri (2012) , Sorzano et al. (2009)

3.6.3. Tomographic reconstruction

The central slice theorem [R. N. Bracewell 1956] states that the Fourier transform of a projection is a 2D central slice of the 3D Fourier transform of the original real-space volume. This principle results in the simplest reconstruction technique in which central slices are calculated from projections, and the resulting 3D Fourier volume is transformed back to real space [De Rosier et al. 1968]. Due to the mechanical limitations of the microscope stage and the increased electron path in the tilted sample, tomograms are typically acquired to maximum tilts of $\pm 50^\circ$ - 70° . The resulting 3D reconstructions, generated by applying the central slice theorem, are incomplete in Fourier space as information corresponding to the missing tilt angles is absent, resulting in a *missing wedge*. The effect of the missing wedge in real space is anisotropic resolution: apparent elongation of features in the direction of the electron beam, combined with absence of horizontal features perpendicular to the beam.

Direct reconstruction of tomograms from megapixel-size cameras using the central slice theorem is computationally inefficient. To speed up computation, modern reconstruction algorithms for single-axis tomography leverage the fact that each layer of voxels parallel to the tilt axis can be reconstructed independently and in parallel [Ramachandran et al. 1971]. The weighted back-projection (WBP) [Harauz et al. 1986; Radermacher 2006] is the most common reconstruction algorithm. WBP is a modified form of the real-space simple back-projection, in which the back projection is further multiplied by a weighting function in Fourier space. This weighting function suppresses frequencies that are overrepresented due to the overlap of the projections in Fourier space, resulting in an analytical reconstruction. The weighting function can also be used to modulate the balance of frequencies: applying higher weights on low frequencies improves the apparent contrast of the reconstruction, while applying lower weights on low frequencies amplifies high frequencies and therefore, the associated noise.

The WBP algorithm does not restore the information in the missing wedge. Furthermore, depending on the applied weighting function, the reconstruction may suffer from poor contrast. Low contrast can not only make identification of particles or features of interest difficult, but can negatively affect subtomogram alignment precision. A number of iterative algorithms have been developed that seek to improve the contrast and fidelity of the reconstructions, and to suppress the apparent noise, typical of WBP. Early versions of these series-expansion-based algorithms, such as algebraic reconstruction techniques (ART) [Gordon et al. 1970], showed improved contrast over equivalent WBP reconstructions. ART iteratively calculates voxel values of the reconstruction based on data from each pixel (expressed as a ray-sum equation) in the projections, until the reconstruction is self-consistent with the projections. However, it was found that ART does not reach stable convergence when over-iterated, and in some cases, can lead to incorrect reconstructions. The simultaneous iterative reconstruction technique (SIRT) [Gilbert 1972] was proposed as an alternative to address ART's instability. Un-

like ART, SIRT processes all the projections, and the cumulative data is then used to update the reconstruction in a quadratic optimization approach. This algorithm results in smoother reconstructions and is less sensitive to noisy projection data, however, it takes longer to converge to a stable solution. The simultaneous algebraic reconstruction technique (SART) [Andersen et al. 1984] was proposed as a compromise between these two approaches. In each iteration, SART uses all the pixels from a projection to update the reconstruction, rather than pixel-by-pixel as is done in ART, but does not need to process all the projections simultaneously as with SIRT.

These iterative algorithms, however, may gain contrast at the cost of the high-resolution information needed for StA. This has led to development of the next generation of algorithms, specifically targeted towards StA. The iterative non-uniform fast Fourier transform (NUFFT) based reconstruction method (INFR) [Yuxiang Chen and Förster 2014] introduced a residual-function-based stopping criterion to prevent over-iteration, and thereby prevent over-fitting. Reconstruction of experimental data with INFR showed partial restoration of the signal in the missing wedge when compared to the WBP reconstruction [Yuxiang Chen and Förster 2014]. A related algorithm, the iterative compressed-sensing optimized non-uniform fast Fourier transform reconstruction (ICON; [Y. Deng et al. 2016]), combines NUFFT with compressed sensing, to restore the information in the missing wedge. Enhanced contrast was apparent in 3D reconstructions from experimental data using ICON compared to WBP. Furthermore, a ribosome structure calculated from 40 subtomograms improved resolution from 47 Å using WBP to 29 Å using ICON. However, both INFR and ICON are much more computationally expensive than WBP due to the number of iterations required to reach convergence. In contrast, a variation of the SART algorithm, super-sampling SART, which oversamples each pixel in a SART-like approach, generally reaches convergence in one iteration, making processing time equivalent to WBP [Kunz et al. 2014]. This algorithm showed fewer aliasing artefacts in Fourier space in comparison to non-oversampled WBP and testing of the reconstructions in StA showed less noise with particle-limited datasets. It should be noted, however, that the iterative algorithms discussed have not yet been extensively used for high resolution StA. More use of these algorithms will be needed to determine if they can achieve higher resolution subtomogram averages and replace WBP as the method of choice.

3.6.4. CTF determination in StA

Signal in electron micrographs is modulated by an oscillating non-linear contrast transfer function (CTF) [Erickson et al. 1971; Wade 1992] of the form:

$$CTF(f) = E(f) \sin(\pi C_s \lambda^3 f^4 / 2 - \pi \lambda d f^2)$$

where C_s is a spherical aberration of electromagnetic lens, λ is the electron wavelength, f is the spatial frequency and d is the applied defocus (negative for underfocus). $E(f)$

is an envelope function describing high-resolution information degradation. A realistic 1D CTF is presented in Figure 3.4A. In 2D, CTF rings called Thon rings are observed in the power spectra of micrographs [Thon 1966]. The oscillation of the CTF inverts the phases of the signal between every second CTF zero, and information at the zero-crossings is permanently lost. Unless the source tomograms are CTF-corrected and the frequencies that have been phase flipped are recovered, the resolution of the resulting StA structures will be limited to the first zero-crossing of the CTF [Kudryashev, Castaño-Díez, and Stahlberg 2012; Zanetti et al. 2009]. By fitting a theoretical CTF curve to the experimentally observed 2D Thon rings of a micrograph, the value of the applied defocus d can be estimated and the effect of the CTF on the signal can be partially reversed. CTF estimation can be complicated by objective lens astigmatism, which makes Thon rings elliptical rather than spherical, and results in defocus variation in different directions in the image. When astigmatism is present, two defocus values and the astigmatism direction, which are derived from the major and minor axis of the elliptical Thon rings, must be estimated. As the dose per micrograph in cryo-ET is low ($1\text{-}3\text{ e}^-/\text{\AA}^2$), there are only a few observable low-resolution Thon rings that can be used to fit the CTF curve and therefore, defocus and astigmatism determination is less precise.

Tomographic data has two additional factors essential for CTF determination and correction:

1. Cryo-ET samples are typically a few hundred nanometers thick, and this increases with tilting (as discussed in Section 3.4 and Figure 3.4B), resulting in a defocus gradient between the top surface and the bottom surface of the sample. Increased inelastic scattering of electrons and this defocus gradient reduces the amplitude of Thon rings at high resolution making estimation of defocus less precise.
2. Tilting also generates a defocus gradient along the direction of the electron beam. The maximal difference in height from the edge of the image below the focal plane (relative to which defocus was set) to the edge of the image above the focal plane is $D_2 = L \sin(\theta)$ where L is the size of the micrograph (Figure 3.6B). It should be noted that, speaking practically, only the maximal height difference between the objects that were in the original field of view in the untilted image is relevant due to the later step of 3D reconstruction. This defocus gradient means that different areas of the micrograph are at different defoci, deteriorating the Thon rings perpendicular to the direction of the tilting axis.

Incorrect estimation of defocus values results in an imprecise correction of the CTF, which limits the resolution of the final reconstruction. For example, an error in the defocus estimation of 250 nm limits the resolution to 10 angstrom, and an error of 63 nm limits the resolution to 5 Å [Kudryashev 2018]. Quantitative estimates of this effect are available for single particle cryo-EM [X. Zhang et al. 2011] and StA [Kudryashev 2018].

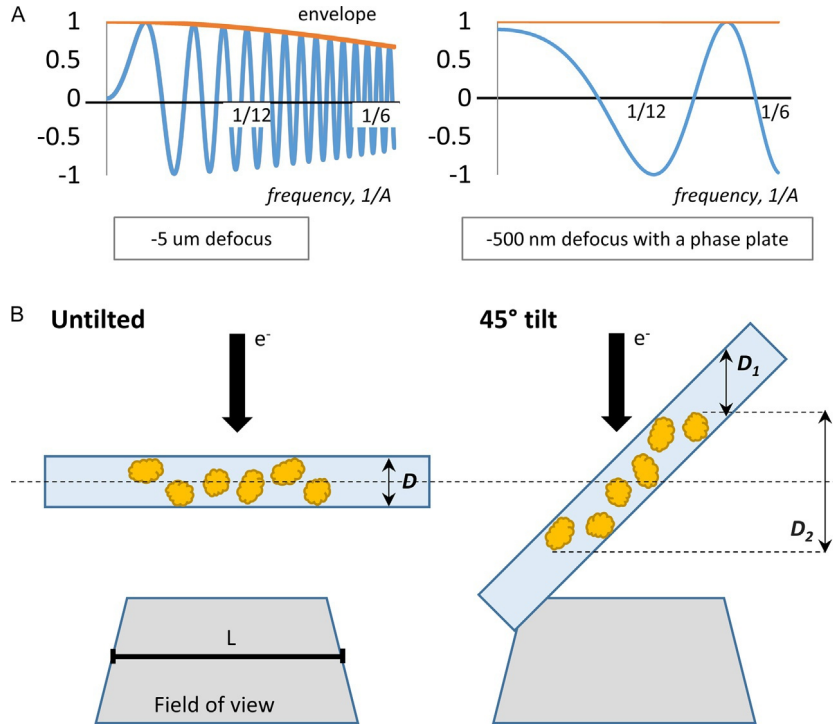


Figure 3.4.: **Contrast transfer function and defocus gradients in cryo-ET.** A) A simulated CTF curve of a 300-kV microscope with $C_s=2.7$ mm and a 3 angstrom pixel size. The left curve is simulated at $-5 \mu\text{m}$ defocus and the right one at $-500 \mu\text{m}$ defocus with a phase shift of 90° . Orange lines represent envelope functions dampening the high frequencies with increasing defocus. B) Effect of tilting on the defocus gradient: sample of thickness D becomes thicker relative to the electron beam while tilting adds a defocus difference D_2 between the top and the bottom of the sample.

CTF determination and correction is conventionally performed prior to reconstruction of the tomogram and operates directly on the 2D-images. In the strip-based periodogram approaches to 2D-CTF correction applied in TomoCTF [J.-J. Fernández, S. Li, et al. 2006] and IMOD [Xiong et al. 2009], each tilt image is divided into strips oriented parallel to the tilt axis, which are treated as areas of uniform defocus. To estimate the defocus at the center of a tilt image, a strip centered on the tilt axis is further subdivided into overlapping tiles and the power spectrum is calculated for each tile. These resulting spectra are averaged together to create a mean spectrum, which is used to estimate the defocus for the strip. This central defocus is then used to extrapolate the defocus for each of the other strips in the images using the simple relationship: $dx = d_0 + d \tan(\theta)$, where dx is the defocus of the strip being calculated, d_0 is the defocus of the tilt-axis strip, d is the distance to the tilt axis, and θ is the tilt angle. For each strip, the extrapolated defocus is used to estimate the CTF for that strip and flip the phase accordingly.

The basic steps of the strip-based periodogram approach can be varied in multiple ways to better compensate for the low signal-to-noise: by defocus estimation directly from multiple strips, by inclusion of tiles from other tilts with equivalent defocus in the tile

average, or even by inclusion of tiles from other tilts with different defoci in the average by shifting the power spectrum to align the CTF zeros. Instead of consecutive strips, the plane can be divided into overlapping strips, or into tiles instead of strips [Winkler and Taylor 2003]. Interpolation of pixel values between strips can be used to ensure smooth transitions at strip edges after correction, and different approaches to background subtraction, amplitude correction, and incorporation of astigmatism have been suggested. The defocus along the tilt axis of each image can also be estimated using programs commonly applied to single-particle data, such as CTFFIND4 [Rohou et al. 2015] or Gctf [K. Zhang 2016], and the results ported into a tomographic 2D-CTF correction algorithm. However, the low signal-to-noise ratio of tomographic tilt images makes estimation of the CTF less robust and precise than with single particle data, as the power spectra of higher tilt images potentially show few Thon rings for fitting. For single particle cryo-EM, the high electron dose per image makes automated detection of geometry possible [Su 2019], while for noisier images from tilt series the orientation of the tilting axis and therefore the relative difference in defocus is known from the geometry of data collection.

As an alternative to detecting CTF from the images directly, Eibauer and colleagues proposed an approach in which two additional images are recorded along the tilt axis on either side of the target recording location [Eibauer et al. 2012]. These two images, recorded on carbon with higher dose than is used for the tilt series images, have much higher signal and their average allows for precise determination of defocus at the target site. StA that reached sub-nanometer resolution using data recorded on CCD cameras [Schur, Hagen, Marco, et al. 2013] focused multiple times very close to the area of interest in order to accurately establish a stable target defocus value. While these approaches may have been necessary prior to the use of direct detector cameras, currently, even low dose images can often provide enough signal for CTF determination.

3.6.5. CTF correction for StA

Once the defocus is estimated, whether from the whole image, or from tiles or strips, and a theoretical CTF is calculated, this information must be applied for CTF correction. The simplest form of CTF correction is phase-only correction in which negative phases are flipped between the zeros of the CTF to compensate for the original inversion [Xiong et al. 2009]. This can also be combined with amplitude correction, which is conventionally implemented through application of a Wiener filter, sometimes with additional filtering included to address high magnitude and noise-dominant components separately [J.-J. Fernández, S. Li, et al. 2006]. Nothing can be done to restore the data lost at the CTF nulls; however, frequency nulls in subtomogram averages can be filled in by including particles from tomograms recorded at different nominal defocus values.

2D-CTF correction only addresses the defocus gradient that stems from the tilting of

the sample. As mentioned in Section 3.6.4 (CTF correction, consideration #1), sample thickness also generates a defocus gradient in the sample parallel to the electron beam. At higher resolutions, the error in CTF determination related to this gradient limits the resolution, and the effect of sample thickness on defocus must be factored into the correction [X. Zhang et al. 2011]. CTF-correction which accounts for both defocus gradients is referred to as 3D-CTF correction. As it is computationally more intensive than 2D CTF correction and only becomes significant at higher resolution, examples of 3D CTF correction being applied to subtomogram averaging are relatively recent.

The currently reported 3D CTF correction algorithms are implementations of a concept presented by Jensen and Kornberg in 2000 for “defocus-gradient corrected back-projection”, which was originally targeted to defocus correction for very large particles such as viruses [Jensen et al. 2000]. The idea is based on the premise that a volume containing particles at multiple z-heights results in a summed projection where each particle in the image was imaged at a different defocus level, and therefore, is affected by a different CTF function. Therefore, the voxels of a slab containing a given particle should be back-projected from a copy of the original micrographs that have been corrected for the CTF appropriate to the defocus of that particle, an approach that was later mathematically validated by [Kazantsev et al. 2010]. Computing power was limiting at the time it was proposed and this hampered the practical implementation. Kunz and Frangakis combined this slab-by-slab reconstruction approach to account for 3D CTF with the SART principle, minimizing the difference between a tilt image and the equivalent CTF-affected projection of the tomogram being reconstructed [Kunz et al. 2017]. Later emClarity [Himes et al. 2018] and NovaCTF [Turoňová et al. 2017] implemented versions of 3D-CTF correction with WBP that replicate Jensen & Kornberg’s original idea and released it as accessible software packages.

Unlike most CTF correction approaches, which are applied on the whole tomogram level, per-particle CTF correction, is applied to subtomograms by accounting for the known height of each particle in each tomogram. This approach has been introduced in Relion [Bharat, Russo, et al. 2015] and in EMAN2 [Jesús G. Galaz-Montoya et al. 2015]. The Relion approach uses a 3D CTF model that combines the defocus information for each particle in the tilt series. These values are determined through a combination of the 3D particle position relative to the tilt axis, and the known global defocus for each image in the tilt series. The EMAN2 approach similarly estimates the defocus for each subtomogram, and explicitly incorporates z-height into the defocus values for each particle. Both of these approaches have the highest precision CTF correction, but both still rely on global defocus estimates and are therefore still sensitive to imprecise determination of this value from noisy micrographs.

3.6.6. Phase plate data and CTF-correction

As discussed in Section 3.6.3, the contrast of a tomogram has an effect on the accuracy of subtomogram alignments. One of the proposed ways to improve the contrast in tomograms and to get intermediate-resolution StA structures with limited data is the use of phase plates. Phase plates, of which the Volta phase plate (VPP) is commercially available, have been introduced as a method of recovering phase contrast and adding low-frequency information, especially close to focus [Danev, Buijsse, et al. 2014], (Figure 3.4A). Asano and colleagues recorded tomograms from vitrified neuronal cells cultured directly on EM grids using a VPP. StA of the 26S proteasome from these tomograms resulted in multiple structures, the best of which had a resolution of 27 Å [Asano, Fukuda, et al. 2015]. Interestingly, the resolution of individual 26S proteasome subtomograms varied between 35 and 55 Å, recapitulating the resolution range of reported StA structures in general (Figure 3.2), suggesting that, in principle, an average StA structure could be done from only a few particles using a VPP. Khoshouei and colleagues collected data on isolated ribosomes to directly compare the effect of the VPP to conventional defocus imaging on StA at near-sub-nanometer resolution. Use of the VPP resulted in a 9.6 Å reconstruction in comparison to the 10.6 Å obtained with the use of defocused data collection, using a relatively small amount of data (1400 particles) [Khoshouei et al. 2017].

However, the application of a phase plate during data collection hampers determination of defocus from the resulting low-dose projection images for two reasons: (1) the need to fit three parameters - defocus, astigmatism and phase shift to the CTF curve as compared to only defocus and astigmatism without a phase plate, and (2) the fact that first zeros of the CTF with the phase plate are in higher resolution frequencies than without a phase plate, making fitting of the CTF less robust (see Figure 3.4A). As a result, most high-resolution StA structures are currently generated using standard defocus imaging instead of a phase plate. Future improvements in phase plate hardware and specialized software for phase plate data may result in higher resolution StA and encourage greater use.

3.7. Subtomogram averaging

3.7.1. Particle picking from tomograms

StA starts with locating the particles of interest in cryo-electron tomograms and defining their coordinates. This process is known as *particle picking*. Identification of the initial orientation of the particles allows a straightforward generation of an initial reference for StA by averaging the particles in their initial orientations. It further reduces the angular search space, minimizing computation time for subtomogram alignment. Several strategies for particle picking exist:

1. *Manual picking of particles in 3D volumes.* Manual picking is a laborious process. Currently, to our knowledge, no sub-nanometer structures have been reported using manual picking.
2. *Particle picking relative to a support geometry such as an axis (e.g., along a filament) or over a 2D surface (e.g., a membrane).* Modelling the support geometry and defining a fixed spacing along the axis or surface allow automatic definition of subtomograms, each containing a putative particle, at regular intervals along the support geometry. This approach allows two out of the three initial orientation angles to be defined based on the direction of the axis or normal to the surface. Examples of using support geometries include defining particles along microtubules [Grange et al. 2017], over the surfaces of vesicles [Kudryashev, Castaño-Díez, Deluz, et al. 2016] or along densely packed protein arrays [Hutchings et al. 2018; Kovtun et al. 2018; Schur, Obr, et al. 2016].
3. *Automated particle picking using template matching* [Förster, B.-G. Han, et al. 2010]. This approach requires a template for picking. The template is computationally rotated and cross-correlated against all positions in the tomogram. Positions and angles corresponding to the highest cross-correlation values are ranked and subtomograms are extracted from the highest ranked locations. The template matching procedure is high-throughput; however, the use of a template has the potential to introduce high resolution bias during particle selection. Therefore, care is needed when this approach is used.
4. *Supervised particle picking by pre-trained neural networks.* In this approach, the user provides an annotated training dataset with regions of the tomograms that contain both the features of interest and the negative controls [M. Chen, Dai, et al. 2017]. A convolutional neural network is trained on these inputs and then applied to identify new instances of the defined feature in multiple tomograms. The approach has been successfully used to segment cellular membranes, microtubules, and to pick large macromolecules, e.g., ribosomes, from cryo-ET data [M. Chen,

Dai, et al. 2017]; however currently, this approach has only been applied to 2D slices of 3D tomograms.

3.7.2. Mechanics of subtomogram averaging

3.7.2.1. Cross-correlation maximization

The classical approach to subtomogram averaging seeks to recover the common signal in the collected particles by an iterative process that alternates *alignment* and *averaging* steps. During the alignment step, each subtomogram is *aligned* against a single reference volume called a *template*; i.e., the procedure determines the translation and rotation needed to transform the subtomogram such that it maximizes the similarity of the template and the subtomogram. These identified alignment parameters are used in the averaging step to produce an improved template. This procedure is iterated until some predetermined convergence criterion is met. In practice, the full dataset is split into two independent datasets that are aligned and averaged separately. This approach, extensively applied in single particle cryo-EM [Scheres and S. Chen 2012], minimizes template bias and overfitting of high frequency information. The half-sets are commonly referred to as *even* and *odd* and are divided based on the particle indexing number, however particles can also be separated on a per tomogram basis or by using the median particle coordinate in a tomogram as a separation threshold.

3.7.2.2. Similarity measurement

The similarity of the rotated template and the particle is measured by means of a *normalized constrained cross-correlation function*. As the particles have a missing wedge in Fourier space, the same missing wedge is applied to the rotated template, filtering it to the frequencies present in the subtomogram. Moreover, usually a real-space mask is also used to limit the similarity measurement to an area of interest. Masking is particularly important when handling particles from a densely populated cellular environment, or those in contact with or proximal to features of high intensity, such as membranes, filaments, or gold beads.

3.7.2.3. Subtomogram alignment step

The alignment step accounts for the most of the computation time in the StA procedure, as for each particle, it performs a search for the three angles (orientations) and three shifts (translations) that maximize the similarity between the particle and the template.

From a technical point of view, rotating and shifting are separated. A rotated version of the template is generated for each of the angle triplets tested. Then, for all possible shifts, the similarity of this rotated template to the particle is measured. In each iteration, the combination of shifts and Euler angles that yields the best merit figure are the alignment parameters assigned to the particle for the next iteration (Figure 3.5). As an alternative to maximizing a cross-correlation value, the Maximum Likelihood framework [Bharat, Russo, et al. 2015; Stölken et al. 2011] aims to generate an average that weights the contribution of every possible geometrical transform of each particle in the dataset.

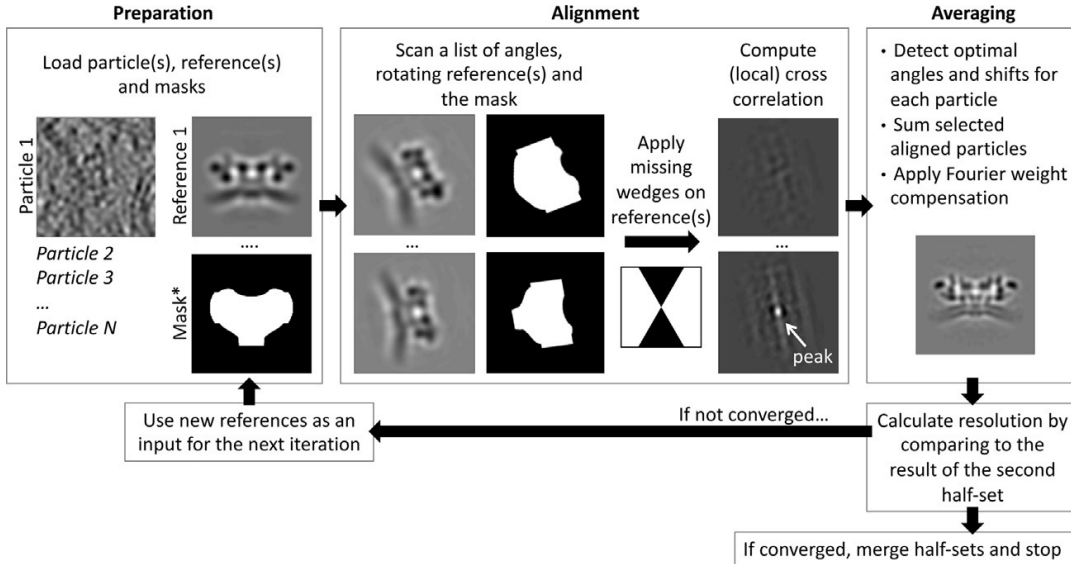


Figure 3.5.: **Mechanics of StA.** Each iteration of StA consists of three main phases: preparation, alignment, and averaging. For the first phase, the preparation phase, the particles, reference(s), and mask(s) are loaded to memory. For the alignment phase, the reference and the mask are rotated through a pre-defined list of search angles. At each of the tested angles, the missing wedge in Fourier space and the rotated mask in real space are applied to the newly rotated reference. The cross-correlation between the reference and every particle is calculated, after which the shifts corresponding to the highest cross-correlation are extracted. For the averaging step, the particles selected for averaging are aligned and averaged using the angles and shifts that gave the best cross-correlation values for those particles. The average is weighted in Fourier space according to the number of times each voxel was measured. At the end of each iteration, the resolution is calculated by comparing the iteration results of two independently processed half-sets. Upon convergence, StA ends, otherwise the updated references and alignment parameters serve as input for the next iteration. *A sharp mask is used when local cross-correlation is calculated, otherwise a soft mask should be used.

Different flavours of this *fast rotational matching* have been suggested. It was initially addressed by [Bartesaghi, Sprechmann, et al. 2008], and based on the similarity of radial projections in a set of shells. This idea was further explored in [Yuxiang Chen, Pfeffer, Hrabe, et al. 2013] and [M. Xu, Beck, et al. 2012], and later refined in [Frazier et al. 2017]. All the implementations measure the similarity of 3D volumes, but deal with

the determination of the shifts differently, as simultaneous acceleration of translational and rotational parameters has not been reported. In practice, fast rotational matching strategies are mostly useful in the initial iterations: for very fine angular discretization, the computation of a full spherical harmonic decomposition can grow prohibitively expensive and numerically unstable. Thus, after an initial estimation of the orientation of the particles using a coarse search grid and fast rotational matching, sets of angles on a finer local grid defined around the previously determined coarse orientation are tested exhaustively.

In both approaches, the angles to be scanned at each iteration are defined by the user. The choice of the angle set is ideally supported by *a priori* information about the particle shape, symmetry, or context within the tomogram (filaments and membranes might define physically sensible constraints to the potential angles around a coarsely defined orientation), and also considers the trade-off between quality with finer angular intervals and computing time. This decision can be made automatically in some implementations [Bharat and Scheres 2016] based on an analysis of the interplay between angular interval, resolution, and size of the box and/or mask.

3.7.2.4. Averaging step

The alignment parameters found for each particle are used to rotate and shift the particles. These particles are then averaged to create a volume that will serve as an updated reference for the next iteration. Since particles that align with different rotation angles contain possibly overlapping, but essentially different areas, of Fourier space, the averaging procedure must weight the final average by the number of subtomograms that actually contribute to each Fourier component.

The averaging step can incorporate different selection policies that downweight or reject subtomograms of lesser quality based on the information gathered during alignment. A straightforward criterion is the *thresholding* of particles whose computed cross-correlation coefficients are below the defined thresholds for the current iteration. If the dataset is large enough, this policy can be refined by grouping subtomograms according to their tomogram of origin and by their orientation [Hutchings et al. 2018] and processing them independently, with the understanding that in such a case the averages will also have missing wedges. In maximum likelihood formulations, downweighting the contributions of lower-quality particles naturally replaces the thresholding criterion used in correlation maximization approaches.

When contextual information is available for each particle, subtomograms may also be rejected based on the alignment parameters themselves. A particle may be excluded from averaging when the geometrical transform that optimizes the cross-correlation criterion forces it into a position or orientation considered unphysical based on its geometrical

relationship within cellular structures such as filaments, membranes, or predicted assemblies of particles in the form of lattices or pseudo-crystals.

The average obtained at the end of an iteration is used to generate a reference volume for the next iteration. Ideally, this new reference will not include any frequency not present in the real signal contained in the set of subtomograms; in other words: it should be low-pass filtered according to the actual *resolution* attained by the current iteration. In the independent half-set refinement approach, this resolution is determined by comparing the independently attained *even* and *odd* averages, aligned to each other. The comparison is performed by means of a Fourier Shell Correlation (FSC), a mathematical operation that measures the agreement of two volumes at each frequency interval. However, the resolution determined in this way is dependent on the particular cut-off criterion used [Heel and Schatz 2005] and on the policy used to compensate for the boosting of FSC values by the use of a mask [S. Chen et al. 2013]. A conservative approach is therefore suggested when generating the reference of the next iteration: in order to minimize the leaking of spurious frequencies into the subsequent computational steps, the attained average is filtered to a slightly lower frequency than the nominal resolution computed by the FSC curve. When the refinement has converged, the sum of the aligned final half-maps filtered to the detected resolution is the result of the StA.

The objective of the StA procedure is a gradual increase in the resolution measured across iterations. Stalling of the resolution improvement per iteration can be overcome by adjusting iteration parameters such as the masks used, the coverage of the angular scanning sets, and/or the level of binning (decided manually by the user or by the software), or by introducing classification. In some cases, further potential improvements might be attained by redefining the subtomograms themselves, as explained in the next section.

3.7.2.5. Subboxing

The *subboxing* technique uses the global alignment parameters determined for a given box size to infer the alignment parameters of newly defined regions inside the averaged particle (*subboxes*), as depicted in Figure 3.6. These subboxes can be aligned and averaged separately, using their orientation and relative location as an initial estimate of alignment parameters that can be relaxed if necessary. This process allows flexible regions or particle composition heterogeneity in the original tomograms to be explicitly accounted for [Peralta et al. 2013]. Note that a potential downside of this technique is the reduction of the amount of signal available to drive the alignment due to smaller box sizes.

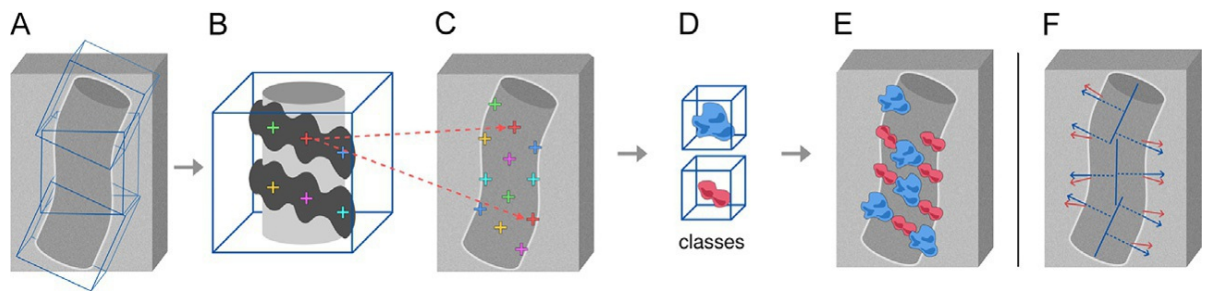


Figure 3.6.: **The subboxing workflow.** A) Initial subtomograms are selected in the tomograms by respecting *a priori* information of the sample geometry. In this example, they are defined along a tubular shape. B) After a few StA iterations, the average reveals a structure previously not seen in the full tomogram (here shown as a helical pattern around the tube). Finer alignment parameters do not allow more details to be resolved, due to the curvature of the tube and the heterogeneous composition of the helical structure. New coordinates of potential particle centres are selected inside the average (indicated with colored “+”). C) These coordinates are traced back to the full tomogram and subboxes with a smaller box size are cropped. D) The subboxes are further aligned and averaged using *a priori* information of their orientation (in this case, perpendicular to the tube surface). Classification reveals two different particle types. E) Placing the final averages at their corresponding coordinates in the full tomogram shows their overall arrangement and potential interactions. F) Illustration of the initial subbox orientation (blue) and the refined (red) subbox orientations. The subboxing reveals the individual particle orientations that could not be resolved from the first average.

3.8. Dealing with heterogeneity

Protein complexes exhibit two types of heterogeneity: compositional, when additional densities are present or absent in some *classes*, and *conformational*, where the same proteins adopt different conformations. Conformational heterogeneity may in turn be *discrete*, when a limited number of conformations are present, or *continuous*, when part of a macromolecule moves unrestrictedly. Classification strategies may be used to address the issue of heterogeneity. The aim of classification is to divide the available particles into subsets (classes) minimizing the differences between the particles within each class and maximizing the differences between the classes.

3.8.1. Principal component analysis (PCA) with multidimensional statistical analysis

PCA is a statistical procedure that defines a set of uncorrelated orthogonal components, which is then used to build a compact representation of the dataset with lower dimensionality. In subtomogram averaging, datasets are composed of particles (typically numbering in the range of thousands) of high dimensionality, as even a moderate box size of 100 pixels implies 10^6 voxels per subtomogram. However, mutually aligned particles from one dataset are assumed to represent different realizations of a much-reduced set of compositional and/or conformational classes, implying that the values attained by a given voxel across the dataset will show a strong correlation with the behaviour of a large number of other voxels. Describing *each* particle in a dataset in terms of its correlated voxel values leads to a redundant representation of the information in the set.

Instead of representing each particle as a linear combination of 10^6 voxels, they can be represented as a linear combination of several eigenvolumes with negligible loss of information. In this case, the coefficients in the linear combination are called eigencoefficients. Eigenvolumes may be calculated by diagonalization of the matrix that holds the similarity values of every pair of particles (the “covariance matrix”). The measure of similarity between two particles is a constrained cross-correlation. During the computation of the covariance matrix, it is important to consider that each particle has a missing wedge and that the covariance should only be calculated with the voxels of Fourier space that are measured (i.e., not affected by missing wedge) in both of the particles [Förster, Pruggnaller, et al. 2008]. Defining eigenvolumes and eigencoefficients is not a classification method itself, but it reduces the complexity of the data, allowing visualization in 2D. Each of the eigenvolumes may be assigned a physical meaning and classification algorithms may be run on only a subset of eigenvolumes, giving a researcher more control over the features on which classification will be done.

Classification may be performed by k -means or any other clustering algorithm that takes the similarity between objects in multidimensional space into account. k -means clustering starts with an initial M random class “centers” and assigns objects to the class with the closest center. The centers are iteratively updated until convergence (marked as X 's in Figure 3.7B). The number of classes, M , is a user-defined parameter. Due to the random initialization, k -means may result in different results across multiple runs on the same data set. The covariance matrix may be calculated using the same mask as is used for alignment. This will result in classification based on the global features of the particle. However, a more restricted mask could be used in order to classify particles based on local differences. Since this restricted mask is not used for alignment of subtomograms, it does not introduce potential overfitting. Chen and colleagues introduced AC3D - an clustering approach that automatically generates masks for classification based on determination of the most variable parts of the subtomogram average map [Yuxiang Chen, Pfeffer, J. J. Fernández, et al. 2014]. Once this mask has been defined, PCA and k -means classification are performed. This approach significantly outperformed Maximum Likelihood-based MLTOMO on synthetic data and was shown to be very powerful in the analysis of compositional heterogeneity in ER-associated ribosomes [Yuxiang Chen, Pfeffer, J. J. Fernández, et al. 2014].

Bartesaghi and colleagues [Bartesaghi, Sprechmann, et al. 2008] and Xu and colleagues [M. Xu, Beck, et al. 2012] used hierarchical assembly instead of k -means classification. Hierarchical assembly also makes use of the covariance matrix. Stopping criteria, which unite the particles from the ‘branches’ of the hierarchical tree into classes, make classification more sensitive and do not depend on initial class assignments (as with k -means). Xu and colleagues further incorporated weights of voxels calculated from the variance of the 3D structure into the calculation of the covariance matrix, which enhanced the sensitivity of the classification algorithm [M. Xu, Beck, et al. 2012]. EmClarity introduced the concept of multi-scale clustering by calculating the similarity between particles in certain frequency ranges [Himes et al. 2018]. This allows the classification to be focused on large or small domain movements, or on finer rearrangements of secondary structure separately. Performing one round of PCA after alignment will result in all of the particles aligning to the same reference, and therefore, large conformational changes may not be accounted for. To address this problem, the approaches of Bartesaghi and Xu introduced iterative refinement of the particles’ alignment parameters, which makes use of the classification results as references for further alignment while minimizing the intra-class differences.

3.8.2. Multi-reference alignment (MRA)

Use of PCA assumes that the subtomograms have been successfully aligned to a common average, a condition that is intrinsically challenged by heterogeneity. While particles with compositional differences might still be able to mutually align due to their common

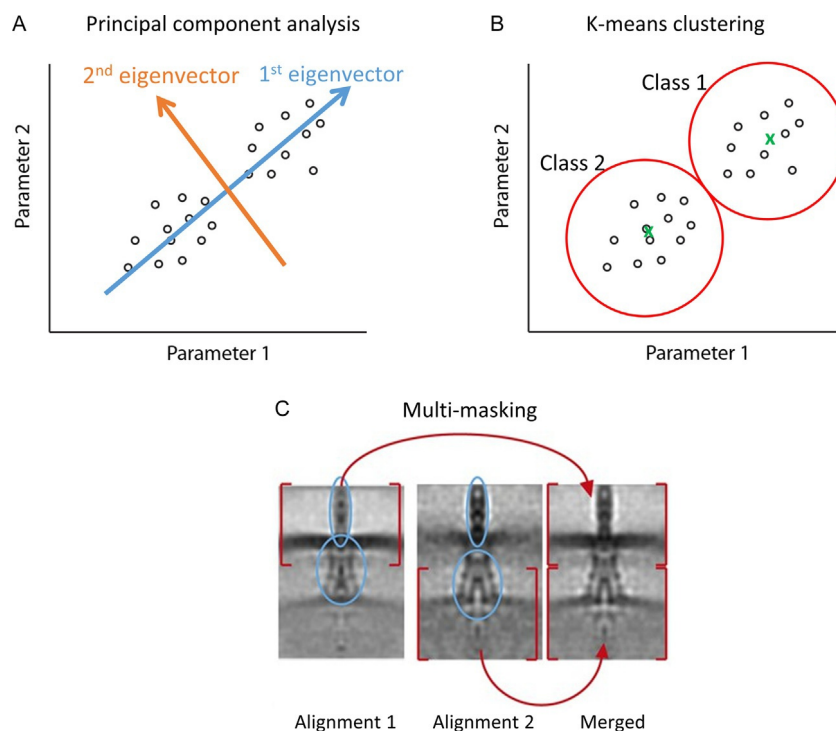


Figure 3.7.: **Visualizing heterogeneity.** A) A scheme for principal component analysis: the first eigenvector is constructed along the axis of greatest variance in the dataset. The second component is constructed in the direction of the second greatest variance perpendicular to the first component, which in 2D is a fixed direction. All remaining eigenvectors in the multidimensional space are perpendicular to the previously defined ones. The new coordinates of each particle (eigencoordinates) in the multidimensional space are recalculated by converting from the projections onto the old basis set {parameter 1, parameter 2, ...} to projections onto the new coordinate system {eigenvector 1, eigenvector 2, ...}. B) Scheme of k -means clustering showing the particles from (A), see the description in the main text. C) An example of multi-masking applied to a flexible bacterial secretion system type 3 located between two bacterial membranes. Two StA structures with two different masks were independently determined and merged in the middle of the box [Kudryashev, Stenta, et al. 2013].

constitutive parts, if several conformations are severely dissimilar globally, then the very notion of a shared underlying signal being able to drive a common alignment breaks down. This ‘chicken-and-egg’ problem can be solved by presenting the particles with more than one reference during the iterative alignment procedure, and grouping the particles based on their similarity to the intermediate class averages generated at the end of each cycle. This “simultaneous alignment and classification” approach was initially used for 2D classification in single particle cryo-EM [Schatz et al. 1990]. Simultaneous alignment and classification by *maximum likelihood* was introduced to cryo-EM for 2D alignment by Fred Sigworth [Sigworth 1998]: instead of finding one optimal alignment for each particle, in maximum likelihood, the resulting structure is a weighted sum of all the rotations and translations of the particle with the weights calculated from the cross-correlation function. This maximum likelihood approach reduces sensitivity to

the starting reference and converges to the correct structure at a higher noise level; however, it does not result in higher resolution and generally takes longer to compute. The extension of maximum likelihood to StA was achieved by accounting for the missing wedge [Scheres, Melero, et al. 2009; Stölken et al. 2011], resulting in the same robustness with respect to starting reference and noise level.

3.8.3. Automated classification

Recently, significant progress has been achieved in supervised- or automated annotation of cryo-ET data by deep learning approaches. These approaches aim to pick the majority of the present particles in potentially crowded cellular environments, automatically identify classes of proteins, and solve the corresponding structures *in situ*. In an example of this type of approach, Xu and colleagues used a hybrid reference-based feature extraction by deep learning with unsupervised classification [M. Xu, G. Yang, et al. 2017]. The resulting implementation was computationally efficient and in addition to recovering the references that were used for particle picking, it was also shown to recover classes that were in the simulated tomographic datasets, but were not used for picking.

3.8.4. Multi-mask refinement

In cases where conformational heterogeneity is detected after a global consensus alignment, defined masks may be introduced to divide macromolecules into segments. For each mask, independent alignments are performed and reconstructions are generated, each of which may reach different resolutions. In the final step, the partial reconstructions are all merged into a complete one. The first examples of merging multi-mask reconstructions was done with hard masks followed by low-pass filtering of the entire reconstruction ([Kudryashev, Stenta, et al. 2013], Figure 3.7C); however, other strategies may include filtering to local resolution or incorporation of soft masks during merging. Subboxing described earlier (see Section 3.7.2.5) is a more general version of multi-masking.

Since the particles used in StA are 3D, multi-mask refinement can be easily incorporated into the workflow. This is in contrast to SPA, where the application of masks to specific molecular domains is confounded by overlap of these domains in the 2D image. Focused refinements in SPA must therefore be combined with partial signal subtraction [Nguyen et al. 2016]. Statistical analysis of the mutual orientations of these masks in SPA allows assessment of the principal motions of a macromolecule [Nakane, Kimanius, et al. 2018], a type of analysis that could be easily applied to StA.

3.9. Software packages for subtomogram averaging

Several open-source software suites are available for subtomogram averaging. These software packages differ in programming languages, data formats, alignment algorithms, and overall image processing workflow.

The *Dynamo* suite has a specific module for StA, written in MATLAB, C++, and CUDA programming languages. *Dynamo* performs iterative refinement based on maximum cross-correlation [Castaño-Díez, Kudryashev, Arheit, et al. 2012]. The software is prepared to run under several computing environments (Windows, Linux, Mac) as well as on GPU and CPU clusters [Castaño-Díez, Kudryashev, Arheit, et al. 2012] and Amazon cloud services [Castaño-Díez 2017]. *Dynamo* is characterized by its user-friendliness and adaptability since it is distributed as MATLAB scripts as well as precompiled executables, thereby supporting algorithm development and enabling users to install and use the software without the purchase of any license. Data management is crucial for StA, therefore *Dynamo* has recently extended its workflow to include two organized databases structured as archiving systems: the *Dynamo repository* (in the *Dynamo* 1.2 series) and the *Dynamo catalogue*. The *Dynamo repository* organizes tilt series data while the *Dynamo catalogue* manages tomograms and keeps track of every transformation, e.g., binning and flipping, and tomographic annotations for particle picking using geometrical models [Castaño-Díez, Kudryashev, and Stahlberg 2017]. Moreover, *Dynamo* offers a streamlined project GUI for StA where projects for classification, refinement, and adaptive bandpass filtering can be designed and tested before batched projects are launched. Additional online documentation describes functionalities in detail and applications to biological datasets [Navarro et al. 2018]. *Dynamo* functionalities have been integrated into pipelines for high-resolution cryo-ET [Hutchings et al. 2018; Kovtun et al. 2018; Schur, Obr, et al. 2016]. Additionally, *Dynamo* provides powerful tools for template matching, mask management [Kudryashev, Castaño-Díez, Deluz, et al. 2016], estimation of symmetry [J. Wang et al. 2017], and subboxing [Peralta et al. 2013], as well as extensive visualization systems [Navarro et al. 2018].

There are also a number of other commonly used packages. The TOM and AV3 packages are also written in MATLAB and provide modules for EM data management, tomographic alignment, and subtomogram averaging by cross-correlation maximization [Förster et al. 2005; Nickell et al. 2005]. PyTOM is a modular toolbox that shares concepts with TOM and AV3. It is written in Python and includes tools for template matching and classification of subtomograms [Hrabe 2015 as well as subtomogram alignment by applying spherical harmonics [Yuxiang Chen, Pfeffer, Hrabe, et al. 2013]. PEET is an open-source software package linked to IMOD for subtomogram alignment and averaging. The alignment algorithm of PEET is based on maximum cross-correlation and includes tools for clustering and classification [Heumann et al. 2011; Nicastro et al. 2006]. MLTOMO is a maximum likelihood-based workflow, also written in MATLAB, that allows subtomogram averaging and classification [Stölken et al. 2011].

Finally, several single-particle software packages have integrated tools for subtomogram averaging into their pipelines. EMAN2 contains a toolbox based on maximum cross-correlation that offers functionalities such as classification of subtomograms, particle picking and, per-particle CTF analysis and correction [Jesús G. Galaz-Montoya et al. 2015, 2017]. The Xmipp package presents several tools based on maximum likelihood for alignment and classification of subtomograms [Scheres, Melero, et al. 2009]. The regularized likelihood refinement algorithm in RELION has been extended to 3D images, including per-particle CTF estimation and correction [Bharat, Russo, et al. 2015].

New approaches for subtomogram averaging classification and alignment refinement have also been recently implemented in emClarity. emClarity is a set of GPU-accelerated programs interfaced with the IMOD package that allows per particle alignment refinement and 3D-CTF correction, as well as exhaustive bandpass filtering for classification. It has been shown to improve resolution in cryo-ET datasets where sub-nanometer resolution was already achieved [Himes et al. 2018]. Further application of these new approaches to more challenging datasets limited in attainable resolution, such as intact cells and cryo-FIB lamellas, will help the identification of potential workflow bottlenecks that could be targeted for improvement in future biological applications of StA.

3.10. Future opportunities and challenges

The first StA on a cryo-preserved sample was performed on tomograms of purified thermosomes and reached a resolution of approximately 20 Å [Walz et al. 1997]. Since 2011, StA structures at sub-nanometer resolution have become more common with a few structures reported at near-atomic resolutions (Figure 3.2). However, the average structure reported by StA has a resolution of 30-40 Å (see EMDB deposition statistics www.ebi.ac.uk/pdbe/emdb). This prevalence of lower-resolution structures partly has to do with the complexity of the StA workflow and partly with the variability of the analysed protein complexes. Large protein complexes like the nuclear pore complex [Appen et al. 2015], bacterial flagellar motors [Zhu et al. 2017] or bacterial secretion systems [Nans et al. 2015] are very flexible and not abundant in tomograms, making it challenging to obtain a high-resolution StA structure. Therefore, the challenge of subtomogram averaging is not only obtaining high-resolution, but also to do it from a limited number of potentially heterogeneous particles.

Further software development may drive improvements in resolution for all StA structures. The StA workflow may be considered as data moving from one functional module to another, as outlined in Figure 3.8. Further improvements in performance could be achieved by either making better performing modules or improving the input-output between the modules. The workflow outlined in Figure 3.8 contains up to five image interpolations between the original tilt series and the final structure, each of which degrades the high-frequency information in the final StA map. Therefore, incorporating the processing into a self-consistent integrated workflow, as has been done by several software suites including IMOD/PEET [Heumann et al. 2011; Nicastro et al. 2006], emClarity [Himes et al. 2018], and *Dynamo* [Castaño-Díez, Kudryashev, Arbeit, et al. 2012], may provide additional gain.

Finally, currently data collection takes about 15-60 minutes per tomogram. While this may provide sufficient data for highly abundant proteins including viral capsid proteins, vesicle coats, repetitive filaments, and cellular ribosomes, for many less abundant proteins it could require prohibitive durations of instrument time to collect several thousand particles. Therefore, progress in more stable microscope stages, faster cameras, and faster data collection routines [Chreifi et al. 2019] could speed up throughput by an order of magnitude, leading to more high-resolution StA structures in the future. As accessibility of hardware and software increases, more researchers will be able to employ cryo-ET and StA as a mainstream technique for high-resolution structural analysis of macromolecules in their native context.

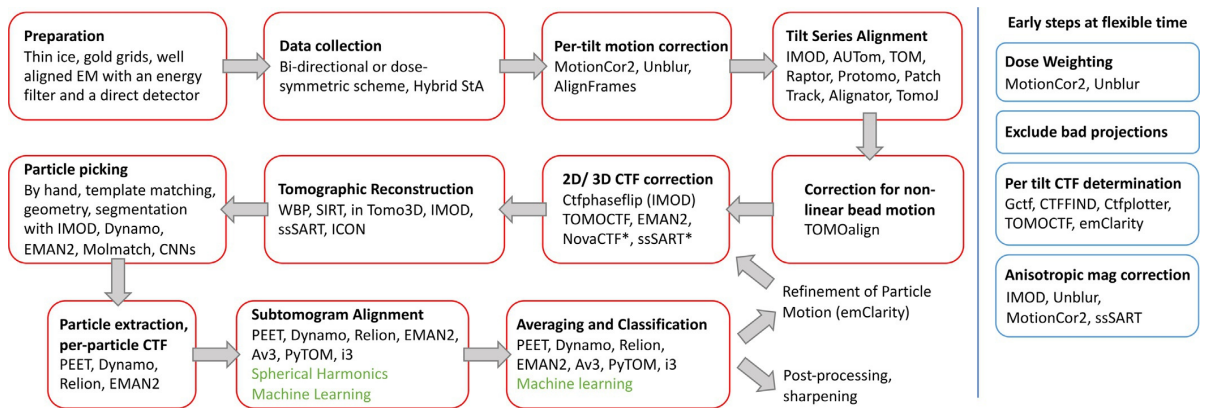


Figure 3.8.: **Data flow in StA.** A scheme describes the data flow from sample preparation to the final structure. The operations in the red boxes have fixed order while blue boxes could be done at several time points early in the processing. The workflow contains 16 operations of various complexity and up to 5 potential image interpolations. Green text indicates potential further improvements. The (*) in CTF correction indicates that CTF correction is performed in one step with tomographic reconstruction.

4. Protocols for Subtomogram Averaging of Virus-Like Particles with *Dynamo*

4.1. Comment

This chapter shows developments that were made in the *Dynamo* software to address the challenges of throughput in STA by streamlining the STA processing pipeline and minimizing the manual user interactions. The results were documented for the scientific community in the form of a protocol paper to be submitted. As first author of this publication I was in charge of all major tasks including designing the processing pipeline, writing the code in MATLAB and *Dynamo*, benchmarking, project management and writing the manuscript titled:

Protocols for Subtomogram Averaging of Virus-Like Particles with *Dynamo*

Stefano Scaramuzza¹, Daniel Castaño-Díez^{2*}

¹ *Center for Cellular Imaging and NanoAnalytics (C-CINA), Biozentrum, University of Basel, Basel, Switzerland*

² *BioEM Lab, Center for Cellular Imaging and NanoAnalytics (C-CINA), Biozentrum, University of Basel, Basel, Switzerland*

*Correspondence to: daniel.castano@unibas.ch

Manuscript under preparation, 2020

4.2. Abstract

Subtomogram averaging (STA) is a powerful image processing technique in electron-tomography and is used to determine the three dimensional structure of macromolecular complexes and organelles in their native environments. It is a fast growing technique with increasing importance in structural biology. Image processing in STA is often very time intensive due to the high complexity of the technique and the lack of automated processes. We therefore streamlined the STA processing pipeline and simultaneously minimized the required manual user interactions with the goal to increase throughput. The command line based workflow is based on the popular *Dynamo* software for STA. The pipeline includes all steps starting from particle picking to the final 3D map. Each of these steps is documented in detail to ensure complete reproducibility. Additionally to reducing processing times for STA, this pipeline can further be used for benchmarking projects or as guide for new users. The used example dataset is based on the EMPIAR database entry 10164 from immature HIV-1 virus like particles, that describe a common geometry found in electron tomography.

4.3. Introduction

Cellular organelles and biological macromolecules such as proteins and complexes thereof play a fundamental role in almost all life sciences. In structural biology, the molecular structure of these particles is studied to gain information about their morphology and function. Electron-tomography is a well-established and quickly evolving technique that, additionally to determining the 3D structure of the particles of interest, also allows to image the particles in situ and therefore to draw conclusions about their cellular context, geometry and interactions with their environment.

A powerful image analysis technique in electron-tomography is subtomogram averaging (STA), where copies of the same particle of interest within a tomogram are extracted independently and then aligned and averaged to a common reference in order to increase the signal and detail of the underlying structure. STA has led to many breakthroughs in structural biology and a lot of effort in method development is still done [Castaño-Díez and Zanetti 2019; Danev, Yanagisawa, et al. 2019; Frank 2013; Schur 2019; W. Wan and Briggs 2016]. A main bottleneck in STA is the low throughput due to the complexity of the technique and the lack of automation. Also, optimization of processing pipelines is difficult because the slow computation times (caused by large datasets and files¹) hinder the systematic search for optimal parameters.

Various software for STA exist. Among the popular ones are *Dynamo* [Castaño-Díez, Kudryashev, Arbeit, et al. 2012; Castaño-Díez, Kudryashev, and Stahlberg 2017], TOM [Nickell et al. 2005], AV3 [Förster et al. 2005], PyTOM [Yuxiang Chen, Pfeffer, Hrabe, et al. 2013; Hrabe 2015], EM-Clarity [Himes et al. 2018], RELION [Bharat and Scheres 2016], EMAN2 [M. Chen, Bell, et al. 2019], PEET [Heumann et al. 2011; Nicastro et al. 2006], M [Tegunov, Xue, et al. 2020] and MLTOMO [Stölken et al. 2011]. Guides and tutorials on how to use these software packages can be found on the corresponding websites. For *Dynamo* and RELION there are published processing protocols covering specific parts of the processing pipeline [Bharat and Scheres 2016; Navarro et al. 2018].

The *Dynamo* software for STA, which is written mainly in MATLAB (MathWorks²), was chosen for this report because of its popularity and versatility. Functions that independently address all steps needed in the STA processing can be individually called and combined with conventional MATLAB scripts, making the software very flexible and allowing to set up customizable processing pipelines with high levels of automation. This versatility is essential for STA because it allows to design and adapt image processing strategies dependent on the often unique geometries of the analyzed samples.

We created this protocol for two reasons: First, we want to demonstrate how STA

¹Typical datasets consist of several thousand subtomograms of about 10 MB size and over 50 tomograms of > 100 GB size.

²www.mathworks.com

projects can be streamlined and automated to improve productivity. Second, we want to provide a complete step-by-step guide on how to set up and run a project specific STA processing pipeline. These goals are achieved by creating a script based approach using mainly the *Dynamo* software for STA and only minimal dependencies on other software. The focus is on the automation and reusability of the presented scripts and functions. We demonstrate how the *Dynamo* tools can be combined with MATLAB scripts and tailored to the specific geometry of a certain project to create a robust, straightforward, versatile and ready-to-use solution. The pipeline also serves as a basis for user specific projects, since it can easily be extended or adapted to other geometries such as, e.g., lipid tubes or other types of surfaces. The protocol is aimed at users wishing to increase automation and for users new to *Dynamo* or STA. It is also aimed at experienced users wishing to refresh or extend their knowledge on the topic.

In this protocol we process the EMPIAR dataset with the ID 10164 (related PDB entry 5l93) from immature HIV-1 virus like particles [Schur, Obr, et al. 2016] using the 5 tomograms that were used in [Turoňová et al. 2017]. We chose this dataset because it has been already used for benchmarking in various other STA projects [Himes et al. 2018]. More important, the sample geometry in this specific dataset consists of particles on the surface of a sphere which is a common sample geometry found in electron-tomography. The same protocol can therefore be used for any similar samples such as, e.g., membrane proteins reconstituted in lipid vesicles or any other type of spherical viruses.

This protocol consists of the following three parts:

1. *Pre-processing*: This part covers drift correction, dose weighting, tilt series alignment and tomogram reconstruction. These steps are covered briefly and shown for the sake of reproducibility.
2. *Subtomogram averaging*: The core of this protocol paper is a command line based script, hereafter referred to as the *processing script*. It is written in MATLAB and includes *Dynamo* functions. It covers all steps from particle-picking to gold standard refinement. The script is designed for minimal manual intervention and minimal dependencies on third party softwares.
3. *Post-processing*: This part covers the resolution estimation, sharpening and filtering. These steps are also covered briefly and shown for the sake of completeness and reproducibility.

4.4. Materials and equipment

4.4.1. Hardware requirements

The following hardware components with the recommended minimal specifications are needed:

- A computer or workstation.
- Sufficient disk storage ($> 3\text{TB}$) and random-access memory (RAM, $> 64\text{GB}$).
- Access to multiple graphic processing units (GPUs) for subtomogram alignment. We suggest a minimum of 2 state of the art GPUs (e.g. NVIDIA GeForce RTX 2080 Ti) but recommend at least 6, since subvolume alignment is the most computationally intensive step in the processing.
- Access to a multi-core computing environment for the averaging of subtomograms (> 12 processing cores).

4.4.2. Software requirements

Operating system:

- Linux (recommended) or MacOS. Windows was not tested and extra steps may be necessary to ensure compatibility.

Pre-processing:

- MotionCor2 [S. Q. Zheng, Palovcak, et al. 2017] for drift correction.
- CTFFIND4 [Rohou et al. 2015] for defocus estimation.
- IMOD [Mastronarde and Held 2017] for tilt series alignment and tomogram reconstruction.

Subtomogram averaging:

- MATLAB (Mathworks) version R2019a or newer. For users unfamiliar with MATLAB or similar coding languages we highly recommend to learn some of its basics. Users should be familiar with terms such as arrays, loops and functions.

Table 4.1.: **Dataset.** Tomogram name and dose rate of the 5 tomograms from the EMPIAR-10164 dataset that are used in the processing.

name	dose ($e^-/\text{\AA}/s$)
TS_01	3.0
TS_03	3.0
TS_43	3.1
TS_45	3.1
TS_54	3.0

- *Dynamo* software for subtomogram averaging (version 1.1.511 or newer). A standalone version of *Dynamo* exists that works independently of MATLAB. For this protocol, however, we recommend to use the MATLAB version. The download links, extensive documentation and guides can be found online³.
- Chimera UCSF [Pettersen et al. 2004] for subtomogram annotations.

Post-processing:

- RELION 3 [Zivanov et al. 2018] for resolution estimation and sharpening.
- Bsoft [Heymann et al. 2007] for local resolution estimation (function `blocres`).

4.4.3. Dataset

From the EMPIAR entry 10164⁴ the frames of the 5 tilt series according to Table 4.1 are used.

The frames were recorded on a FEI Titan Krios transmission electron microscope operated at 300 keV equipped with a Gatan K2 direct electron detector using the dose-symmetric tilt scheme [J.-J. Fernández, Sam Li, and Agard 2019]. The calibrated 4K pixel size is 1.35 angstrom. More details about data acquisition is found in the supplementary material of the corresponding publication [Schur, Obr, et al. 2016].

³www.dynamo-em.org

⁴Download here: www.ebi.ac.uk/pdbe/emdb/empiar/entry/10164

Table 4.2.: **Pre-processing parameters.** Parameters used in MotionCor2 and CTFFIND4.

MotionCor2	
parameter	value
patch	5×5
iterations	30
B-factor	200
tolerance	0.5

CTFFIND4	
parameter	value
amplitude spectrum size	512
resolution range	10-50 Å
defocus range	10000-60000 Å
defocus search step	100 Å
astigmatism restraint	300 Å

4.5. Procedure

4.5.1. Pre-processing

Drift correction of the frames and Fourier binning (Penczek, Fang, et al. 2014) to 3710×3838 pixels is done using MotionCor2. The used parameters are listed in Table 4.2.

Defocus estimation is done using CTFFIND4 on each tilt. For defocus estimation, only the area of a tilt is used that corresponds to the projection of the imaged area at the 0° tilt. This angle dependent cropping leads to a more robust defocus estimation⁵. The parameters used in CTFFIND4 are listed in Table 4.2.

Dose weighting is done after defocus estimation on each tilt using a MATLAB implementation of the algorithm introduced in Unblur [Grant et al. 2015b] and using the accumulated dose corresponding to the last frame of each tilt (reduced by 20% to be more conservative). It is worth mentioning here that we observed a significant improvement in resolution of the final average when using dose-weighted tilt series compared to unweighted tilt series..

We prepared MATLAB scripts that perform all of the previous mentioned tasks in an organized and compact manner using wrappers (for MotionCor2 and CTFFIND4) and self written functions. They are freely available and documented on the author’s GitHub repository *TomographyTools*⁶.

⁵The same procedure was used in Chapter 6 and is illustrated in Figure 6.6.

⁶www.github.com/sscaramuzza/TomographyTools

Tilt series alignment and tomogram reconstruction is done in IMOD. The seed model for gold fiducials is first generated automatically and then completed manually in order to obtain about 8-16 bead tracks per tilt series. Fiducials are tracked automatically and gaps are fixed manually. Fine alignment is done by estimating only one rotation and keeping all other parameters fixed. Residuals are minimized according to our online guide⁷. Residuals should be optimized until a root mean square (RMS) of below 2 pixels is achieved. Defocus estimation in IMOD is skipped and the results from CTFFIND4 are used instead. The CTFFIND4 output file can be transformed into an IMOD compatible defocus file using the tool `ctffind2imod.m` from the *TomographyTools* repository. Contrast transfer function (CTF) correction is done using `phaseflip`. Finally, only one full sized tomogram is generated for each tilt series using weighted backprojection (WBP). Any necessary binning will be done on the fly directly on the subvolumes themselves during their alignment.

The final tomograms should be named after the *Dynamo* filename convention⁸. Here, we expect to have the 5 following tomograms at the end of the processing:

```
b001ts001.rec  
b001ts003.rec  
b001ts043.rec  
b001ts045.rec  
b001ts054.rec
```

4.5.2. Preparing data structure for processing script

Before running the processing script, a consistent data structure needs to be set up. This is best done by following the *Dynamo* convention as explained in the next paragraphs.

First, the three following directories should be created within the main project directory:

- **catalogues:** contains files related to the *Dynamo catalogue* including the *doc* and *vll* files.
- **particles:** contains the various particle folders that will be created during the processing.
- **projects:** contains the processing script itself, all alignment projects and individual files (e.g., masks) that are generated during processing.

⁷www.dynamo-em.org/w/index.php/Considerations_for_tilt_series_alignment_in_IMOD

⁸www.dynamo-em.org/w/index.php/Practical_Suggestions_for_Tomographic_Reconstruction

Next, a *volume list* or *vll* file named `tomograms.vll` that contains the full path to the tomograms and their volume label needs to be created and stored in the `catalogues` folder (it will be used to load the tomograms into the *Dynamo catalogue*). Its content should be the following:

```
/full_path_to_tomogram/b001ts001.rec
* label = unlabelled_volume

/full_path_to_tomogram/b001ts003.rec
* label = unlabelled_volume_2

/full_path_to_tomogram/b001ts043.rec
* label = unlabelled_volume_3

/full_path_to_tomogram/b001ts045.rec
* label = unlabelled_volume_4

/full_path_to_tomogram/b001ts054.rec
* label = unlabelled_volume_5
```

Then, a *doc* file that also contains the full path to the tomograms and their volume ID needs to be created also stored in the `catalogues` folder. This file will be used to extract subvolumes from the tomograms. Its content should be the following:

```
1 /full_path_to_tomogram/b001ts001.rec
2 /full_path_to_tomogram/b001ts003.rec
3 /full_path_to_tomogram/b001ts043.rec
4 /full_path_to_tomogram/b001ts045.rec
5 /full_path_to_tomogram/b001ts054.rec
```

Two MATLAB functions are needed to assist the processing. The function `cmm2mat.m` is needed for the communication between MATLAB and Chimera USCF and the function `filterByCC.m` will be used for particle picking. Both functions can be downloaded from the *TomographyTools* repository and should be saved in the folder `projects`.

Also the processing script (`processing_script.m`) needs to be saved into the folder `projects`. The script can be found in the supplementary material (see Appendix C) or downloaded from the *TomographyTools* repository where it is maintained and constantly updated.

Finally, the catalogue has to be set up by first opening MATLAB and loading *Dynamo*. After navigating to the catalogue folder and opening a new catalogue with the

command `dcm`, the tomograms can be imported by loading the previously created file `tomograms.v11`.

4.5.3. Description of processing script

The processing script forms the core of this protocol. It includes all processing steps starting from particle picking to generating the two gold standard half-maps of the structure. It is completely written in MATLAB and *Dynamo*. All steps are fully automated except the tomogram and subtomogram annotations.

The script is structured in 9 main processing *steps* that are further divided into so called *blocks* (see flowchart in Figure 4.1). In this report, the functionality of each step is explained in a dedicated section. Each section contains in the beginning a general description of the corresponding step, followed by a detailed explanation of each block. Details about single commands are further commented directly in the code of the script itself. More information about the used commands can also be found using the command `help` for MATLAB functions or `dhhelp` for *Dynamo* functions.

It is recommended to follow the protocol by opening two windows side by side, displaying this report on one side and the code of the processing script on the other (ideally in the MATLAB editor itself). The script is designed in a way that allows to pause and resume processing after every block. Only the first step that loads global inputs has to be run once every time MATLAB is restarted.

The script sets up and runs alignment projects locally in the directory `projects`. To run the alignment projects on an another location (e.g., on a cluster), users should use the `dvtar` command instead of `dvrn` and follow the corresponding online guidelines for transferring alignment projects to other locations⁹.

Before starting with the first step of the processing script, it should be verified that the script is located in the folder `projects`. To run the script, MATLAB should be opened inside the same folder and the script has to be loaded in the MATLAB editor. There are 3 instances during processing where manual intervention is needed (see Figure 4.1). We therefore recommend to run the script by selecting the parts in between those instances and then clicking the button *run selection* of the MATLAB user interface. Alternatively, the script can be split into 4 sub-scripts¹⁰ that can be run separately before and after the manual interventions either via the button *run* or by typing the filename of the sub-scripts in the command line.

⁹www.dynamo-em.org/w/index.php/Tarring_projects

¹⁰Since the concatenation of the sub-scripts is identical to the processing script shown in Appendix C, they are not included in this thesis.

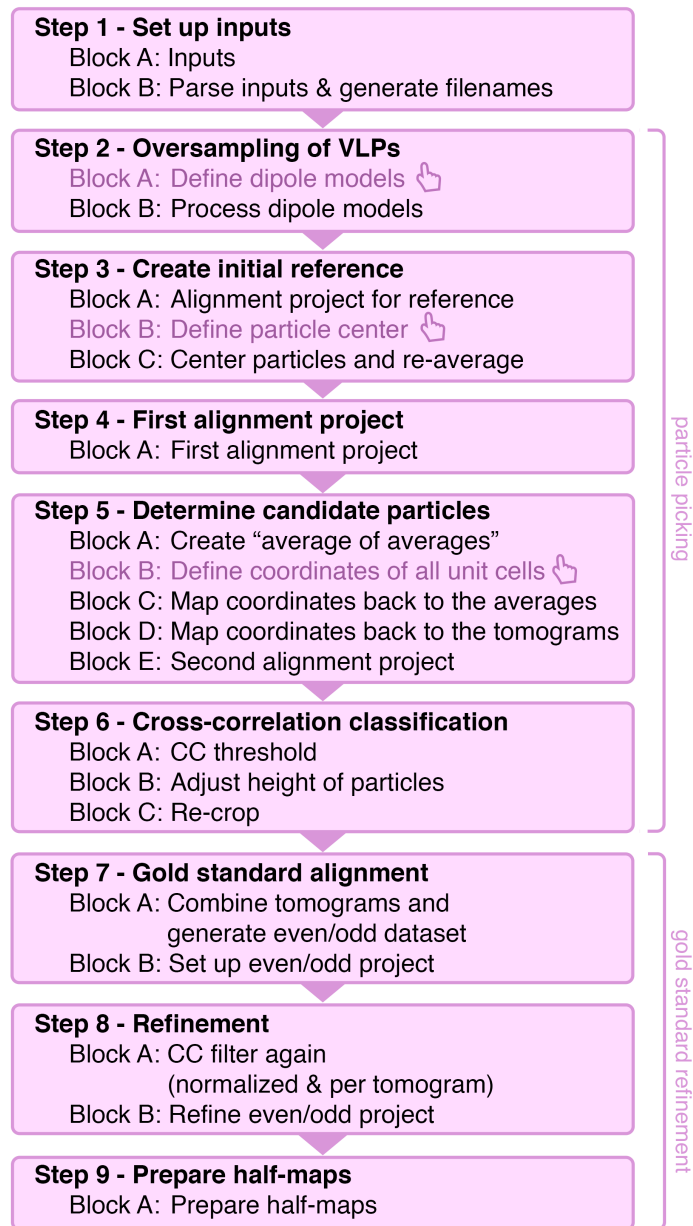


Figure 4.1.: **Flowchart of processing script.** Overview of all steps and blocks of the processing script. All steps are automated apart from the tomogram and subtomogram annotations, where the processing is paused (marked with the hand symbol). These breaks are managed either by running selected parts of the processing script or by the use of sub-scripts (see Section 4.5.3). The two main processing categories (particle picking and gold standard refinement) are highlighted.

4.5.4. Step 1: Set up inputs

Description: Inputs that will be used throughout the script are defined in this step. This includes filenames, directory paths and processing parameters.

Block A: Inputs. User specific inputs that may need to be adapted to the user environment. The path to the *Dynamo catalogue*, *doc*-file and particle folder may be entered relative to the scripts location or absolute. The geometry related parameters are optimized for this dataset and should not be adapted, unless another type of dataset is used. The reasoning behind the values of these parameters is explained in the block where the parameters are used for the first time. Computation related inputs need to match the users hardware setup.

Block B: Parse inputs and generate filenames. Filenames that are automatically generated or derived from the previous inputs. These do not need to be adapted.

4.5.5. Step 2: Oversampling of VLPs

Description: In this step, the surface of the VLPs is oversampled and the first set of subvolumes is extracted. The goal of oversampling is to extract enough overlapping subvolumes such that every unit cell of the hexameric lattice (i.e., every 18-meric assembly of the capsid protein p24) that forms the VLPs has the chance to be present in at least one subvolume. In this process also initial orientations normal to the VLP surface are imposed on the subvolumes.

Block A: Define dipole models. To generate the surface parametrization of the VLPs (segmentation), only their center and radius needs to be manually defined. This is done using the *dipole models* from *Dynamo*. For this, the tomograms are opened through the *catalogue* in *dtmslice*. A *dipole model set* is then opened and every visible VLP is marked with only two clicks: one on its center and one on its surface. Pressing *enter* saves the current dipole in the set and activates the next dipole. This annotation does not need to be very accurate at this point, since the following alignment projects are designed to cope with inaccuracies introduced at this step (inaccuracies up to 40 pixels are tolerable). Also VLPs with defects should be annotated, since bad/junk particles will be excluded in a dedicated step later on. About 8-9 VLPs per tomogram should be marked. More details about the creation of *dipole set* models is given in the online guide¹¹.

Block B: Process dipole models. Each dipole is processed by running the so called *model workflow* to create a regular lattice of coordinates (about 800-1000 per tomogram)

¹¹www.dynamo-em.org/w/index.php/Walkthrough_for_lattices_on-vesicles

on the surface (see Figure 4.2a). These coordinates, or crop points, will be the center of the extracted (or cropped) subvolumes. The oversampling is achieved by setting the spacing (or separation) between the crop points to 120 pixels, which is a bit less than half the sidelength (or box-size) of the cropped subvolumes (256 pixels). This sidelength is large enough to fit multiple unit cells of the lattice. Coordinates of the individual unit cells will be identified later. For each tomogram, the subvolumes are extracted and stored in a tomogram specific directory named `pa_ts???_s256`, where the question marks are replaced by the tomogram number. A simple average without alignment should already reveal a curved shape (see Figure 4.2b).

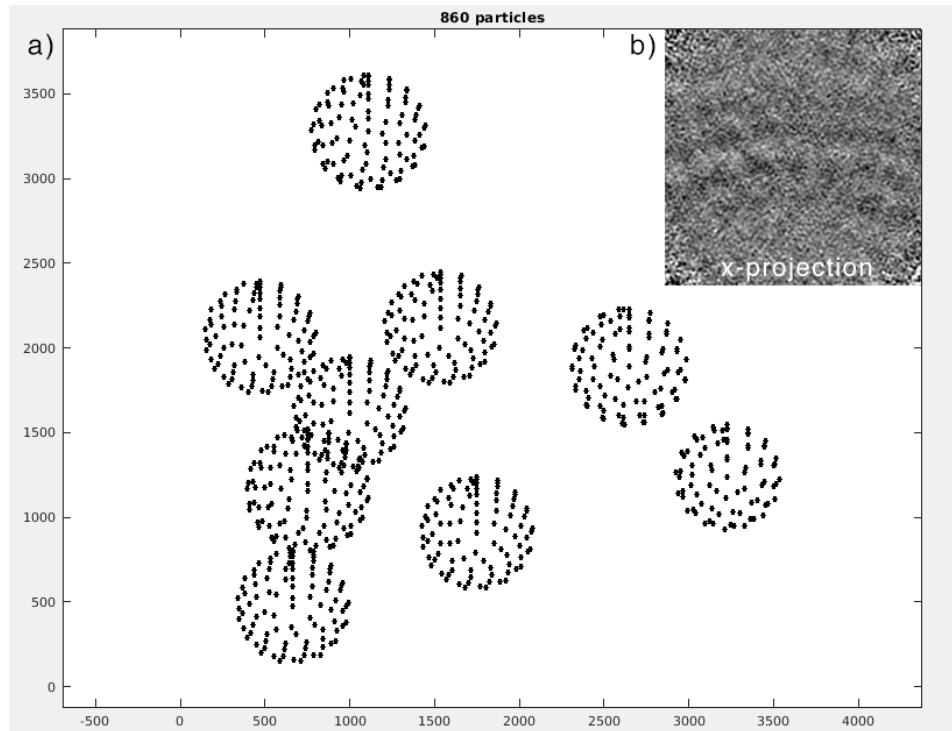


Figure 4.2.: **Oversampling of VLPs and average.** a) Crop points of tomogram *ts001* (z-view) visualized with the *Dynamo* command `dtpplot`. The crop points are located with a regular spacing on the surface of spheres. b) Average of cropped particles (projected in x-view). The curved shape of the VLP surface is visible.

4.5.6. Step 3: Create initial reference

Description: The initial reference that will be used for later projects is generated. This is done by aligning the particles from tomogram `b001ts001.rec` and by readjusting the center of the resulting average.

Block A: Alignment project for reference. First, a template for the alignment

project is generated by averaging the particles from tomogram `b001ts001.rec` with a randomized azimuth angle. This randomization is necessary to prevent systematic errors caused by the missing wedge. The alignment project is then set up using *Dynamo* commands. This is traditionally done manually via the *dcp* GUI but here the aim is to minimize user intervention. The alignment project is created with the command `dcp.new` and by passing the inputs for the data folder, the table and the template. After that, the project parameters are defined. The project consists of 2 rounds (or parameters sets) with 3 iterations each. The description of the parameters is given in the script. The angular search range and the allowed shifts are rather large, since this is the first alignment done on the particles. To speed up the processing, subvolumes are binned on the fly by defining their sidelength (parameter `dim`). There is also no symmetry imposed to avoid any initial bias. The lowpass filter is set at 23 Fourier pixels (corresponding to 15 Å based on the sidelength of 256 pixels and pixel size of 1.35 Å). If a higher lowpass filter is preferred, an additional round can be added in the beginning. Here 15 Å is used as a starting value to reduce the processing time for this protocol. After running the project, an additional copy of the resulting average is saved with inverted contrast and strong lowpass filter. This copy will be used later for visualization purposes in Chimera USCF.

Block B: Define particle center. The previously saved average with the filename `result_pr_ts001_0_INVERTED.em` is opened in Chimera USCF. Using the *volume tracer* tool, the center of the most central unit is marked as shown in Figure 4.3. The coordinate is then stored by saving the *current marker set* with the filename `reference_center.cmm`.

Block C: Center particles and re-average. The resulting average from the alignment project is adjusted such that the center of the previously marked unit cell matches the center of the subvolume. This is achieved by first transforming the coordinates of all particles in the table using the previously defined center coordinate and then re-averaging all subvolumes. The resulting average will be the starting reference for the next alignment projects.

4.5.7. Step 4: First alignment project

Description: In this step, all subvolumes from each tomogram are aligned separately to the previously created reference. The resulting tomogram averages will form the basis for the particle picking, where the coordinates of the individual lattice units will be determined.

Block A: First alignment project. Using a loop over all tomograms, the particles of each tomogram are aligned to the previously created reference. The azimuth of the subvolumes is randomized again to minimize potential missing wedge artifacts. The

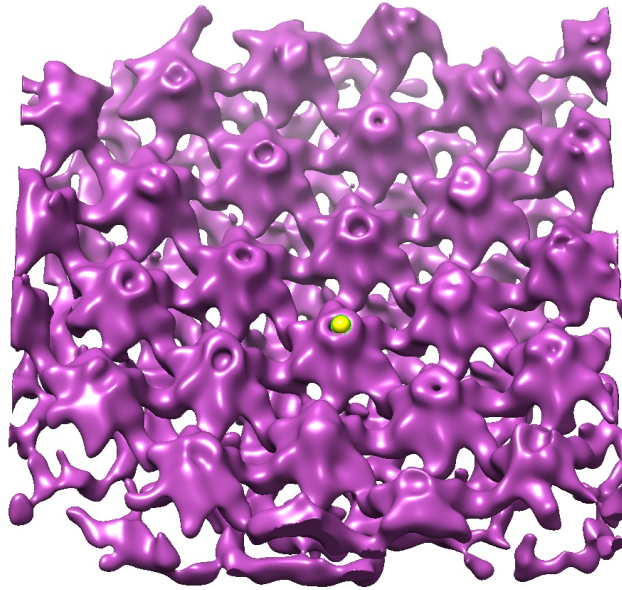


Figure 4.3.: **Center unit cell defined in Chimera UCSF.** The center of a unit cell (yellow dot) was marked by first rotating the average upside down and then marking the tip of the CA-N terminal domain using the *volume tracer* tool.

alignment parameters are identical to the previous reference project, with the only difference that from now on a C6 symmetry is imposed. The resulting coordinates (see Figure 4.4) are expected to have moved away from their initial positions (compare Figure 4.2) and to have adapted to the shape of the VLPs, that is not strictly spherical.

4.5.8. Step 5: Determine candidate particles

Description: The aim of particle picking is to determine the coordinate of every unit cell of the hexameric lattice (or every 18-meric assembly of the capsid protein p24). In this step, the first part of particle picking is done, in which all candidate coordinates are determined (false coordinates will be excluded in the following step). Using the results from the previous alignment projects, the candidate coordinates will be determined using a two-step subboxing procedure¹². In principle, one subboxing step would suffice, in which all unit cells in each tomogram average are marked and mapped back into the corresponding tomogram. However, this would have to be done for each tomogram

¹²In subboxing, coordinates of a specific structural feature are first defined in an average. Since the average is composed by multiple subvolumes with individual orientations, these coordinates can be then translated (or mapped) onto each of those subvolumes and finally also onto the tomograms themselves. With this method, positions of features only visible in an average can be annotated in the full tomograms. See also the online guide: www.dynamo-em.org/w/index.php/Advanced_starters_guide#Subboxing

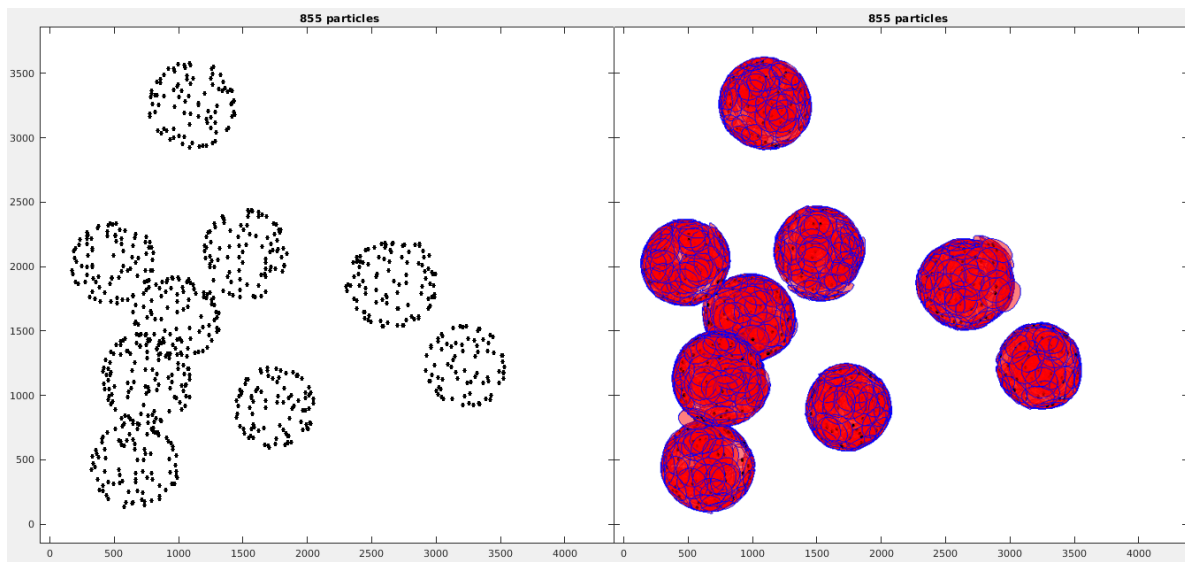


Figure 4.4.: **Results of first alignment.** The left plot shows the coordinates of tomogram *ts001* (z-view) visualized with the *Dynamo* command `dtp1ot` using the resulting table from the first alignment. The coordinates left their initial positions (compare Figure 4.2) and adapted to the shape of the VLPs. The cropped subvolumes are large enough to cover all the empty spaces between the coordinates. This is visualized in the plot on the right where disks with a diameter matching the sidelength of the subvolumes (256 pixels) are placed at each coordinate and successfully cover the whole surface of the VLPs.

individually. To avoid the extra labor, an extra subboxing step is introduced in which all tomogram averages are first aligned to each other to form an “average of averages”. All unit cells visible in this “average of averages” are marked only once and then mapped back to the tomogram averages in a first step. In a second step they are then mapped from the averages onto the tomograms, leading to a new set of coordinates. The process is illustrated in Figure 4.5a. Using these new coordinates, new subvolumes are extracted and aligned.

Block A: Create “average of averages”. The “average of averages” is created by setting up and running a small alignment project and treating the tomogram averages as input data. The corresponding data folder is created by copying the tomogram averages into it and by renaming them following the *Dynamo* convention for particle filenames¹³. Here, each particle tag number corresponds to the tomogram number. A minimal *Dynamo* table is created and the initial template is formed by a simple average of the data folder. The alignment parameters are set up the same way as the previous ones. The alignment project runs quickly, because it only contains 5 particles. The resulting “average of averages” is lowpass filtered and its contrast is inverted for visualization in Chimera USCF.

Block B: Define coordinates of all unit cells. The “average of averages” with the file-

¹³www.dynamo-em.org/w/index.php/Data_folder

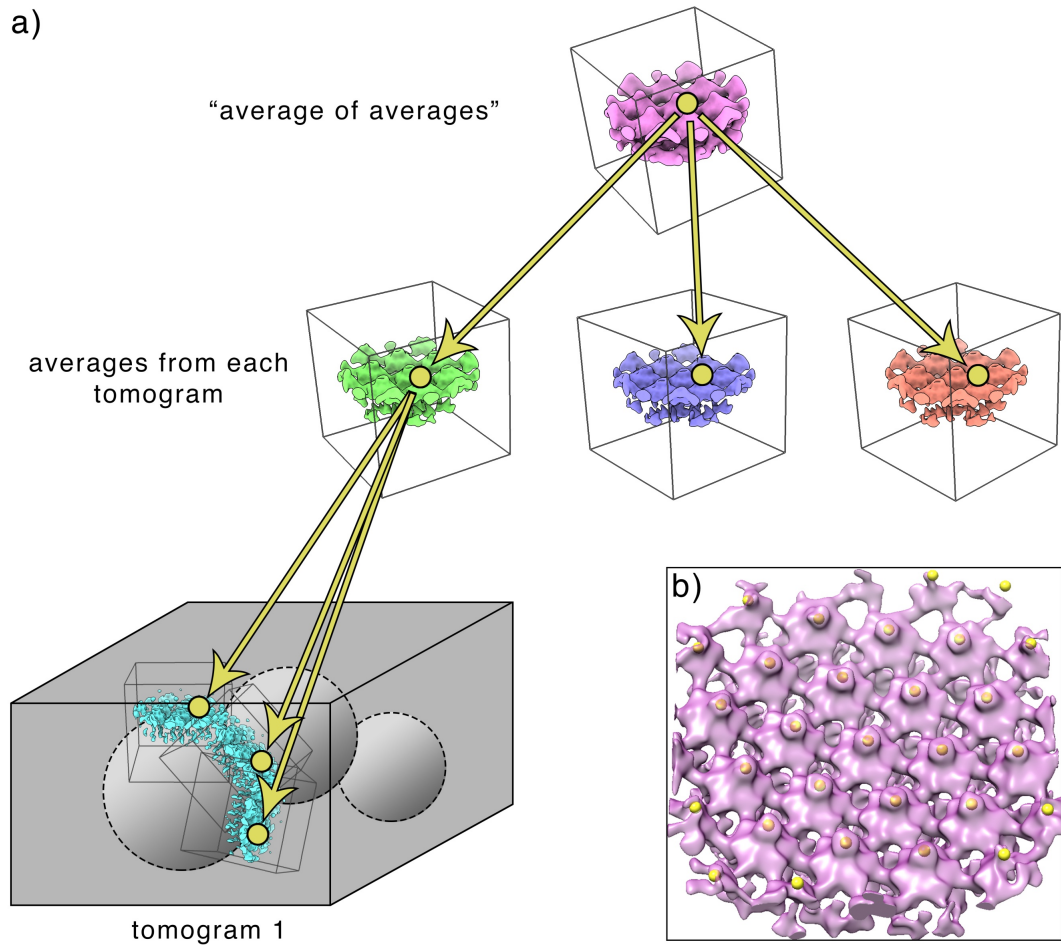


Figure 4.5.: **Two-step subboxing for particle picking.** a) Coordinates of all unit cells are marked in the “average of averages” (in this illustration only one coordinate is shown for simplicity). The coordinates are first mapped onto the tomogram averages and finally on the corresponding tomograms themselves (only one tomogram shown). b) All marked centers of the unit cells (yellow dots) on the actual “average of averages” produced with this protocol. The coordinates were marked in Chimera UCSF using the *volume tracer* tool.

name `result_pr_ts001_0_INVERTED.em` is opened in Chimera UCSF. Using the *volume tracer* tool, the centers of all lattice unit cells are manually marked as shown in Figure 4.5b. The current marker set is then saved with the filename `particle_centers.cmm`.

Block C: Map coordinates back to the averages. Here, the first step of subboxing is performed, where the clicked coordinates are mapped back to each average. First, the resulting table of the alignment project and the clicked coordinates are read into the workspace and prepared to be processed. Then, using the *Dynamo* command `dynamo_subboxing_table`, the actual subboxing is performed resulting in a temporary mini table for each tomogram average. This mini table contains the unit cell coordinates that are expressed relative to the origin of the tomogram average. Finally, the coordinates are extracted from the mini tables and read into a cell array that will be used for

the second step of subboxing.

Block D: Map coordinates back to the tomograms. The second step of subboxing is performed here, where the coordinates are mapped from the averages to the tomograms. First, for every tomogram, the previously computed coordinates and the table from the first alignment project are loaded and used in the `dynamo_subboxing_table` function for subboxing. For each coordinate, a table is then generated that contains the transformed coordinate relative to every subvolumes origin. The tables from all coordinates are merged, resulting in a final table that contains the candidate positions of all lattice units in the tomogram. Due to the previous oversampling, we expect many coordinates to overlap. The table can be corrected for this effect by using the *Dynamo* function `dpktnl.exclusionPerVolume` that reduces coordinates within a user specified radius to a single coordinate. Coordinates that incidentally describe defect or non-existing particles will be removed in the next step. The final coordinates are visualized in Figure 4.6. About 5000-9000 coordinates per tomogram should be defined. We use those to extract a new set of subvolumes with a sidelength of 192 pixels, that generously fit a full unit cell of the hexameric lattice. The average of these subvolumes will contain artifacts, since their axis orientation is inherited from the previous average and does not take into account the surface curvature of the VLPs. This will be fixed in the second alignment project.

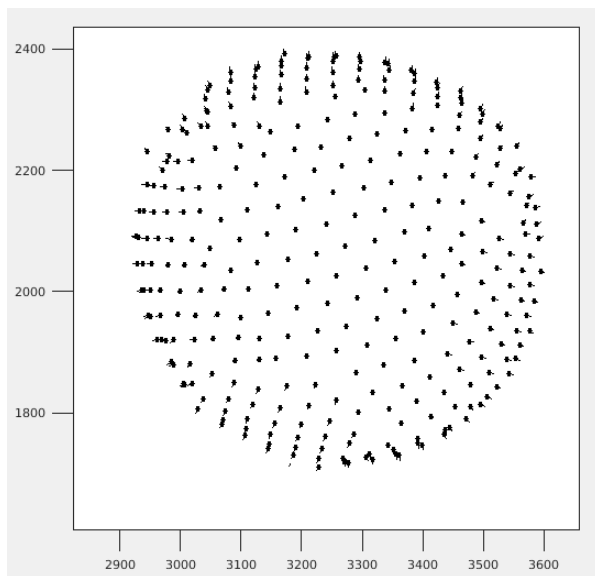


Figure 4.6.: **Resulting coordinates from particle picking.** Particle coordinates on the surface of one VLP from tomogram *ts001* are shown using the *Dynamo* command `dtplot` to demonstrate the results from the particle picking. The hexagonal lattice structure inherent to the immature HIV-1 CA-SP1 is clearly visible. A slight deviation from a perfect sphere is also notable.

Block F: Second alignment project. The new particles are aligned in a second align-

ment project for each tomogram. Because the particle positions are now more accurate, the angular search space and shift limit is reduced compared to the first alignment project. Subvolumes are still binned on the fly, since at this point high resolution is not of interest yet. The results will be used for the following classification step.

4.5.9. Step 6: Cross-correlation classification

Description: This is the second step of particle picking, in which subvolumes that contain defect particles (or none at all) are automatically removed from the dataset. This is again done a for each tomogram separately using cross correlation (CC) thresholding.

Block A: CC threshold. The cross correlation between each aligned subvolume and the final average is stored in the last generated table. A histogram of the CC score shows two populations. The population with the lower CC score is assumed to be the "bad" class that needs to be excluded from the processing. It contains mainly particles with particularly bad quality (e.g., stemming from defects) or subvolumes that contain just noise. To automate the exclusion process, a gaussian mixture model (GMM) is fitted to the CC score distribution. GMMs are commonly used for classification and the specific one used here describes the combination of two Gaussian distributions. Using the MATLAB function `fitgmdist`, the GMM is fitted to the CC score distribution. The threshold is then defined by taking the minimum between the two Gaussian peaks and by adding an empirically defined constant of 0.01. An example of the threshold determination for one tomogram is shown in Figure 4.7a and the resulting particle exclusion is visualized in Figure 4.7b. Coordinates that describe the same particle are again fixed and a new average for each tomogram is computed.

Block B: Adjust height of particles. In the next step, all subvolumes from all tomograms will be combined into one single dataset. Since they have been processed independently so far, the center of their unit cell might vary between tomograms. It therefore needs to be ensured that the unit cells from different tomograms share the same z -height inside the subvolume (axis orientation and x/y -shifts are already consistent due to the imposed C6 symmetry). This is done by aligning the average of the tomogram to a synthetic reference and then apply the resulting transformation parameters (here just a shift in z -direction) to all particles in the corresponding table.

Block C: Re-crop. The particle picking is completed and using the coordinates from the last table, all subvolumes are re-extracted one last time (using the previous sidelength of 192 pixels). About 2000-5000 particles per tomogram are expected. This dataset now consists of subvolumes that all contain one centered unit cell. The quality of the particles and their initial orientation is good enough to serve as a basis for the following gold standard alignment. Figure 4.8 shows a compilation of all tomogram averages. Note the structural differences caused by the different defoci of the tomograms.

4.5.10. Step 7: Gold standard alignment

Description: Now that all particles have been picked, the gold standard refinement can be started, i.e., the subvolumes from all tomograms are first combined and then split into two datasets of the same size that are processed independently in two different alignment projects.

Block A: Combine tomograms and generate even/odd dataset. First, the tables from all tomograms are merged. Then, using the *star file* functionality of *Dynamo*, the 5 tomogram datasets are combined by creating a single *star file* that contains the absolute path to all subvolumes. This *star file* will later serve as data input for the alignment projects. Since the *star file* also contains the particle tag numbers, the combined table can be used in the conventional way. This method is preferred because it does not require to copy or move any subvolumes from their original location. The combined table is split into a dataset containing the even numbered particle tags and another one containing the odd number ones (about 8500 particles each). An average for each half dataset is finally generated that will serve as reference for the following alignment projects.

Block B: Set up even/odd projects. The two half-datasets are processed in two independent alignment projects using the starting references that have been created before. 3 rounds with 3 iterations each are set up. The parameter search space is reduced after each round. The lowpass filter is increased to 32 pixels (8.1 Å) and the last 2 rounds are run on full sized particles.

4.5.11. Step 8: Refinement

Description: The previous results are refined by pruning again the dataset and running a final alignment project with adapted parameters.

Block A: CC filter again (normalized and per tomogram). To remove particles of low quality, the dataset is again reduced through a CC thresholding. For each half-dataset, the thresholding is done for each tomogram separately since the different defocus values of the tomograms influence the overall CC score. Subvolumes with a CC score lower than 1 standard deviation below the mean are removed. Prior to computing the threshold, the CC score is normalized for the angle of latitude, since particles at the equator of the VLPs have generally a higher CC score than particles on the poles due to missing wedge effects. The normalization is done with the function `filterByCC.m` by fitting the first two terms of a general Fourier series to the data¹⁴. Using the reduced tables, a new average is computed that will serve as reference for the last alignment project.

¹⁴The same procedure was used in Chapter 6 and is visualized in Figure B.12.

Block B: Refine even/odd projects. Before creating the alignment project, an alignment mask that roughly follows the curvature of the VLPs is defined. The two alignment projects are then set up using the same parameters as the last round of the previous project but with a slightly increased lowpass filter (38 fourier pixels corresponding to 6.8 Å) and using the new alignment mask.

4.5.12. Step 9: Prepare half-maps

Description: The two resulting averages (half-maps) from the gold standard processing are saved for post-processing.

Block A: Prepare half-maps. The even half-map is aligned to the odd half-map and the resulting transformation parameters are used to transform the table corresponding to the even half-map. The table is then used to re-average the even particles. This re-averaging is done to avoid edge artifacts caused by the half-map alignment. The two half-maps can now be used for the gold-standard Fourier shell correlation (FSC) computation. A final map, which will also be used for sharpening, is additionally computed by re-averaging all particles of the full dataset. Here, the re-averaging is necessary to ensure a correct Fourier compensation of the final map¹⁵.

4.5.13. Post-processing

The resolution estimation is done in RELION by computing the mask corrected FSC curve between the two half-maps and using the cutoff criterion of 0.143. A tight and soft mask is used for the FSC computation. This mask is created by Gaussian filtering and binarizing the final average in an iterative manner until the full central unit cell is included inside the mask and the Gaussian fall-off of the mask does not overlap with the structure. Our resolution estimate is 4.5 Å (see FSC curve in Figure C.1a). This resolution is identical to the resolution estimated in Turoňová et al. 2017 using the same dataset and 2D CTF correction.

Local resolution is estimated using the `bloccres` function from the Bsoft software package. A box size of 23 pixels can be used with an FSC cutoff criterion of 0.5. and C6 symmetry. The results of local resolution estimation are shown in Figure C.1b.

The final density map is generated with the RELION command `relion_image_handler` using a B-factor of -270, which is slightly stronger compared to the Guinier plot estimate (-240 in our case). The lowpass filter is set to the estimated resolution of 4.5 Å. Finally,

¹⁵www.dynamo-em.org/w/index.php/Fourier_compensation_during_averaging

the hand of the map is adjusted using the command `clip flipyz` from IMOD. Details of the final density map including a fit of the molecular structure are shown in Figure 4.9. Orthogonal sections of the final average are shown in Figure C.1c.

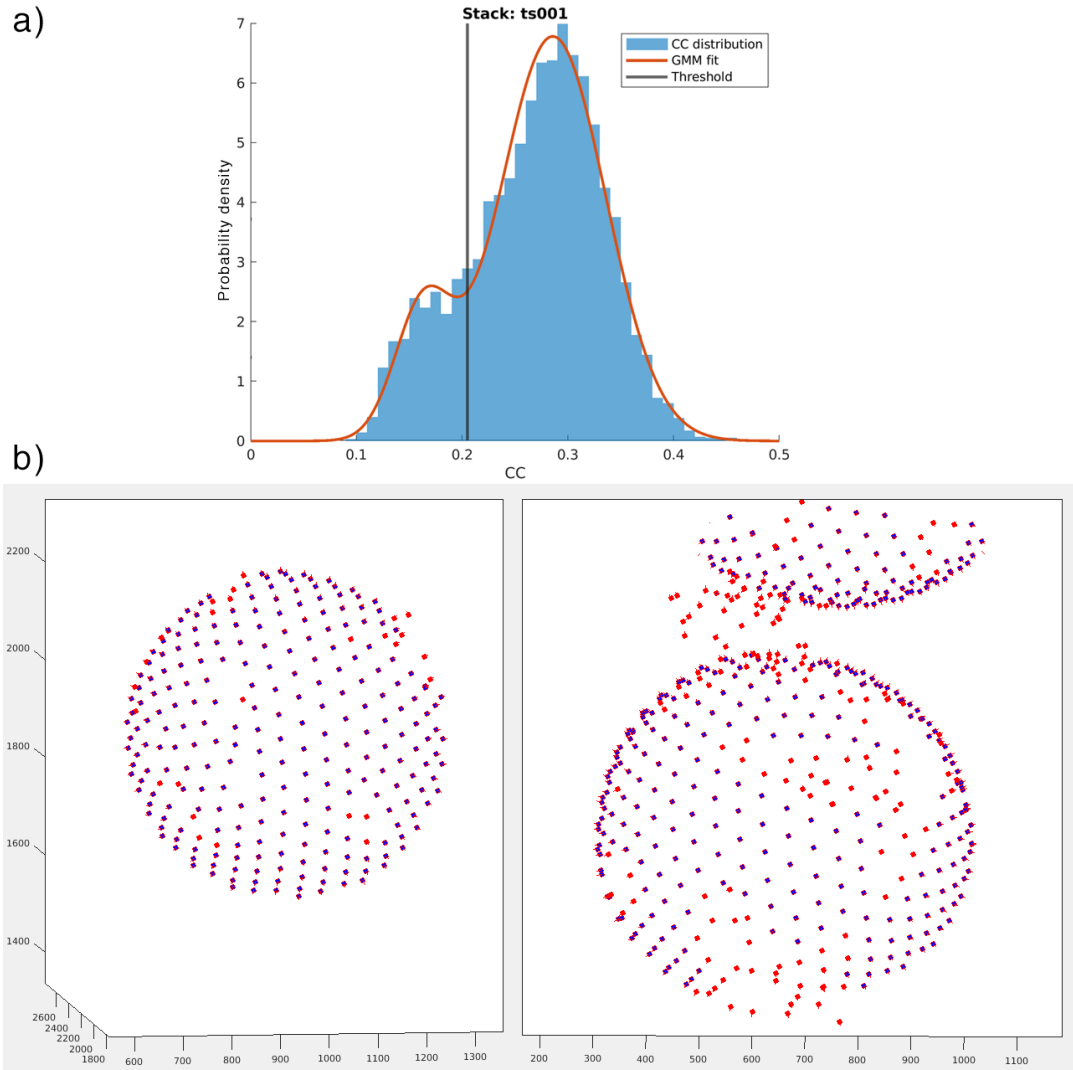


Figure 4.7.: **Particle exclusion through Cross-correlation classification.** a) GMM fit to the CC score distribution of the particles from tomogram *ts001* and the automatically defined threshold for particle exclusion. b) Example of excluded particle coordinates (red) of some VLPs from tomogram *ts001*. Particles that do not fit in the expected lattice geometry are excluded. Visualized using the *Dynamo* command `dtplot`.

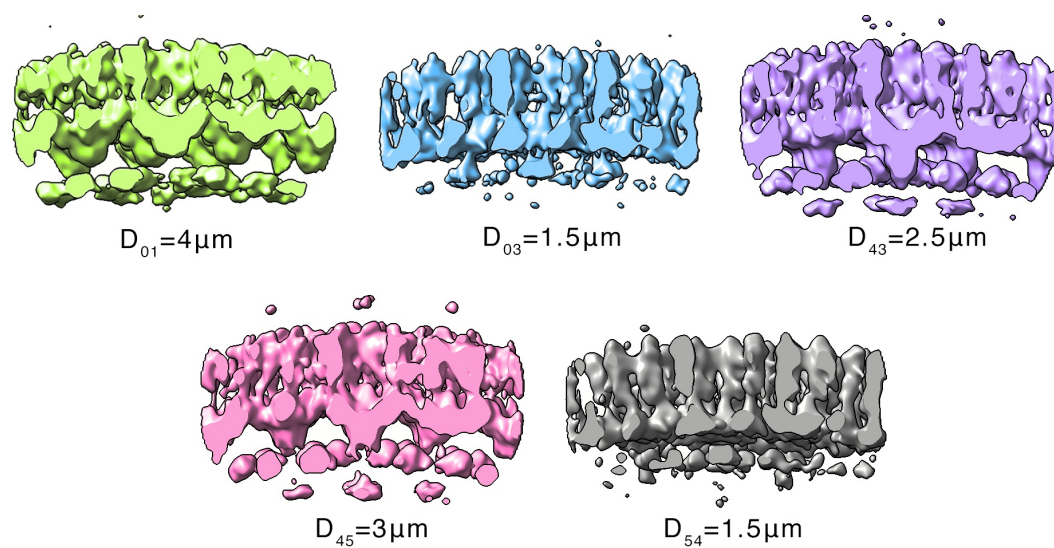


Figure 4.8.: **Results of per-tomogram subtomogram averages.** Overview of all subtomogram averages from all tomograms (lowpass filtered and cut through center). Structural differences caused by the different defoci of the tomograms are visible.

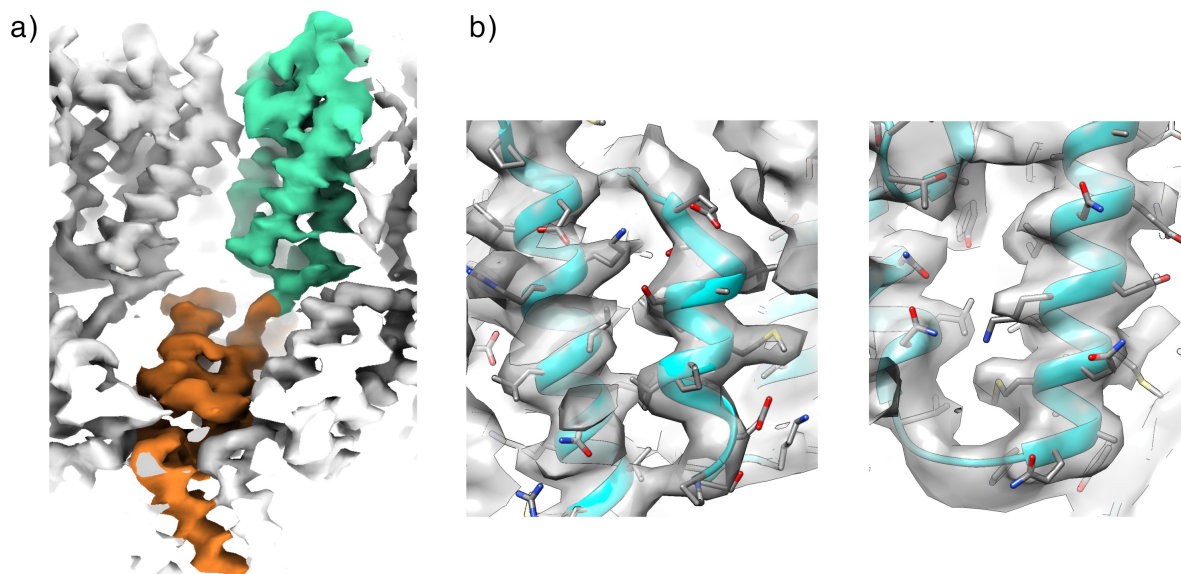


Figure 4.9.: **Electron density map after post-processing.** a) A CA-SP1 monomer is shown with highlighted CA-N-terminal domain (orange) and CA-C-terminal domain (green). For an easy comparison of the structures, a similar view to the one shown in Turoňová et al. 2017 is displayed. b) A rigid fit of the corresponding PDB entry 5l93 shows the quality of the map.

4.6. Conclusion

The two goals of this protocol paper were to demonstrate how the STA processing pipeline can be streamlined and to provide a detailed and complete guideline for STA. We did this by creating and documenting a complete processing pipeline for STA, in which the main part is solely based on the *Dynamo* software package in combination with self written MATLAB functions. The procedure was applied on a dataset of immature HIV-1 virus like particles (EMPIAR-10164), representing a common geometry found in cryo-ET. We validated our pipeline by successfully reproducing the results from Turoňová et al. 2017 that were generated with the same dataset.

By combining and automating key processing tasks and by eliminating redundant steps we managed to set up a streamlined pipeline that is almost completely automated. The only user interactions are the manual annotations of features in the tomograms and subtomograms. These interactions were specifically designed to minimize the manual effort: Only two points per VLP need to be marked and only two averages need to be annotated once for centering and once for subboxing. All other steps including classification by cross correlation thresholding were automated. By introducing the two-step subboxing for particle picking we provided an alternative for a robust particle coordinate determination. We also proved that using the full sized WBP tomograms from the very beginning of the processing is sufficient for this type of data and that the use of pre-binned tomograms or tomograms with alternative reconstruction methods is not necessarily needed. However, for difficult datasets, e.g., tomograms with more complex geometry, smaller particles or lower signal-to-noise ratio, we still recommend to start with high contrast reconstruction methods such as, e.g., SIRT or similar algorithms. The use of binned tomograms is however redundant, as binning of the subvolumes can be done on the fly during their alignment.

We documented the core of the STA pipeline (i.e., the processing script) in great detail through this report and through extensive comments in the code itself. We further provided multiple links to additional online guides and documentations. The script itself is available through the GitHub repository *TomographyTools*¹⁶ where it will be maintained and constantly updated. Users are welcome to submit feedback or suggestions for improvements. We additionally documented all relevant steps and parameters for the pre- and post-processing to enable users to reproduce the results.

We hope that the provided material will serve as a basis for various other projects, benchmarking efforts and teaching purposes.

¹⁶www.github.com/sscaramuzza/TomographyTools

5. Automated Alignment of Tilt Series for Cryo-Electron Tomography in *Dynamo*

5.1. Comment

This chapter shows developments that were made in the *Dynamo* software to address the challenges of throughput in STA by implementing a new algorithm for automatic and fast tilt series alignment. This chapter is the manuscript of a paper that is under preparation for submission. My main contributions as shared co-first author were the prototyping of functions, establishing compatibility with external softwares, writing of software wrappers, benchmarking, acquisition of experimental test data, testing of the algorithms and assisting in writing the following manuscript:

Automated Alignment of Tilt Series for Cryo-Electron Tomography in the *Dynamo* Software Package

Paula P. Navarro¹#, **Stefano Scaramuzza**²#, Henning Stahlberg², Daniel Castaño-Díez³*

Equal contribution

¹ *Department of Molecular Biology, Massachusetts General Hospital, Harvard Medical School, Boston, USA*

² *Center for Cellular Imaging and NanoAnalytics (C-CINA), Biozentrum, University of Basel, Basel, Switzerland*

³ *BioEM Lab, Center for Cellular Imaging and NanoAnalytics (C-CINA), Biozentrum, University of Basel, Basel, Switzerland*

*Correspondence to: daniel.castano@unibas.ch

Manuscript under preparation, 2020

5.2. Abstract

With the advent of modern technologies for cryo-electron tomography (cryo-ET), high-quality tilt series are more rapidly acquired than processed and analysed. Thus, a robust and fast-automated alignment for batch processing in cryo-ET is needed. While different software packages enabled several approaches for automated marker-based alignment of tilt series, manual user intervention remains necessary for many data sets, preventing high-throughput tomography.

We have developed a MATLAB-based framework in the *Dynamo* software package that automatically detects the maximum amount of fiducial markers in a tilt series and precisely centers and tracks them in an iterative manner. The computed marker coordinates are used to generate the aligned tilt series for tomographic reconstruction. Combined with our new batching system, this approach enables high-throughput unsupervised volume reconstruction. This new module also extends *Dynamo* with a large repertory of tools for tomographic alignment and reconstruction, such as specific visualization browsers and localized reconstruction systems, allowing users to rapidly assess the biological relevance of the data set. Our alignment approach has been successfully applied in a broad range of datasets of diverse biological samples.

5.3. Introduction

5.3.1. Motivation

Electron tomography (ET), particularly cryo-electron tomography (cryo-ET), is the method of choice for visualizing the near-native arrangement of cellular organelles and macromolecules within their biological context [Asano, Benjamin D. Engel, et al. 2016; Gan et al. 2012; Lučić et al. 2013]. The ET pipeline has been classically recognized as a time-consuming workflow with identified bottlenecks in data acquisition and image processing, so far preventing high-throughput cryo-ET. In brief, a series of micrographs are collected at several tilt angles, called tilt series, by physically rotating the specimen around a single axis perpendicular to the electron beam [Beck et al. 2016; Tocheva et al. 2010]. Subsequently, tilt series are aligned and used to reconstruct a 3D-volume, called a tomogram. Thus, tilt series alignment and tomogram reconstruction are essential steps in cryo-ET with a direct impact on the attainable resolution of the resulting 3D structure [Mastronarde and Held 2017].

High-resolution cryo-ET has only been possible in combination with subtomogram averaging (STA) [Briggs 2013]. STA exploits the fact that biological features are present in multiple copies within a tomogram and provides a framework to determine structural information by the numerical analysis of many noisy, randomly oriented subtomograms. STA computationally extracts subtomograms containing the structure of interest from a given tomogram. After subtomogram extraction, STA performs 3D alignment to compute a final average that retrieves a 3D signal-enhanced structure. Importantly, typical limitations linked to cryo-ET such as the missing wedge, sample geometry and low SNR, can be overcome by computational means in STA [Briggs 2013; Diebolder et al. 2012; W. Wan and Briggs 2016]. Several high-resolution 3D structures below the nanometer have been determined using STA [Hutchings et al. 2018; Khoshouei et al. 2017; Kovtun et al. 2018; Pfeffer et al. 2015; Schur, Obr, et al. 2016]. Currently, a variety of software packages specialized for STA exist: *Dynamo* [Castaño-Díez, Kudryashev, Arheit, et al. 2012], RELION [Bharat, Russo, et al. 2015], PEET [Heumann et al. 2011], Jsubtomo [Huiskonen et al. 2014], EMAN2 [Jesús G. Galaz-Montoya et al. 2015], PyTom [Hrabe et al. 2012], M [Tegunov, Xue, et al. 2020] and emClarity [Himes et al. 2018].

Dynamo is a software package specialized in image processing for STA that adapts to a variety of high-performance computing platforms such as GPU or CPU clusters [Castaño-Díez, Kudryashev, Arheit, et al. 2012]. *Dynamo* is also characterized by user-friendliness and flexibility to create new algorithms and combine them with other external tools. The backbone of *Dynamo* is written in the programming languages MATLAB, CUDA and C++, so that *Dynamo* is distributed both as MATLAB scripts as well as precompiled executables for different computing environments (Windows, Linux, macOS) [Castaño-Díez 2017].

Important improvements in microscope hardware and software for automated acquisition have recently allowed rapid collection of high-quality tilt series [Chreifi et al. 2019; Hagen et al. 2017; Mastronarde 2005; Suloway et al. 2009; Q. S. Zheng et al. 2004]. Accordingly, several software packages have implemented tilt series alignment and tomogram reconstruction in their workflow, with IMOD being the most popular [Mastronarde and Held 2017]. Other software packages including such workflows are Protomo [Noble and Stagg 2015], AuTom [R. Han et al. 2017], TOM [Nickell et al. 2005] and UCSF tomography [S. Q. Zheng, Keszthelyi, et al. 2007]. These software packages provide a well defined pipeline, yielding to effective tilt series alignment and tomogram reconstruction. There are efforts made for local refinements of tilt series, in which the final resolution of the subtomogram average is not directly dependent on the quality of the initial marker based alignment [Himes et al. 2018]. However, most STA structures are currently still generated by marker based alignment. Softwares for high precision tilt series alignment will therefore always remain important for these “classic” STA approaches but also for applications that depend only on full sized tomograms, e.g., segmentation, particle picking and initial tomograms used in refinements.

Even though currently available software packages for tilt series alignment are known to provide good results, they lack the combination of automation for high throughput and precise alignment. The most important high-resolution STA structures have therefore only been realized using manual aided tilt series alignment [Briggs 2013; Hutchings et al. 2018; Kovtun et al. 2018; Schur, Obr, et al. 2016; W. Wan and Briggs 2016]. The main task demanding manual intervention is often the precise detection of bead centers and their tracking over all tilts. Taking also into account the increasing speed of data acquisition, we are therefore in the need for an automated, fast and robust tilt series alignment in cryo-ET that also enables batch processing and aims to be integrated with high-resolution STA strategies.

Here, we present the implementation of an automatic tilt series alignment within *Dynamo*. The core of the algorithm is an elaborate method for automatic fiducial detection and tracking. Its implementation is optimized for high throughput, minimal manual intervention and minimal input parameters. The alignment pipeline can be controlled through a GUI or the command line. It is further equipped with a broad range of diagnostic tools. Together with the alignment pipeline we also developed additional features for localized reconstruction and the handling of large datasets.

5.3.2. Tilt series alignment with markers in cryo-electron tomography

During the acquisition of a tilt series, there are three interrelated systems: the specimen, the microscope and the projection plane. The *specimen* is physically rotated inside

the *microscope* to collect several *projection images* at different tilt angles. Thus, these players are geometrically related to each other; however, during the acquisition process, the relationship between them has been interfered with mechanical imperfections at the microscope and stage level. This relationship can be determined by tilt series alignment.

First, we need to understand the acquisition process where the three systems coexist. The coordinate systems for each of them are defined as $S = \{s_1, s_2, s_3\}$ for the specimen, a 3D object suspended inside the microscope by the stage; $M = \{m_1, m_2, m_3\}$ for the microscope, which defines the projection direction and the electron beam; and $B_i = \{u_i, v_i\}$ for the projection image plane, where $i = 1, \dots, I$ where I is the number of micrographs or projection images in a tilt series. Thus, a marker point j within the specimen, in S , is denoted as the coordinate vector $r_j = (x_j, y_j, z_j)$, where $j = 1, \dots, J$ with J being the number of markers identified. The final goal is to relate the microscope and specimen coordinate systems, M and S . Thus, simulating imaging conditions, M is projected into each micrograph of the system B_i along the projection direction, m_3 . Therefore, the M and B_i axes can be equalized: $u_i = m_1$ and $v_i = m_2$. Then, the alignment problem can be formulated as

$$p_{ij} = PR(\alpha_i)R(\theta_i)R(\psi_i)T_i r_j + d_j \quad (5.1)$$

where P is the projection matrix $\begin{pmatrix} 1 & 0 & 0 \\ 0 & 1 & 0 \end{pmatrix}$ and R is a rotation matrix with α_i being the elevation angle with respect to the m_1 axis (also referred to as beam tilt Castaño-Díez, Seybert, et al. 2006), i.e., non-perpendicularity between the electron beam axis, m_3 , and the tilt axis, m_2 . θ_i is the tilt angle around the m_2 axis, and ψ_i is the azimuth angle that rotates around the optical axis of the microscope, m_3 (also referred to as in-plane rotation). d_1 represents the image shifts with respect to the reference center; $d_i = (\Delta u_i, \Delta v_i)$; and r_j is the estimated 3D position of the marker in the projection model: $r_j = (x_j, y_j, z_j)$. The matrix

$$T_i = \begin{pmatrix} (h_i + \omega_i) \cos \delta_i & 0 & 0 \\ (h_i + \omega_i) \sin \delta_i & h_i & 0 \\ 0 & 0 & h_i \theta_i \end{pmatrix} \quad (5.2)$$

represents specimen changes during tilt series acquisition that involve size changes. h_i is the scaling factor, ω_i is an additive factor such that $h_i + \omega_i$ is the scaling along the specimen axis s_1 . δ_i is the skew angle, a rotation of s_1 towards s_2 , e.g., shrinkage. θ_i is a multiplicative factor for thinning along s_2 [Mastrorade 2008].

If we postulate that we search for the minimal difference between the observations and the estimated projected marker locations, p_{ij} , for all marker locations, we face a classical leastsquares problem of finding an approximation to the data observations by determining a set of parameters:

$$\frac{1}{\sum_{j=1, \dots, J} \#\Lambda_j} \sum_{j=1, \dots, J} \sum_{j \in \Lambda_j} \rho(|p_{ij} - q_{ij}|^2) := \mathcal{M}(\mathbf{r}, \boldsymbol{\alpha}, \boldsymbol{\theta}, \boldsymbol{\psi}, \mathbf{d}, \mathbf{h}, \boldsymbol{\omega}, \boldsymbol{\delta}, \boldsymbol{\tau}) \rightarrow \min! \quad (5.3)$$

where q_{ij} represents the observed marker positions. Λ_j is the set of tilt indexes where a q_{ij} is present for a given j . $\#$ represents the cardinality, the total number of a given set of indexes. $\mathbf{r} = \{r_j\}_{j \in 1, \dots, J}$ and $\boldsymbol{\alpha} = \{\alpha_i\}_{i \in 1, \dots, \Lambda_j}$ represent sets of a given alignment parameter depending on either j (the number of markers) or i (the number of micrographs). This analogously applies to the rest of parameters described. ρ represents a function that penalizes differences between observations and estimations in the model.

Now, if we are confident about the accuracy of the parameters present in Equation 5.1 to describe the alignment problem, ideally, all of them should be solved following Equation 5.3:

$$\hat{\mathbf{r}}, \hat{\boldsymbol{\alpha}}, \hat{\boldsymbol{\theta}}, \hat{\boldsymbol{\psi}}, \hat{\mathbf{d}}, \hat{\mathbf{h}}, \hat{\boldsymbol{\omega}}, \boldsymbol{\delta}, \hat{\boldsymbol{\tau}} = \arg \min_{\mathbf{r}, \boldsymbol{\alpha}, \boldsymbol{\theta}, \boldsymbol{\psi}, \mathbf{d}, \mathbf{h}, \boldsymbol{\omega}, \boldsymbol{\delta}} \mathcal{M}(\mathbf{r}, \boldsymbol{\alpha}, \boldsymbol{\theta}, \boldsymbol{\psi}, \mathbf{d}, \mathbf{h}, \boldsymbol{\omega}, \boldsymbol{\delta}, \boldsymbol{\tau}) \quad (5.4)$$

where $\hat{\mathbf{r}}$ indicates that we solve for all the possible values of a defined parameter. This analogously applies to the rest of parameters described.

The alignment model contains more parameters than need to be estimated. An estimation of all parameters may lead to overfitting which can greatly deteriorate the quality of the final reconstructed tomogram [Briggs 2013; Mastronarde 2008; Mastronarde and Held 2017; W. Wan and Briggs 2016]. The default projection model in *Dynamo* therefore assumes that the electron microscope is optimally calibrated and aligned. Thus, the value of α_i is not considered. Also tilt angles are not solved, since the value of θ_i is known from the acquisition scheme used. Furthermore, the specimen changes described by T_i are also neglected. Thus, in *Dynamo*, the default alignment parameters are defined as

$$p_{ij} = PR(\psi_i) r_j + d_i \quad (5.5)$$

leading to:

$$\frac{1}{\sum_{j=1, \dots, n_t} \#\Lambda_j} \sum_{j=1, \dots, n_t} \sum_{i \in \Lambda_j} \rho(|p_{ij} - q_{ij}|^2) := \mathcal{M}(\mathbf{r}, \boldsymbol{\psi}, \mathbf{d}) \rightarrow \min! \quad (5.6)$$

The parameters of the projection model can be found by solving an optimization problem where a nonlinear least-squares problem is approached [Amat, Castaño-Díez, et al. 2010; Lawrence 1992]. Thus, for fixed values of $\boldsymbol{\psi}$, the values of $\hat{\mathbf{r}}$ and $\hat{\mathbf{d}}$ can be determined by solving a linear system:

$$\hat{\mathbf{r}}, \hat{\boldsymbol{\psi}}, \hat{\mathbf{d}} := \mathcal{L}(\boldsymbol{\psi}) = \arg \min_{\mathbf{r}, \mathbf{d}} \mathcal{M}(\mathbf{r}, \boldsymbol{\psi}, \mathbf{d}) \quad (5.7)$$

In *Dynamo*, we first test different values of $\boldsymbol{\psi}$, to then fix the value which gives us minor differences between q_{ij} and p_{ij} , and use it for all the images in the tilt series. Optionally, *Dynamo* can solve for a value of $\boldsymbol{\psi}$ per tilt.

5.4. Algorithm

5.4.1. General workflow

The algorithm presented here bases on an initial separation of tasks: (1) *detection* of gold bead positions and (2) *indexing* of detected gold bead positions into trails. In brief, detection is performed to create a set of unindexed observations per micrograph that represents putative positions of gold beads. Then, observations are indexed into an initial set of trails, which can be then inserted in Equation 5.6 to calculate an initial 3D model. Consequently, the accuracy of the outputted 3D model is limited by the errors committed in previous steps, e.g., missing observations, false positives gathered during detection or wrongly trailed assignments during indexing. The algorithm applies then different computational approaches based on utilizing 3D projection models to meliorate indexing and detection, thus, iteratively refining the alignment solution model. The rest of this section is devoted to describing the details of the alignment workflow.

5.4.2. Detection

5.4.2.1. Overview

The *Detection* stage of the algorithm aims at creating a set of 2D positions defined across the tilt series, which represent putative positions of gold beads. This putative set of gold beads is defined as G_{il} , where $l = 1, \dots, L$ is the index that represents the number of markers extracted per micrograph. An initial G_{il} is created by selecting the peaks of the cross-correlation (CC) images resulting by comparing the micrographs to a gold bead template. The neighborhood of the peaks is analyzed in a process called feature extraction in order to eliminate false positives (i.e., CC peaks that do not correspond to gold beads).

The final cloud of observations G_{il} produced at this point is neither accurate (putative gold bead positions are not precisely centered) nor pure (false positives might have been included) nor exhaustive (some actual gold bead projections might have escaped detection or have been wrongly removed from the observation set). Later refinements will take care of these inaccuracies.

5.4.2.2. Cross-correlation

Automated detection of gold beads is performed by a peak-searching algorithm based on normalized cross correlation (NCC). A synthetic, fiducial marker template, which is created in line with the gold bead radius in pixels provided by the user, is compared in each micrograph. NCC peaks are located and used to create an averaged image of a gold bead in the tilt series (Figure 5.1). The CC map of each micrograph against the new refined template is computed, producing a finer estimation of putative gold bead centers (Figure 5.1). This step explicitly overestimates the number of possible gold beads to be found on each micrograph, suggesting a default value of $L=300$, which is well above the number of beads typically available in regular micrographs.

5.4.2.3. Feature extraction

Each image patch around a CC peak has a CC value associated to it. In this step, further features are computed for each patch, to be optionally used for selection of patches that truly contain gold beads. The most consistently useful feature is the rotational merit of each patch, defined in this context as the minimum CC attained by a patch when it is compared against a series of rotated versions of itself (each rotation angle being a multiple of 40°). This arbitrary definition is conceived as a rough figure of merit to estimate the *rotational symmetry* of each patch.

Additionally, non-default computable features as Sobel (Mastronarde and Held 2017) and bandpass filtering or combination of both may be applied to template and patch before computing their CC values; by estimating the inertia moment of each patch, and by calculating the components of each patch along the basis of principal components of the set of all patches, along the usual lines of Principal Component Analysis (PCA) (Heel, R. V. Portugal, et al. 2016).

5.4.2.4. Peak selection step

The default selection method only uses the rotational merit and NCC. The L peaks are ordered by their CC merit in descending order and only the values possessing a CC merit above the threshold computed by Otsu's method are selected [Otsu 1979]¹. This procedure is repeated on the L peaks but now considering their rotational merit. In our algorithm, the default selection method outputs the set of peaks that score above the Otsu threshold both for CC and rotational merit. The intersection of all such sets of

¹Otsu thresholding is a binarization algorithm to distinguish signal from a noisy background by iteratively searching for a threshold that provides the maximum variance between two classes.

all micrographs is the *initial observation set*, G_{il} , and defines what we called the *peak selection step* in our alignment workflow.

For difficult micrographs, alternative options for peak selection were developed including clustering in the bidimensional space of rotational merit and CC value or N-dimensional clustering in the space of principal component analysis (PCA)(Figure 5.2). We have compared the resolving efficiency of PCA followed by clustering using Gaussian mixture models (GMM) and the default Otsu's method to differentiate foreground from background (Figure 5.2). By PCA, of all candidate marker locations, two classes are clearly identified when ice contamination is low, no carbon layer is present and gold beads tend to be sparsely located across the tilt series (Figure 5.2A). Both methods, PCA/GMM and Otsu were able to identify false positives under these conditions (Figure 5.2A-C). However, when few gold beads exist at the central tilts combined with pronounced ice contamination and gold bead clustering towards the carbon layer, a homogenous class is uniquely determined (Figure 5.2D). In this case, PCA/GMM does not properly discern between marker and background containing patches (Figure 5.2E). By contrast, Otsu's method selects gold bead containing patches from the foreground under the same conditions (Figure 5.2F).

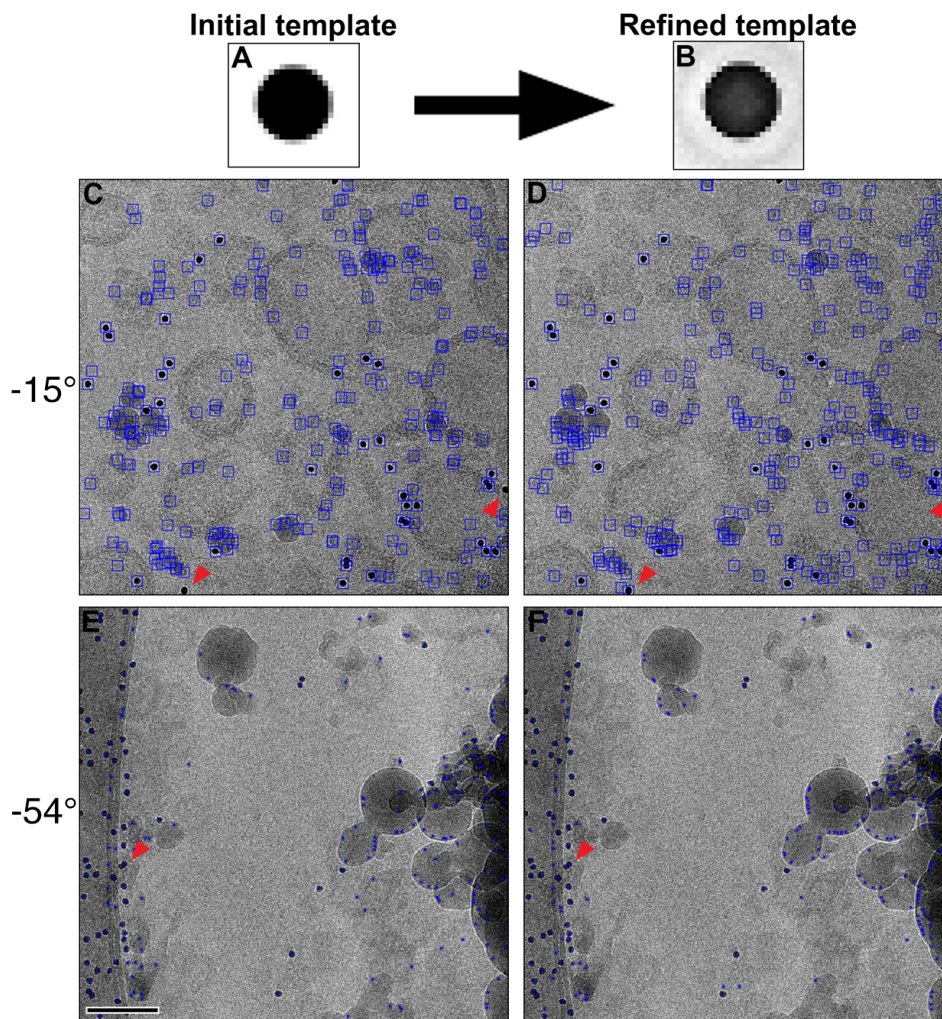


Figure 5.1.: **Automated marker detection in *Dynamo*.** (A) A template generated by *Dynamo* based on the input parameters defining the marker radius. (B) The refined template obtained by averaging 300 peak location images with maximum CC values from tilt series. (C) -15° tilt image. Detected marker locations by the *gold finder* in *Dynamo* using the template shown in A for CC matrix calculation by NCC and assessment of CC scores. Red arrowheads represent gold bead locations not detected when using the template in A as reference for template matching. (D) Same micrograph as shown in C where the *gold finder* uses the template shown in B as reference for template matching. Red arrowheads represent the same gold beads, now detected as marker locations. (E) -54° tilt image, showing gold bead clustering in the presence of the carbon layer in an EM grid. (F) Same micrograph as shown in E. Blue boxes: detected marker locations; blue squares: marker location center; scale bar: 100 nm. Micrographs belong to the tilt series data set of proteoliposomes (Table A.1).

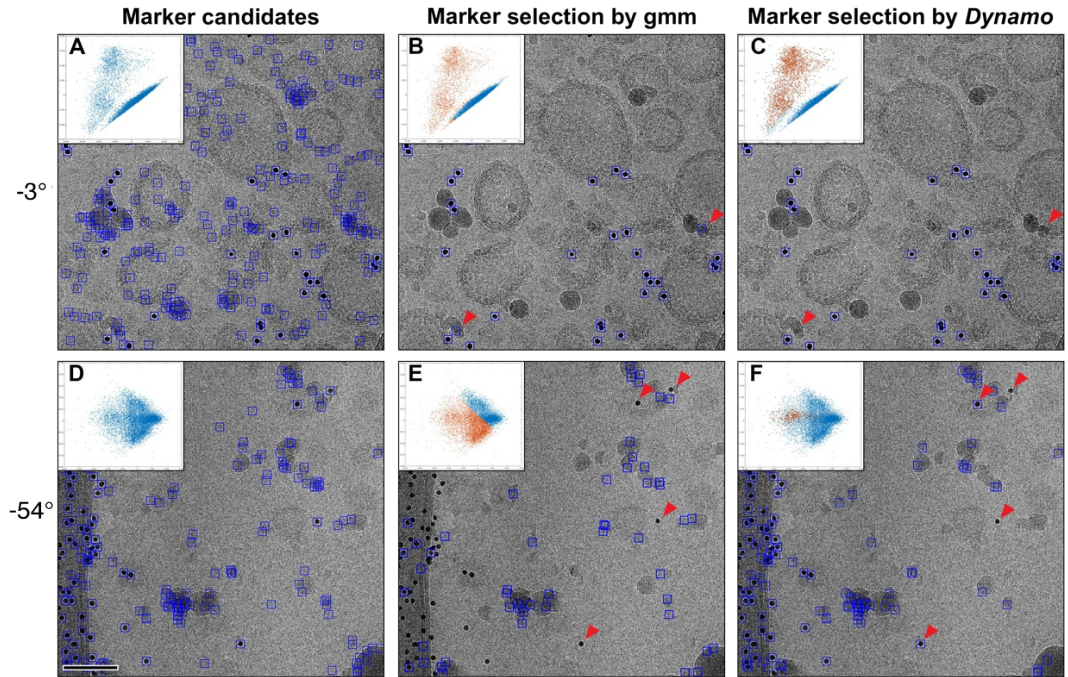


Figure 5.2.: **Automated marker selection in *Dynamo*.** TEM micrographs acquired at -3° (A-C) and -57° (D-F) with their selected marker locations (blue boxes), together with the corresponding 2D PCA scatterplot comparing the *Dynamo* criteria for peak selection with the GMM approach. In the scatterplots, orange data points represent selected particles. (A) Candidate marker locations after NCC in *Dynamo*. (B) Selected marker locations by applying GMM. Red arrowheads indicate detection of false positives. (C) Selected marker locations by *Dynamo* after applying rotational symmetry and Otsu's method as selection criteria. Red arrowheads indicate image locations that lead to false positive in B. (D) Candidate marker locations after NCC in *Dynamo*, showing gold bead clustering and presence of carbon in the sample. (E) Selected marker locations by GMM. Red arrowheads indicate non-detected gold beads. (F) Selected marker locations by *Dynamo* after applying rotational symmetry and Otsu's method as selection criteria. Red arrowheads indicate gold beads that were not detected in E. Scale bar: 100 nm. Micrographs belong to tilt series of proteoliposomes (Table A.1).

5.4.3. Indexing

5.4.3.1. Overview

In indexing, unique marker identities are attributed to the marker positions G_{il} , resulting in a *trail* of coordinates for each marker, spanning multiple tilts or ideally the full tilt series. The indexing step is a core task in marker based alignment and is achieved through a series of operations explained in the following.

5.4.3.2. Pairwise shifting

In the initial indexing of G_{il} all marker locations in two consecutive micrographs are considered and matched pairwise as $[G_{il}, G_{i+1,l'}]$. This procedure is called *cloud shifting* between micrographs, and consists in exhaustively computing the number of matches between the observations of two subsequent micrographs for all possible relative shifts between two micrographs. A match is defined as:

$$U_{ik} = (l, l'), \quad k = 1, \dots, K \quad (5.8)$$

where U_{ik} is a match between i and $i + 1$, and k is the match index, which runs from 1 to K , where K is the total number of matches found between i and $i + 1$.

The number of matches per micrograph, U_{ik} , is designated with a shift value with respect to the previous image, i :

$$\{U_{ik}\} = U_i(s^*), \quad s \in \mathcal{S}, \quad s \in B \quad (5.9)$$

where s represents the shifts between a pair of images that belong to \mathcal{S} , a system in \mathcal{R}^2 , where $\mathcal{S} = (1, 1), \dots, \mathcal{T} \cdot \mathcal{T}$ is the maximum shift allowed, and is set in pixels by default, but it can also be modified by the user. Therefore, $s = (s_u, s_v)$, and s^* is the shift which results in the maximum number of matches per pair of micrographs:

$$\mathbf{s}^* = \arg \max_{\mathbf{s} \in \mathcal{S}} \#U_i(\mathbf{s}) \quad (5.10)$$

Finally, a match is defined as:

$$(l, l') \in U_i(s^*) \Leftrightarrow |G_{il} - G_{i+1,l} + s^*| < \mathcal{T} \quad (5.11)$$

this means that a match is only valid when the difference between the position of a given marker in a micrograph, G_{il} , and its shifted position in the next micrograph, $G_{i+1,l} + s^*$, is lower than a certain tolerance threshold, \mathcal{T} .

In other words, a match is defined as two observations in subsequent micrographs whose relative distance falls below a predetermined matching threshold after shifting one of the micrographs. The relative shift that produces the maximum number of matches among two micrographs is stored. This procedure is repeated for each pair of micrographs. The parameters to be provided by the user are the matching threshold and the maximal shifts to be tested.

5.4.3.3. Chains of matches

After collection of all possible matched pairs, the algorithm constructs *chains* of matched observations across the tilt series. A chain is defined as a subset of observations in which each individual observation belongs to a different micrograph and is matched to a second observation on consecutive micrographs. Thus, a chain is generated based on the concatenation of matches:

$$U_{ik} \ominus U_{i+1,k} \rightarrow (l, l')_{ik} \ominus (l, l')_{i+1,k} \Leftrightarrow l'_{ik} = l_{i+1,k} \quad (5.12)$$

where the symbol \ominus means concatenation. This can be easily explained by assuming that a set of matches is defined after solving Equation 5.11 as shown in Figure 5.3. Based

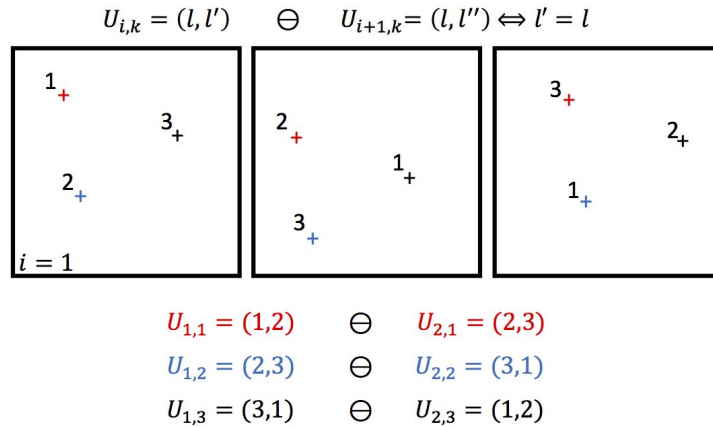


Figure 5.3.: **Pair-wise correspondence of marker trajectories in a tilt series by *Dynamo*.**

The correspondence of matches to build complete chains, describing the trajectories of the markers across the tilt series is represented. Black boxes: tilt images composing a tilt series, $i = 1, 2, 3$.

on this, a chain is defined:

$$\mathbb{C}_a = \{U_{ik}\} \Leftrightarrow \forall i \in I_a - \max(I_a) \ \& \ U_{i,k} \ominus U_{i+1,k} \quad (5.13)$$

where $a = 1, \dots, A$, is the chain index. A chain is a set of concatenated matches that belong to the set of images, $I_a - \max(I_a)$. The generation of chains is illustrated in Figure 5.4.

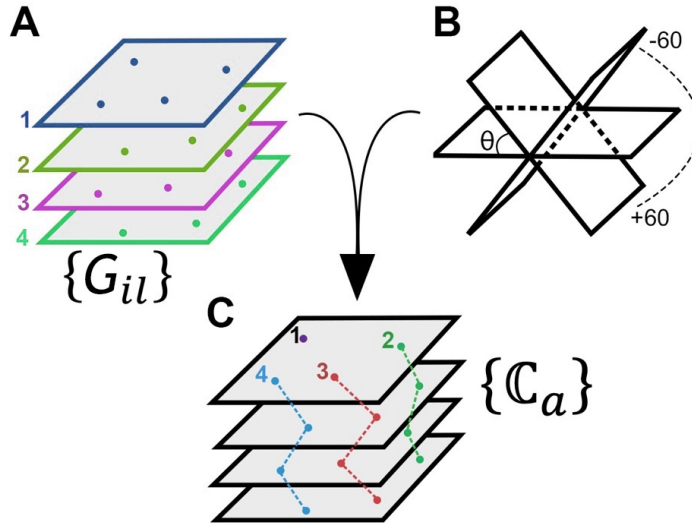


Figure 5.4.: **Scheme of the geometrical operations performed by the command shifter to compute chains.** (A) a set of markers, per micrograph, $\{G_{il}\}$, serves as input for the **shifter**. (B) The geometry of the acquisition scheme of the tilt series is inputted in the **shifter**, θ . (C) The **shifter** outputs a set of chains representing the trajectories of the markers across the tilt series, $\{C_a\}$, according to the measured marker positions, $\{G_{il}\}$, and the geometry of the tilt series.

In summary, this step of the algorithm selects an initial observation in a micrograph randomly, then – and only if a matched observation is available in a consecutive micrograph – it adds the matched observation. This operation is repeated on the recently joined matched observation, until added observations have no matches on consecutive micrographs, or till the last micrograph has been attained. The chain is said to be maximal if it includes all those observations from the initial set that it can contain.

Ideally, each chain or trail represents a single physical gold bead, *trail purity*, and therefore, all projections of a given gold bead are contained in the same trail, *trail completeness*. However, at this initial stage, the trails may not possess neither of these features. Wrong matches of observation can easily happen when the projection of two or more gold beads lay within a close distance in a micrograph, thus, preventing trail purity. Besides that, chains may be interrupted when a match in a given observation is missing or unidentified, thus, lacking trail completeness. As a result, observation of one single given gold bead might be assigned to different experimental observation trails (each defined on a different set of subsequent tilt indices, i).

²It is recommended to track as many markers as possible and to only exclude markers if they dramatically distort the alignment results. A range of tracked markers between 20 and 100 should be adequate to compute an optimal alignment.

5.4.3.4. Trail selection

Trails composed by too few observations are rejected. The default policy is to exclude trails that include less than 15 observations². The remaining trails are used to solve equation Equation 5.6, giving a first estimation of the 3D position of the markers, the tilt axis angle and the shifts.

At this step, a further selection of trails is performed, based on the estimated 3D position of the marker corresponding to the trail. When two markers or more have close 3D positions (defined by a threshold), only the one with the better residual is kept. Removal close markers in 3D serves a double goal: (1) It handles trail duplication, as it effectively gets rid on (non-overlapping) trails correspond to the same three dimensional marker. (2) Clusters of physically markers are avoided.

5.4.3.5. Iterative re-indexing

The surviving 3D positions of the markers in the model fitted from the selected trails are reprojected onto the 2D micrographs. Each 3D marker induces thus a set of positions, each on a different micrograph. Note that a marker does not need to be present at every micrograph, as the coordinates of its reprojection might fall out of scope in some tilts. The set of reprojections of a given marker is called *reprojection trail* which has a unique index that identifies the 3D marker. The set of all reprojection trails is used to re-index the cloud of observations. The indexing of the observations created in previous steps is now discarded and recomputed from scratch: each reprojected trail is analyzed by visiting sequentially its reprojected positions on each micrograph. The experimental observation on that position that falls closest to a reprojected position is assigned to the marker index of that trail, provided this distance is smaller than a given threshold parameter.

The newly created set of trails can then be fitted to produce a refined set of 3D markers, which can then be used again to generate a further set of trails. By default, this procedure is repeated till no further improvement in the fitting quality is measured, or till a maximal number of iterations (a default number of 10 is used by default). An illustration of the re-indexing procedure is given in Figure 5.5.

5.4.3.6. Tilt gap filling

The set of 3D markers created by the iterative refinement is used to locate imperfections inherited from previous processing steps. In particular, the pairwise shifting procedure applied to generate a first tentative indexing of the experimental observations did not

incorporate any assumption on the shifts among the micrographs, nor on the general projection geometry. This might lead to wrong matches or low numbers of correct matches. If all the matches in a micrograph are wrong, the re-indexing step will reject all experimental observations in that micrograph, as they will not be coherent with the model induced by the majority of the observations. This will thus produce a *full tilt gap*, i.e., a micrograph in which observations have not been indexed.

Micrographs that have not been indexed can be revisited after the iterative re-indexing has generated an initial geometry model. Similarly to the pairwise shifting procedure described above, the set of all predicted positions generated by projecting all 3D markers on one micrograph is compared to the set of all available observations on that micrograph. If for this given micrograph a shift is found in which a number of projected markers is sufficiently close to a set of experimental observations (CC peaks), those observations are indexed, each one with the index of the closest projected marker. The criterion for sufficient closeness between an individual observation and a projection is defined by the user as a static number of pixels, or in terms of the typical residuals read in other micrographs.

After indexing a gap micrograph, the model is recomputed and used to index other possible missing micrographs.

5.4.3.7. Marker extension

The final step in the construction of the trails addresses the recovery of 3D markers whose observations have not been indexed in any trail in the current trail set. The rotations and shifts corresponding to the current projection model are applied onto all non-indexed cross correlation peaks. This allows to check for new putative trails. In this step, a putative trail is defined as a set of aligned observations from different micrographs whose distance is below a given threshold. Each observation belongs to an unique putative trail, chosen to minimize the distance between observations from subsecutive micrographs.

Putative trails that contain more than a given number of observations (default value is 10), are tested for coherence with respect to the alignment model: the hypothetical position of their 3D marker is computed and reprojected onto the micrographs where the putative trail is defined. If a sufficient number of observations in this putative trail are sufficiently close to their respective reprojections, the putative trail is assigned a new trail index and added to the set of trails. Here, only the observations whose distance to their reprojections falls below a threshold will be included onto this trail. After analysis of all possible putative trails, a new projection model is defined, feeding the new set of trails as data for a least squares regression.

5.4.4. Trail refinement

5.4.4.1. Overview

All the steps described in the previous section work towards the creation a series of indexed trails, based on positions computed through cross correlation. In this section, the image patches at those positions are analyzed in order to refine both the position of observations and the composition of the trails.

5.4.4.2. Position refinement

The position of each gold bead on each observation is refined to subpixel precision by alignment of the patches cropped around the original observations. In this procedure, an average image is produced for each trail, and the observations are recomputed using this average image as template. The new position of each observation is computed by locating the cross correlation peak closest to the position predicted by the projection model.

5.4.4.3. Trail gap filling

Missing observations inside a trail are called *trail gaps*. Trail gaps might happen due to physical absence of a given 3D marker in a particular micrograph. This happens when markers are located far away from the tilt axis: projections of such markers might be present at high tilts but not in the central tilts. Further reasons for a trail gap might be the occlusion of gold beads by other high contrast objects, as other gold beads, ice or biological features such as membranes. This interference might cause spurious CC peaks that are located far away from the actual center of the gold bead. In such cases, previous indexing steps based on thresholds might leave the index assignment of an observation unassigned, if the distance between the observation and the closest reprojection is large.

This step adopts the strategy of scanning the behaviour of the CC in the neighbourhood of the reprojection: peaks detected inside a given radius of the reprojection are indexed into the trail if no further peaks are found inside an outer threshold radius. The inner threshold radius is set by default to the mean residual plus two standard deviations. The outer threshold radius prevents indexing CC peaks whose location might have been corrupted by the presence of a close neighbouring high intensity structure.

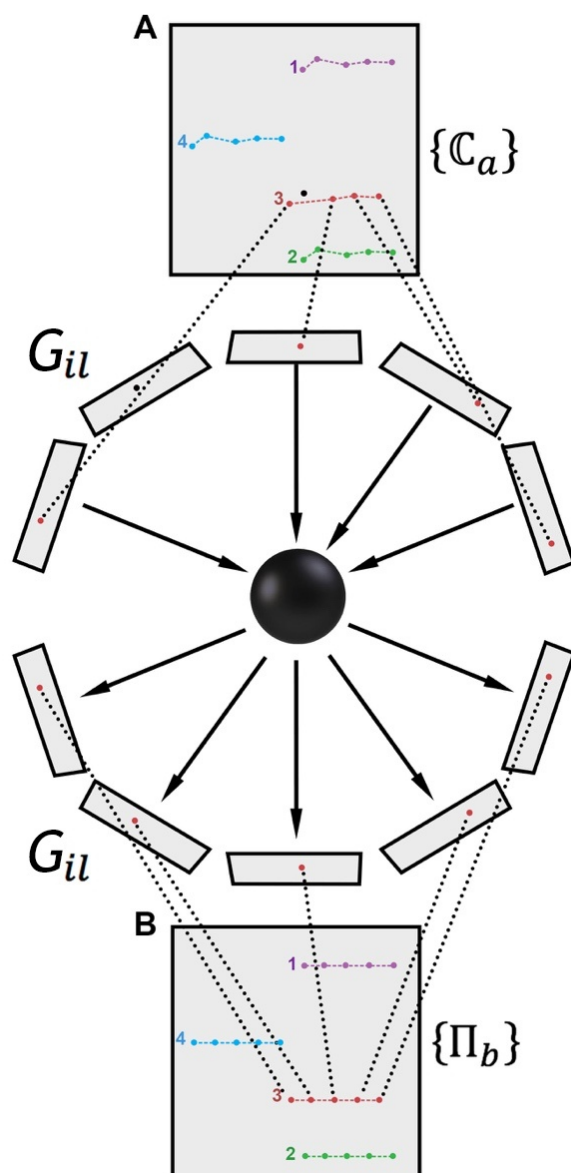


Figure 5.5.: **Scheme of the geometrical operations performed by the reindexer.**(A) Projected stack of all the images composing the tilt series. The set of marker trajectories, $\{C_a\}$, is represented as four gold bead trajectories with different colour (purple, blue, red and green), where $a = \{1, 2, 3, 4\}$. $\{C_a\}$ is used to calculate the 3D position of the defined gold bead markers represented by the black sphere at the centre. The observations, G_{il} , are represented across each tilt image; red dots: observations included in the chain $\{C_3\}$; black dot: observation excluded in the chain $\{C_3\}$. (B) 3D gold bead markers are reprojected into the tilt images. The **reindexer** rescue an observation that is now included in the refined trace Π_3 . A new set of refined traces, $\{\Pi_b\}$, is calculated by the **reindexer**. Refined traces are represented in the aligned stack of tilt images composing the tilt series.

5.5. Software package

5.5.1. Implementation of algorithm

All the previously described steps of the algorithm have been fully implemented in *Dynamo*. The functions are accessible either individually or within a *Dynamo workflow* capable of mapping a tilt series into a reconstruction in a fully automated manner. The only necessary parameter requested from the user is an estimation of the gold fiducial diameter.

The *Dynamo workflow* GUI allows for sequential application of all described steps of the algorithm (Figure 5.6). Various additional applications are attached to each step, allowing users to visually and quantitatively inspect the output generated, guiding them towards a finer tuning of parameters or towards visiting the algorithmic steps in a non-sequential order³.

Every step accessible through the GUI can also be called from the command line, allowing the users to design their own specialized workflows. Specific syntax and formats are described in the online documentation⁴. For large datasets, *Dynamo* offers a module for automatic alignment on full sets of tilt series called batching system. In the batching system, a list of tilt series alignment parameters is fed into the software module that governs the automatic alignment of a full dataset with multiple tilt series (Figure 5.7).

5.5.2. Auxiliary tools

Together with the development of the automated tilt series alignment, a broad range of auxiliary tools were established, as listed in the following:

- **Gold bead edition:** Gold beads included in the trail set in a any given moment of the processing can be shown in an interactive gallery, where the user can quickly manually eliminate or recenter a gold bead. This depiction is linked to other inspection tools, enabling the user to locate quickly the contextual information attached to a given goldbead, such as its position in the projected trail, its location in the micrograph, the cross correlation and the residual values.
- **Edition of trail projections:** Trail projections can be generated using the trail locations in the unaligned tilt series or in the aligned tilt series. In both cases, they

³www.dynamo-em.org/w/index.php/Walkthrough_on_GUI_based_tilt_series_alignment

⁴www.dynamo-em.org/w/index.php/Walkthrough_on_command_line_based_tilt_series_alignment

provide a powerful diagnosis tool to visually estimate the quality of an alignment model. *Dynamo* enables the user to compare graphically trails of observations selected by their features (residuals, spatial locations), together with their respective trails of reprojections. Such plots are interactive, allowing users to select individual observations (or groups of them) in order to visualize them in the linked viewing systems (similar to the gold bead gallery or the micrograph editor) and include or exclude them from the current set of markers.

- **Localized reconstruction of subtomograms:** This feature allows to directly reconstruct only user defined regions of a tomogram. This is very helpful to save processing time and storage space in case only a small region of a tomogram is of interest. Until now, the full tomogram had to be reconstructed before allowing to reduce its size.
- **Repository:** The *Dynamo* repository is an internal database system allowing to easily structure all types of files and directories. It is the backbone of the batching system. It is particularly useful for large datasets. Its usage is explained in the online manual⁵.
- **Wrappers:** Through wrappers, *Dynamo* can use CTFFIND4 [Rhou et al. 2015] for CTF estimation. Users can then use IMODs ctfphaseflip [Xiong et al. 2009] or NovaCTF [Turoňová et al. 2017] for CTF correction. Tomographic reconstruction of aligned tilt series in *Dynamo* is usually performed by WBP with the choice of different filters (e.g. SIRT-like filter). Alternatively, IMOD is also available for 3D reconstruction of tilt series through the wrappers. A list of selected wrappers is given in Table 5.1). The wrappers can be found online⁶.

The combination of these auxiliary tools allows to perform the complete tomographic reconstruction in a streamlined workflow for large datasets within *Dynamo* (Figure 5.7).

⁵www.dynamo-em.org/w/index.php/Programmatic_control_of_alignment_and_reconstruction_workflows

⁶www.github.com/sscaramuzza/TomographyTools

Table 5.1.: **MATLAB wrappers in *Dynamo*.** *Dynamo* wrappers can be found online: www.github.com/sscaramuzza/TomographyTools.

Source	Command	Definition	Comments
IMOD	<code>binvol</code>	Bins volume 4 times	It uses <code>binvol</code> from IMOD
	<code>ctf2rec</code>	Reconstructs tomogram from aligned tilt series	From CTF-corrected tilt series. It uses <code>tilt</code> from IMOD.
	<code>ctffind2imod</code>	Transforms CTFFIND4 defocus output file to an IMOD-compatible defocus file	Inside <code>ctffind_wrapper</code> in <i>Dynamo</i>
	<code>ctffOutput2matrix</code>	Creates a matrix from CTFFIND4 defocus file to feed the function <code>matrix2imodDef</code>	Alternative to <code>ctffind2imod</code> . Use in combination with <code>matrix2imodDef</code>
	<code>dctfphaseflip</code>	CTF correction in IMOD	It uses <code>ctfphaseflip</code> from IMOD
MATLAB	<code>flipYZ</code>	Flips YZ axes in a tomogram	It uses <code>binvol</code> from IMOD
	<code>imodmodel2xf</code>	Obtains the rotation files (<code>.tltxf</code> and <code>.tlt</code>) from an IMOD model	It uses <code>tiltalign</code> from IMOD
	<code>imodtxt2imodmodel</code>	Creates an IMOD model from a text file containing the marker coordinates.	It uses <code>point2model</code> from IMOD
	<code>matrix2imodDef</code>	Converts a CTFFIND4 defocus file to an IMOD-compatible defocus file.	Integrated in <code>ctffind4_wrapper</code>
	<code>transfromFiles2ali</code>	Creates rotation files and the aligned stack.	It uses <code>newstack</code> from IMOD
CTFFIND4	<code>ctffind_wrapper</code>	Calls CTFFIND4	If you choose the parameter <code>imodFormat</code> ; the function will produce an IMOD-compatible output file
NovaCTF	<code>novaCtfWrapper</code>	Calls NovaCTF	IMOD and CTFFIND4 defocus files are compatible.

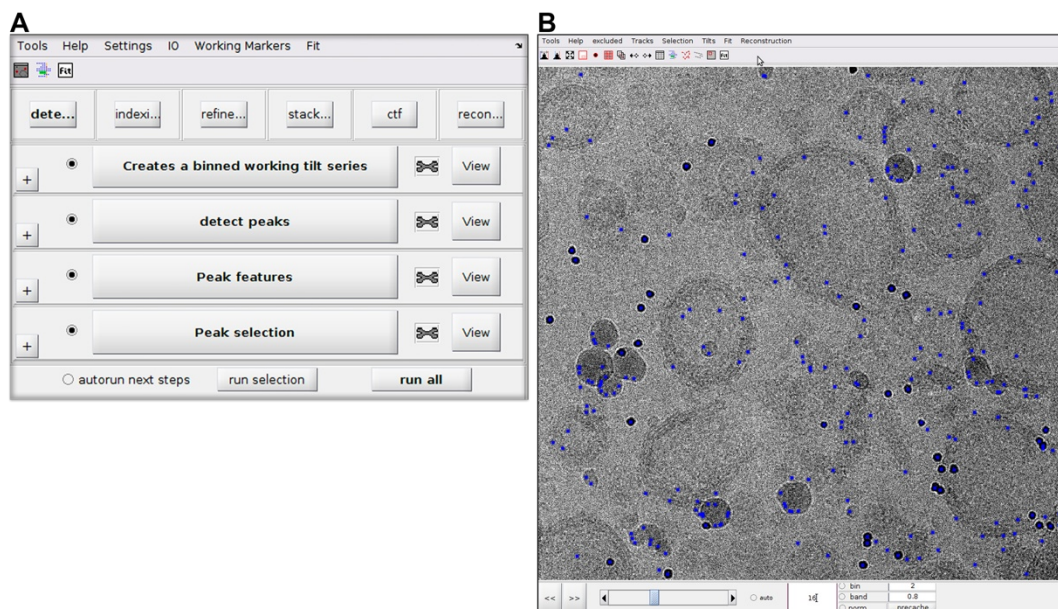


Figure 5.6.: **Workflow *Dynamo* GUIs for tilt series alignment (*dtsa* and *dmarkers*).** (A) General *Dynamo* tilt series alignment workflow (*dtsa*). By clicking on the button View, different panels for visualization of selected markers in working tilt series are available. The most useful is *dmarkers*. To load data in the GUI go to *IO*→*tiltseries matrix*→*browse*. Nominal angles can be included by clicking on *IO*→*nominal angles*→*browse* or manually by clicking on *IO*→*nominal angles*→*manual input*. The angles are given in MATLAB format by the user, e.g., if a dose-symmetric scheme was used in an angular range of -60° to 60° , with an angular increment of 3° , then the input should be $-60:3:60$. Marker radius is indicated in the panel button detect marker, after enabling the button +. (B) *dmarkers* offers manual picking and fixing of markers as well as accessory supplementary tools for tilt series and selecting markers. Furthermore, generation of fiducial model can be easily be done in *dmarkers*. Toolbox buttons from left to right: automatic contrast fit (full histogram); launch manual contrast tool; reset to full view; zoom in: select a box to zoom in; enter new shape (new contour in IMOD); auxiliary view selected markers; track for selected marker visualization (useful to fix centers if needed), automatically move after click to the left consecutive tilt from current tilt; automatically move after click to the right consecutive tilt from current tilt; summary of current defined shapes (counters in IMOD); graphical sketch of occupancy of current traces; view all raw tilt traces; view all tilt traces (fit traces); auxiliary view of full micrograph (region); compute fitting. See how *dmarkers* GUI is used step-by-step go to: www.dynamo-em.org/w/index.php/Walkthrough_on_manual_marker_clicking.

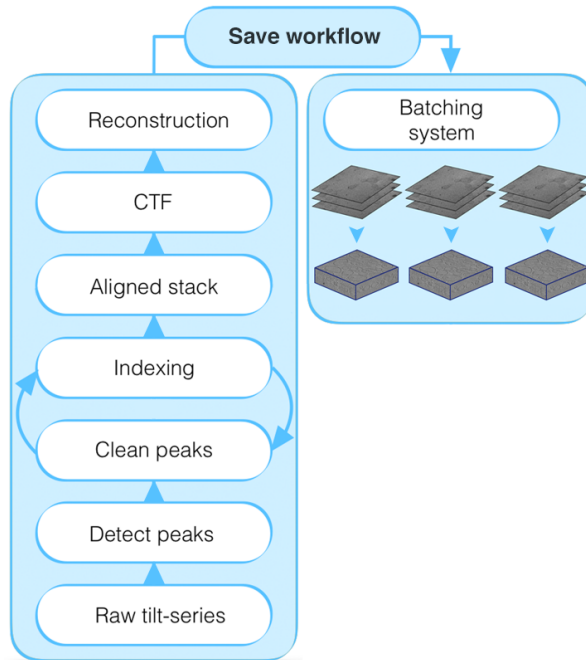


Figure 5.7.: ***Dynamo* workflow for tilt series alignment.** Tilt series are acquired in a TEM microscope generating a stack of 2D images (projections), here referred to as raw tilt series. In *Dynamo*, raw tilt series are used to detect peaks by template matching, assigning a cross-correlation (CC) map to each 2D image forming the tilt series. Peaks in the map are candidate marker locations. Classification of peaks to exclude false positive is carried out by exhaustive exploration of identifiable features in the fiducial markers (e.g. rotational symmetry). Selected peaks as marker containing patches are indexed into traces by pairwise correspondence of all peaks in neighbouring 2D images to represent the trajectories of the fiducial markers across the tilt series. To refine traces and recover possible missing marker points along the tilt series, indexing and re-selection of fiducial markers is performed in an iterative manner. Trails are used to estimate the alignment parameters. The aligned stack is CTF corrected by the use of MATLAB functions in *Dynamo* that make use of third party software packages for CTF estimation and correction. Finally, the aligned tilt series are reconstructed into a tomogram to recover 3D information. The batching module allows to store the alignment parameter defined in one tilt series and to automatically apply them on a full dataset.

5.6. Conclusion and outlook

Based on the need for image processing automation in cryo-ET, we successfully implemented an automatic marker based tilt series alignment workflow in *Dynamo*. The algorithm is optimized to detect the maximum amount of fiducial markers, to center them on the sub-pixel level and to reliably track them over all tilts to generate aligned tilt series with high precision. With the automation of these processes we significantly increased the throughput for tomographic image processing projects. We also developed a set of auxiliary tools for visualization, parameter editing, database control and communication with other software packages.

We tested the alignment workflow on several EMPIAR datasets (Table A.1). The computational speed was found to be 1-3 minutes per tilt series (Table A.2). To assess the alignment quality so far we relied on visual inspection of the marker trails and the root mean square (RMS) of the residuals resulting from the least square fitting. This value however depends a lot on the number of beads included in the model and on the choice of alignment parameters. It therefore does not serve as a reliable quality criteria. We therefore plan to implement the STA processing pipeline introduced in Chapter 4 to validate the alignment algorithm by reconstructing a high-resolution electron density map.

For future developments, we plan to include the option to apply masks on the micrographs to exclude larger regions that have a negative impact on the alignment quality (e.g., ice deformations next to carbon). This feature could also be useful when using localized reconstruction. Other developments are planned to expand our algorithm to include markerless alignment (e.g., for cryo-FIB data) by adapting existing algorithms [Castaño-Díez, Scheffer, et al. 2010; R. Han et al. 2017; Mastronarde and Held 2017; Noble and Stagg 2015]. The combination of the implemented automatic alignment procedure, the local reconstruction algorithm and the repository system serves as a basis for future developments in *Dynamo* to realize localized refinement of tilt series similar to current implementations of this idea [M. Chen, Bell, et al. 2019; Himes et al. 2018; Tegunov, Xue, et al. 2020]. Such algorithms minimize negative effects of distortions caused by, e.g., beam induced motion [J.-J. Fernández, Sam Li, and Agard 2019; J.-J. Fernández, Sam Li, Bharat, et al. 2018].

6. Molecular architecture of the SNX-BAR membrane coat for endosomal sorting

6.1. Comment

This chapter shows the structural study of the protein coat formed by the endosomal SNX-BAR sorting complex on membrane tubules. This chapter is the manuscript of a paper that is under preparation for submission. My main contributions as shared co-first author were performing the complete image processing for cryo-electron tomography and subtomogram averaging as well as writing and creating figures for the related parts in the manuscript. The challenging sample asked for advanced applications of *Dynamo* including the development of scripts and functions tailored to the geometry of this specific sample. The method section presented at the end of this chapter is therefore more elaborated than the one included in the official manuscript. The following publication is planned:

Molecular architecture of the SNX-BAR membrane coat for endosomal sorting

Carlos López-Robles¹#, **Stefano Scaramuzza**²#, Soledad Baños-Mateos¹, Miguel Romero³, Elsa N Astorga-Simon¹, Ander Vidaurrezaga¹, Juan Fernandez-Recio^{4,5,6}, Adriana L Rojas¹, Daniel Castaño-Díez⁷ *, Aitor Hierro^{1,8*}

Equal contribution

¹*CIC bioGUNE, Basque Research and Technology Alliance (BRTA), Bizkaia Technology Park, Derio, Spain*

²*Center for Cellular Imaging and NanoAnalytics (C-CINA), Biozentrum, University of Basel, Basel, Switzerland*

³*Life Sciences Department, Joint BSC-CRG-IRB Research Program in Computational Biology,*

Barcelona Supercomputing Center (BSC), Barcelona, Spain

⁴*Barcelona Supercomputing Center (BSC), Barcelona, Spain*

⁵*Instituto de Ciencias de la Vid y del Vino (ICVV), Consejo Superior de Investigaciones Científicas (CSIC) - Universidad de La Rioja - Gobierno de La Rioja, Logroño, Spain*

⁶*Institut de Biologia Molecular de Barcelona (IBMB), Consejo Superior de Investigaciones Científicas (CSIC), Barcelona, Spain*

⁷*BioEM Lab, Center for Cellular Imaging and NanoAnalytics (C-CINA), Biozentrum, University of Basel, Basel, Switzerland*

⁸*Ikerbasque, Basque Foundation for Science, Maria Diaz de Haro, Bilbao, Spain*

*Correspondence to: ahierro@cicbiogune.es, daniel.castaño@unibas.ch

Manuscript under preparation, 2020

6.2. Abstract

The endosomal network is a major hub for protein trafficking and contributes to the ability of a cell to sense and respond to its environment. Defects in sorting and trafficking of cargo from endosomes have been linked to multiple neurodegenerative disorders. Among the key protein machineries involved in sorting and recycling are members of the sorting nexin (SNX) family. Heterodimeric combinations of SNX1 with SNX5 belong to the endosomal SNX-BAR sorting complex for promoting exit-1 (ESCPE-1) and have shown the ability to mediate cargo recycling independently of the retromer core and to form endosome-derived tubular carriers with functionally distinct membrane coats. How SNX-BAR proteins coordinate lipid-binding, cargo selection and membrane deformation through organized lattices remains largely unknown.

We therefore studied the structure of the SNX1-SNX5 heterodimer and how it is recruited to the membrane to form coated tubules for cargo transport. Using a combination of X-ray crystallography, cryo-electron microscopy, biochemistry and analytical modeling we describe the molecular basis for the BAR domain heterodimerization and the determinants for its membrane recruitment. Cryo-electron tomography and subtomogram averaging revealed the architecture of SNX1-SNX5 assembled on membrane tubules. The lattice-forming coat exhibits a distinctive array of tip-to-PX and tip-to-tip contacts and suggest how cargo potentiates oligomerization via cooperative interactions. The geometric constraints of the lattice differ from the yeast retromer coat and suggest a general mechanism for cargo retrieval in higher metazoans, in a retromer-independent manner.

6.3. Introduction

The endosomal network is a major hub in protein trafficking. It receives a large number of transmembrane proteins, receptors and ligands (termed cargo) from the secretory and endocytic pathways which then are routed to the lysosome for degradation, or recycled back to the plasma membrane or the *trans*-Golgi network for re-use. The dynamic spatiotemporal distribution of cargo from the endosomal network contributes to the ability of a cell to sense and respond to its environment. Defects in sorting and trafficking of cargo from endosomes have been linked to multiple neurodegenerative disorders including Alzheimer's disease (AD), Parkinson's disease (PD), and Down's syndrome (DS) [Cullen et al. 2018; Small et al. 2015].

Just as cargoes enter the endosomal network, key protein machineries contribute to particular recycling circuits via bulk flow and cargo-specific processes. Selective transport involves coat protein complexes that guide the enclosing of cargo into vesicles and membrane tubules. Generally, short peptide motifs present in the cytoplasmic tail of transmembrane proteins interact with adaptor subunits of a coat complex leading to cargo clustering and membrane deformation. While these mechanisms are well characterized in double-layer spherical coats like the COP-I/-II and clathrin-adaptor assemblies [Faini et al. 2013], they are not widely applicable to other protein coats from the endosomal network due to its tubular, dynamic and transient nature.

Prominent sorting/recycling machineries at endosomes include the evolutionary conserved retromer complex, the recently identified retromer-like complex known as retriever, and members of the sorting nexin (SNX) family [K.-E. Chen et al. 2019; McNally et al. 2018]. The SNX protein family is defined by the presence of a phox-homology (PX) domain which typically binds phosphatidylinositol phospholipids (PtdInsPs), but may also participate in protein-protein interactions [Chandra and Collins 2018]. The PX domain is frequently flanked by other domains of various functions for its integration into distinct cellular processes. Twelve members, out of the 33 annotated mammalian SNXs, contain an additional C-terminal Bin/Amphiphysin/Rvs (BAR) domain that are collectively denoted as the PX-BAR or SNX-BAR subfamily. BAR domains play important roles in membrane remodeling by inducing and/or stabilizing membrane curvature but also exhibit restricted patterns of homo- and heterodimerization linked to their activity. SNX-BAR proteins are therefore key players in cellular functions that involve extensive membrane sculpting like endosomal sorting, endocytosis, and autophagy.

Retromer and its associated sorting nexin (SNX) adaptors, are primary sorting machineries from endosomes. Retromer was first identified in *Saccharomyces cerevisiae* as a stable heteropentamer divided in two subcomplexes: a core formed the vacuolar protein sorting (VPS)26, VPS29 and VPS35 subunits, and a heterodimer of VPS5-VPS17 required for membrane association and membrane remodeling via PX and BAR domains [Horazdovsky et al. 1997; Seaman et al. 1998]. Recently, the retromer core along VPS5

homodimers from the thermophilic fungus *Chaetomium thermophilum* have been reconstituted in model membranes and visualized by cryo-electron tomography [Kovtun et al. 2018]. The inner part of the coat, in contact with the membrane, is composed by a pseudo-helical array of VPS5 dimers that form tip-to-tip contacts between consecutive BAR domains, and PX contacts between laterally adjacent molecules. On top of the VPS5 array, the retromer core forms arched dimers docked to VPS5 via the VPS26 subunit. In mammals, genetic divergence of VPS5 derived in SNX1 and SNX2 orthologues, whereas VPS17 derived in SNX5, SNX6, and SNX32 orthologues [Haft et al. 2000; Horazdovsky et al. 1997; Koumandou et al. 2011; Wassmer et al. 2007]. The mammalian SNX orthologues of VPS5/VPS17 have not retained the interaction, or at least not in the same way, with the VPS26-VPS29-VPS35 trimer [Swarbrick et al. 2011], albeit other SNX proteins such as SNX3 and SNX27 are well established retromer cargo adaptors [Clairfeuille et al. 2016; Gallon et al. 2014; Harrison et al. 2014; Harterink et al. 2011; Lucas et al. 2016; Steinberg et al. 2013; Tabuchi et al. 2010]. In addition, SNX-BARs and SNX27 can simultaneously cooperate with retromer for the recycling of a subset of cargos that contain two recycling motifs [Yong et al. 2020]. Nonetheless, there is compelling evidence that heterodimeric combinations of SNX1 or SNX2 with SNX5 or SNX6 can mediate cargo recycling independently of the retromer core and form functionally distinct membrane coats [Kvainickas et al. 2017; Nisar et al. 2010; Prosser et al. 2010; Simonetti, Danson, et al. 2017]. Accordingly, the mammalian retromer refers to the VPS26-VPS29-VPS35 trimer [Burd et al. 2014; Seaman 2012], whilst heterodimeric combinations of SNX1 or SNX2 with SNX5 or SNX6/SNX32 have been designated as the Endosomal SNX-BAR sorting complex for promoting exit-1 (ESCPE-1).

Mechanistically, the formation of tubular transport carriers by members of the ESCPE-1 coat complexes require the coordinated action between at least five elements. First, the formation of BAR heterodimers through a yet not well-defined pattern of favored contacts to form a banana-shaped structure that associates with its concave side to the curved membrane. Second, the presence of an N-terminal amphipathic helix (AH), predicted in all SNX-BAR proteins by similarity to the classical N-BARs, that partially embeds into the outer lipid monolayer of the membrane to promote curvature. Third, the association of the PX domain with specific PtdInsPs, most commonly with the endosomal-enriched PtdIns3P, which functions as a mechanical anchor point to the membrane. Fourth, the interaction of the PX domains of SNX5 or SNX6/SNX32 with the recycling motifs of transmembrane cargo, which provides an additional anchor point to the membrane and might contribute to protein clustering. Fifth, the tip-to-tip and lateral contacts between SNX-BAR coat proteins to promote the longitudinal expansion of the tubular membrane. The precise spatial organization of these five elements contributes to the formation of distinct endosome-derived tubular carriers. The tubular shape creates a large surface-to-volume ratio that maximizes the loading capacity of transmembrane receptors for recycling. However, how SNX-BAR proteins coordinate lipid-binding, cargo selection and membrane deformation through organized lattices remains largely unknown.

In this article, we report the structure of the SNX1-SNX5 heterodimer and how it is recruited to the membrane to form coated tubules for cargo transport. Using a combination of X-ray crystallography, cryo-electron tomography, biochemistry and analytical modeling we describe the molecular basis for the BAR domain heterodimerization and the determinants for its membrane recruitment. We also reveal the architecture of SNX1-SNX5 assembled on membrane tubules. The lattice-forming coat exhibits a distinctive array of tip-to-PX and tip-to-tip contacts and suggest how cargo potentiates oligomerization via cooperative interactions. The geometric constraints of the lattice differ from the yeast retromer coat and suggest a general mechanism for cargo retrieval in higher metazoans, in a retromer-independent manner.

6.4. Results

6.4.1. Crystal structure of the SNX1-SNX5 BAR heterodimer

Heterodimerization between the SNX-BARs of ESCPE-1 is an evolutionarily conserved feature but, without reported structures, there is a major gap in understanding how heterodimers might facilitate synergistic activities through higher levels of structural organization. Initial screening experiments started with the full-length SNX1-SNX5 complex but yielded no crystals. We therefore focused on the heterodimeric BAR domain complex.

We determined the structure of the SNX1^{BAR}-SNX5^{BAR} complex by single isomorphous replacement with anomalous scattering (SIRAS) using a K₂PtBr₄ derivatized crystal, and refined the final model against native data to 2.5 Å resolution. The overall conformation of the SNX1^{BAR}-SNX5^{BAR} complex is very similar to other banana-shaped BAR domains, consisting of an antiparallel heterodimer of three-helix bundles (Figure 6.1A). Intermolecular contacts between SNX1^{BAR}-SNX5^{BAR} heterodimers in the crystal lattice lack any lateral associations suggestive of spirals or tip-to-tip interactions (Figure B.1A, B). Indeed, the tip of SNX5^{BAR} has no crystal contacts and the electron-density map for residues 326-343 is very weak, indicating flexibility of this region (Figure B.1C). Structural models of the tip of SNX5BAR generated by the DaReUS-Loop - web server illustrate some mobility of this region. The curvature of the SNX1^{BAR}-SNX5^{BAR} heterodimer would fit a circle of about ~ 32 nm in diameter similar to that observed for the canonical BAR domain Amphiphysin, but smaller than SNX33 and SNX9, (Figure B.1D). However, unlike other BAR homodimers, the SNX1^{BAR}-SNX5^{BAR} heterodimer exhibits an asymmetric structure. In this sense, when the SNX5^{BAR} is superimposed onto the SNX1^{BAR} using the central region as reference, the distal arm of SNX5^{BAR} is shorter and less bended than the equivalent arm in SNX1 (Figure 6.1B). Similarly, on the basis of residue conservation and electrostatic potential, there are asymmetric patches on the surface of the SNX1^{BAR}-SNX5^{BAR} heterodimer (Figure 6.1C). In particular, basic residues in the concave face of the dimer are locally concentrated at the tip of SNX1^{BAR}, whereas the equivalent basic patch on SNX5^{BAR} covers a more elongated area. There is also a large negatively charged patch that extends along the SNX1-central side area that is absent on SNX5. In contrast, there are two conserved hydrophobic patches, one on each side of the BAR heterodimer, that on the basis of the PX-BAR crystal structures of SNX9 and SNX33, and the cryo-EM structure of the yeast Mvp1, could correspond to the binding area for the respective PX domains of SNX1 and SNX5 (Figures 6.1C and B.1E).

The recent structure of the yeast PX-BAR protein Mvp1 shows a tetrameric organization in solution where the BAR dimers embrace each other occluding their lipid-binding surfaces [D. Sun et al. 2020]. Mvp1 possesses a low-complexity N-terminal region that is

essential for tetramerization [D. Sun et al. 2020]. Interestingly, Mvp1 shares homology with several mammalian SNXs, including SNX1 (17% identity). Like Mvp1, SNX1 bears a low-complexity N-terminal region, and has been proposed to form tetramers [L.-S. Chin et al. 2001; Kurten et al. 2001], and weak homodimers [Sierecki et al. 2014; Van Weering et al. 2012]. Thus, we examined whether SNX1-SNX5 could form similar oligomers in solution and its ability to tubulate liposomes in vitro. Size-exclusion chromatography coupled with multiangle light scattering (SEC-MALS) revealed that SNX1-SNX5 has a molecular mass in solution consistent with a single heterodimer (Figure 6.1D). Notably, purified SNX1 formed stable homodimers whereas SNX5 was monomeric indicating that tetramerization is not a general feature of ESCPE-1 proteins. In line with previous reports, we observed that SNX1 dimers, but not SNX5 monomers, were able to tubulate liposomes in vitro [Van Weering et al. 2012]. We tested SNX1-SNX5 heterodimers and observed tubule formation, confirming that membrane-remodeling is also an intrinsic property of heterodimers (Figure 6.1E).

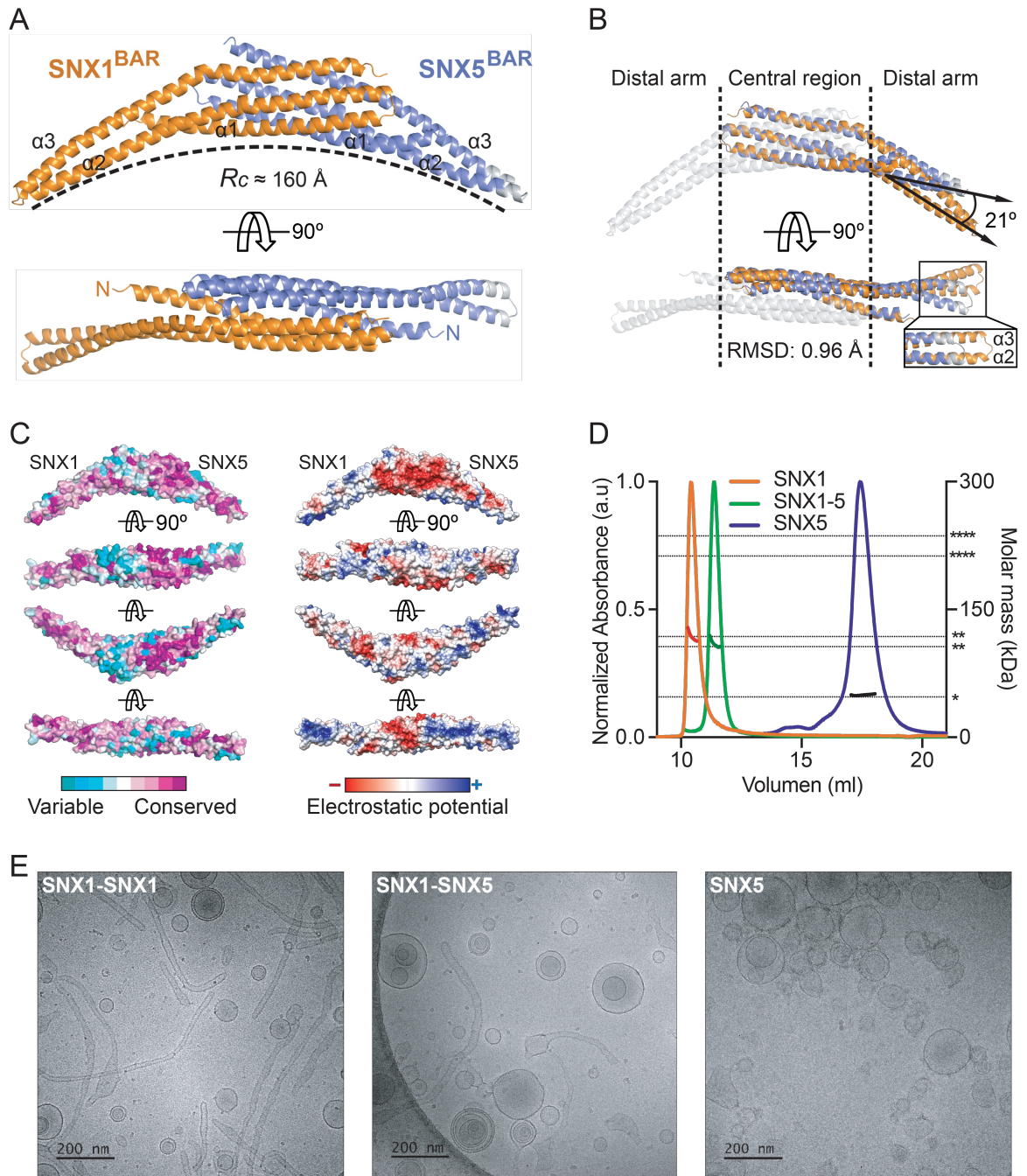


Figure 6.1.: **Structure of the SNX1^{BAR}-SNX5^{BAR} heterodimer.** (A) Ribbon representation of the SNX1^{BAR} domain in complex with the SNX5^{BAR} domain. Side view showing the radius of curvature (dotted line). (B) Superposition of SNX1^{BAR} onto SNX5^{BAR} through the central three-helix bundle highlighting the differences in curvature (top image) and tip lengths (bottom image, inset). Residues in grey color at the tip of SNX5^{BAR} modeled using DaReUS-Loop web-server. (C) Rotating views showing distribution or residue conservation (left series) and electrostatic surface potential (right series). (D) SNX5 behaves as monomer in solution whereas SNX1 and the SNX1-SNX5 complex behave as homodimers and heterodimers respectively. Molecular weights determined using SEC-MALS. Curves normalized to give the same peak heights. Calculated molar masses are shown across the elution peaks. Theoretical molecular weights for monomeric (*), dimeric (**), and tetrameric (****) forms are shown. (E) Cryo-EM images of liposomes incubated with SNX1 (left), SNX1-SNX5 complex (middle) and SNX5 (right) showing the ability to induce membrane tubulation.

6.4.2. A conserved pattern of electrostatic complementarity and protruding aromatic residues govern heterodimerization

In order to determine why SNX1 preferentially forms heterodimers over homodimers, and why SNX5 prevents homodimerization, we carried a comprehensive characterization of the interface residues based on conservation, energetic contribution, hydrophobicity and electrostatic potential (Figure 6.2A-D).

The SNX1^{BAR}-SNX5^{BAR} interface buries a large area of 5114 Å² from which 78% corresponds to polar surface. Interestingly, while the distribution of hydrophobic residues is relatively uniform across the interface, other parameters such as conservation, energetic contribution and electrostatic potential exhibit clear patterns that define the binding interfaces. Accordingly, we identified three main sections along the interface of SNX1 and SNX5 which we have defined as proximal, central and distal with respect to the tip of the BAR domain. In this regard, conserved residues in SNX5 are clearly located at the proximal and central regions, whereas conserved residues in SNX1 cover most of the contact interface with especial emphasis on the central and distal areas in a complementary scheme with SNX5. In parallel, we searched for residues that most contribute to the binding energy. We used the resEnergy pyDock module [Romero-Durana et al. 2019] which combines electrostatics, desolvation and van der Waals scoring functions to estimate the energetic contribution of individual interface residues (Figure B.2A,B). From this analysis, two clusters formed by F347 and W511 on SNX1, and F273 and F401 on SNX5 were found to have the largest contributions to the binding energy. Yet, only F347 and W511 on SNX1 are conserved, indicating that these residues likely form a binding hot spot. Additionally, we identified in SNX5 two residues, R388 and Q395, that establish favorable contacts at the heterodimer interface, but, to the contrary, their electrostatic and solvation energy contribution is largely unfavorable on a SNX5 homodimer model (Figure B.3). It is well known that surface electrostatics plays important long-range guidance for bringing together interacting partners. On this point, SNX1 and SNX5 exhibit distinct positively and negatively charged patches at their respective interfaces that act as electrostatic fingerprints with complementary polarity (Figure 6.2D). As such, the distal region of SNX1 has a large negative patch that is complemented by a positive patch at the proximal region of SNX5. Similarly, a positive patch on the proximal region of SNX1 is complemented by a negative patch on the distal region of SNX5. Remarkably, the central region of SNX1 displays a neutral surface while the equivalent central region on SNX5 exhibits a negative patch that is consistent with previous homology predictions [Van Weering et al. 2012]. Specifically, the conserved E280 within the central negative patch in SNX5 is occupied by H281 at the equivalent position in SNX1 explaining the lower electronegativity in this area (Figure 6.2D and B.3).

In summary, the SNX1 binding interface displays a complementary charge distribution not only with SNX5 (heterodimer), but also with an equivalent SNX1 molecule in an antiparallel orientation (homodimer). In contrast, the presence of a negative patch in

the central area of SNX5 will obstruct homodimerization by self-electrostatic repulsion and unfavorable polar desolvation energies.

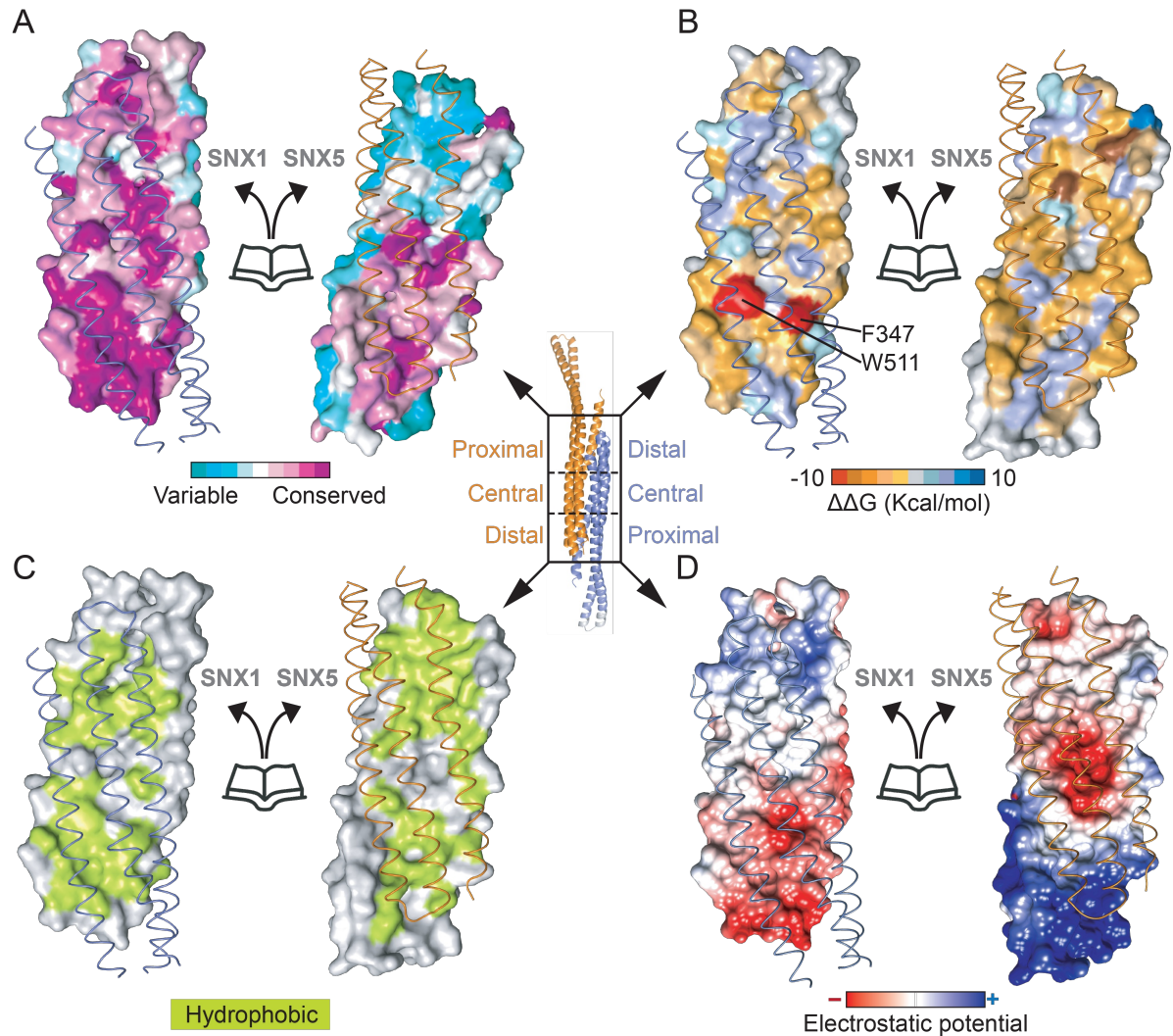


Figure 6.2.: **Analysis of the SNX1^{BAR}-SNX5^{BAR} interface.** Representation of the opened interface where contact surfaces are facing the viewer. Surfaces are colored by different attributes: (A) Evolutionary conservation of residues analyzed by Consurf web-server, (B) Energetic contribution, (C) hydrophobicity, and (D) electrostatic potential.

6.4.3. Site directed mutations block homo- and heterodimerization

To further validate the SNX1-SNX5 structure, we generated various interface mutations influencing SNX1 homodimerization and heterodimerization. We introduced the F347A

and W511A double mutant in SNX1 based on residue conservation and energetic scores (Figure B.2). This resulted in disruption of SNX1 homodimers but not SNX1-SNX5 heterodimers which is consistent with a higher interface stability between heterodimers than homodimers, and the ability of SNX5 to outcompete homodimers of SNX1 to form heterodimers (Figure 6.3). On the other hand, the SNX5 interface does not exhibit clear conserved hotspots. Thus, in a compromise between conservation scores and energy contribution, we introduced four-point mutations (Y219A, M233A, V240A, and R368A) within the central and proximal regions of the SNX5 interface (Figure B.2). These mutations were unable to impede heterodimer formation even in presence of the SNX1 double mutant (Figure 6.3). Finally, the introduction of two additional mutants (I398A and F401A) at the distal region of the SNX5 interface, resulting in a six-point mutant, was sufficient to prevent the heterodimerization with the SNX1 double mutant but not with the wild type. None of these mutants significantly altered the secondary structure of the proteins. This observation is consistent with a recognition pattern where the binding energy landscape for SNX5 is spread over a wider region than in SNX1. As such, SNX1 contributes with a core of two bulky aromatic residues that insert into SNX5, whilst SNX5 provides a complementary surface rim that enhances heterodimer formation. Overall, this data sustains that electrostatic repulsion disfavors SNX5 homodimerization whilst heterodimerization is favored by the presence of two aromatic/bulky residues in SNX1 that stick into SNX5 following a mechanism that resembles a two-pin plug and socket connector.

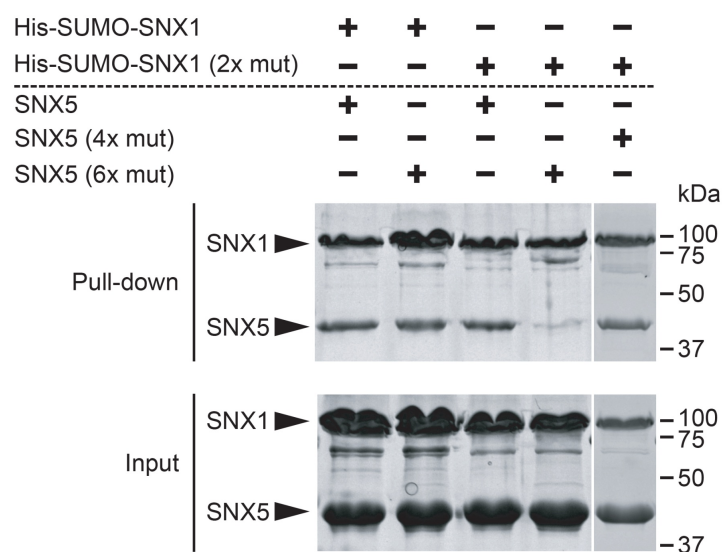


Figure 6.3.: **Competition assay between SNX1 versus SNX5 and mutants.** SDS-PAGE of samples before competition assay (input) and after incubation of proteins and washing of the resin (pull-down). His-SUMO SNX1 (WT or mutant) were captured in the pull-down resin (Ni-NTA). SNX5 (WT or mutants) were incubated with His-tagged SNX1, washed, and the bound proteins were analyzed by SDS-PAGE. SNX5 WT was able to displace SNX1 homodimers to form SNX1/SNX5 heterodimers (lane 1) and up to 8 mutations were needed to break the heterodimer (lane 4).

6.4.4. SNX5 tolerates dimerization in response to stabilizing mutations at the interface

To address the contribution of E280 in preventing SNX5 homodimerization we introduced the E280H mutant, which mimics H281 position in SNX1, and examined whether dimerization was tolerated. When SNX5_{E280H} was subjected to size-exclusion chromatography it eluted into a mixture of monomers and dimers. In this sense, although a large fraction of SNX5_{E280H} was still monomeric, the tendency to dimerize indicated that the natural self-repulsion of E280 in SNX5 was counteracted by the E280H mutant. This observation is consistent with previous immunoprecipitation assays in HEK-293 cells using a SNX5_{E280A;E383A} double mutant [Van Weering et al. 2012]. However, when introduced the two bulky aromatic residues present in SNX1 (F347 and W511) at the equivalent positions in SNX5 (T247F and L394W), we observed a larger proportion of dimers than monomers. Furthermore, when the three mutants (T247F, E280H, and L394W) were introduced together, the proportion of SNX5 homodimers was even greater. Thus, the ability to engineer SNX5 homodimers provided experimental proof and biophysical explanation of the principles that govern SNX1-SNX5 heterodimerization.

Next, we selected the mutants that impaired SNX1 homodimerization and SNX1-SNX5 heterodimerization to examine their membrane tubulation activity. As expected, a severe tubulation defect was observed indicating that dimerization is important for the membrane remodeling activity. Indeed, the SNX1_{F347A,W511A} mutant, which tolerates heterodimerization, retains its tubulation activity in presence of SNX5. On the other hand, the engineered SNX5 dimer failed to remodel liposomes into tubules, although this was most likely originated from the lack of association between SNX5 and the membrane (as stated below).

6.4.5. CI-MPR cargo plays a major role in SNX1-SNX5 membrane recruitment

In testing the influence of the interface mutations on membrane association we noticed that SNX1 and related mutants displayed similar interactions with model membranes whereas SNX5 and related mutants did not associate with liposomes. Previous phosphoinositide interaction studies with the PX domain of SNX1 and SNX5 have shown either weak-to-moderate binding, or even no interaction, towards PtdIns3P and other PtdInsPs [Ceccato et al. 2016; Chandra, Y. K.-Y. Chin, et al. 2019; Cozier et al. 2002; Koharudin et al. 2009; H. Liu et al. 2006; Merino-Trigo et al. 2004; Zhong et al. 2002]. Thus, we examined by liposome flotation assays the contribution of different PtdInsPs in recruiting SNX1 and SNX5 to model membranes via their PX-domains. Unexpectedly, neither SNX5 nor the PX of SNX1 were significantly recruited to membranes as compared with the well-established PtdIns3P-SNX3 association. Interestingly, only the

BAR domain of SNX1 as dimer, but not as monomer, associated with membranes. Previous analyses with the yeast SNX-BAR retromer have shown that cargo facilitates its membrane recruitment [Harrison et al. 2014; Purushothaman et al. 2018]. To address whether this was the case with the SNX1-SNX5 complex, we selected as model cargo the cytoplasmic domain of the cation-independent mannose 6-phosphate receptor (CI-MPR) which interacts directly with the PX domain of SNX5 [Simonetti, Paul, et al. 2019; Yong et al. 2020]. To mimic the juxtamembrane position of the cytoplasmic tail of CI-MPR, we anchored the N terminus to the surface of liposomes by chemical crosslinking with maleimide-functionalized lipids. In contrast to the inclusion of phosphoinositides, which did not enhance significantly the recruitment of SNX1 or SNX5 in liposome flotation assays, the presence of CI-MPR on the membrane not only triggered the recruitment of SNX5 alone but also contributed to augment the recruitment of the SNX1-SNX5 heterodimer. This observation suggests that cargo recognition, rather than phosphoinositide binding, leads the recruitment of SNX1-SNX5 to membranes.

6.4.6. The BAR domain of SNX1 enhances cargo recognition

We next used isothermal titration calorimetry (ITC) to measure the binding of the bipartite sorting signal present in the CI-MPR cytoplasmic domain, residues 2347-2375, to the isolated PX domain of SNX5. The binding affinity showed a dissociation constant (K_d) of $\sim 12 \mu\text{M}$, consistent with reported values under similar assay conditions [Simonetti, Paul, et al. 2019; Yong et al. 2020]. Similarly, the interaction between the cytoplasmic domain of CI-MPR and the full length SNX5 exhibited a comparable K_d of $\sim 14 \mu\text{M}$. However, the binding to the SNX1-SNX5 heterodimer revealed an affinity about five times higher with a K_d of $\sim 1.5 \mu\text{M}$. Likewise, the CI-MPR₂₃₄₇₋₂₃₇₅ peptide showed very similar values, with a K_d of $\sim 2.3 \mu\text{M}$, for the binding to the SNX1-SNX5 heterodimer.

These results indicated that SNX1, either directly or indirectly, contributed to enhance the binding between the PX of SNX5 and CI-MPR. In this sense, to examine the relationship between SNX1 and the increased affinity, we next evaluated whether the CI-MPR₂₃₄₇₋₂₃₇₅ peptide had additional interactions aside from the PX domain of SNX5. Consistent with the specificity of CI-MPR₂₃₄₇₋₂₃₇₅ towards the PX of SNX5 [Simonetti, Paul, et al. 2019; Yong et al. 2020], we found no additional interactions of this peptide with SNX1^{PX}, the full-length SNX1, or the SNX1^{BAR}-SNX5^{BAR} heterodimer as measured in solution by ITC. In contrast, we observed a K_d of $\sim 2.5 \mu\text{M}$ for the interaction of CI-MPR₂₃₄₇₋₂₃₇₅ with SNX1^{BAR}-SNX5, which is comparable to that observed for the full-length heterodimer. Of note, in this assay SNX1 contributed only with its BAR domain. Based on the structural data of the SNX1-SNX5 heterodimer, the BAR domain of SNX1 and the PX domain of SNX5 are far apart from each other to promote the interaction with CI-MPR₂₃₄₇₋₂₃₇₅. According to this, we hypothesized that the increase in affinity might result from the cooperative action between the PX domain of SNX5

and the BAR domain of SNX1 but from a separate heterodimer. Therefore, we titrated CI-MPR₂₃₄₇₋₂₃₇₅ into a mixture of the two isolated domains and found a K_d of $\sim 6 \mu\text{M}$ which indicated that the binding to SNX5^{PX} was significantly stronger in presence of SNX1^{BAR}. These results confirmed a cooperative interplay between the BAR domain of SNX1 and the PX domain of SNX5 in CI-MPR recognition.

6.4.7. Cryo-electron Tomography and subtomogram averaging reveals the coat architecture

To understand how coat assembly, cargo sorting and membrane deformation are coordinated it is necessary to visualize the architectural organization of the coat in its membrane bound state. In this regard, we performed cryo-electron tomography (cryo-ET) on the tubulation reaction of SNX1-SNX5 with CI-MPR₂₃₄₇₋₂₃₇₅ reconstituted in membranes *in vitro* and solved the 3D structure of the protein coat by subtomogram averaging.

The liposome-derived tubules seen in the tomograms were relatively homogeneous and were all decorated with a helically arranged protein coat (Figure 6.4A). The tube lengths varied from $\sim 100 \text{ nm}$ to $\sim 1600 \text{ nm}$ with an average of $\sim 460 \text{ nm}$ (Figure B.5). Initial subtomogram averaging of short tube segments revealed right-handed helices around the membrane with different number of helical starts depending on the tubes (Figure 6.9B). While tubes with one start represented only $\sim 5\%$ occurrences, tubes with two, three and four helical starts were equally common with $\sim 32\%$, $\sim 27\%$ and $\sim 36\%$ occurrences respectively (Figure B.11B).

By further subtomogram averaging using advanced helical sub-boxing techniques (see methods in Section 6.6), we generated two different averages (electron density maps): one average that included the structure of three complete consecutive particles (3-particles average) solved at $\sim 12\text{\AA}$ resolution (Figure 6.4B and B.6) and a finer average that included the structure of an individual particle (1-particle average) at $\sim 10\text{\AA}$ resolution (Figure 6.4C, B.6 and B.10). At this resolution, the PX and BAR domains were clearly resolved in the cryo-EM maps revealing a network of tip-to-tip and tip-to-PX interactions that contribute to stabilize the lattice (Figure 6.4D). The SNX1-SNX5 heterodimer forms helical rows that are held together mainly through two intertwined tip-to-px contacts between the edge of one BAR domain and the PX domain of the next heterodimer. This interaction is entirely consistent with the observed cooperative effect between the BAR domain of SNX1 and the PX domain of SNX5 for binding to CI-MPR and supports a head-to-tail interlinkage. According to this, we were able to derive the relative positions of the heterodimers by fitting the X-ray structure of the SNX1_{BAR}-SNX5_{BAR}, together with the structures of SNX1_{PX} and SNX5_{PX} bound to CI-MPR into the density map. Still, the lack of high resolution precluded to distinguish between the two possible

directional polarities (Figure 6.4E) and forced us to treat the particles as symmetric homodimers.

Using the coordinates of the 1-particle average, the geometrical lattice parameters were derived by overlapping the relative positions of all neighboring particles of each particle, generating a so called neighborhood plot (Figure 6.4F). The neighborhood plot shows that neighbors at the tips are more concentrated around a fixed point, compared to lateral neighbors that are distributed over an elongated area. This indicates that tip-to-PX contacts are more conserved than lateral contacts. Figure B.8 shows a 3D representation of this neighborhood analysis. It is worth mentioning that the lattice parameters (a , b , α , radius) show only a minimal variation between tubes with a different number of helical starts (< 1 nm and $< 1^\circ$, Figure B.7A-F) and the curvature of the heterodimers themselves is also independent on the number of helical starts (Figure B.10). Only the relative angle between two consecutive particles varies slightly to adapt to the changing curvature of the helix caused by different lead angles (Figure B.7F). Based on this conservation of lattice parameters we therefore do not expect any functional differences between tubes with different numbers of helical starts.

A cut through the three particle average further shows the bending of the membrane imposed by the SNX1-SNX5 heterodimers (Figure 6.4G). The average peripheral membrane diameter was 28 ± 2 nm. The membrane was decorated with a ~ 3.7 nm thick protein coat. The overall diameter of the tubes generated by SNX1-SNX5, albeit slightly smaller than the previously reported VPS5-retromer-coated tubules ($\sim 31 \pm 6$ nm thick) [Kovtun et al. 2018], indicate that both protein coats induce and stabilize tubular membranes with similar curvature. The SNX1-SNX5 heterodimer associates with the membrane through the conserved positively charged residues present at the tips of the BAR domains as well as in the PX domains. In contrast, the central portion of the BAR domain is negatively charged and does not contact the membrane (Figure 6.4G,H). The membrane-interaction regions correlate with the tip-to-tip and tip-to-PX lattice contacts of the coat, suggesting that peripheral protein scaffolding contributes to membrane bending.

SNX-BAR proteins contain an amphipathic helix next to the N-terminus of the BAR domain (referred as H0) that is analogous to the one present in the N-BAR protein family [Van Weering et al. 2012]. These amphipathic H0 helices are important for lipid binding and curvature generation through partial embedding of hydrophobic residues into the outer leaflet of the lipid bilayer. The amphipathic H0 in SNX1 (residues 281-298) and in SNX5 (residues 183-200) [Van Weering et al. 2012] fall within a linker region between the PX and BAR domains. In order to generate a pseudo-atomic model of the SNX1-SNX5 coat we performed rigid body fitting of the available structures of SNX1^{PX}, SNX5^{PX} and our x-ray structure of SNX1^{BAR}-SNX5^{BAR}, into the EM map. Next, we generated homology models of the linker regions and conducted flexible fitting of the ensemble into the EM map which allowed us to produce a more complete model of the coat. A closer inspection of the lattice contacts provided insights of the individual secondary

structure elements involved in the assembly of the coat. As such, the modeled linker regions between the PX and BAR domains contain two short α -helices, denoted as α L1 and α L2 (Figure 6.4I), where α L1 closely matches the boundaries of the predicted H0. Tip-to-tip contacts occur between the side-tips of the α 2 helices from each BAR domain, whereas tip-to-PX contacts take place between the side-tips of the α 3 helices from each BAR domain and the α L2 helix of the linker (Figure 6.4I). Residues at the tip-to-tip and tip-to-PX contacts are significantly conserved which further support the geometry of the coat (Figure 6.4J). Of note, the sorting motif of CI-MPR, that is recognized by the PX of SNX5, and the amphipathic α L1 (helix H0) are in close proximity to the tip-to-PX contact between SNX1 and SNX5 (Figure 6.4K). The spatial proximity between these three elements suggest that cargo recognition, coat assembly and membrane deformation might be synchronized through cooperative interactions.

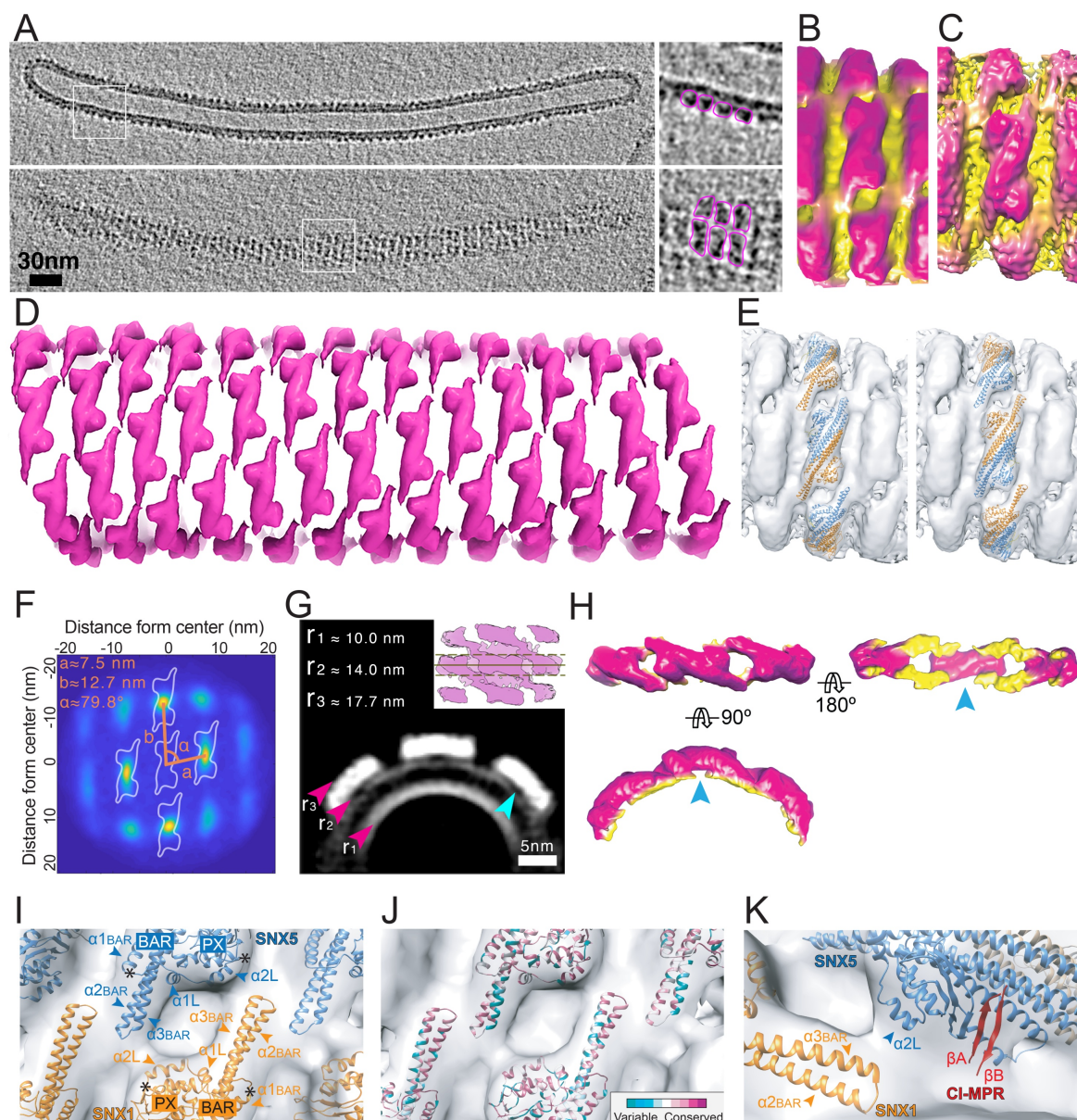


Figure 6.4.: **Structure of the SNX1-SNX5 membrane coat with CI-MPR₂₃₄₇₋₂₃₇₅ on lipid tubules determined by subtomogram averaging.** (A) Computational sections through the middle (top) and surface (bottom) of a representative tube. Top and side views of individual heterodimers are highlighted in the zoom. (B) Top view of the 3-particle average and (C) the 1-particle average. The colors yellow and pink roughly match the membrane and the PX-BAR domains, respectively. (D) 1-particle average (smoothed) on a tube surface placed at the coordinates that resulted from STA. The helical lattice is formed by tip-to-tip and tip-to-PX interactions. (E) Atomic models of SNX1-SNX5 fitted into the cryo-ET map at two possible orientations. (F) Projection of the neighborhood plot, showing the superimposition of the relative positions of the neighboring particles of each particle. Geometrical parameters were computed in 3D using k-mean clustering (3D representation in Figure B.8) (G) Cross section through center of the 3-particles average (averaged over 15 pixels as shown in the top right corner). The marked red arrows show

the radii of the inner and outer leaflet of the membrane and the protein coat. The blue arrow shows the spacing between protein and membrane. This central region is negatively charged as compared with the positively charged areas in contact with the membrane. (H) Details of membrane contact areas colored in yellow. The blue arrow indicates the absence of contact between the membrane and the central part of the BAR heterodimer. (I-K) Close-up views of the SNX1-SNX5 chimeric model fitted into the cryo-ET density map. (I) Detail of the tip-to-tip and tip-to-PX contacts. Asterisks limit the linker region between the PX and BAR domains modeled with I-TASSER. (J) Same view showing residue conservation calculated by ConSurf server. (K) Close-up view of the spatial arrangement between the CI-MPR binding site on the PX domain of SNX5 and the tip-to-PX contact of the SNX1^{BAR} domain.

6.4.8. The SNX1-SNX5 scaffold differs from the yeast VPS5

Most cryo-EM studies of BAR proteins reconstituted on model membranes have shown helical or pseudo-helical arrays formed by tip-to-tip interactions between BAR domains that are clustered along the tube axis by side interactions (Figure 6.5A). The presence of a PX-BAR tandem domain in SNX-BARs presumed distinct inter-subunit interactions. Indeed, dimers of the PX-BAR protein VPS5 from the yeast *Chaetomium thermophilum* display extensive tip-to-tip contacts between consecutive BAR domains as well as between the PX domains from adjacent rows (Figure 6.5B). Quite unexpectedly, however, we found that the lattice organization of SNX1-SNX5 heterodimers is different. First, the BAR domains exhibit an opposite orientation relative to the axial direction of the tube (Figure 6.5B). Second, the tip-to-tip contacts are limited to just the tip ends with some local variability between adjacent rows (Figure 6.4F and 6.5B). Finally, there are no PX-to-PX contacts. In fact, the observed tip-to-PX contacts in SNX1-SNX5 are compatible with the binding mode of bipartite signals for cargo retrieval such as CI-MPR [Yong et al. 2020]), whereas the PX-to-PX contacts observed in VPS5 would occlude an equivalent binding mode.

In the VPS5-retromer coat, the VPS26 subunit of retromer provides the sole contact with the VPS5 lattice [Kovtun et al. 2018]. However, in higher metazoans retromer does not form stable complexes with SNX dimers [Arighi et al. 2004; Swarbrick et al. 2011]. When analyzing the distribution of VPS26 contacts on the VPS5 lattice, VPS26 forms dimers that dock on the extensive intertwined tip-to-tip contacts between consecutive dimers as well as between neighboring rows (Figure 6.5C). The existence of two different scaffolding systems might explain why in higher metazoans retromer does not bind to SNX1/SNX2-SNX5/SNX6 heterodimers as it does in yeast.

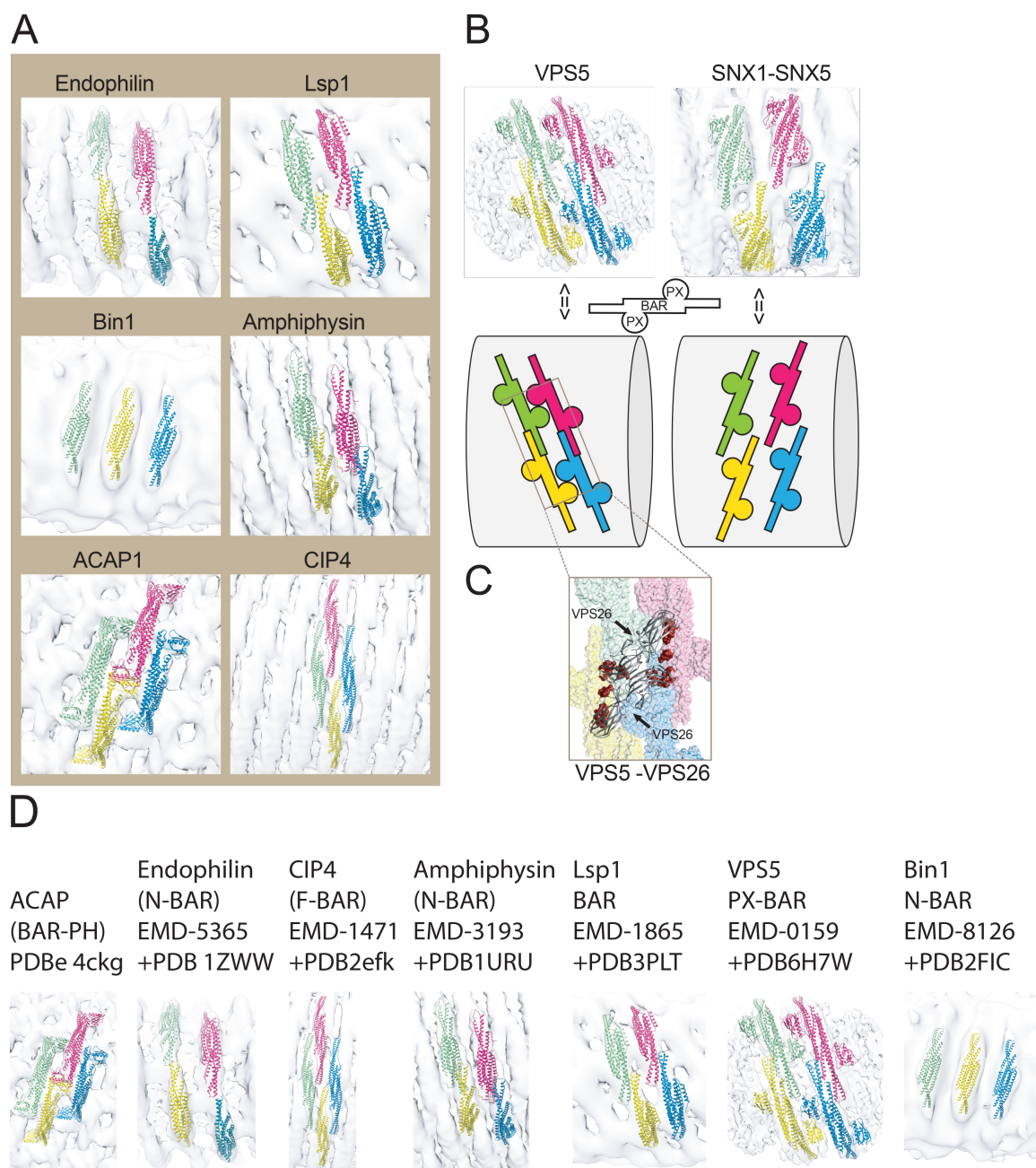


Figure 6.5.: **VPS5 and SNX1-SNX5 exhibit different PX-BAR coat organizations.** (A) Top-view of distinct membrane reconstituted BAR domain scaffolds obtained by cryo-EM. (B) Top view comparison between yeast retromer-VPS5 (PDB-6H7W fitted into EM map EMD-0158) and mammalian SNX1-SNX5 coated tubules centered at the PX-BAR lattice. Each image illustrates four adjacent dimers in different color. Retromer layer has been clipped for clarity. Schematic depiction of how SNX-BARs are organized on tubular surfaces through distinct geometric patterns. (C) Contacts of the VPS26 dimer over the VPS5 lattice highlighted in red. (D) References to the PDB and EMDB entries of the shown maps.

6.5. Conclusion

Protein machineries involved in sorting and recycling play a major role in cells. Dysfunctions in those processes are linked to various diseases. How SNX-BAR proteins coordinate lipid-binding, cargo selection and membrane deformation through organized lattices remains largely unknown. We therefore studied the structure of the SNX1-SNX5 heterodimer and how it is recruited to the membrane to form coated tubules for cargo transport.

We observed that SNX1 preferentially forms heterodimers over homodimers and that SNX5 prevents homodimerization. Based on the crystal structure of the SNX1^{BAR}-SNX5^{BAR} complex (2.5 Å resolution) we could explain this behavior with an interface analysis that showed that electrostatic repulsion disfavors SNX5 homodimerization whilst heterodimerization is favored by complementary charge distributions. Mutations of these key regions could prevented homo- and heterodimerization. We also observed (and confirmed through various mutation experiments) that liposome tubulation only happens in the presence of SNX1 homodimers and SNX1-SNX5 heterodimers. Through liposome flotation assays we found evidence that the presence of the cargo protein CI-MPR (that only binds to the PX domain of SNX5) significantly enhanced the recruitment of SNX1-SNX5 to membranes, meaning that cargo recognition, rather than phosphoinositide binding, leads the recruitment of SNX1-SNX5 to membranes. Using ITC we further observed that the BAR domain of SNX1 enhances the binding between the PX domain of SNX5 and CI-MPR. Because in a SNX1-SNX5 heterodimer the BAR domain of SNX1 is far apart from the PX domain of SNX5, we hypothesize that the increase in affinity might result from cooperative interactions with the BAR domain of SNX1 from a separate heterodimer.

Cryo-electron tomography and subtomogram averaging of SNX1-SNX5 heterdimers reconstituted in lipid tubules in the presence of the cytoplasmic domain of CI-MPR revealed a lattice with tip-to-tip and tip-to-PX interactions. The lattice showed a helical geometry with tubules having different numbers of helical starts. The relative position of the heterodimers and the tube radii were however conserved over all tubules. We identified the membrane-interaction regions at the tip-to-tip and tip-to-PX lattice contact, suggesting that well-ordered oligomeric scaffolds, rather than passive crowding, contribute to membrane bending. The most interesting observation was however that the BAR domain of SNX1 and the PX domain of SNX5 including the CI-MPR are in fact in close proximity, as we postulated by the previous assessments. The proximity of these three elements adds to the hypothesis that cargo recognition, coat assembly and membrane deformation are synchronized through the cooperative interactions of these elements. Finally, the difference in lattice geometry when compared to the yeast VPS5 gives an explanation why retromer does not bind to ESCPE-1 coats.

All in all, our results reveal a mechanism for cargo sorting at endosomes via the ESCPE-1

complex with two mayor breakthroughs in the areas of membrane-remodeling machineries and signal dependent transport. First, reconstitution of biologically relevant full length SNX-BAR heterodimers has provided a novel view of lattice organization were scaffolding and wedging are intimately related for controlling membrane curvature. And second, the current view that cargo is a passive subject displaying a recycling signal has been challenged as its presence is fundamental in recruiting SNX-BARs to the membrane and explains how tubulation activity can be promoted at specific cargo locations.

6.6. Methods for cryo-electron tomography and subtomogram averaging

6.6.1. Grid preparation

Quantifoil R2/2 300-mesh copper grids were hydrophilised by plasma treatment using a Glow discharge/carbon evaporation MED 020 system (BALTEC). They were vitrified in liquid ethane using a FEI vitrobotTM Mark III. The grids were stored at liquid nitrogen temperatures. An average ice thickness of ~ 180 nm was measured by analyzing the reconstructed tomograms (Figure B.4).

6.6.2. Data acquisition

The tomogram acquisition was done using state of the art hardware and procedures. The tilt series were recorded on an FEI Titan Krios transmission electron microscope running at 300 keV using the Gatan K2 Summit direct electron detector camera in counting mode with a calibrated pixel size of 2.73 \AA . The data acquisition was automated using the Serial-EM software [Mastronarde 2005]. The tilt range of the stage was set from -60° to 60° with intervals of 3° and was covered using the dose-symmetric tilt scheme [Hagen et al. 2017] with a 2 by 2 grouping the angles, i.e., $(0^\circ, 3^\circ, -3^\circ, -6^\circ, 6^\circ, 9^\circ, -9^\circ, \dots)$. For each tilt, a movie of 10 frames was recorded. The total dose of a complete tilt series was $120 e^-/\text{\AA}^2$. The defocus range was between $-2 \mu\text{m}$ to $-5 \mu\text{m}$, in $0.5 \mu\text{m}$ steps. 57 out of 59 acquired tilt series were used for further processing.

6.6.3. Pre-processing and CTF estimation/correction

The pre-processing of the data consisted of two steps: Drift correction and dose weighting. Each movie was individually drift corrected using Motioncor2 [S. Q. Zheng, Palovcak, et al. 2017]. Each resulting micrograph was then weighted by the cumulative radiation dose using a Matlab (MathWorks) implementation of the algorithm from Grant et al. 2015b. The input value used for the accumulated dose per micrograph was taken from the last frame of the movie of the corresponding tilt and was then reduced by 20%, to be more conservative.

The CTF was estimated using CTFFIND4 [Rohou et al. 2015] and the CTF-correction was done using the `ctfphaseflip` command from IMOD [Kremer et al. 1996; Xiong et al. 2009]. The CTF at each tilt was estimated prior to dose-weighting. The estimation was done using only the micrograph area that corresponds to a projection of the imaged area

at the zero tilt (see Figure 6.6). This strategy was used in [Hutchings et al. 2018] and proved to lead to more precise and robust defocus estimations (see Figure 6.7). The estimated defocus and astigmatism was later used to correct the aligned tilt series by phase-flipping.

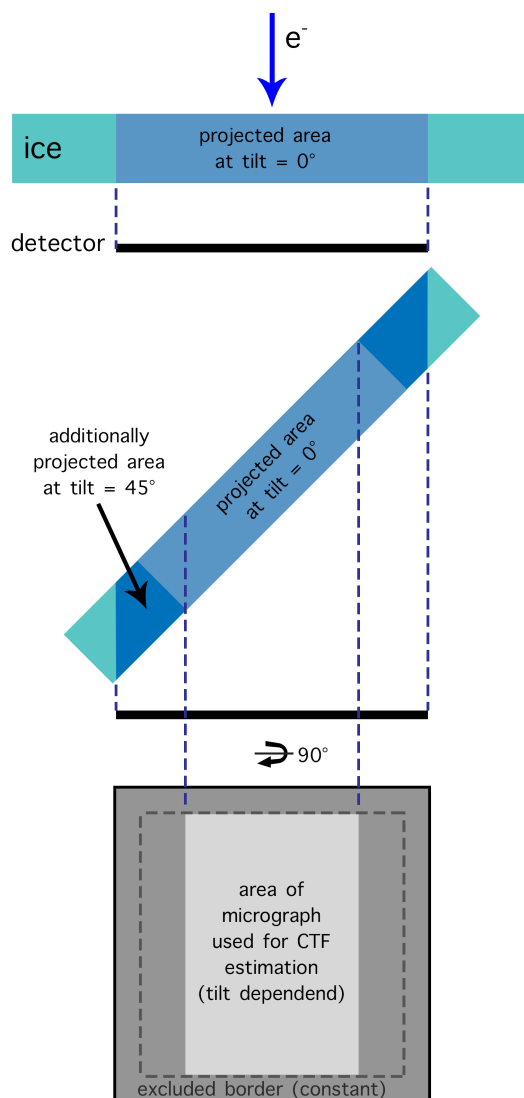


Figure 6.6.: **Illustration of area used for CTF estimation.** Only the micrograph area that corresponds to a projection of the imaged area at the 0° tilt is used. The used area in this example at the 30° tilt is shown in light grey. A constant border on each tilt was additionally excluded to remove potential carbon.

To ensure the correct hand of the tomograms, i.e., the correct sign of the tilt angles, the defocuses of the left and right side of each micrograph of a tilt series were additionally estimated. With this it was determined whether the right or the left side of a tilt is closer to focus. This allowed to set the correct sign of the tilt angle based on the conventions

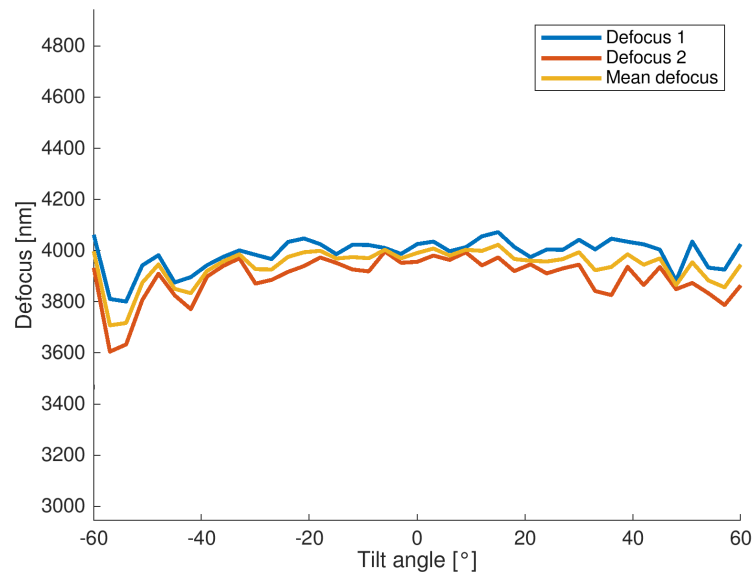


Figure 6.7.: **Defocus estimation of one tilt series.** Using a reduced area for defocus estimation leads to more stable defocus measurements over the tilt series.

of the used processing softwares.

A set of customizable Matlab scripts and functions were written to automate all of the pre-processing steps, the CTF estimation and the setting up of the data structure. The scripts can be found in the GitHub repository of the author of this thesis¹.

6.6.4. Tilt series alignment and tomogram reconstruction

Tilt series alignment and tomogram reconstruction was done using IMOD. For the fiducial model, 6 to 30 gold beads per micrograph were used. The alignment parameter options were set to “group rotation”, “group magnifications” and “fixed tilt angles”. This parameter choice gave the best alignment quality, while still being conservative enough to avoid overfitting. The alignment quality was assessed by examining the symmetry of the gold beads in the 3D reconstruction and by the mean residual error, which was between 0.5 and 1 pixels throughout the whole dataset.

Two types of tomograms were reconstructed: Binned by factor 2 tomograms using the fake SIRT-like filter from IMOD (equivalent to 50 iterations) and full sized tomograms using the default weighted back projection parameters. For simplification purposes these two tomogram types will be called SIRT-tomograms and WBP-tomograms hereafter.

¹www.github.com/sscaramuzza/TomographyTools

6.6.5. particle picking for sub-tomogram averaging

Using the *Dynamo* software for STA [Castaño-Díez, Kudryashev, Arheit, et al. 2012; Castaño-Díez, Kudryashev, and Stahlberg 2017], all intact tubes with a minimum length of ~ 160 nm and no extreme curvatures were manually traced along their center in all tomograms. The coordinates were saved in a database for further processing. In total, 180 tubes were used for further processing. The average tube-length was ~ 466 nm and the maximum length ~ 1500 nm (see Figure B.5a). All the tubes were accommodated within the XY-plane of the ice. The tubes showed no preferred orientations (Figure 6.8).

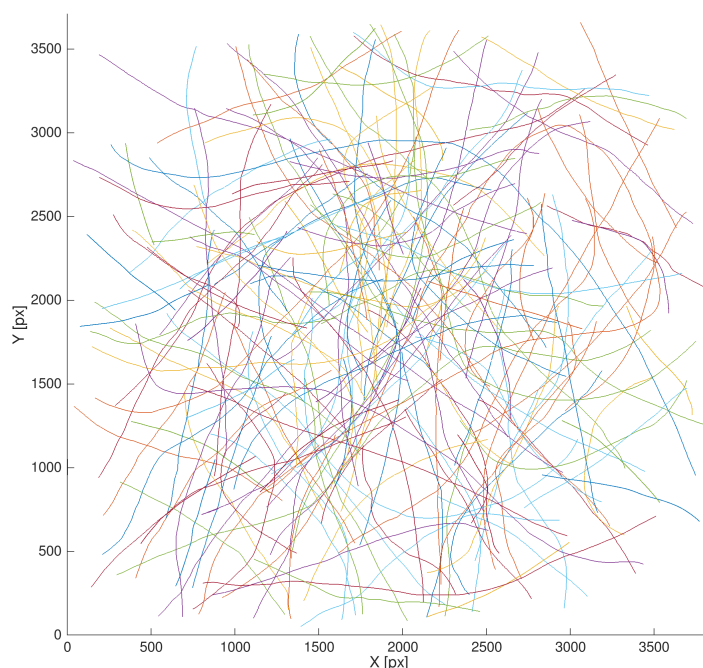


Figure 6.8.: **Overlap of projection of coordinates from all selected tubes.** No preferred orientation can be seen.

To locate the initial particle coordinates, the following steps were performed for each tube individually:

1. **Tube average:** Based on the previously defined tube coordinates, the tubes were oversampled by extracting sub-tomograms (box size 224^3 pixels) every 36 pixels along the tube using the WBP-tomograms (Figure 6.9A). The size of the sub-tomograms was large enough to contain a full segment of the tube. The particles were aligned within 6 iterations using a starting reference based on the raw particle

average and a lowpass filter set at 60 Å at the first iteration and 40 Å in the last iteration. The resulting tube-average revealed helices around the tubes (Figure 6.9B) with different number of helical starts depending on the tubes.

2. **Helical sub-boxing:** To extract smaller subvolumes along the helix of the tube-average (sub-boxing), the helix first had to be parametrized. This was done by computing the radius, the helical pitch and the number of helical starts automatically using a set of self-written MATLAB scripts and functions (see Appendix B.1). Sub-boxing was then performed using the SIRT-tomogram by extracting subvolumes of size 64^3 pixels every 16 pixels along the helix (oversampling). The azimuth angle of each sub-volume was corrected by the value of the helical lead angle in order to force the X-axis of the sub-volumes to point in the direction of the helix. The particles were aligned within 6 iterations using a mask that excludes laterally neighboring particles (Figure 6.9) and a lowpass filter set at 50 Å at the first iteration and 30 Å in the last iteration. The resulting average included three clearly visible particles (Figure 6.9C). These coordinates were the basis for the 3-particles average.
3. **Individual sub-boxing:** The coordinates of the individual particles were determined by further sub-boxing the previously obtained average. The coordinates of the three visible particles for each tube were manually marked. Obtained coordinates with similar positions (within a range of 8 pixels) were reduced to the coordinate with the highest cross-correlation value with the reference of the previous alignment. Using these new coordinates, the particles were extracted into smaller subvolumes (box size 48^3 pixels) from the SIRT-tomogram, aligned during 13 iterations and starting lowpass filter set at 50 Å at the first iteration and 24 Å at the last iteration. A mask that excludes lateral neighbors was used again. These coordinates were the basis for the 1-particle average (Figure 6.9D).
4. **Outlier exclusion:** Subvolumes that fulfilled at least one of the following criteria were excluded from further processing (the complete outlier exclusion was automated using self-written MATLAB functions and is presented in more details in Appendix B.2:
 - *Extreme radius:* Sub-volume coordinate too close or too far from the tube center.
 - *Extreme angle:* Normal vector of sub-volume differs too much from normal vector of tube surface.
 - *Missing neighbor:* Subvolume has not 4 neighboring particles (as it is expected from the lattice).
 - *Low cross correlation:* Cross-correlation (normalized for angle of latitude

within tomogram) of subvolume to the reference is 1.5 times the standard deviation lower than the mean.

To avoid that the same particle is present in two independent subvolumes, coordinates with similar positions were reduced to the one coordinate with the highest cross-correlation value to the reference of the latest alignment. The resulting final coordinates were considered as trusted particles and were used for further processing. All final tube averages were aligned to one C2-symmetrized low resolution reference and the coordinates of the corresponding particles adjusted accordingly. This re-centering was done to ensure that the particles across all tubes shared the same center. The particle picking resulted in 15116 subvolumes for the 1-particle dataset and 12955 subvolumes for the 3-particles dataset.

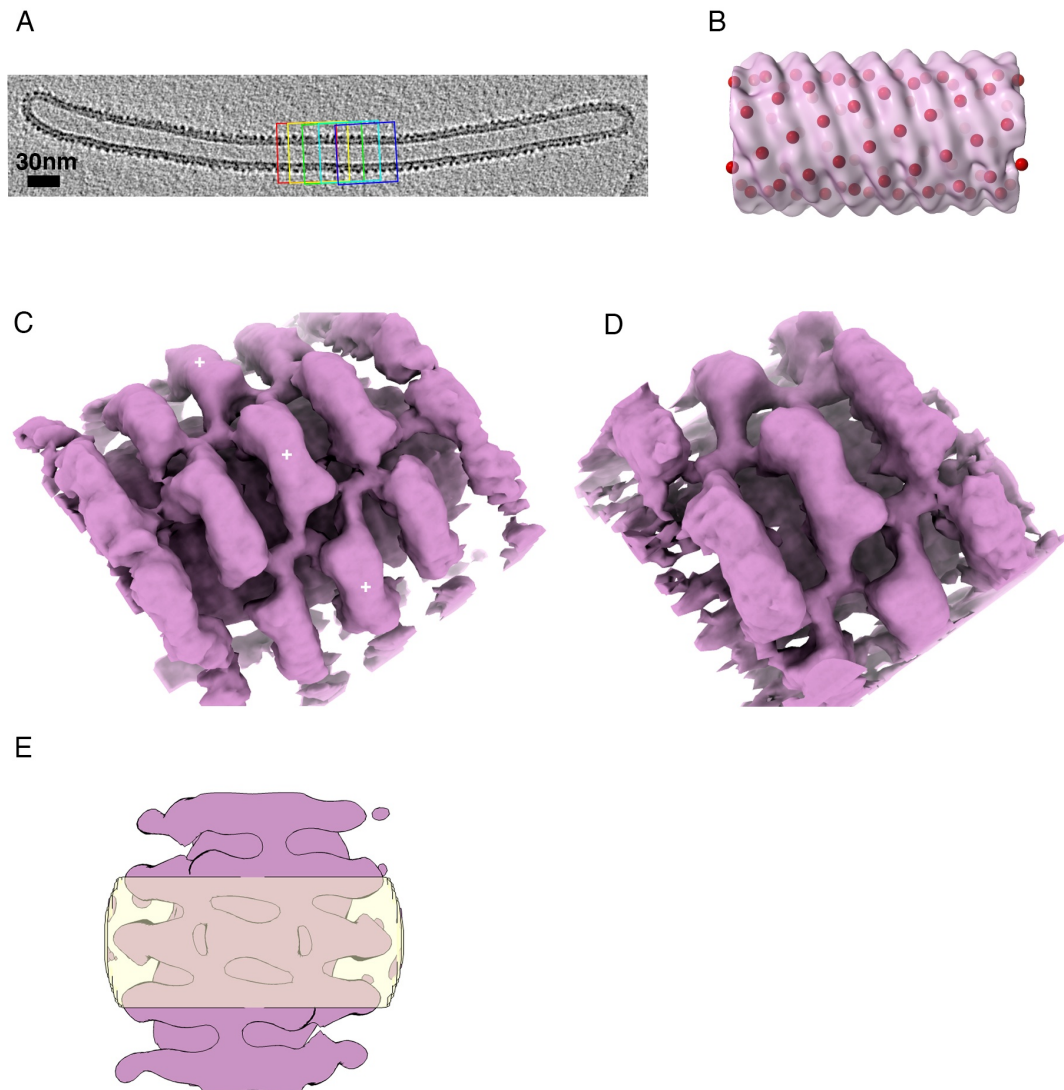


Figure 6.9.: **Particle picking for subtomogram averaging.** A) Computational section from a tomogram of a representative tube through its center. 5 cropped subvolumes for the tube average are illustrated. B) Tube average of the same tube and automatically determined coordinates along the helix for the helical sub-boxing. On this tube, 4 helical starts were measured. C) Result of helical sub-boxing and manually selected coordinates of individual heterodimers for the individual sub-boxing (white crosses). D) Result of individual sub-boxing showing one individual heterodimer in the box center. E) Top view of reference (purple) and alignment mask (yellow) used for helical sub-boxing. Three consecutive particles are included in the mask, while the lateral neighbors are mostly excluded.

6.6.6. Sub-tomogram averaging

The coordinates obtained from the particle picking were used to extract subvolumes from the WBP- tomograms with a box-size of 96^3 pixels for the 1-particle subvolumes and 128^3 pixels for the 3-particle subvolumes. The further processing for both subvolume sizes was the identical.

The dataset was split in two half-sets (even/odd) and each half-set was processed independently (gold standard method for refinement). After initial tests we realized that we cannot resolve the asymmetry of the heterodimers and thus decided to do the subtomogram averaging using imposed C2 symmetry. 12 iterations of subtomogram averaging were done using an initial lowpass filter set at 2.73 \AA , a mask that excludes the inner leaflet of the membrane and an orientation parameter space that would get finer with each iteration. A last refinement round of 3 iterations was done without any imposed symmetry to avoid overestimating the resolution.

6.6.7. Resolution estimation and post-processing

The resolution estimation and post-processing was carried out with RELION [Scheres 2012]. The mask-corrected Fourier shell correlation (FSC) was determined and the resolution at the 0.143 cut-off was found to be 10 \AA for the 1-particle map and 12 \AA for the 3-particles average (see Appendix B.6). B-factor sharpening was done with an empirical B-factor of -500 for the 1-particle average and -450 for the 3-particle average respectively.

Code availability

Scripts and functions used in the processing can either be found in the dedicated GitHub repository² or are available upon request.

²www.github.com/sscaramuzza/TomographyTools

7. Conclusion and outlook

Structural biology deals with determining the structure and dynamics of biological macromolecules. This is important for almost all life sciences and in particular for pharmacology. Cryo-ET is a promising technique in structural biology that allows to visualize macromolecules in their native or near-native environment at high resolution. Its popularity among the major structural biology techniques grew rapidly after major technical advances in all main aspects such as sample preparation, imaging hardware and image processing. A powerful image analysis technique in cryo-ET is STA, in which repetitions of biological structures within tomograms are computationally extracted and averaged to create a high resolution three dimensional representation of the structure. A popular and versatile software for STA is the in-house developed software *Dynamo*.

The goal of this thesis was to advance the field of STA by improving related computational methods. This was motivated by the huge potential that cryo-ET has in structural biology and by the fact that STA is among the leading image analysis techniques for cryo-ET. Developments were made mainly in *Dynamo* by targeting the prevalent bottleneck of throughput in STA. Two projects for the automation of image processing were therefore designed. An additional project involved the application of developed algorithms to answer current biological questions.

In the first project dealing with automation in STA (Chapter 4), a complete and streamlined image processing pipeline that requires minimal user intervention was established and documented in detail for the community. This *Dynamo* based pipeline was validated and benchmarked by successfully reproducing results from milestone publications on high resolution STA. The pipeline is meant to provide a basis for new and experienced users to set up and optimize their own STA workflows. It further provides a basis for additional benchmarking projects, which are urgently needed in this field (e.g., to optimize alignment parameters). The next step of this project would be the integration of the pipeline into a user-friendly GUI to facilitate implementation and modification of the workflow without any need for prior knowledge in MATLAB. The continuation of this project would also include efforts to integrate algorithms for automatic segmentation to remove the remaining steps that still require manual intervention.

In the second project dealing with automation (Chapter 5), the alignment of tomographic tilt series was fully automated in *Dynamo*. The new algorithms allow to align tilt series based on fiducial markers and to reconstruct the final tomogram through a user friendly

GUI. These developments significantly reduce processing times compared to conventional methods that require extensive user interaction for the marking and tracing of fiducial markers. The next step of this project would be to implement fiducial-less alignment algorithms for samples that prevent the use of fiducial markers. Tilt series alignment algorithms based on full micrographs, such as presented here, do not take into account local distortions of the sample (e.g., caused by beam induced motion). The future for high-resolution STA lies therefore in localized refinement of tilt series. The presented tilt series alignment workflow serves as a framework for the implementation of such algorithms in *Dynamo*. Alignment based on full micrographs will however still remain important because localized refinement techniques still rely on an initial tomogram for particle picking. Also tomograms that are only analyzed through segmentation (without any STA) will still depend on global tilt series alignment techniques.

In the project involving the application of developed algorithms (Chapter 6), the architecture of the SNX-BAR membrane coat was successfully determined and the differences to related protein coats were identified. The processing script that was established in Chapter 4 was used as a basis for the image analysis in this project. The particularly challenging sample properties (particle size of ~ 105 kDa, lattice irregularities and lack of symmetry) lead to the development of a broad range of specialized analysis tools that have been integrated in *Dynamo* and that will also be used in follow-up experiments (e.g., automatic helix fitting and lattice neighbor analysis). To be able to resolve the helix polarities, these follow-up experiments should be aimed at a smaller pixel size during data acquisition. The current results can still be used for predictions (e.g., through coarse grained molecular dynamics simulations) on how the protein coat might accommodate full sized cargo proteins. From the image processing point of view, this project was an excellent example to apply and validate the previously developed processing pipeline but also to identify and solve individual image processing challenges in STA. It further highlighted the importance of versatile software packages for STA to cope with the often complex geometries found in cryo-ET.

We conclude this thesis and formulate an outlook as follows: Based on the existing *Dynamo* software for STA, we successfully accomplished projects that target the important bottleneck of low throughput. In the bigger picture, faster processing times allow to systematically run large numbers benchmarking projects and thus open doors to validate approaches that target other common challenges in cryo-ET (e.g., CTF correction). In combination with current developments for faster data acquisition, the faster processing times also allow to process larger numbers of particles and therefore allow to get higher quality 3D maps. The processing framework established in this thesis can further be used as a basis for developments in *Dynamo* that target high resolution reconstructions. In summary, with the work of this thesis we successfully managed to advance STA and laid a foundation for future developments. A natural continuation of the work of the thesis would build on this foundation by developing the ideas mentioned in the previous paragraphs. An improvement of STA and cryo-ET with larger impact would however additionally include all relevant aspects such as sample preparation, data acquisition

and TEM hardware improvements, as highlighted in the next paragraph.

Currently, STA and cryo-ET are in a phase where a lot of research and improvements are made. This growth is mainly driven by recent advancements in cryo-EM – in particular by the success of SPA¹ – and by the promising predictions for cryo-ET. Significant progress is made in sample preparation, data acquisition, hardware and image analysis. For sample preparation, efforts are made to integrate CLEM and FIB/SEM in the same microscope under cryo-conditions for efficient preparation of FIB-milling samples [Gorelick et al. 2019]. To overcome the limitation of sample size, lift-out techniques are being developed [Schaffer et al. 2019]. Grid-preparation improvements are made by enabling the use of sample volumes in the nanoliter range [Schmidli et al. 2019] or by alternative on-grid preparation techniques [Peitsch et al. 2016]. Current efforts in TEM hardware include the improvements of detectors [M. Sun et al. 2020], reduction of radiation damage by single-electron packets imaging [Ryabov et al. 2020; VandenBussche et al. 2019], understanding the influence of electron energy on the image quality [Naydenova et al. 2019], developments of faster acquisition schemes [Bouvette et al. 2020] and the continuous development of phase plates [Buijsse et al. 2020] and their alternatives [Schwartz et al. 2019]. Particularly important for tomogram acquisition is the current research made to develop microscope stages that are faster, more stable and capable of broader tilt ranges [Chreifi et al. 2019]. Regarding image processing hardware, GPUs and solid state drives (SSDs) are constantly getting faster and more affordable. For image processing software, many successful concepts from SPA are progressively being integrated in STA such as local tilt series refinements and per-particle CTF correction [M. Chen, Bell, et al. 2019; Tegunov, Xue, et al. 2020]. Applications of machine learning methods such as deep learning are increasingly implemented as well, e.g., for tomogram segmentation [M. Chen, Dai, et al. 2017] or SNR improvements [Palovcak et al. 2020]. Finally, efforts are made to increase productivity by combining the major image analysis softwares into one single suite [De la Rosa-Trevín et al. 2016].

For cryo-ET and STA it is expected for the near future, that the aforementioned improvements will allow to solve structures at higher resolution in the same routinized way as SPA does today. More efficient sample preparation and data acquisition will lead to big datasets that will soon require particularly efficient image processing methods². This is one more reason, why right now it is the right time to invest in image analysis solutions targeting these specific problems. As mentioned, high-resolution STA is moving in a direction where per-particle refinements become increasingly relevant. Global operations on tomograms and tilt series will therefore only remain interesting for initial tomograms or for tomogram analysis techniques not involving STA. To fully overcome the problem of the missing wedge, alternative grid or stage designs will be necessary, because with today's technology even a microscope stage capable of a 360° rotation would cause obstructions of the electron path at high tilts by the surrounding ice, the grid

¹Recently, atomic resolution by SPA was reported [Nakane, Kotecha, et al. 2020].

²Already now, datasets of > 300 tomograms are being acquired [Yao et al. 2020]

or the stage itself. Looking further into the future we can expect to achieve routinely sub-nanometer resolution even for difficult samples such as cells prepared through FIB milling. If the limits of sample thickness and resolution can be pushed far enough, the vision of the reconstruction of full cells at atomic resolution might one day be within reach. The remaining unsolved parameter would be time. While with today's knowledge it seems impossible to record real-time electron tomograms of biological samples, it is more realistic to cryo-fixate and image a biological process at different stages in time and to combine the corresponding tomograms in the correct sequence to generate a 3D movie³. In combination with integrative approaches, the importance of cryo-ET and STA will steadily grow within structural biology.

³Various efforts for time-resolved cryo-EM have been made [Venkata P Dandey et al. 2020; Frank 2017; Kontziampasis et al. 2019; Peitsch et al. 2016; Schmidli et al. 2019].

8. Summary of my PhD

In this thesis, my three main projects were presented. A summary of all my projects, contributions and activities during my PhD at the Biozentrum is given in the following. A complete CV is furthermore attached at the end of this document.

Publications:

- Leigh, Kendra E., Paula P. Navarro, Stefano Scaramuzza, Wenbo Chen, Yingyi Zhang, Daniel Castaño-Díez, and Misha Kudryashev (2019). “Subtomogram averaging from cryo-electron tomograms”. In: *Methods in Cell Biology*. Vol. 152. Elsevier, pp. 217-259
- Stefano Scaramuzza, Daniel Castaño-Díez. “Protocols for Subtomogram Averaging of Virus-Like Particles with *Dynamo*”. In preparation
- Paula P. Navarro & Stefano Scaramuzza, Henning Stahlberg, Daniel Castaño-Díez. “Automated Alignment of Tilt Series for Cryo-Electron Tomography in the *Dynamo* Software Package”. In preparation
- Carlos López-Robles & Stefano Scaramuzza, Soledad Baños-Mateos, Miguel Romero, Elsa N Astorga-Simon, Ander Vidaurrazaga, Juan Fernandez-Recio, Adriana L Rojas, Daniel Castaño-Díez, Aitor Hierro. “Molecular architecture of the SNX-BAR membrane coat for endosomal sorting”. In preparation
- Pierre De Rossi, Amanda J Lewis, Johanna Furrer, Stefano Scaramuzza, Carolin Böing, Daniel Castano-Diez, Ashraf Alamoudi, Laura De Vos, Manuela Pérez-Berlangua, Tammaryn Lashley, Henning Stahlberg, Magdalini Polymenidou. “Subtypes of frontotemporal dementia present different TDP-43 assemblies carrying distinct seeding properties”. In preparation

Organizing and teaching of *Dynamo* workshops:

- Diamond Light Source, Oxfordshire, November 2017
- Basel Workshops in August of 2017, 2018 and 2019
- Created material for EMBO workshop at EMBL Heidelberg, September 2018

Lab visits:

- Zanetti Lab, Birkbeck College, London, February 2018
- De Marco Lab, Monash University, Melbourne, May 2019

Conferences:

- Conference on electron Tomography, Les Diablerets, September 2018

- Biozentrum Symposium and PhD retreat in 2017, 2018 and 2019

Created online material:

- Numerous guidelines/tutorials on *Dynamo* manual page: www.dynamo-em.org
- Numerous STA processing tools: www.github.com/sscaramuzza

Member of PhD Representatives of the Biozentrum:

- Organizer of the PhD Retreat 2019

Additional teaching activities:

- Teaching of SPA software during “Block course on Structural Biology and Biophysics” at Biozentrum, 2019
- Organizing of “Journal Club” seminar at C-CINA, 2019

Additional projects without publication:

- Cryo-ET of the 5-Hydroxytryptamine (5-HT) type 3 receptor (serotonin gated ion channel) reconstituted in lipid vesicles under the influence of different ligands.
- Cryo-ET of the ExbB/ExbD complex (proton channel) reconstituted in lipid vesicles.
- SPA of the Gcn2 kinase.

A. Supplementary material: "Automated Alignment of Tilt Series"

Table A.1.: Information on data sets analysed in this study. *data set used for figures.

Source	Data set	# tilt series	Sample type
<i>In-house</i>	FtsH*	68	Reconstituted protein in liposomes
	5HT3	75	Reconstituted protein in liposomes
	T6SS	9	Bacteria
	Collaborators	30	Purified organelles
<i>EMPIAR</i>	10009	27	Reconstituted protein in liposomes
	10037	1	Virus-like particles
	10046	46	Reconstituted protein in liposomes
	10047	1	Bacteria
	10048	1	Bacteria
	10062	11	Yeast
	10064	11	Purified ribosomes
	10110	16	Bacteria
	10113	4	Bacteria
	10114	7	Bacteria
	10115		Bacteria
	10164		Virus-like particles
	TOTAL	-	355

Table A.2.: Computational time for FtsH data set. *writing time = 24.3 sec; **writing time = 19.61.

Step	Single core	Multicore (14 units)
<i>Marker detection</i>	51.55	24.37
<i>Marker selection</i>	40.83	7.38
<i>Shifter</i>	4.54	2.56
<i>Indexing</i>	6.2	3.41
<i>Binned 2 alignment</i>	5.9	4.44
<i>Full size marker scaling</i>	5.6	3.1
<i>Full size alignment</i>	37.56*	16.8**
TOTAL	2 min 29 sec	1 min 4 sec

B. Supplementary material:
"Molecular Architecture of the
SNX-BAR Membrane Coat"

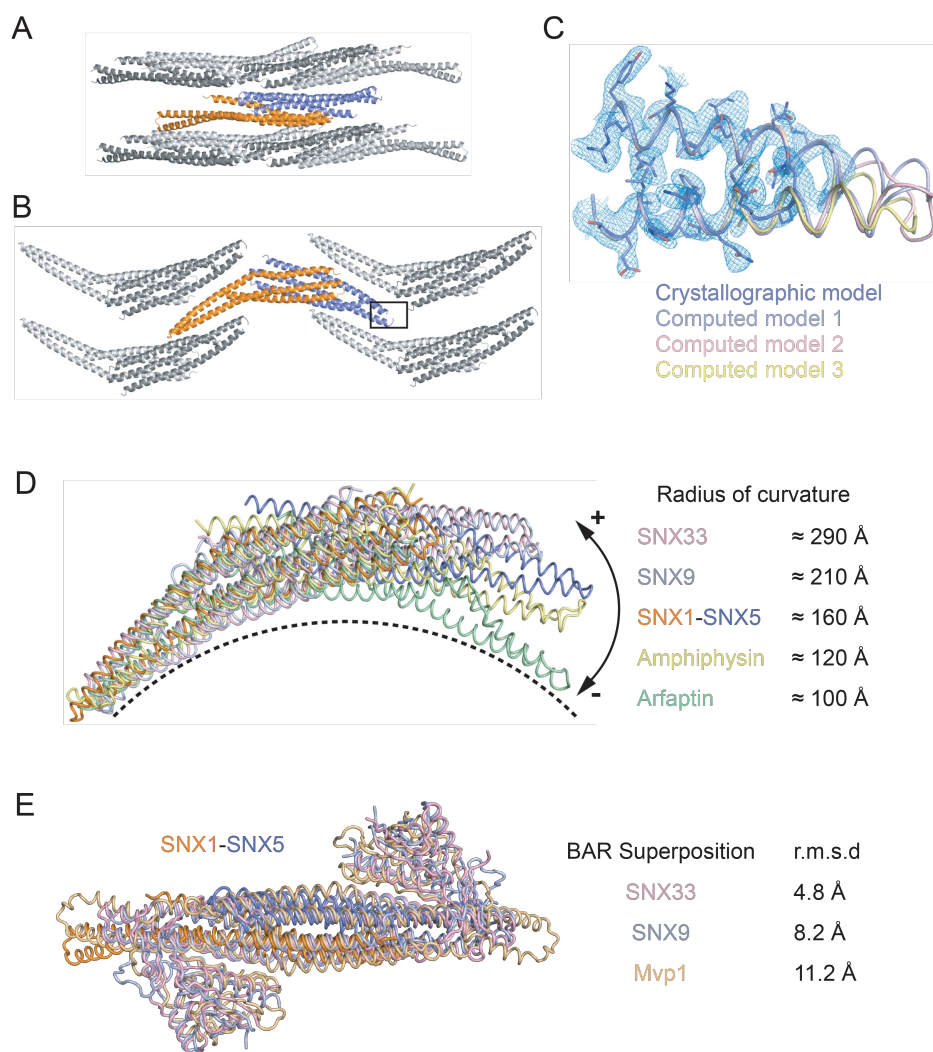


Figure B.1.: **Crystal packing of the SNX1^{BAR}-SNX5^{BAR} heterodimer and representative electron density.** (A, B) Lattice contacts for the SNX1^{BAR}-SNX5^{BAR} heterodimer. Chains in the foreground and background have been removed for clarity. The view in (A) shows the lateral contacts whereas the view in (B) is rotated 90 degrees and shows the top and bottom contacts. (C) 2Fo-Fc electron density map (contour 1.0 σ) at the tip of the SNX5^{BAR} domain (area box noted in (B)). The main chain is shown as a tube (slate color) and side chains are shown as sticks. Predicted structures by the DaReUS-Loop web-server are superimposed over the crystal structure. Model 1 represents the structure with the lowest statistical potential as determined by KORP. (D) Comparison of the curvature of SNX1^{BAR}-SNX5^{BAR} heterodimer with other BAR domains. To evidence differences in curvature, the structures were compared by superimposing SNX1^{BAR} with one subunit from each dimer. (E) Superposition of known PX-BAR structures (SNX33, PDB 4AKV (to be published); SNX9, PDB 2RAI; Mvp1, PDB 6Q0X) over the SNX1^{BAR}-SNX5^{BAR} heterodimer. The distal arm of SNX5^{BAR} is shorter than the equivalent arm in SNX1.

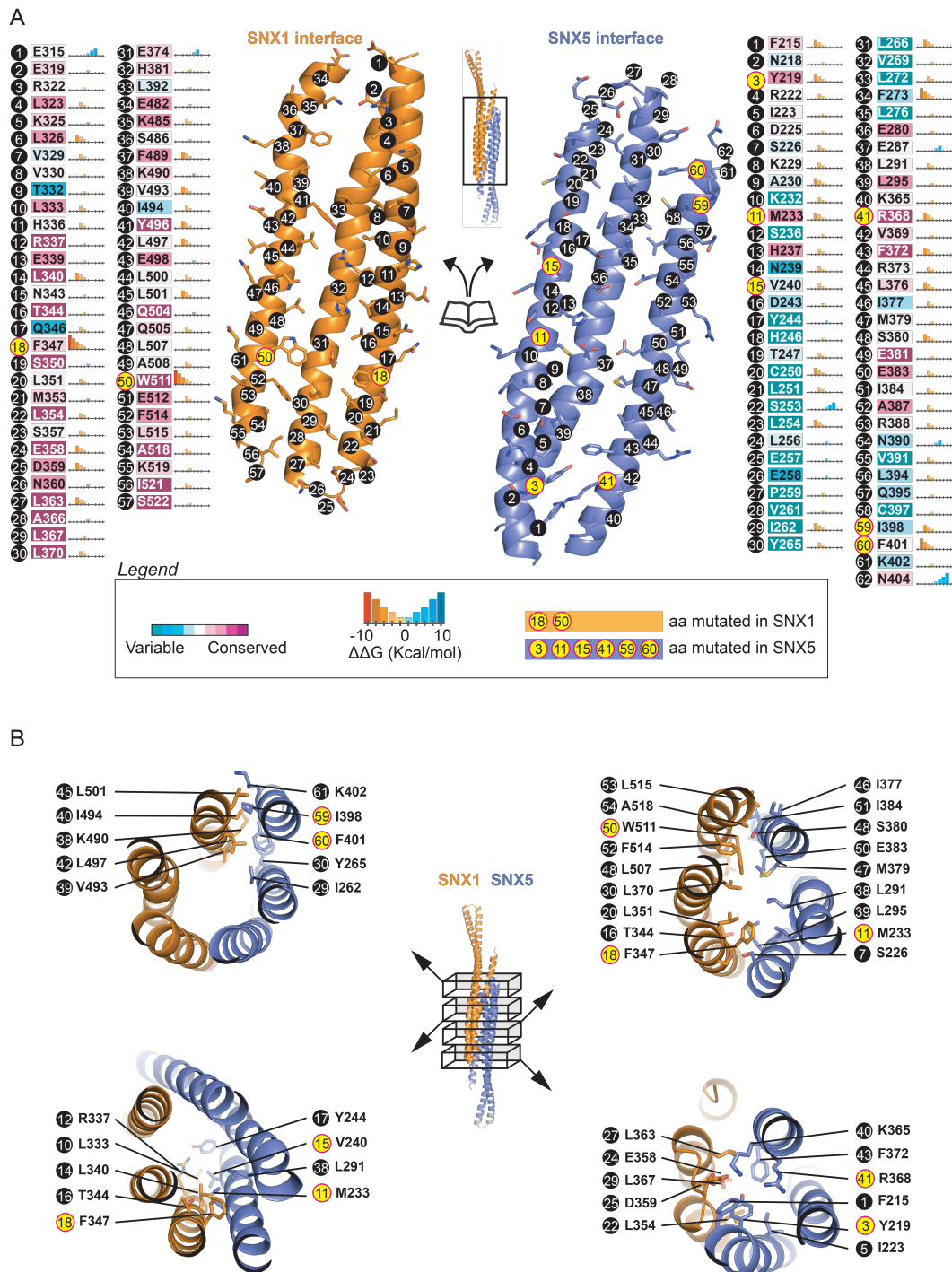


Figure B.2.: **Interface characterization.** (A) Detailed per-residue conservation and energetic analysis of the SNX1^{BAR}-SNX5^{BAR} interface. Mutated residues that affect dimer formation are highlighted in yellow. (B) Detailed view of neighboring sites of amino acids that were systematically mutated at the proximal and central regions of the BAR domains to interfere with dimerization.

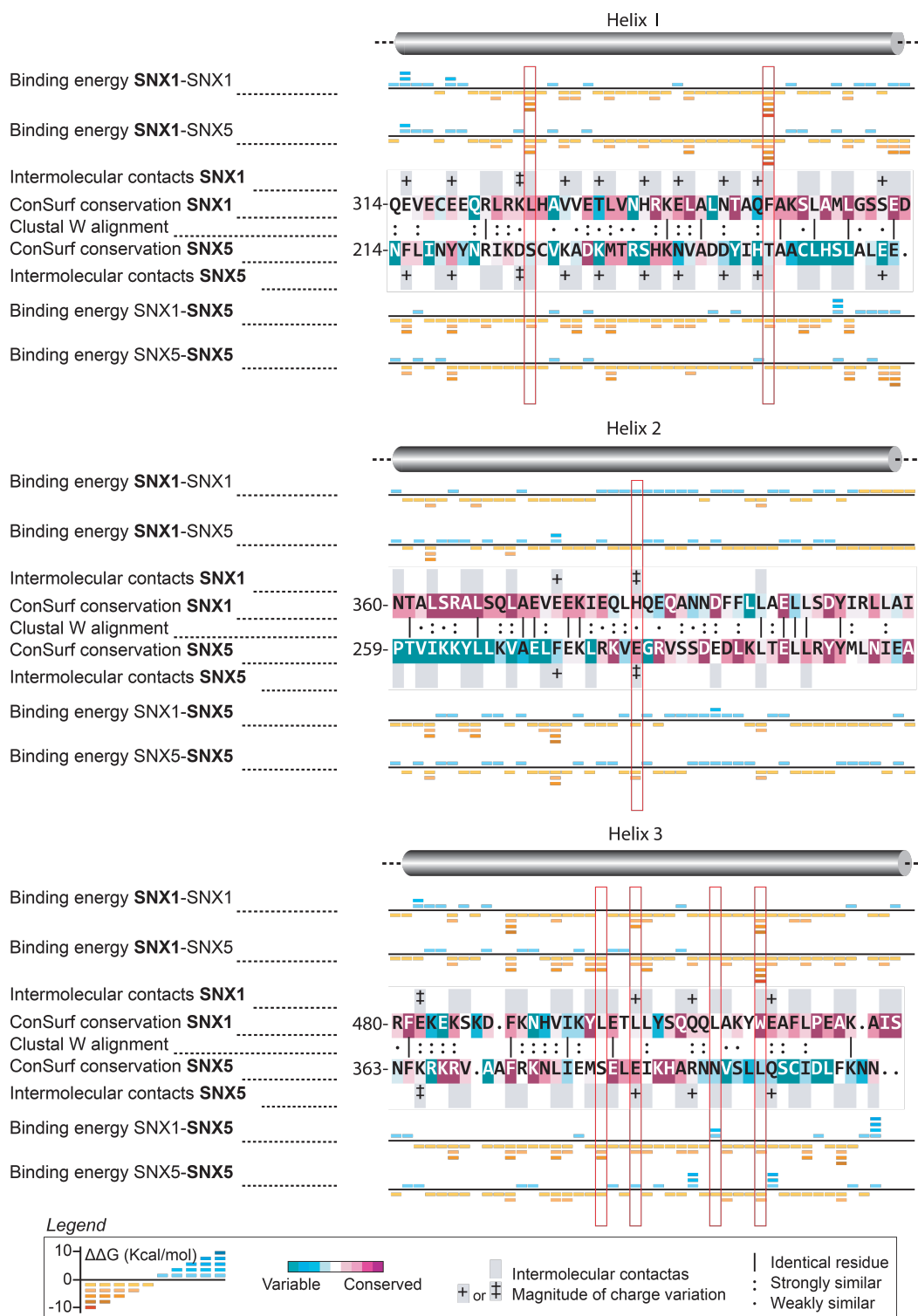


Figure B.3.: **Pairwise comparison of interfaces.** Alignment generated from the structural superposition of SNX1^{BAR}-SNX5^{BAR} central regions. Alignments also include per-residue energetic contribution in theoretical SNX1 and SNX5 homodimers generated by homology modeling using our SNX1^{BAR}-SNX5^{BAR} crystal structure as template. Energetic values in each row correspond to the molecule highlighted in bold within the respective complex. Red boxes mark residues that were mutated to interfere with dimerization.

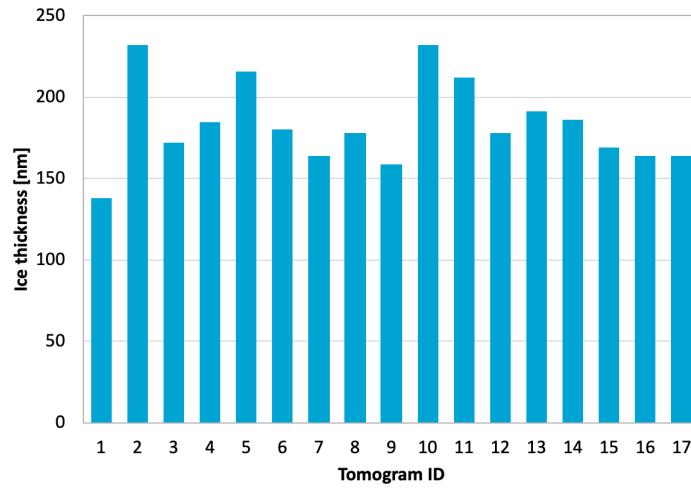


Figure B.4.: **Measured ice thickness of tomograms.** Ice thickness of of grids measured using randomly selected tomograms. Average thickness is ~ 180 nm.

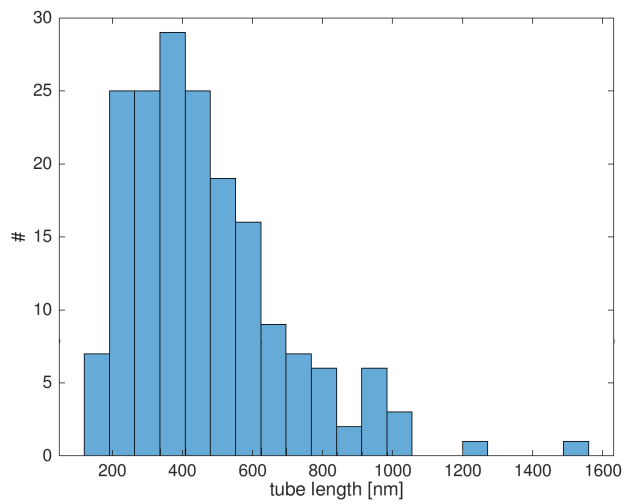


Figure B.5.: **Histogram of tube lengths.** The mean length is $466 \sim 224$ nm, the minimum length is 157 nm and the maximum length is 1552 nm.

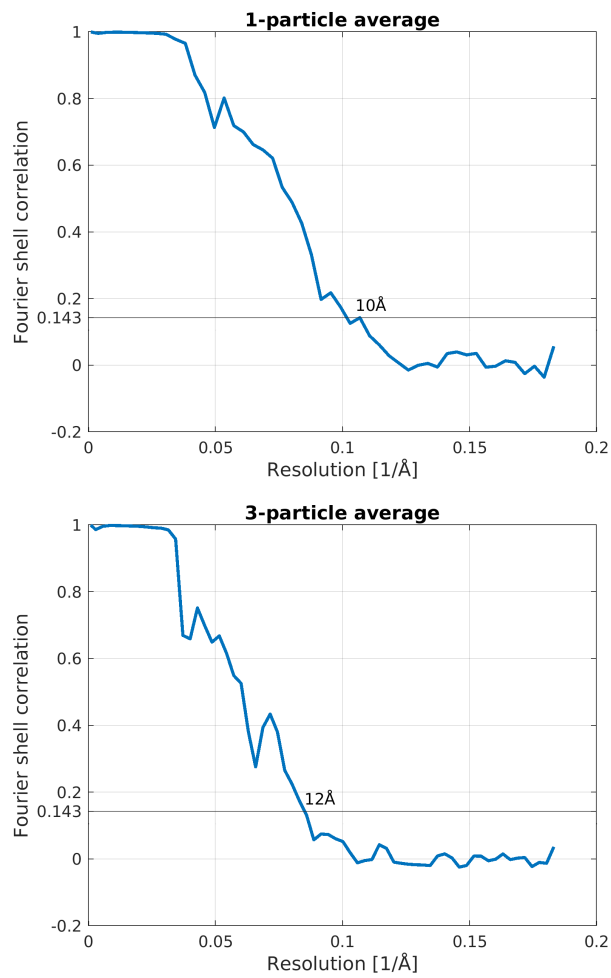


Figure B.6.: Mask corrected FSC of the 1- and 3-particle averages.

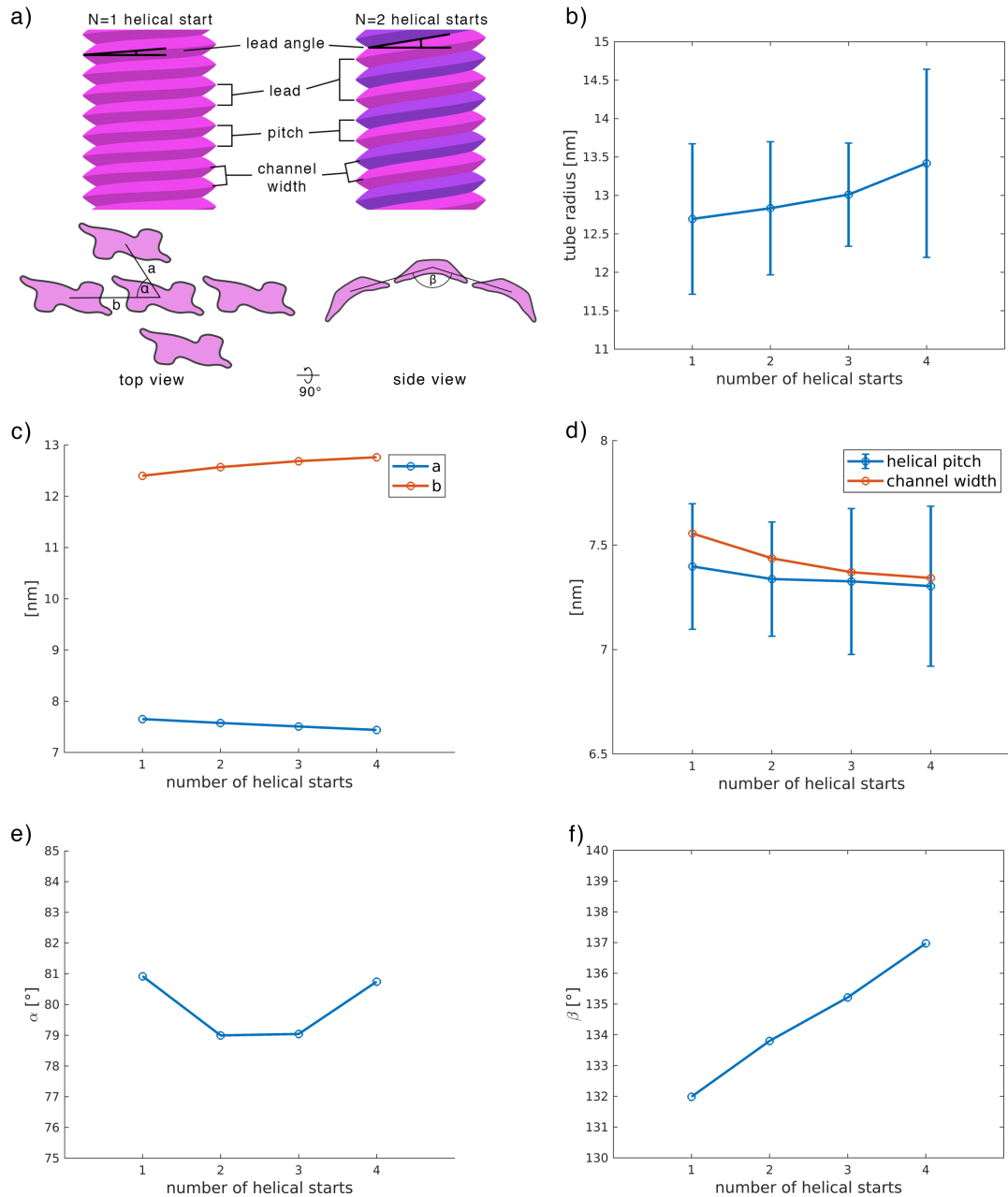


Figure B.7.: **Lattice parameters of the SNX1-SNX5 protein coat.** a) Definition of analyzed helical and lattice parameters. b) The tube radius shows a minimal increase with the number of helical starts. c) Distances a and b vary lightly as the lattice adapts to the new curvatures below the helix as the lead angle changes due to the different number of helical starts. d) The pitch stays constant while the channel width decreases with an increased number of helical starts. The pitch seems to be slightly underestimated as it can not be smaller than the channel width. The measurements are not accurate enough to analyze this in more detail. e) Angle α between lateral neighbors seems to be independent of the number of helical starts. b) Angle β shows a clear dependency on the number of helical starts. This is expected since the radius under the helix increases with an increased lead angle.

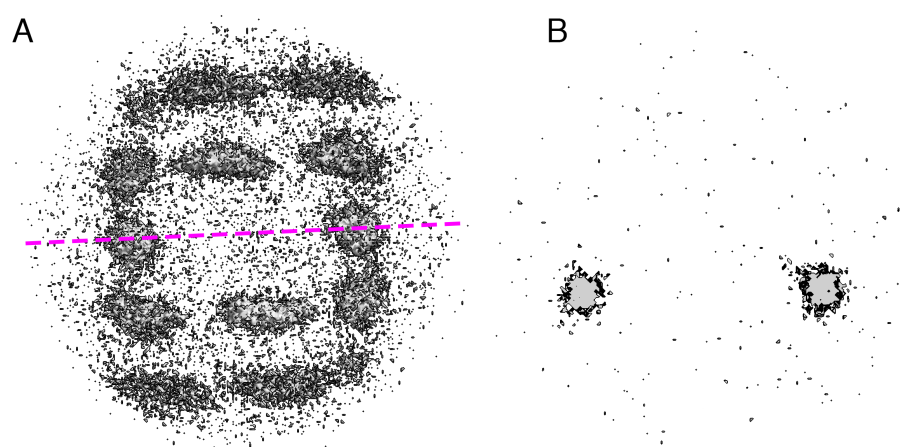


Figure B.8.: **3D neighborhood plot.** a) The neighborhood plot as shown in Figure 6.4F. The annotated cross section through the center shows (b) that distribution of neighboring particles at the tips is spherical, contrary to the elongated distribution of lateral neighbors.

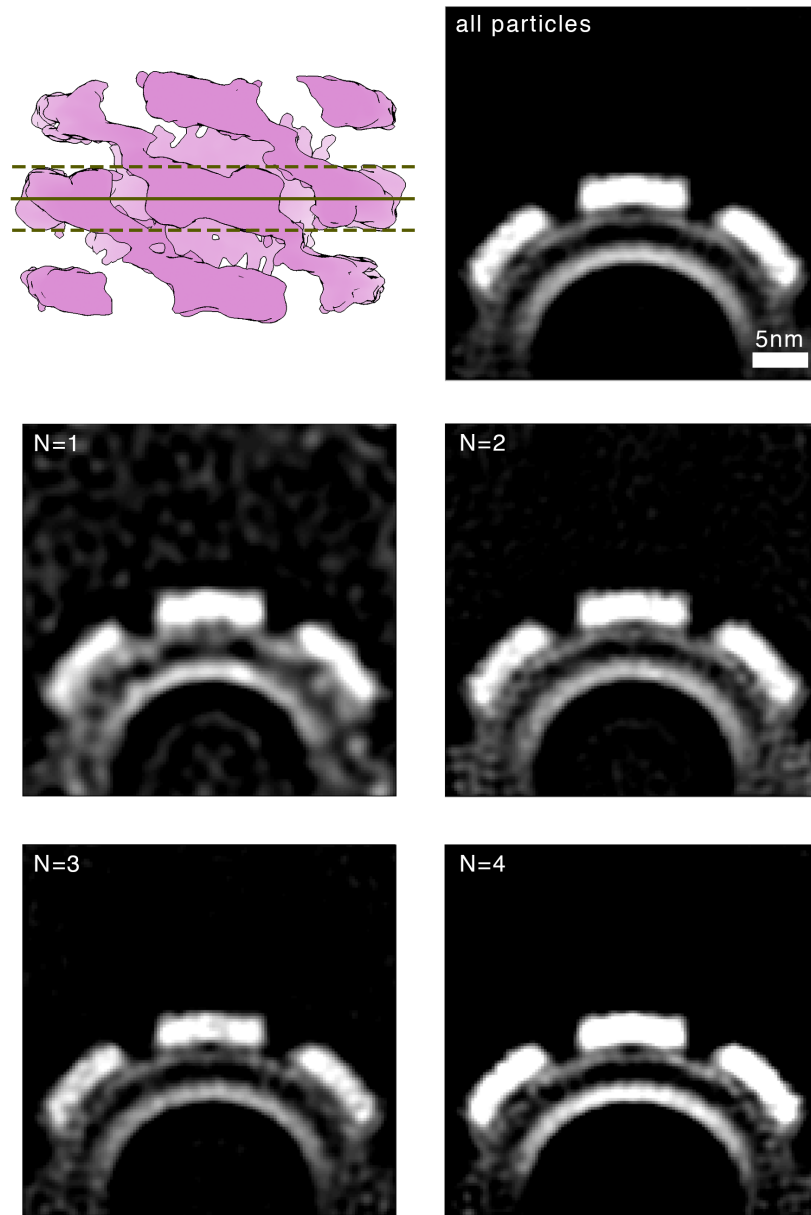


Figure B.9.: **Cross section of coat.** Cross section through center of the 3-particle average (averaged over 15 pixels as illustrated in the top left corner) from all particles and $N=1, 2, 3$ and 4 helical starts. The observations made in Figure 6.4G are true in all cases. Since the cross section is taken at an angle corresponding to the lead angle of the helix, an increase of the radius under the helix can be observed with increasing number of helical starts. The true radius of the tube itself, however, follows the observations made in Figure B.7.

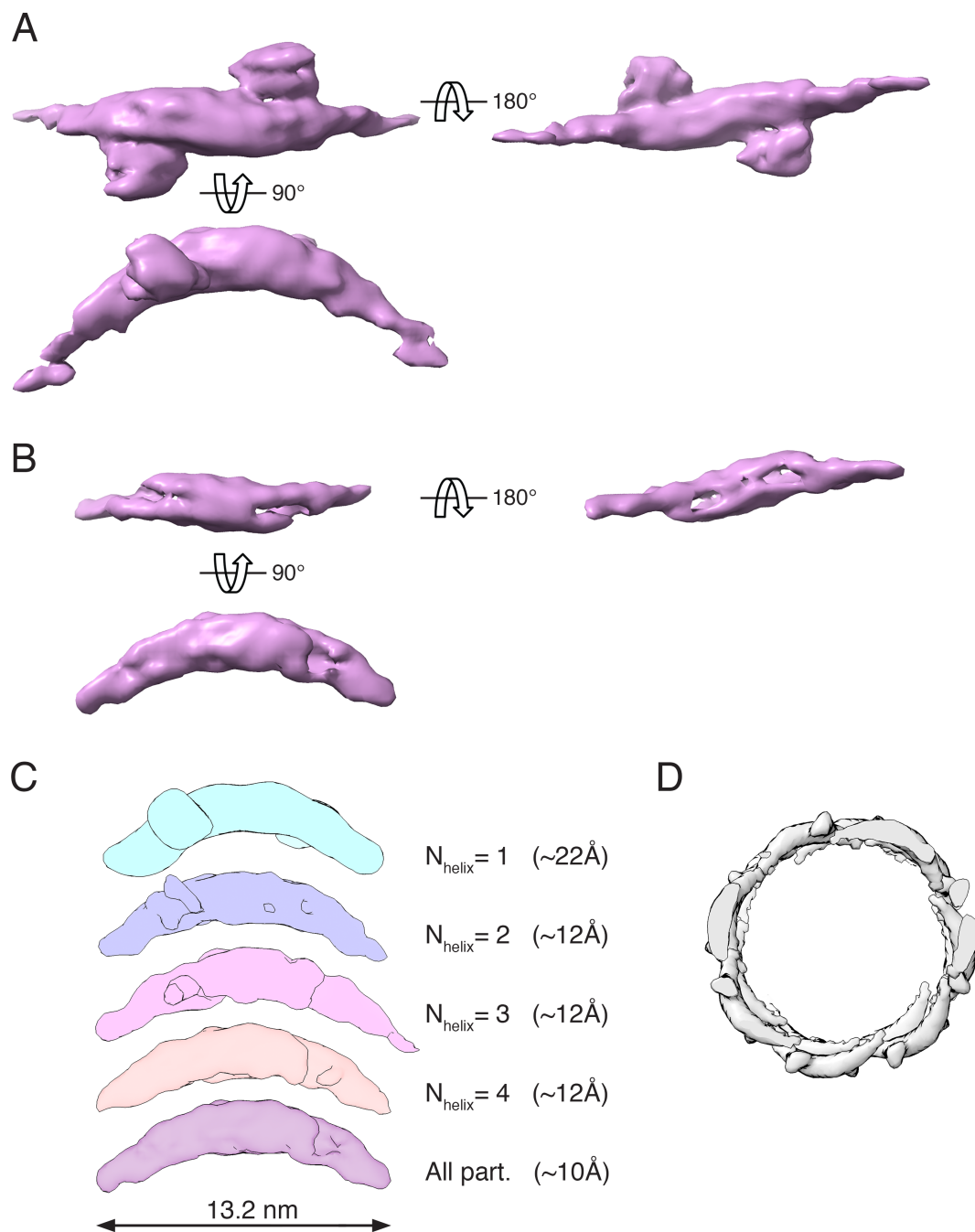


Figure B.10.: **Electron density map of the 1-particle average.** A) Different views of the 1-particle average. The PX and BAR domains are clearly distinguishable. B) A lower volume threshold shows hints of the alpha helices on the BAR domains. C) Side views of averages using only particles from tubes with the same number of helices. The curvature of the heterodimers is constant for all maps. Only the map formed from particles from tubes with one helical start seems to engulf a smaller radius. Due to its low resolution and low particle count it is however hard to say how strong this effect is. D) Cross section of the heterodimers arranged on the tube surface.

B.1. Automatic computation of helix parameters

B.1.1. Automatic radius calculation

Using the WBP-tomograms, the radius was automatically measured for each tube individually by first aligning and averaging the subtomograms of the segments from the oversampled tube. The resulting tube average was then projected along the tube direction. The projected tube average was then radially averaged. Using the automatic peak-detection algorithm from MATLAB, the radius was measured from the center of the tube to the point between the inner layer of the membrane and the protein coat, corresponding approximately to the outer layer of the membrane. The full radius calculation was automated using self-written Matlab functions and scripts.

B.1.2. Automatic helical pitch calculation

The helical pitch of a tube-average was calculated by performing an auto-correlation of the tube-average in its Z-direction. The distance between zero and the first peak of the auto-correlation represents the helical pitch. The full helical pitch calculation was automated using self-written Matlab functions and scripts.

B.1.3. Automatic helical starts calculation

The number of helical starts within a tube-average was computed by first expressing the tube in cylindrical coordinates. After this coordinate transformation, the helix around the tube for a given radius is represented as a series of parallel stripes in the 2D-plane defined by the height and azimuth angle. The inclination of the stripes was determined by locating the positions of the peaks in the corresponding Fourier transform. The number of helical starts N could then be computed by

$$N \approx \frac{\tan(a)/r}{p}$$

where a is the inclination, r the radius and p the helical pitch. The full helical starts calculation was automated using self-written Matlab functions and scripts.

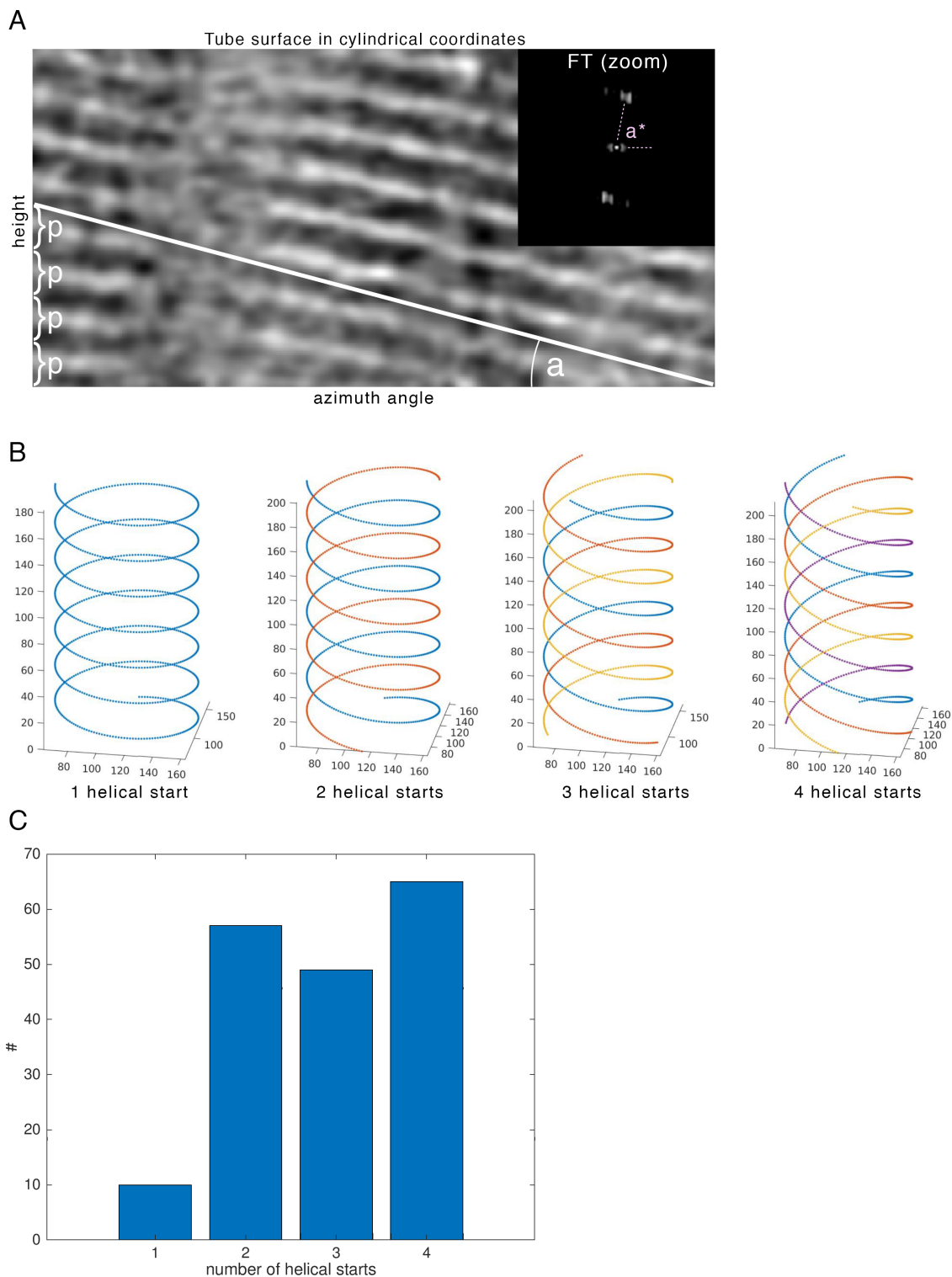


Figure B.11.: **Automatic helical starts calculation.** A) By expressing the tube surface in cylindrical coordinates, the helices become straight stripes. The Fourier transform (zoom) reveals diffraction-like spots that describe the periodicity and orientation these stripes. The angle a of the inclination can be derived from the angle a^* to then compute the number of helical starts based on the previously computed pitch. B) Simulation of helices with 1,2,3 and 4 starts (constant pitch). C) Measured distribution of number of helical starts of tubes in the dataset.

B.2. Automatic outlier exclusion

The automated outlier exclusion was done as follows for each tube separately. It was fully automated using a set of self-written Matlab functions and scripts that can be found in the GitHub repository of the author of this thesis¹ or are available upon request.

- **Extreme radius:** The distance of each subvolume from the tube center was computed and the overall mean distance and standard deviation was determined. A subvolume was excluded if the distance between the subvolume and the mean was larger than 2.5 times the standard deviation. This way, particles that are too close or too far from the tube center are excluded.
- **Extreme angle:** The normal vector of the sub-volume and the normal vector of the tube surface (at the closest location to the subvolume) were computed. If the angle between the two vectors was larger than 2.5 times the variance of all angles of the tube, the corresponding sub-volume was excluded. This way, particles with extreme orientations were excluded.
- **Missing neighbor:** A sphere that fits a full particle was defined at all 4 locations where according to the lattice geometry a neighboring particle is to be expected. Particles for which each of the 4 spheres was occupied by a neighboring particle were used for further processing.
- **Low cross correlation:** Particles with a cross-correlation (to the reference) lower than 1.5 times the standard deviation from the mean were discarded. The cross-correlation was normalized to compensate for missing wedge effects. The normalization was done by plotting the cross-correlation of the particles against their angle of latitude and then fitting the first two terms of a general Fourier series to the curve. The fitted curve was then used to weight and normalize the cross-correlation values (see Figure B.12).

¹www.github.com/sscaramuzza/TomographyTools

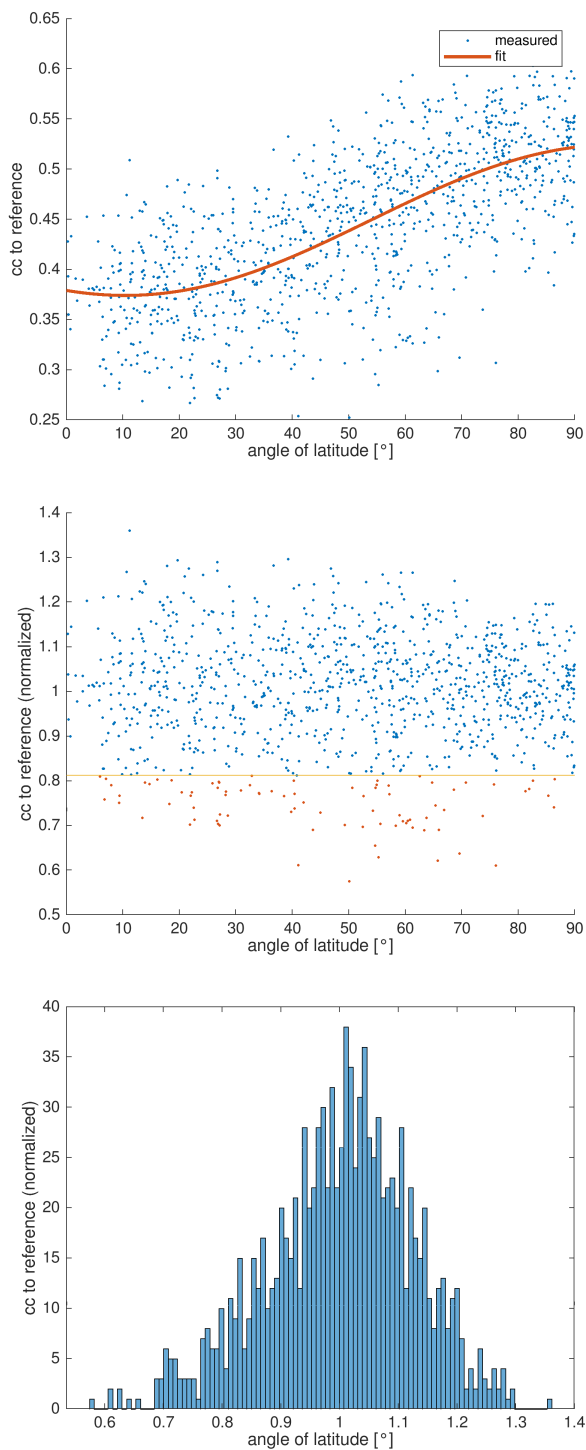


Figure B.12.: **Process to define the cross-correlation threshold for the outlier exclusion.** Example for one representative tube. Top: Fitting the data. Middle: Normalizing and thresholding. Particles with a cc value below the threshold (yellow line) are excluded (red). The remaining particles (blue) are kept for further processing. Bottom: Histogram of the normalized data.

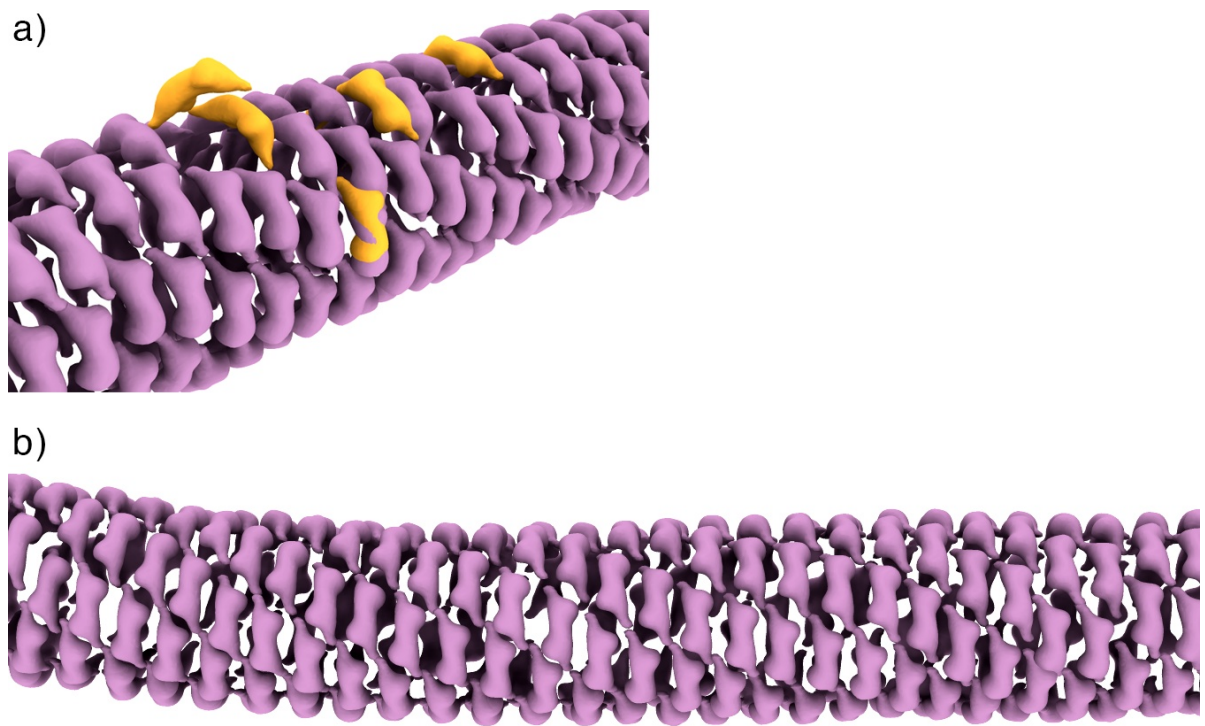


Figure B.13.: **Outlier exclusion.** a) Example of particles excluded with the described procedure (excluded particles colored in orange). Electron maps corresponding to the 1-particle average of the SIRT-tomograms. b) Example of result of a tube after outlier exclusion.

C. Supplementary material:
"Protocols for STA of VLPs"

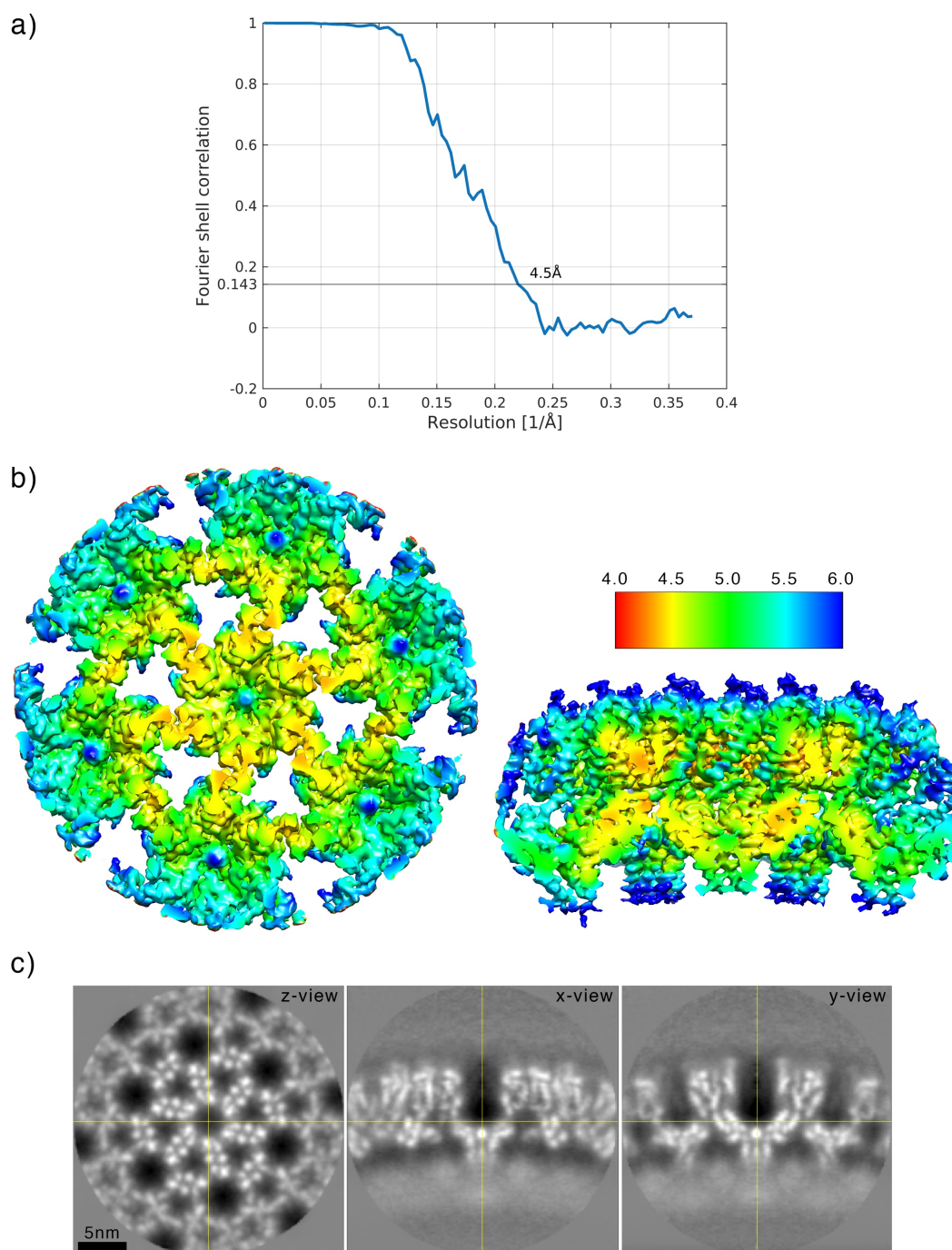


Figure C.1.: **Resolution estimation and final average.** a) Mask corrected FSC curve showing a global resolution estimation of 4.5 angstrom at the 0.143 cutoff. a) Local resolution estimation (cutoff 0,5) showing variations in resolution across the map. c) Orthogonal slices of the final average. The yellow lines show the positions of the slices.

Listing C.1: Complete processing script.

```

1 %%%%%%%%%%%%%%%%%%%%%%%%%%%%%%%%%%%%%%%%%%%%%%%%%%%%%%%%%%%%%%%%%%%%%%%%%%% Step 1: Set up inputs
2
3 %%%%%%%%%%%%%%%%%%%%%%%%%%%%%%%%%%%%%%%%%%%%%%%%%%%%%%%%%%%%%%%%%%%%%%%%%%%
4 % Block A: Inputs %
5 %%%%%%%%%%%%%%%%%%%%%%%%%%%%%%%%%%%%%%%%%%%%%%%%%%%%%%%%%%%%%%%%%%%%%%%%%%%
6 %
7 % User specific and geometry specific inputs. May need to be adapted.
8
9 % catalogue related inputs:
10 catPath      = '../catalogues/c001';
11 docFilePath  = '../catalogues/tomograms.doc';
12
13 % particle folders path (will contain all particle folders)
14 particleFolderPath = '../particles/';
15
16 % geometry related inputs:
17 sep          = 120; % separation in pixel for oversampling of dipole model surfaces
18 boxSizeFirst = 256; % box size for first alignment project
19 boxSizeSecond = 192; % box size for second alignment project
20 dTh          = 37; % distance threshold to eliminate particle duplicates
21
22 % computation related inputs:
23 mw           = 16; % number of matlab workers (CPU cores) for averaging
24 gpu          = [0:7]; % GPU id's for alignment projects
25
26
27 %%%%%%%%%%%%%%%%%%%%%%%%%%%%%%%%%%%%%%%%%%%%%%%%%%%%%%%%%%%%%%%%%%%%%%%%%%%
28 % Block B: Parse inputs & generate filenames %
29 %%%%%%%%%%%%%%%%%%%%%%%%%%%%%%%%%%%%%%%%%%%%%%%%%%%%%%%%%%%%%%%%%%%%%%%%%%%
30 %
31 % Setting up filenames for automatically generated files. This can be left as it is.
32
33 % read and parse doc file
34 fileID = fopen(docFilePath); D = textscan(fileID, '%d %s'); fclose(fileID);
35 tomoID = D{1,1}'; % get tomogram ID
36 nTomo  = length(D{1,2}); % get total number of tomograms
37
38 % project names
39 pr_0   = 'pr_ts001_0'; % project to generate reference
40 pr_a   = 'pr_a'; % alignment project of averages
41 pr_E0  = {'pr_E' , 'pr_0' }; % even/odd projects
42 pr_E0_2 = {'pr_E_2', 'pr_0_2'}; % evon/odd projects refinement
43
44 % table names
45 tE0_ccGood_TableName{1} = 'tE_ccGood.tbl'; % cc filtered even for refinement
46 tE0_ccGood_TableName{2} = 't0_ccGood.tbl'; % cc filtered odd for refinement
47 tableFileNameE0{1}      = 'merged_particlesE.tbl'; % merged particles even
48 tableFileNameE0{2}      = 'merged_particles0.tbl'; % merged particles odd
49 tableFileName            = 'merged_particles.tbl'; % merged particles all
50
51 % star file name for merged particles
52 starFileName            = 'merged_particles.star';
53
54 % em maps names
55 template_name_h = 'axis_alignment_template_h.em';
56 refFilenameE0   = {'referenceE.em', 'reference0.em'};
57 refEven         = 'aE_for_refinement.em';
58 refOdd          = 'a0_for_refinement.em';
59 refMask         = 'mem_mask_merged_adapted.em';
60
61 % create tomogram specific strings (idx = array index of tomogram and not tomogram ID)
62 for idx = 1:nTomo
63
64     % stack name
65     stackName{idx} = D{1,2}{idx,1}(end-8:end-4);

```

```

66
67 % particle folders
68 targetFolder_1{idx} = [particleFolderPath 'pa_' stackName{idx} '_s256'   ];
69 targetFolder_2{idx} = [particleFolderPath 'pa_' stackName{idx} '_s192_sb1'];
70 targetFolder_3{idx} = [particleFolderPath 'pa_' stackName{idx} '_s192_sb2'];
71
72 % project names
73 pr_1{idx} = ['pr_' stackName{idx} '_1'];
74 pr_2{idx} = ['pr_' stackName{idx} '_2'];
75
76 end
77
78 % folder name for particles of alignment project of averages
79 folderAllaverages = [particleFolderPath 'pa_averages.pr1'];
80
81
82 %%%%%%%%%%%%%%%%%%%%%%%%%%%%%%%%%%%%%%%%%%%%%%%%%%%%%%%%%%%%%%%%%%%%%%%%% Step 2: Oversampling of VLPS
83
84 %%%%%%%%%%%%%%%%%%%%%%%%%%%%%%%%%%%%%%%%%%%%%%%%%%%%%%%%%%%%%%%%%%%%%%%%%
85 % Block A: Define dipole models %
86 %%%%%%%%%%%%%%%%%%%%%%%%%%%%%%%%%%%%%%%%%%%%%%%%%%%%%%%%%%%%%%%%%%%%%%%%%
87 %
88 % Manually create dipole models for each VLP through catalogue.
89
90
91 %%%%%%%%%%%%%%%%%%%%%%%%%%%%%%%%%%%%%%%%%%%%%%%%%%%%%%%%%%%%%%%%%%%%%%%%%
92 % Block B: Process dipole models %
93 %%%%%%%%%%%%%%%%%%%%%%%%%%%%%%%%%%%%%%%%%%%%%%%%%%%%%%%%%%%%%%%%%%%%%%%%%
94 %
95 % Create crop points on VLP surface (oversampling).
96
97 % read dipole models from catalogue into matlab workspace
98 dcmmodels(catPath,'tc','dipoleSet','gm',1,'ws','o');
99
100 % loop over tomograms and run model workflow
101 for idx = 1:nTomo
102
103     % read model
104     ds = o.models{idx};
105
106     c=1; tv=[];
107     for i=1:length(ds.dipoles)           % loop over models
108
109         % vesicle workflow
110         v = dmodels.vesicle();           % create empty vesicle model
111         v.center = ds.dipoles{i}.center; % add dipole center to vesicle model
112         v.radius = norm( ds.dipoles{i}.north ...
113             - ds.dipoles{i}.center);     % add radius
114         v.separation = sep;               % separation of crop points (in px)
115         v.crop_distance_from_surface = 0;
116         v.updateCrop();                  % update vesicle model
117
118         tv{c} = v.grepTable();            % create crop table from vesicle model
119         tv{c}(:,22) = i;                  % add model number to table
120
121         % check consistency
122         if ~strcmp(ds.cvolumes{end-8 : end-4}, stackName{idx})
123             warning('CAREFUL: Model index and tomogram ID not consistent.')
124         end
125
126         tv{c}(:,20) = tomoID(idx);        % add tomogram number to table
127         c=c+1;
128     end
129
130 % merge model specific tables to tomogram specific table and visualize
131 tAll = dynamo_table_merge(tv,'linear_tags',1);

```

```

132 figure; dtplot(tAll,'pf','oriented_positions'); axis equal
133
134 % crop particles
135 dtcrop(docFilePath,tAll,targetFolder_1{idx},boxSizeFirst,'mw',mw);
136 finalTable = dread([targetFolder_1{idx} '/crop.tbl']);
137
138 % average particles, save in same particle folder and visualize
139 oa = daverage(targetFolder_1{idx},'t',finalTable,'fc',1,'mw',mw);
140 dwrite(oa.average,[targetFolder_1{idx} '/template.em']);
141 dview(oa.average)
142 end
143
144
145 %%%%%%%%%%%%%%%%%%%%%%%%%%%%%%%%%%%%%%%%%%%%%%%%%%%%%%%%%%%%%%%%%%%%%%%%% Step 3: Create initial reference
146
147 %%%%%%%%%%%%%%%%%%%%%%%%%%%%%%%%%%%%%%%%%%%%%%%%%%%%%%%%%%%%%%%%%%%%%%%%%
148 % Block A: Alignment project for reference %
149 %%%%%%%%%%%%%%%%%%%%%%%%%%%%%%%%%%%%%%%%%%%%%%%%%%%%%%%%%%%%%%%%%%%%%%%%%
150 %
151 % Generate an initial reference average using one tomogram.
152
153 % define which particles will be used to create reference
154 targetFolder_0 = targetFolder_1{1};
155
156 % create first template with randomized azimuth
157 tOri = dread([targetFolder_0 '/crop.tbl']);
158 tRandAz = dynamo_table_randomize_azimuth(tOri);
159 oa = daverage(targetFolder_0,'t',tRandAz,'fc',1,'mw',mw);
160 dwrite(oa.average,[targetFolder_0 '/template_RandAz.em']);
161 dwrite(tRandAz, [targetFolder_0 '/crop_RandAz.tbl']);
162
163 % create alignment project
164 dcp.new(pr_0,'d',targetFolder_0,'t',[targetFolder_0 '/crop_RandAz.tbl'], ...
165 'template',[targetFolder_0 '/template_RandAz.em'],'masks','default','show',0);
166
167 % set alignment parameters for 2 rounds
168 dvput(pr_0,'ite', [3 3]); % n iterations
169 dvput(pr_0,'dim', [64 128]); % subvolume sidelength (binning)
170 dvput(pr_0,'low', [23 23]); % lowpass filter
171 dvput(pr_0,'cr', [60 30]); % cone range
172 dvput(pr_0,'cs', [10 5]); % cone search step
173 dvput(pr_0,'ir', [90 30]); % inplane rotation
174 dvput(pr_0,'is', [10 5]); % inplane search step
175 dvput(pr_0,'rf', [5 5]); % refinement
176 dvput(pr_0,'rff', [2 2]); % refinement factor
177 dvput(pr_0,'lim', [80 20]); % shift limit
178 dvput(pr_0,'limm',[1 2]); % limit mode
179 dvput(pr_0,'sym', 'c1'); % symmetry
180
181 % set computational parameters
182 dvput(pr_0,'dst','matlab_gpu','cores',1,'mwa',mw);
183 dvput(pr_0,'gpus',gpu);
184
185 % check/unfold/run
186 dvrn(pr_0,'check',true,'unfold',true);
187
188 % prepare resulting average for chimera
189 aPath = ddb([pr_0 ':a']);
190 a = dread(aPath);
191 dwrite(dynamo_bandpass(a,[1 23])*(-1),['result_' pr_0 '_INVERTED.em']);
192
193
194 %%%%%%%%%%%%%%%%%%%%%%%%%%%%%%%%%%%%%%%%%%%%%%%%%%%%%%%%%%%%%%%%%%%%%%%%%
195 % Block B: Define particle center %
196 %%%%%%%%%%%%%%%%%%%%%%%%%%%%%%%%%%%%%%%%%%%%%%%%%%%%%%%%%%%%%%%%%%%%%%%%%
197 %

```

```

198 % Define manually center of particle in chimera ucsf (for next step).
199 % Save coordinate as: reference_center.cmm
200
201
202 %%%%%%%%%%%%%%%%%%%%%%%%%%%%%%%%%%%%%%%%%%%%%%%%%%%%%%%%%%%
203 % Block C: Center particles and re-average %
204 %%%%%%%%%%%%%%%%%%%%%%%%%%%%%%%%%%%%%%%%%%%%%%%%%%%%%%%%%%%
205 %
206 % Center the initial reference.
207
208 % prepare coordinates
209 cmmFile = 'reference_center.cmm'; % read coordinate from .cmm file
210 newCenter = cmm2mat(cmmFile,1,1); % create new variable with center
211 newCenter = round(newCenter); % round the coordinates
212 boxCenter = (boxSizeFirst/2+1) * [1,1,1]; % center of box
213
214 % compute vector pointing from box center to new coordinate
215 rSubunitFromCenter = newCenter - boxCenter;
216
217 % get table from project that will be transformed
218 tOriPath = ddb([pr_0 ':rt']);
219 tOri = dread(tOriPath);
220
221 % transform table
222 T = dynamo_rigid('shifts',-rSubunitFromCenter); % create transformation
223 tSub = dynamo_table_rigid(tOri,T); % transform table
224
225 % re-average, save and visualize
226 % this will be the starting reference for the next projects
227 oa = daverage(targetFolder_0,'t',tSub,'fc',1,'mw',mw);
228 dwrite(oa.average,['result_' pr_0 '_recentered.em']);
229 dview(oa.average)
230
231
232 %%%%%%%%%%%%%%%%%%%%%%%%%%%%%%%%%%%%%%%%%%%%%%%%%%%%%%%%%%% Step 4: First alignment project
233
234 %%%%%%%%%%%%%%%%%%%%%%%%%%%%%%%%%%%%%%%%%%%%%%%%%%%%%%%%%%%
235 % Block A: First alignment project %
236 %%%%%%%%%%%%%%%%%%%%%%%%%%%%%%%%%%%%%%%%%%%%%%%%%%%%%%%%%%%
237 %
238 % Run an alignment project for each tomogram.
239
240 for idx = 1:nTomo
241
242     % randomize azimuth of table before using it in project
243     tOri = dread([targetFolder_1{idx} '/crop.tbl']);
244     tRandAz = dynamo_table_randomize_azimuth(tOri);
245     dwrite(tRandAz, [targetFolder_1{idx} '/crop_RandAz.tbl'])
246
247     % reference is centered final average from previous project
248     templatePath = dread(['result_' pr_0 '_recentered.em']);
249
250     % define first alignment project
251     dcp.new(pr_1{idx},'d',targetFolder_1{idx}, ...
252         't',[targetFolder_1{idx} '/crop_RandAz.tbl'],'template', templatePath{1,1}, ...
253         'masks','default','show',0);
254
255     % set alignment parameters for 2 rounds
256     dvput(pr_1,'ite', [3 3]);
257     dvput(pr_1,'dim', [64 128]);
258     dvput(pr_1,'low', [23 23]);
259     dvput(pr_1,'cr', [60 30]);
260     dvput(pr_1,'cs', [10 5]);
261     dvput(pr_1,'ir', [90 30]);
262     dvput(pr_1,'is', [10 5]);
263     dvput(pr_1,'rf', [5 5]);

```

```

264     dvput(pr_1,'rff', [2 2]);
265     dvput(pr_1,'lim', [80 20]);
266     dvput(pr_1,'limm',[1 2]);
267     dvput(pr_1,'sym', 'c6');    % from now on c6 symmetry
268
269     % set computational parameters
270     dvput(pr_1{idx},'dst','matlab-gpu','cores',1,'mwa',mw);
271     dvput(pr_1{idx},'gpup','gpu');
272
273     % check/unfold/run
274     dvrn(pr_1{idx},'check',true,'unfold',true);
275
276     % check resulting table with visualization in plot
277     tPath = ddb([pr_1{idx} ':rt']);
278     t = dread(tPath);
279     figure; dtplot(t,'pf','oriented_positions'); axis equal
280     %dpktbl.plots.disks(t,'r',boxSizeFirst/2)
281
282 end
283
284
285 %%%%%%%%%%%%%%%%%%%%%%%%%%%%%%%%%%%%%%%%%%%%%%%%%%%%%%%%%%%%%%%%%%%%%%%%% Step 5: Determine candidate particles
286
287 %%%%%%%%%%%%%%%%%%%%%%%%%%%%%%%%%%%%%%%%%%%%%%%%%%%%%%%%%%%%%%%%%%%%%%%%%
288 % Block A: Create 'average of averages' %
289 %%%%%%%%%%%%%%%%%%%%%%%%%%%%%%%%%%%%%%%%%%%%%%%%%%%%%%%%%%%%%%%%%%%%%%%%%
290 %
291 % Align averages from first alignment project to prepare first step of subboxing.
292
293 % copy previous averages into new folder (particle tag number = tomogram number)
294 for idx = 1:nTomo
295     aPath = ddb([pr_1{idx} ':a']);
296     copyfile(aPath{1}, ...
297         [folderAllaverages '/particle_' num2str(tomoID(idx),'%06.f') '.em'];)
298 end
299
300 % create corresponding table and save it in new particle folder
301 ta = dynamo_table_blank(nTomo);
302 ta(:,13) = 0; % no missing wedge compensation needed
303 ta(:,20) = ta(:,1); % set particle tag number = tomogram number
304 ta(:,24:26) = 129*ones(nTomo,3); % set centers
305 dwrite(ta,[folderAllaverages '/crop.tbl'])
306
307 % create template, put it in particle folder and visualize
308 oa = daverage(folderAllaverages,'t',[folderAllaverages '/crop.tbl'],'fc',1);
309 dwrite(oa.average,[folderAllaverages '/template.em']);
310 dview(oa.average) % visualize
311
312 % create the alignment project of averages to align the 5 particles (averages)
313 dcp.new(pr_a,'d',folderAllaverages,'t',[folderAllaverages '/crop.tbl'], ...
314     'template',[folderAllaverages '/template.em'],'masks','default','show',0);
315
316 % set alignment parameters for 2 rounds
317 dvput(pr_a,'ite', [3 3]);
318 dvput(pr_a,'dim', [64 128]);
319 dvput(pr_a,'low', [23 23]);
320 dvput(pr_a,'cr', [60 30]);
321 dvput(pr_a,'cs', [10 5]);
322 dvput(pr_a,'ir', [90 30]);
323 dvput(pr_a,'is', [10 5]);
324 dvput(pr_a,'rf', [5 5]);
325 dvput(pr_a,'rff', [2 2]);
326 dvput(pr_a,'lim', [80 20]);
327 dvput(pr_a,'limm',[1 2]);
328 dvput(pr_a,'sym', 'c6');
329

```

```

330 % set computational parameters
331 dvput(pr_a,'dst','matlab_gpu','cores',1,'mwa',mw);
332 dvput(pr_a,'gpus',0:7);
333
334 % check/unfold/run
335 dvrn(pr_a,'check',true,'unfold',true);
336
337 % prepare resulting average for chimera
338 aPath = ddb([pr_a ':a']);
339 a = dread(aPath);
340 dwrite(dynamo_bandpass(dynamo_csym(a,6),23)*(-1),['result_' pr_a '_INVERTED.em']);
341
342
343 %%%%%%%%%%%%%%%%%%%%%%%%%%%%%%%%%%%%%%%%%%%%%%%%%%%%%%%%%%%%%%%%%%%%%%%%%
344 % Block B: Define coordinates of all unit cells %
345 %%%%%%%%%%%%%%%%%%%%%%%%%%%%%%%%%%%%%%%%%%%%%%%%%%%%%%%%%%%%%%%%%%%%%%%%%
346 %
347 % Define manually center of all unit cells in chimera (for next step).
348 % Save coordinate as: particle_centers.cmm
349
350
351 %%%%%%%%%%%%%%%%%%%%%%%%%%%%%%%%%%%%%%%%%%%%%%%%%%%%%%%%%%%%%%%%%%%%%%%%%
352 % Block C: Map coordinates back to the averages %
353 %%%%%%%%%%%%%%%%%%%%%%%%%%%%%%%%%%%%%%%%%%%%%%%%%%%%%%%%%%%%%%%%%%%%%%%%%
354 %
355 % First step of subboxing, where the coordinates are mapped back onto the averages.
356
357 % get table from the alignment project of averages
358 tOriPathCombined = ddb([pr_a ':rt']);
359 tOriCombined = dread(tOriPathCombined);
360
361 % prepare coordinates
362 cmmFileCombined = 'particle_centers.cmm'; % read coordinates from .cmm file
363 newCenterCombined = cmm2mat(cmmFileCombined,1,1); % create new variable with center
364 newCenterCombined = round(newCenterCombined); % round the coordinates
365 boxCenterCombined = (boxSizeFirst/2+1) * [1,1,1]; % center of box
366
367 % compute vector from box center to new coordinate for each coordinate
368 % and create mini table for each average that contains the corresponding coordinates
369 for i=1:length(newCenterCombined(:,1))
370     disp(['working on point: ' num2str(i)])
371     rSubunitFromCenterCombined(i,:) = newCenterCombined(i,:) - boxCenterCombined;
372     tSubCombined{i} = ...
373         dynamo_subboxing_table(tOriCombined,rSubunitFromCenterCombined(i,:));
374 end
375
376 % merge mini tables
377 tSubAllCombined = dynamo_table_merge(tSubCombined,'linear_tags',1);
378
379 % create the newCenter variable for each average that will be used in next steps
380 for idx = 1:nTomo
381     tSubOneCombined = tSubAllCombined(tSubAllCombined(:,20)==tomoID(idx),:);
382     newCenterCell{idx} = tSubOneCombined(:,24:26);
383 end
384
385
386 %%%%%%%%%%%%%%%%%%%%%%%%%%%%%%%%%%%%%%%%%%%%%%%%%%%%%%%%%%%%%%%%%%%%%%%%%
387 % Block D: Map coordinates back to the tomograms %
388 %%%%%%%%%%%%%%%%%%%%%%%%%%%%%%%%%%%%%%%%%%%%%%%%%%%%%%%%%%%%%%%%%%%%%%%%%
389 %
390 % Second step of subboxing, where coordinates are mapped back into the tomograms.
391
392 % subbox each tomogram
393 for idx = 1:nTomo
394
395     % get table from first alignment

```

```

396 tOriPath = ddb([pr_1{idx} ':rt']);
397 tOri = dread(tOriPath);
398
399 % prepare coordinates
400 newCenter = newCenterCell{tomoID(idx)}; % get centers from subboxing
401 newCenter = round(newCenter); % round the coordinates
402 boxCenter = (boxSizeFirst/2+1) * [1, 1, 1]; % center of box
403
404 % compute vector from box center to new subbox center and perform subboxing
405 for i=1:length(newCenter(:,1))
406     disp(['working on: ' num2str(i)])
407     rSubunitFromCenter(i,:) = newCenter(i,:) - boxCenter;
408     tSub{i} = dynamo_subboxing_table(tOri,rSubunitFromCenter(i,:));
409 end
410
411 % merge tables
412 tSubAll = dynamo_table_merge(tSub,'linear-tags',1);
413
414 % exclude coordinates describing the same unit cell
415 tSubAllEx = dpktbl.exclusionPerVolume(tSubAll,dTh);
416
417 % plot and save table
418 figure; h = dpktbl.plots.sketch(tSubAllEx,'haxis',gca()); h.zlength.value=100;
419 dwrite(tSubAllEx,['subbox_' stackName{idx} '.tbl'])
420 end
421
422 % crop particles for each tomogram
423 for idx = 1:nTomo
424
425     % re-crop subboxed particles
426     tSubAllEx = dread(['subbox_' stackName{idx} '.tbl']);
427     dtcrop(docFilePath,tSubAllEx,targetFolder_2{idx},boxSizeSecond,'mw',mw);
428
429     % re-average subboxed particles
430     finalTable = dread([targetFolder_2{idx} '/crop.tbl']);
431     oa = daverage(targetFolder_2{idx},'t',finalTable,'fc',1,'mw',mw);
432     dwrite(oa.average,[targetFolder_2{idx} '/template.em']);
433     dview(oa.average)
434 end
435
436
437 %%%%%%%%%%%%%%%%%%%%%%%%%%%%%%%%%%%%%%%%%%%%%%%%%%%%%%%%%%%
438 % Block E: Second alignment project %
439 %%%%%%%%%%%%%%%%%%%%%%%%%%%%%%%%%%%%%%%%%%%%%%%%%%%%%%%%%%%
440 %
441 % run second alignment project with new table and template
442
443 for idx = 1:nTomo
444
445     % set up project
446     dcp.new(pr_2{idx},'d',targetFolder_2{idx}, ...
447         't',[targetFolder_2{idx} '/crop.tbl'], ...
448         'template',[targetFolder_2{idx} '/template.em'], ...
449         'masks','default','show',0);
450
451     % set alignment parameters for 1 round with 3 iterations
452     dvput(pr_2{idx},'ite', 3);
453     dvput(pr_2{idx},'dim', 96);
454     dvput(pr_2{idx},'low', 23);
455     dvput(pr_2{idx},'cr', 45);
456     dvput(pr_2{idx},'cs', 5);
457     dvput(pr_2{idx},'ir', 30);
458     dvput(pr_2{idx},'is', 5);
459     dvput(pr_2{idx},'rf', 4);
460     dvput(pr_2{idx},'rff', 2);
461     dvput(pr_2{idx},'lim', [30,30,30]);

```

```

462     dvput(pr_2{idx}, 'limm', 3);
463     dvput(pr_2{idx}, 'sym', 'c6');
464
465     % set up computational parameters
466     dvput(pr_2{idx}, 'dst', 'matlab-gpu', 'cores', 1, 'mwa', mw);
467     dvput(pr_2{idx}, 'gpus', gpu);
468
469     % check/unfold/run
470     dvrn(pr_2{idx}, 'check', true, 'unfold', true);
471 end
472
473
474 %%%%%%%%%%%%%%%%%%%%%%%%%%%%%%%%%%%%%%%%%%%%%%%%%%%%%%%%%%%%%%%%%%%%%%%%%%% Step 6: Cross-correlation classification
475
476 %%%%%%%%%%%%%%%%%%%%%%%%%%%%%%%%%%%%%%%%%%%%%%%%%%%%%%%%%%%%%%%%%%%%%%%%%%%
477 % Block A: CC threshold %
478 %%%%%%%%%%%%%%%%%%%%%%%%%%%%%%%%%%%%%%%%%%%%%%%%%%%%%%%%%%%%%%%%%%%%%%%%%%%
479 %
480 % Automatically exclude false-positive subvolumes by cc thresholding.
481
482 for idx = 1:nTomo
483
484     % get table
485     tPath = ddb([pr_2{idx} 'rt']);
486     t = dread(tPath);
487
488     % fit gaussian mixture model (GMM) to cc distribution
489     gmdist = fitgmdist(t(:,10), 2);
490     gmsigma = gmdist.Sigma;
491     gmmu = gmdist.mu;
492     gmwt = gmdist.ComponentProportion;
493
494     % define threshold at minimum between gaussians plus constant
495     x = 0:0.001:0.5;
496     TF = islocalmin(pdf(gmdist, x));
497     thresh = x(TF)+0.01;
498
499     % plot results of fit
500     figure;
501     hold on;
502     histogram(t(:,10), 'Normalization', 'pdf', 'EdgeColor', 'none')
503     plot(x, pdf(gmdist, x'))
504     xline(thresh)
505     xlim([0 0.5])
506     legend('CC distribution', 'GMM fit', 'Threshold')
507     title(['Stack: ' stackName{idx}])
508     xlabel('CC')
509     ylabel('Occurencies')
510
511     % visualize kept/excluded particles
512     figure;
513     hold on
514     h = dpktbl.plots.sketch(t(t(:,10)>thresh,:), 'haxis', gca());
515     h.centerSettings.colorFill = 'b';
516     h = dpktbl.plots.sketch(t(t(:,10)<thresh,:), 'haxis', gca());
517     h.centerSettings.colorFill = 'r';
518     title(['Particles excluded by CC filtering, stack: ' stackName{idx}])
519
520     % define cc filtered table
521     t_ccFilt = t(t(:,10)>thresh,:);
522
523     % Exclude coordinates describing the same unit cell
524     t_ccFilt_Ex = dpktbl.exclusionPerVolume(t_ccFilt, dTh);
525     dwrite(t_ccFilt_Ex, ['t_ccFilt_Ex_' stackName{idx} '.tbl']);
526 end
527

```

```

528 % make new average and save it
529 for idx = 1:nTomo
530     t_ccFilt_Ex = dread(['t_ccFilt_Ex_' stackName{idx} '.tbl']);
531     oa = daverage(targetFolder_2{idx},'t',t_ccFilt_Ex,'fc',1,'mw',mw);
532     dwrite(oa.average,[targetFolder_2{idx} '/average_ccFilt_Ex.em']);
533     dview(oa.average)
534 end
535
536
537 %%%%%%%%%%%%%%%%%%%%%%%%%%%%%%%%%%%%%%%%%%%%%%%%%%%%%%%%%%
538 % Block B: Adjust height of particles %
539 %%%%%%%%%%%%%%%%%%%%%%%%%%%%%%%%%%%%%%%%%%%%%%%%%%%%%%%%%%
540 %
541 % Create consistent height of particles across all tomograms.
542
543 % create synthetic reference for alignemnt to height
544 mr = dpkto.examples.motiveTypes.Membrane(); % create membrane object
545 mr.thickness = 104; % choose thickness of membrane
546 mr.radius = 348; % choose radius of membrane
547 mr.sidelength = 192; % choose sidelength of box
548 mr.getMask(); % compute mask
549 template_h = (mr.mask)*(-1)+1; % invert contrast
550 dwrite(template_h,template_name_h)
551 dview(template_h)
552
553 for idx = 1:nTomo
554
555     % read average
556     template_average = dread([targetFolder_2{idx} '/average_ccFilt_Ex.em']);
557
558     % align average to template (only z-shift allowed)
559     sal = dalign(dynamo_bandpass(template_average,[1 23]), ...
560         dynamo_bandpass(template_h,[1 23]),'cr',1,'cs',1,'ir',1,'is',1,'dim',96, ...
561         'limm',1,'lim',[1,1,20],'rf',5,'rff',2);
562     dview(sal.assigned_particle);
563
564     % apply transformation to table
565     t_ccFilt_Ex = dread(['t_ccFilt_Ex_' stackName{idx} '.tbl']);
566     t_ccFilt_Ex_Ali = dynamo_table_rigid(t_ccFilt_Ex,sal.Tp);
567
568     % Exclude again coordinates describing the same unit cell
569     t_ccFilt_Ex_Ali_Ex = dpktbl.exclusionPerVolume(t_ccFilt_Ex_Ali,dTh);
570     dwrite(t_ccFilt_Ex_Ali_Ex,['t_ccFilt_Ex_Ali_Ex_' stackName{idx} '.tbl']);
571 end
572
573
574 %%%%%%%%%%%%%%%%%%%%%%%%%%%%%%%%%%%%%%%%%%%%%%%%%%%%%%%%%%
575 % Block C: Re-crop %
576 %%%%%%%%%%%%%%%%%%%%%%%%%%%%%%%%%%%%%%%%%%%%%%%%%%%%%%%%%%
577 %
578 % Extract subvolumes using latest table.
579
580 for idx = 1:nTomo
581     % read table and re-crop particles
582     t_ccFilt_Ex_Ali_Ex = dread(['t_ccFilt_Ex_Ali_Ex_' stackName{idx} '.tbl']);
583     dtcrop(docFilePath,t_ccFilt_Ex_Ali_Ex,targetFolder_3{idx},192,'mw',mw);
584 end
585
586 for idx = 1:nTomo
587     % Make and save average of last particle folder for sanity check
588     finalTable = dread([targetFolder_3{idx} '/crop.tbl']);
589     oa = daverage(targetFolder_3{idx},'t',finalTable,'fc',1,'mw',mw);
590     dwrite(oa.average,[targetFolder_3{idx} '/template.em']);
591     dview(oa.average)
592 end
593

```

```

594
595 %%%%%%%%%%%%%%%%%%%%%%%%%%%%%%%%%%%%%%%%%%%%%%%%%%%%%%%%%%% Step 7: Gold standard alignment
596
597 %%%%%%%%%%%%%%%%%%%%%%%%%%%%%%%%%%%%%%%%%%%%%%%%%%%%%%%%%%%
598 % Block A: Combine tomograms and generate even/odd dataset %
599 %%%%%%%%%%%%%%%%%%%%%%%%%%%%%%%%%%%%%%%%%%%%%%%%%%%%%%%%%%%
600 %
601 % Combine all particles from all tomograms and then split them in an even/odd dataset
602
603 % create table array
604 for idx = 1:nTomo
605     tableName{idx} = [targetFolder_3{idx} '/crop.tbl'];
606 end
607
608 % create ParticleListFile object (this object only exists temporarily in matlab)
609 plfClean = dpkdata.containers.ParticleListFile.mergeDataFolders( ...
610     targetFolder_3,'tables',tableName);
611
612 % create and write the .star file
613 plfClean.writeFile(starFileName)
614
615 % create merged table
616 tMergedClean = plfClean.metadata.table.getClassicalTable();
617
618 % write full/even/odd merged tables
619 dwrite(tMergedClean,tableFileName)
620 dwrite(tMergedClean(2:2:end,:),tableFileNameE0{1})
621 dwrite(tMergedClean(1:2:end,:),tableFileNameE0{2})
622
623 % create and save even/odd references
624 oaE = daverage(starFileName,'t',tableFileNameE0{1},'fc',1,'mw',mw);
625 oaO = daverage(starFileName,'t',tableFileNameE0{2},'fc',1,'mw',mw);
626 dwrite(oaE.average,refFilenameE0{1});
627 dwrite(oaO.average,refFilenameE0{2});
628
629
630 %%%%%%%%%%%%%%%%%%%%%%%%%%%%%%%%%%%%%%%%%%%%%%%%%%%%%%%%%%%
631 % Block B: Set up even/odd project %
632 %%%%%%%%%%%%%%%%%%%%%%%%%%%%%%%%%%%%%%%%%%%%%%%%%%%%%%%%%%%
633 %
634 % Run first even/odd alignment projects.
635
636 for r = 1:2 % loop over even/odd
637
638     % define alignment project
639     dcp.new(pr_E0{r},'t',tableFileNameE0{r},'d',targetFolder_3{1}, ...
640         'template',refFilenameE0{r},'show',0,'masks','default');
641     dvput(pr_E0{r},'data',starFileName)
642
643     % set alignment parameters for 3 rounds
644     dvput(pr_E0{r},'ite',[3 3 3]);
645     dvput(pr_E0{r},'dim',[96 192 192]);
646     dvput(pr_E0{r},'low',[23 28 32]);
647     dvput(pr_E0{r},'cr',[45 12 6]);
648     dvput(pr_E0{r},'cs',[5 2 1]);
649     dvput(pr_E0{r},'ir',[30 12 6]);
650     dvput(pr_E0{r},'is',[5 2 1]);
651     dvput(pr_E0{r},'rf',[5 4 3]);
652     dvput(pr_E0{r},'rff',[2 2 2]);
653     dvput(pr_E0{r},'lim',[30 12 6]);
654     dvput(pr_E0{r},'limm',[2 2 2]);
655     dvput(pr_E0{r},'sym','c6')
656
657     % set computational parameters
658     dvput(pr_E0{r},'dst','matlab-gpu','cores',1,'mwa',mw);
659     dvput(pr_E0{r},'gpus',gpu);

```

```

660
661     % check/unfold/run
662     dvrn(pr_E0{r}, 'check', true, 'unfold', true);
663 end
664
665
666 %%%%%%%%%%%%%%%%%%%%%%%%%%%%%%%%%%%%%%%%%%%%%%%%%%%%%%%%%%%%%%%%%%%%%%%%%%% Step 8: Refinement
667
668 %%%%%%%%%%%%%%%%%%%%%%%%%%%%%%%%%%%%%%%%%%%%%%%%%%%%%%%%%%%%%%%%%%%%%%%%%%%
669 % Block A: CC filter again (normalized & per tomogram) %
670 %%%%%%%%%%%%%%%%%%%%%%%%%%%%%%%%%%%%%%%%%%%%%%%%%%%%%%%%%%%%%%%%%%%%%%%%%%%
671 %
672 % Before the refinemet we exclude particiles with low CC again
673
674 % get last tables
675 tEPath = ddb([pr_E0{1} ':rt']);
676 t0Path = ddb([pr_E0{2} ':rt']);
677 tE     = dread(tEPath);
678 t0     = dread(t0Path);
679
680 % remove particles per tomogram based on normalized CC
681 for idx = 1:nTomo
682     [tE_ccGood_Array{idx}, tE_ccBad_Array{idx}] = filterByCC(tE( tE(:,20)==idx ,:));
683     [t0_ccGood_Array{idx}, t0_ccBad_Array{idx}] = filterByCC(t0( t0(:,20)==idx ,:));
684 end
685
686 % merge tables of accepted particles
687 tE0_ccGood{1} = dynamo_table_merge(tE_ccGood_Array);
688 tE0_ccGood{2} = dynamo_table_merge(t0_ccGood_Array);
689
690 % save tables
691 dwrite(tE0_ccGood{1}, tE0_ccGood_TableName{1});
692 dwrite(tE0_ccGood{2}, tE0_ccGood_TableName{2});
693
694 % make averages for new references and save them
695 oaE = daverage(starFileName, 't', tE0_ccGood_TableName{1}, 'fc', 1, 'mw', mw);
696 oa0 = daverage(starFileName, 't', tE0_ccGood_TableName{2}, 'fc', 1, 'mw', mw);
697 dwrite(oaE.average, refEven);
698 dwrite(oa0.average, refOdd);
699
700
701 %%%%%%%%%%%%%%%%%%%%%%%%%%%%%%%%%%%%%%%%%%%%%%%%%%%%%%%%%%%%%%%%%%%%%%%%%%%
702 % Block B: Refine even/odd project %
703 %%%%%%%%%%%%%%%%%%%%%%%%%%%%%%%%%%%%%%%%%%%%%%%%%%%%%%%%%%%%%%%%%%%%%%%%%%%
704 %
705 % Last even/odd alignment project. With alignment mask and stricter lowpass.
706
707 % create adapted mask and visualize it
708 mr = dpktomo.examples.motiveTypes.Membrane();
709 mr.thickness = 145;
710 mr.sidelength = 192;
711 mr.radius = 348;
712 mr.shifts = [0 0 5];
713 mr.getMask();
714 mem_mask = mr.mask;
715 cyl_mask = dynamo_cylinder(87, 192, [97 97 97]);
716 final_mask = mem_mask.*cyl_mask; % subtract cylinder
717 dwrite(final_mask, refMask)
718 dview(final_mask)
719
720 % read averages (for template)
721 aE0Path{1} = refEven;
722 aE0Path{2} = refOdd;
723
724 for r = 1:2
725

```

```

726 % define alignment project
727 dcp.new(pr_E0_2{r},'t',tE0_ccGood_TableName{r},'d',targetFolder_3{1}, ...
728     'template',aE0Path{1,r} ,'show',0,'masks','default');
729 dvput(pr_E0_2{r},'data',starFileName)
730 dvput(pr_E0_2{r},'file_mask',refMask)
731
732 % set alignment parameters for 1 round
733 dvput(pr_E0_2{r},'ite_r1', 3);
734 dvput(pr_E0_2{r},'dim_r1', 192);
735 dvput(pr_E0_2{r},'low_r1', 38);
736 dvput(pr_E0_2{r},'cr_r1', 6);
737 dvput(pr_E0_2{r},'cs_r1', 1);
738 dvput(pr_E0_2{r},'ir_r1', 6);
739 dvput(pr_E0_2{r},'is_r1', 1);
740 dvput(pr_E0_2{r},'rf_r1', 3);
741 dvput(pr_E0_2{r},'rff_r1', 2);
742 dvput(pr_E0_2{r},'lim_r1', [6,6,6]);
743 dvput(pr_E0_2{r},'limm_r1',2);
744 dvput(pr_E0_2{r},'sym_r1','c6'); % symmetry introduced
745
746 % set computational parameters
747 dvput(pr_E0_2{r},'dst','matlab_gpu','cores',1,'mwa',mw);
748 dvput(pr_E0_2{r},'gpus',gpu);
749
750 % check/unfold/run
751 dvrn(pr_E0_2{r},'check',true,'unfold',true);
752 end
753
754
755 %%%%%%%%%%%%%%%%%%%%%%%%%%%%%%%%%%%%%%%%%%%%%%%%%%%%%%%%%%%%%%%%%%%%%%%%% Step 9: Prepare half-maps
756
757 %%%%%%%%%%%%%%%%%%%%%%%%%%%%%%%%%%%%%%%%%%%%%%%%%%%%%%%%%%%%%%%%%%%%%%%%%
758 % Block A: Prepare half-maps %
759 %%%%%%%%%%%%%%%%%%%%%%%%%%%%%%%%%%%%%%%%%%%%%%%%%%%%%%%%%%%%%%%%%%%%%%%%%
760 %
761 % Align half-maps and save them for post-processing.
762
763 % get last maps
764 aEPath = ddb([pr_E0_2{1} ':a']);
765 a0Path = ddb([pr_E0_2{2} ':a']);
766 aE = dread(aEPath);
767 a0 = dread(a0Path);
768
769 % get last tables
770 tEPath = ddb([pr_E0_2{1} ':rt']);
771 t0Path = ddb([pr_E0_2{2} ':rt']);
772 tE = dread(tEPath);
773 t0 = dread(t0Path);
774
775 % align even to odd (with C6 imposed)
776 sal = dalign(dynamo_csym(aE,6),dynamo_csym(a0,6),'cr',3,'cs',1,'ir',3,'is',1, ...
777     'dim',192,'limm',1,'lim',[3,3,3],'rf',5,'rff',2, ...
778     'destination','matlab_gpu','gpu-identifier-set',1);
779
780 % transform even table (of which halfmap was aligned)
781 tEr = dynamo_table_rigid(tE,sal.Tp);
782
783 % make average
784 oaEr = daverage(starFileName,'t',tEr,'fc',1,'mw',mw);
785
786 % save aligned halfmaps (with symmetry) for FSC estimation
787 dwrite(dynamo_csym(oaEr.average,6) * (-1), 'half1_final_reaveraged_unfil.mrc')
788 dwrite(dynamo_csym(a0 ,6) * (-1), 'half2_final_reaveraged_unfil.mrc')
789
790 % reaverage all particles for post-processing (correct fourier compensation)
791 oAll = daverage(starFileName,'t',dynamo_table_merge({tEr,t0}),'fc',1,'mw',mw);

```

```
792 | dwrite(dynamo_csym(oAll.average,6) * (-1), 'final_reaveraged.mrc')
```


List of Abbreviations

2D two-dimensional

3D three-dimensional

BAR bin/amphiphysin/rvs

CC cross-correlation

CCD charge-coupled device

CEMOVIS cryo-electron microscopy of vitreous section

CI-MPR cation-independent mannose 6-phosphate receptor

CLEM correlative light electron microscopy

CLSM confocal laser scanning microscopy

COP coat protein complex II

CPU central processing unit

Cryo-EM cryo-electron microscopy

Cryo-ET cryo-electron tomography

Cryo-FIB cryo-focus ion beam

CTF contrast transfer function

DED direct electron detector

DNA deoxyribonucleic acid

DQE detective quantum efficiency

ED electron diffraction

EM electron microscopy

EMDB electron microscopy data bank

EMPIAR electron microscopy public image archive

ENS enteric nervous system

ESCPE-1 endosomal SNX–BAR sorting complex for promoting exit-1

ET electron tomography

FFT fast Fourier transform

FHV flock house virus

FIB focus-ion-beam

FRC Fourier ring correlation

FSC Fourier shell correlation

FT Fourier transform

GMM Gaussian mixture models

GPU graphical processing unit

GUI graphical user interface

HD hard disk

HPC high-performance computing

ITC isothermal titration calorimetry

LM light microscopy

MRA multi-reference alignment

MSA multivariate statistical analysis

MTF mutual transfer function

NCC normalized cross-correlation

NMR nuclear magnetic resonance

PCA principal component analysis

PDB protein data bank

PSF point spread function

PX phox-homology

RAM random access memory

RMS root-mean-square value

RNA ribonucleic acid

ROI region of interest

SBF-SEM serial block face scanning electron microscopy

SEM scanning electron microscopy

SGD stochastic gradient descent

SIRT simultaneous iterations reconstruction technique

SNR signal-to-noise ratio

SNX sorting nexin

SPA single particle analysis

SSD solid state drive

STA subtomogram averaging

TEM transmission electron microscope

VPS vacuolar protein sorting

WBP weighted back-projection

WPOA weak-phase object approximation

XRD X-ray diffraction

List of Figures

1.1. Illustration of the STA workflow.	19
3.1. Scales and techniques in molecular and cell biology.	27
3.2. Resolution trends for subtomogram averaging.	29
3.3. Tilt series alignment workflow.	39
3.4. Contrast transfer function and defocus gradients in cryo-ET.	44
3.5. Mechanics of StA.	50
3.6. The <i>subboxing</i> workflow.	53
3.7. Visualizing heterogeneity.	56
3.8. Data flow in StA.	61
4.1. Flowchart of processing script.	73
4.2. Oversampling of VLPs and average.	75
4.3. Center of unit cell defined in Chimera UCSF.	77
4.4. Results of first alignment.	78
4.5. Two-step subboxing for particle picking.	79
4.6. Resulting coordinates from particle picking.	80
4.7. Particle exclusion through cross-correlation classification.	85
4.8. Results of per-tomogram subtomogram averages.	86

4.9. Electron density map after post-processing.	86
5.1. Automated marker detection in <i>Dynamo</i>	98
5.2. Automated marker selection in <i>Dynamo</i>	99
5.3. Pair-wise correspondence of marker trajectories in a tilt series by <i>Dynamo</i>	101
5.4. Scheme of the geometrical operations performed by the command <code>shifter</code> to compute chains.	102
5.5. Scheme of the geometrical operations performed by the <code>reindexer</code>	106
5.6. Workflow <i>Dynamo</i> GUIs for tilt series alignment	110
5.7. <i>Dynamo</i> workflow for tilt series alignment.	111
6.1. Structure of the SNX1 ^{BAR} -SNX5 ^{BAR} heterodimer.	121
6.2. Analysis of the SNX1 ^{BAR} -SNX5 ^{BAR} interface.	123
6.3. Competition assay between SNX1 versus SNX5 and mutants.	124
6.4. Cryo-ET structure of the SNX1-SNX5 membrane coat with CI-MPR ₂₃₄₇₋₂₃₇₅ on lipid tubules.	130
6.5. VPS5 and SNX1-SNX5 exhibit different PX-BAR coat organizations.	132
6.6. Illustration of area used for CTF estimation.	136
6.7. Defocus estimation of one tilt series.	137
6.8. Overlap of projection of coordinates from all selected tubes.	138
6.9. Particle picking for subtomogram averaging.	141
B.1. Crystal packing of the SNX1 ^{BAR} -SNX5 ^{BAR} heterodimer and representative electron density.	152
B.2. Interface characterization.	153

B.3. Pairwise comparison of interfaces.	154
B.4. Measured ice thickness of tomograms.	155
B.5. Histogram of tube lengths.	155
B.6. FSC of 1- and 3-particle averages.	156
B.7. Lattice parameters of the SNX1-SNX5 protein coat.	157
B.8. 3D neighborhood plot.	158
B.9. Cross section of coat.	159
B.10. Electron density map of the 1-particle average.	160
B.11. Automatic helical starts calculation.	162
B.12. Process to define the cross-correlation threshold for the outlier exclusion.	164
B.13. Outlier exclusion.	165
C.1. Resolution estimation and final average.	168

List of Tables

3.1. Software packages for tilt series alignment.	40
4.1. Dataset.	68
4.2. Pre-processing parameters.	69
5.1. MATLAB wrappers in <i>Dynamo</i>	109
A.1. Information on data sets analysed in this study.	149
A.2. Computational time for FtsH data set	150

Bibliography

- Abeyrathne, Priyanka D., Marcel Arheit, Fabian Keibel, Daniel Castaño-Díez, Kenneth N. Goldie, Mohamed Chami, Henning Stahlberg, Ludovic Renault, and Werner Kühlbrandt (Dec. 2012). “1.15 Analysis of 2-D Crystals of Membrane Proteins by Electron Microscopy”. In: vol. 1, pp. 277–310 (cit. on p. 12).
- Alberts, Bruce, Alexander Johnson, Julian Lewis, David Morgan, Martin Raff, Peter Walter Keith Roberts, et al. (2018). “Molecular biology of the cell”. In: (cit. on p. 9).
- Amat, Fernando, Daniel Castaño-Díez, Albert Lawrence, Farshid Moussavi, Hanspeter Winkler, and Mark Horowitz (2010). “Alignment of cryo-electron tomography datasets”. In: *Methods in enzymology*. Vol. 482. Elsevier, pp. 343–367 (cit. on pp. 36, 37, 94).
- Amat, Fernando, Farshid Moussavi, Luis R. Comolli, Gal Elidan, Kenneth H. Downing, and Mark Horowitz (2008). “Markov random field based automatic image alignment for electron tomography”. In: *Journal of Structural Biology* 161.3, pp. 260–275 (cit. on p. 37).
- Al-Amoudi, Ashraf, Daniel Castaño-Díez, Matthew J. Betts, and Achilleas S. Frangakis (Dec. 2007). “The molecular architecture of cadherins in native epidermal desmosomes”. In: *Nature* 450, p. 832 (cit. on p. 31).
- Al-Amoudi, Ashraf, Jiin-Ju Chang, Amélie Leforestier, Alasdair McDowall, Laurée Michel Salamin, Lars PO Norlén, Karsten Richter, Nathalie Sartori Blanc, Daniel Studer, and Jacques Dubochet (Sept. 2004). “Cryo-electron microscopy of vitreous sections”. In: *The EMBO Journal* 23.18, p. 3583 (cit. on pp. 30, 31).
- Andersen, Anders H. and Avinash C. Kak (1984). “Simultaneous algebraic reconstruction technique (SART): a superior implementation of the ART algorithm”. In: *Ultrasonic imaging* 6.1, pp. 81–94 (cit. on p. 42).
- Appen, Alexander von, Jan Kosinski, Lenore Sparks, Alessandro Ori, Amanda L. DiGiulio, Benjamin Vollmer, Marie-Therese Mackmull, Niccolo Banterle, Luca Parca, Panagiotis Kastiris, Katarzyna Buczak, Shyamal Mosalaganti, Wim Hagen, Amparo Andres-Pons, Edward A Lemke, Peer Bork, Wolfram Antonin, Joseph S. Glavy, Khanh Huy Bui, and Martin Beck (Sept. 2015). “In situ structural analysis of the human nuclear pore complex”. In: *Nature* 526, p. 140 (cit. on p. 60).
- Arheit, Marcel, Daniel Castaño-Díez, Raphaël Thierry, Bryant R. Gipson, Xiangyan Zeng, and Henning Stahlberg (2013). “Image processing of 2D crystal images”. In: *Electron crystallography of Soluble and membrane proteins*. Springer, pp. 171–194 (cit. on p. 12).
- Arighi, Cecilia N, Lisa M Hartnell, Ruben C Aguilar, Carol R Haft, and Juan S Bonifacino (2004). “Role of the mammalian retromer in sorting of the cation-independent

- mannose 6-phosphate receptor". In: *The Journal of cell biology* 165.1, pp. 123–133 (cit. on p. 131).
- Asano, Shoh, Benjamin D. Engel, and Wolfgang Baumeister (2016). "In situ cryo-electron tomography: a post-reductionist approach to structural biology". In: *Journal of molecular biology* 428.2, pp. 332–343 (cit. on pp. 14, 91).
- Asano, Shoh, Yoshiyuki Fukuda, Florian Beck, Antje Aufderheide, Friedrich Förster, Radostin Danev, and Wolfgang Baumeister (Jan. 2015). "A molecular census of 26S proteasomes in intact neurons". In: *Science* 347.6220, p. 439 (cit. on p. 47).
- Bai, Xiao-chen, Israel S. Fernandez, Greg McMullan, and Sjors H. W. Scheres (Feb. 2013). "Ribosome structures to near-atomic resolution from thirty thousand cryo-EM particles". In: *eLife* 2. Ed. by Werner Kühlbrandt, e00461 (cit. on p. 35).
- Bartesaghi, Alberto, Federico Lecumberry, Guillermo Sapiro, and Sriram Subramaniam (2012). "Protein Secondary Structure Determination by Constrained Single-Particle Cryo-Electron Tomography". In: *Structure* 20.12, pp. 2003–2013 (cit. on p. 32).
- Bartesaghi, Alberto, P. Sprechmann, J Liu, G. Randall, G. Sapiro, and Sriram Subramaniam (2008). "Classification and 3D averaging with missing wedge correction in biological electron tomography". In: *Journal of structural biology* 162.3, pp. 436–450 (cit. on pp. 50, 55).
- Beck, Martin and Wolfgang Baumeister (2016). "Cryo-electron tomography: can it reveal the molecular sociology of cells in atomic detail?" In: *Trends in cell biology* 26.11, pp. 825–837 (cit. on p. 91).
- Bepler, Tristan, Alex J. Noble, and Bonnie Berger (2019). "Topaz-Denoise: general deep denoising models for cryoEM". In: *bioRxiv*, p. 838920 (cit. on p. 16).
- Bharat, Tanmay A. M., Danguole Kureisaite-Ciziene, Gail G. Hardy, Ellen W. Yu, Jessica M. Devant, Wim J. H. Hagen, Yves V. Brun, John A. G. Briggs, and Jan Löwe (Apr. 2017). "Structure of the hexagonal surface layer on *Caulobacter crescentus* cells". In: *Nature Microbiology* 2, p. 17059 (cit. on p. 28).
- Bharat, Tanmay A. M., Christopher J. Russo, Jan Löwe, Lori A. Passmore, and Sjors H. W. Scheres (2015). "Advances in single-particle electron cryomicroscopy structure determination applied to sub-tomogram averaging". In: *Structure* 23.9, pp. 1743–1753 (cit. on pp. 19, 32, 36, 46, 50, 59, 91).
- Bharat, Tanmay A. M. and Sjors H. W. Scheres (2016). "Resolving macromolecular structures from electron cryo-tomography data using subtomogram averaging in RELION". In: *Nature protocols* 11.11, pp. 2054–2065 (cit. on pp. 51, 65).
- Bouvette, Jonathan, Hsuan-Fu Liu, Xiaochen Du, Ye Zhou, Andrew P Sikkema, Juliana Da Fonseca Rezende E Mello, Bradley Klemm, Rick Huang, Roel M. Schaaper, Mario J. Borgnia, et al. (2020). "Beam image-shift accelerated data acquisition for near-atomic resolution single-particle cryo-electron tomography". In: *bioRxiv* (cit. on p. 145).
- Bracewell, R. N. (June 1956). "Strip Integration in Radio Astronomy". In: *Australian Journal of Physics* 9.2, pp. 198–217 (cit. on p. 41).
- Bracewell, Ronald N (1956). "Strip integration in radio astronomy". In: *Australian Journal of Physics* 9.2, pp. 198–217 (cit. on p. 12).

- Branden, Carl Ivar and John Tooze (2012). *Introduction to protein structure*. Garland Science (cit. on pp. 9, 10).
- Brandt, Sami, Jukka Heikkonen, and Peter Engelhardt (Jan. 2001). “Multiphase Method for Automatic Alignment of Transmission Electron Microscope Images Using Markers”. en. In: *Journal of Structural Biology* 133.1, pp. 10–22 (cit. on p. 37).
- Briggs, John A. G. (2013). “Structural biology in situ—the potential of subtomogram averaging”. In: *Current opinion in structural biology* 23.2, pp. 261–267 (cit. on pp. 14, 91, 92, 94).
- Brilot, Axel F., James Z. Chen, Anchi Cheng, Junhua Pan, Stephen C. Harrison, Clinton S. Potter, Bridget Carragher, Richard Henderson, and Nikolaus Grigorieff (2012). “Beam-induced motion of vitrified specimen on holey carbon film”. In: *Journal of Structural Biology* 177.3, pp. 630–637 (cit. on p. 35).
- Buijsse, Bart, Piet Trompenaars, Veli Altin, Radostin Danev, and Robert Glaeser (2020). “Spectral DQE of the Volta Phase Plate”. In: *bioRxiv* (cit. on pp. 11, 145).
- Burd, Christopher and Peter J. Cullen (2014). “Retromer: a master conductor of endosome sorting”. In: *Cold Spring Harbor perspectives in biology* 6.2, a016774 (cit. on p. 117).
- Cai, Shujun, Chen Chen, Zhi Yang Tan, Yinyi Huang, Jian Shi, and Lu Gan (Oct. 2018). “Cryo-ET reveals the macromolecular reorganization of *S. pombe* mitotic chromosomes in vivo”. In: *Proceedings of the National Academy of Sciences* 115.43, p. 10977 (cit. on p. 31).
- Castaño-Díez, Daniel (2017). “The Dynamo package for tomography and subtomogram averaging: components for MATLAB, GPU computing and EC2 Amazon Web Services”. In: *Acta Crystallographica Section D: Structural Biology* 73.6, pp. 478–487 (cit. on pp. 58, 91).
- Castaño-Díez, Daniel, Mikhail Kudryashev, Marcel Arheit, and Henning Stahlberg (2012). “Dynamo: a flexible, user-friendly development tool for subtomogram averaging of cryo-EM data in high-performance computing environments”. In: *Journal of structural biology* 178.2, pp. 139–151 (cit. on pp. 19, 21, 58, 60, 65, 91, 138).
- Castaño-Díez, Daniel, Mikhail Kudryashev, and Henning Stahlberg (2017). “Dynamo catalogue: geometrical tools and data management for particle picking in subtomogram averaging of cryo-electron tomograms”. In: *Journal of Structural Biology* 197.2, pp. 135–144 (cit. on pp. 19, 21, 58, 65, 138).
- Castaño-Díez, Daniel, Margot Scheffer, Ashraf Al-Amoudi, and Achilleas S. Frangakis (2010). “Alignator: a GPU powered software package for robust fiducial-less alignment of cryo tilt-series”. In: *Journal of structural biology* 170.1, pp. 117–126 (cit. on pp. 38, 112).
- Castaño-Díez, Daniel, Anja Seybert, and Achilleas S. Frangakis (2006). “Tilt-series and electron microscope alignment for the correction of the non-perpendicularity of beam and tilt-axis”. In: *Journal of structural biology* 154.2, pp. 195–205 (cit. on p. 93).
- Castaño-Díez, Daniel and Giulia Zanetti (2019). “In situ structure determination by subtomogram averaging”. In: *Current opinion in structural biology* 58, pp. 68–75 (cit. on pp. 18, 65).

- Ceccato, Laurie, Gaëtan Chicanne, Virginie Nahoum, Véronique Pons, Bernard Payras-tre, Frédérique Gaits-Iacovoni, and Julien Viaud (2016). “PLIF: A rapid, accurate method to detect and quantitatively assess protein-lipid interactions”. In: *Science signaling* 9.421, rs2–rs2 (cit. on p. 125).
- Cerofolini, Linda, Marco Fragai, Enrico Ravera, Christoph A. Diebolder, Ludovic Renault, and Vito Calderone (2019). “Integrative Approaches in Structural Biology: A More Complete Picture from the Combination of Individual Techniques”. In: *Biomolecules* 9.8, p. 370 (cit. on pp. 10, 11).
- Chandra, Mintu, Yanni K-Y Chin, Caroline Mas, J. Ryan Feathers, Blessy Paul, Sanchari Datta, Kai-En Chen, Xinying Jia, Zhe Yang, Suzanne J. Norwood, et al. (2019). “Classification of the human phox homology (PX) domains based on their phosphoinositide binding specificities”. In: *Nature communications* 10.1, pp. 1–14 (cit. on p. 125).
- Chandra, Mintu and Brett M. Collins (2018). “The Phox homology (PX) domain”. In: *Protein Reviews–Purinergic Receptors*, pp. 1–17 (cit. on p. 116).
- Chen, Kai-En, Michael D Healy, and Brett M Collins (2019). “Towards a molecular understanding of endosomal trafficking by Retromer and Retriever”. In: *Traffic* 20.7, pp. 465–478 (cit. on p. 116).
- Chen, Muyuan, James M. Bell, Xiaodong Shi, Stella Y. Sun, Zhao Wang, and Steven J. Ludtke (2019). “A complete data processing workflow for cryo-ET and subtomogram averaging”. In: *Nature methods*, pp. 1–8 (cit. on pp. 16, 65, 112, 145).
- Chen, Muyuan, Wei Dai, Stella Y. Sun, Darius Jonasch, Cynthia Y. He, Michael F. Schmid, Wah Chiu, and Steven J. Ludtke (2017). “Convolutional neural networks for automated annotation of cellular cryo-electron tomograms”. In: *Nature methods* 14.10, p. 983 (cit. on pp. 15, 48, 145).
- Chen, Shaoxia, Greg McMullan, Abdul R. Faruqi, Garib N. Murshudov, Judith M. Short, Sjors H. W. Scheres, and Richard Henderson (2013). “High-resolution noise substitution to measure overfitting and validate resolution in 3D structure determination by single particle electron cryomicroscopy”. In: *Ultramicroscopy* 135, pp. 24–35 (cit. on p. 52).
- Chen, Yuxiang and Friedrich Förster (2014). “Iterative reconstruction of cryo-electron tomograms using nonuniform fast Fourier transforms”. In: *Journal of Structural Biology* 185.3, pp. 309–316 (cit. on p. 42).
- Chen, Yuxiang, Stefan Pfeffer, José Jesús Fernández, Carlos Oscar S. Sorzano, and Friedrich Förster (Oct. 2014). “Autofocused 3D Classification of Cryoelectron Subtomograms”. en. In: *Structure* 22.10, pp. 1528–1537 (cit. on p. 55).
- Chen, Yuxiang, Stefan Pfeffer, Thomas Hrabe, Jan Michael Schuller, and Friedrich Förster (2013). “Fast and accurate reference-free alignment of subtomograms”. In: *Journal of structural biology* 182.3, pp. 235–245 (cit. on pp. 50, 58, 65).
- Cheng, Yifan, Robert M. Glaeser, and Eva Nogales (2017). “How cryo-EM became so hot”. In: *Cell* 171.6, pp. 1229–1231 (cit. on p. 12).
- Cheng, Yifan, Nikolaus Grigorieff, Pawel A. Penczek, and Thomas Walz (2015). “A primer to single-particle cryo-electron microscopy”. In: *Cell* 161.3, pp. 438–449 (cit. on p. 13).

- Chin, Lih-Shen, Mathew C Raynor, Xiaolong Wei, Hui-Qi Chen, and Lian Li (2001). “Hrs interacts with sorting nexin 1 and regulates degradation of epidermal growth factor receptor”. In: *Journal of Biological Chemistry* 276.10, pp. 7069–7078 (cit. on p. 120).
- Chreifi, Georges, Songye Chen, Lauren Ann Metskas, Mohammed Kaplan, and Grant J. Jensen (2019). “Rapid tilt-series acquisition for electron cryotomography”. In: *Journal of structural biology* 205.2, pp. 163–169 (cit. on pp. 16, 60, 92, 145).
- Clairfeuille, Thomas, Caroline Mas, Audrey SM Chan, Zhe Yang, Maria Tello-Lafoz, Mintu Chandra, Jocelyn Widagdo, Markus C. Kerr, Blessy Paul, Isabel Mérida, et al. (2016). “A molecular code for endosomal recycling of phosphorylated cargos by the SNX27–retromer complex”. In: *Nature structural & molecular biology* 23.10, p. 921 (cit. on p. 117).
- Cozier, Gyles E., Jez Carlton, Alex H. McGregor, Paul A. Gleeson, Rohan D. Teasdale, Harry Mellor, and Peter J. Cullen (2002). “The phox homology (PX) domain-dependent, 3-phosphoinositide-mediated association of sorting nexin-1 with an early sorting endosomal compartment is required for its ability to regulate epidermal growth factor receptor degradation”. In: *Journal of Biological Chemistry* 277.50, pp. 48730–48736 (cit. on p. 125).
- Cullen, Peter J. and Florian Steinberg (2018). “To degrade or not to degrade: mechanisms and significance of endocytic recycling”. In: *Nature reviews Molecular cell biology* 19.11, pp. 679–696 (cit. on p. 116).
- Cyrklaff, Marek, Friedrich Frischknecht, and Mikhail Kudryashev (Aug. 2017). “Functional insights into pathogen biology from 3D electron microscopy”. In: *FEMS Microbiology Reviews* 41.6, pp. 828–853 (cit. on p. 28).
- Dahl, Rolf and L. Andrew Staehelin (1989). “High-pressure freezing for the preservation of biological structure: Theory and practice”. In: *Journal of Electron Microscopy Technique* 13.3, pp. 165–174 (cit. on p. 31).
- Dandey, Venkata P, William C Budell, Hui Wei, Daija Bobe, Kashyap Maruthi, Mykhailo Kopylov, Edward T Eng, Peter A Kahn, Jenny E Hinshaw, Nidhi Kundu, et al. (2020). “Time-resolved cryo-EM using Spotiton”. In: *Nature Methods* 17.9, pp. 897–900 (cit. on p. 146).
- Danev, Radostin, Bart Buijsse, Maryam Khoshouei, Jürgen M. Plitzko, and Wolfgang Baumeister (Nov. 2014). “Volta potential phase plate for in-focus phase contrast transmission electron microscopy”. In: *Proceedings of the National Academy of Sciences* 111.44, p. 15635 (cit. on p. 47).
- Danev, Radostin, Haruaki Yanagisawa, and Masahide Kikkawa (2019). “Cryo-electron microscopy methodology: current aspects and future directions”. In: *Trends in biochemical sciences* 44.10, pp. 837–848 (cit. on pp. 18, 65).
- Davies, Karen M., Mike Strauss, Bertram Daum, Jan H. Kief, Heinz D. Osiewacz, Adriana Rycovska, Volker Zickermann, and Werner Kühlbrandt (2011). “Macromolecular organization of ATP synthase and complex I in whole mitochondria”. In: *Proceedings of the National Academy of Sciences* 108.34, pp. 14121–14126 (cit. on p. 30).
- De la Rosa-Trevín, JM, A Quintana, L Del Cano, A Zaldivar, I Foche, J Gutierrez, J Gomez-Blanco, J Burguet-Castell, J Cuenca-Alba, V Abrishami, et al. (2016).

- “Scipion: A software framework toward integration, reproducibility and validation in 3D electron microscopy”. In: *Journal of structural biology* 195.1, pp. 93–99 (cit. on p. 145).
- De Rosier, D. J. and A. Klug (Jan. 1968). “Reconstruction of Three Dimensional Structures from Electron Micrographs”. In: *Nature* 217.5124, pp. 130–134 (cit. on p. 41).
- Deng, Yuchen, Yu Chen, Yan Zhang, Shengliu Wang, Fa Zhang, and Fei Sun (2016). “ICON: 3D reconstruction with ‘missing-information’ restoration in biological electron tomography”. In: *Journal of Structural Biology* 195.1, pp. 100–112 (cit. on p. 42).
- Diebold, Christoph A., Abraham J. Koster, and Roman I. Koning (2012). “Pushing the resolution limits in cryo electron tomography of biological structures”. In: *Journal of microscopy* 248.1, pp. 1–5 (cit. on p. 91).
- Dobro, Megan J., Linda A. Melanson, Grant J. Jensen, and Alasdair W. McDowell (2010). “Plunge freezing for electron cryomicroscopy”. In: *Methods in enzymology*. Vol. 481. Elsevier, pp. 63–82 (cit. on p. 12).
- Dubochet, Jacques, Marc Adrian, Jiin-Ju Chang, Jean-Claude Homo, Jean Lepault, Alasdair W. McDowell, and Patrick Schultz (1988). “Cryo-electron microscopy of vitrified specimens”. In: *Quarterly Reviews of Biophysics* 21.2, pp. 129–228 (cit. on p. 30).
- Dubochet, Jacques and Alasdair W. McDowell (1981). “Vitrification of pure water for electron microscopy”. In: *Journal of Microscopy* 124.3, pp. 3–4 (cit. on p. 30).
- Eibauer, Matthias, Christian Hoffmann, Jürgen M. Plitzko, Wolfgang Baumeister, Stephan Nickell, and Harald Engelhardt (2012). “Unraveling the structure of membrane proteins in situ by transfer function corrected cryo-electron tomography”. In: *Journal of Structural Biology* 180.3, pp. 488–496 (cit. on p. 45).
- Erickson, H. P. and Aaron Klug (1971). “Measurement and compensation of defocusing and aberrations by Fourier processing of electron micrographs”. In: *Philosophical Transactions of the Royal Society of London. B, Biological Sciences* 261.837, pp. 105–118 (cit. on p. 42).
- Faini, Marco, Rainer Beck, Felix T. Wieland, and John AG Briggs (2013). “Vesicle coats: structure, function, and general principles of assembly”. In: *Trends in cell biology* 23.6, pp. 279–288 (cit. on p. 116).
- Fernández, Jose-Jesus (2012). “Computational methods for electron tomography”. In: *Micron* 43.10, pp. 1010–1030 (cit. on p. 15).
- Fernández, Jose-Jesus, S. Li, and R. A. Crowther (2006). “CTF determination and correction in electron cryotomography”. In: *Ultramicroscopy* 106.7, pp. 587–596 (cit. on pp. 44, 45).
- Fernández, Jose-Jesus, Sam Li, and David A. Agard (2019). “Consideration of sample motion in cryo-tomography based on alignment residual interpolation”. In: *Journal of structural biology* 205.3, pp. 1–6 (cit. on pp. 16, 33, 34, 37, 38, 68, 112).
- Fernández, Jose-Jesus, Sam Li, Tanmay A. M. Bharat, and David A. Agard (2018). “Cryo-tomography tilt-series alignment with consideration of the beam-induced sample motion”. In: *Journal of structural biology* 202.3, pp. 200–209 (cit. on pp. 37, 112).
- Förster, Friedrich, Bong-Gyoon Han, and Martin Beck (2010). “Chapter Eleven - Visual Proteomics”. In: *Cryo-EM, Part C: Analyses, Interpretation, and Case studies*. Ed.

- by Grant J. Jensen. Vol. 483. *Methods in Enzymology*. Academic Press, pp. 215–243 (cit. on p. 48).
- Förster, Friedrich, Ohad Medalia, Nathan Zauberman, Wolfgang Baumeister, and Deborah Fass (2005). “Retrovirus envelope protein complex structure in situ studied by cryo-electron tomography”. In: *Proceedings of the National Academy of Sciences* 102.13, pp. 4729–4734 (cit. on pp. 58, 65).
- Förster, Friedrich, Sabine Pruggnaller, Anja Seybert, and Achilleas S. Frangakis (2008). “Classification of cryo-electron sub-tomograms using constrained correlation”. In: *Journal of Structural Biology* 161.3, pp. 276–286 (cit. on p. 54).
- Frank, Joachim (2006). *Three-dimensional electron microscopy of macromolecular assemblies: visualization of biological molecules in their native state*. Oxford University Press (cit. on pp. 11, 13).
- (2013). *Electron tomography: three-dimensional imaging with the transmission electron microscope*. Springer Science & Business Media (cit. on pp. 14, 18, 65).
- (2017). “Time-resolved cryo-electron microscopy: Recent progress”. In: *Journal of structural biology* 200.3, pp. 303–306 (cit. on p. 146).
- Frazier, Zachary, Min Xu, and Frank Alber (2017). “TomoMiner and TomoMinerCloud: A Software Platform for Large-Scale Subtomogram Structural Analysis”. In: *Structure* 25.6, 951–961.e2 (cit. on p. 50).
- Galaz-Montoya, Jesús G, Corey W Hecksel, Philip R Baldwin, Eryu Wang, Scott C Weaver, Michael F Schmid, Steven J Ludtke, and Wah Chiu (2016). “Alignment algorithms and per-particle CTF correction for single particle cryo-electron tomography”. In: *Journal of structural biology* 194.3, pp. 383–394 (cit. on p. 18).
- Galaz-Montoya, Jesus G. and Steven J. Ludtke (2017). “The advent of structural biology in situ by single particle cryo-electron tomography”. In: *Biophysics reports* 3.1-3, pp. 17–35 (cit. on p. 18).
- Galaz-Montoya, Jesús G., John Flanagan, Michael F. Schmid, and Steven J. Ludtke (2015). “Single particle tomography in EMAN2”. In: *Journal of structural biology* 190.3, pp. 279–290 (cit. on pp. 19, 46, 59, 91).
- Galaz-Montoya, Jesús G. and Steven J. Ludtke (June 2017). “The advent of structural biology in situ by single particle cryo-electron tomography”. en. In: *Biophysics Reports* 3.1-3, pp. 17–35 (cit. on p. 59).
- Gallon, Matthew, Thomas Clairfeuille, Florian Steinberg, Caroline Mas, Rajesh Ghai, Richard B. Sessions, Rohan D. Teasdale, Brett M. Collins, and Peter J. Cullen (2014). “A unique PDZ domain and arrestin-like fold interaction reveals mechanistic details of endocytic recycling by SNX27-retromer”. In: *Proceedings of the National Academy of Sciences* 111.35, E3604–E3613 (cit. on p. 117).
- Gan, Lu and Grant J. Jensen (2012). “Electron tomography of cells”. In: *Quarterly reviews of biophysics* 45.1, pp. 27–56 (cit. on p. 91).
- Gemmi, Mauro, Enrico Mugnaioli, Tatiana E Gorelik, Ute Kolb, Lukas Palatinus, Philippe Boullay, Sven Hovmöller, and Jan Pieter Abrahams (2019). “3D electron diffraction: the nanocrystallography revolution”. In: *ACS central science* 5.8, pp. 1315–1329 (cit. on p. 12).

- Gilbert, Peter (1972). “Iterative methods for the three-dimensional reconstruction of an object from projections”. In: *Journal of Theoretical Biology* 36.1, pp. 105–117 (cit. on p. 41).
- Glaeser, Robert M. (2016). “Chapter Two - Specimen Behavior in the Electron Beam”. In: *The Resolution Revolution: Recent Advances In cryoEM*. Ed. by Anthony R Crowther. Vol. 579. Methods in Enzymology. Academic Press, pp. 19–50 (cit. on p. 35).
- (Mar. 2018). “Proteins, interfaces, and cryo-EM grids”. en. In: *Current Opinion in Colloid & Interface Science* 34, pp. 1–8 (cit. on p. 30).
- Glaeser, Robert M. and Bong-Gyoon Han (June 2017). “Opinion: hazards faced by macromolecules when confined to thin aqueous films”. en. In: *Biophysics Reports* 3.1-3, pp. 1–7 (cit. on p. 30).
- Gordon, Richard, Robert Bender, and Gabor T. Herman (1970). “Algebraic Reconstruction Techniques (ART) for three-dimensional electron microscopy and X-ray photography”. In: *Journal of Theoretical Biology* 29.3, pp. 471–481 (cit. on p. 41).
- Gorelick, Sergey, Genevieve Buckley, Gediminas Gervinskas, Travis K. Johnson, Ava Handley, Monica Pia Caggiano, James C. Whisstock, Roger Pocock, and Alex de Marco (2019). “PIE-scope, integrated cryo-correlative light and FIB/SEM microscopy”. In: *Elife* 8, e45919 (cit. on pp. 16, 145).
- Grange, Michael, Daven Vasishtan, and Kay Grunewald (2017). “Cellular electron cryo tomography and in situ sub-volume averaging reveal the context of microtubule-based processes”. In: *Journal of Structural Biology* 197.2, pp. 181–190 (cit. on p. 48).
- Grant, Timothy and Nikolaus Grigorieff (2015a). “Automatic estimation and correction of anisotropic magnification distortion in electron microscopes”. In: *Journal of Structural Biology* 192.2, pp. 204–208 (cit. on p. 32).
- (2015b). “Measuring the optimal exposure for single particle cryo-EM using a 2.6 Å reconstruction of rotavirus VP6”. In: *elife* 4, e06980 (cit. on pp. 16, 32, 35, 36, 69, 135).
- Grimm, Rudo, Hapreet Singh, Reinhard Rachel, Dieter Typke, Wolfram Zillig, and Wolfgang Baumeister (1998). “Electron Tomography of Ice-Embedded Prokaryotic Cells”. In: *Biophysical Journal* 74.2, pp. 1031–1042 (cit. on p. 32).
- Haft, Carol Renfrew, Maria de la Luz Sierra, Richard Bafford, Maxine A. Lesniak, Valarie A. Barr, and Simeon I. Taylor (2000). “Human orthologs of yeast vacuolar protein sorting proteins Vps26, 29, and 35: assembly into multimeric complexes”. In: *Molecular biology of the cell* 11.12, pp. 4105–4116 (cit. on p. 117).
- Hagen, Wim J. H., William Wan, and John A. G. Briggs (2017). “Implementation of a cryo-electron tomography tilt-scheme optimized for high resolution subtomogram averaging”. In: *Journal of structural biology* 197.2, pp. 191–198 (cit. on pp. 14, 92, 135).
- Han, Renmin, Xiaohua Wan, Zihao Wang, Yu Hao, Jingrong Zhang, Yu Chen, Xin Gao, Zhiyong Liu, Fei Ren, Fei Sun, et al. (2017). “Autom: a novel automatic platform for electron tomography reconstruction”. In: *Journal of structural biology* 199.3, pp. 196–208 (cit. on pp. 92, 112).

- Harauz, George and Marin van Heel (1986). “Exact filters for general geometry three dimensional reconstruction”. In: *Optik (Stuttgart)* 73.4, pp. 146–156 (cit. on pp. 19, 41).
- Harrison, Megan S., Chia-Sui Hung, Ting-ting Liu, Romain Christiano, Tobias C. Walther, and Christopher G. Burd (2014). “A mechanism for retromer endosomal coat complex assembly with cargo”. In: *Proceedings of the National Academy of Sciences* 111.1, pp. 267–272 (cit. on pp. 117, 126).
- Harterink, Martin, Phillip Port, Magdalena J. Lorenowicz, Ian J. McGough, Marie Silhankova, Marco C. Betist, Jan R. T. Van Weering, Roy G. H. P. Van Heesbeen, Teije C. Middelkoop, Konrad Basler, et al. (2011). “A SNX3-dependent retromer pathway mediates retrograde transport of the Wnt sorting receptor Wntless and is required for Wnt secretion”. In: *Nature cell biology* 13.8, pp. 914–923 (cit. on p. 117).
- Heel, Marin van, Rodrigo Portugal, A. Rohou, C. Linnemayr, C. Bebeacua, R. Schmidt, T. Grant, and M. Schatz (2006). “Four-dimensional cryo-electron microscopy at quasi-atomic resolution: IMAGIC 4D”. In: *International tables for crystallography*, pp. 624–628 (cit. on p. 13).
- Heel, Marin van, Rodrigo V Portugal, Michael Schatz, et al. (2016). “Multivariate statistical analysis of large datasets: single particle electron microscopy”. In: *Open Journal of Statistics* 6.04, p. 701 (cit. on p. 96).
- Heel, Marin van and Michael Schatz (2005). “Fourier shell correlation threshold criteria”. In: *Journal of Structural Biology* 151.3, pp. 250–262 (cit. on p. 52).
- Henderson, Louie D. and Morgan Beeby (2018). “High-Throughput Electron Cryo-tomography of Protein Complexes and Their Assembly”. In: *Protein Complex Assembly: Methods and Protocols*. Ed. by Joseph A Marsh. New York, NY: Springer New York, pp. 29–44 (cit. on p. 34).
- Heumann, John M., Andreas Hoenger, and David N. Mastronarde (2011). “Clustering and variance maps for cryo-electron tomography using wedge-masked differences”. In: *Journal of structural biology* 175.3, pp. 288–299 (cit. on pp. 19, 58, 60, 65, 91).
- Heymann, J. Bernard and David M. Belnap (2007). “Bsoft: image processing and molecular modeling for electron microscopy”. In: *Journal of structural biology* 157.1, pp. 3–18 (cit. on p. 68).
- Himes, Benjamin A. and Peijun Zhang (2018). “emClarity: software for high-resolution cryo-electron tomography and subtomogram averaging”. In: *Nature methods* 15.11, pp. 955–961 (cit. on pp. 16, 19, 46, 55, 59, 60, 65, 66, 91, 92, 112).
- Horazdovsky, Bruce F., Brian A. Davies, M. N. Seaman, Steven A McLaughlin, S.-H. Yoon, and Scott D. Emr (1997). “A sorting nexin-1 homologue, Vps5p, forms a complex with Vps17p and is required for recycling the vacuolar protein-sorting receptor.” In: *Molecular biology of the cell* 8.8, pp. 1529–1541 (cit. on pp. 116, 117).
- Hrabe, Thomas (2015). “Localize. pytom: a modern webserver for cryo-electron tomography”. In: *Nucleic Acids Research* 43.W1, W231–W236 (cit. on pp. 58, 65).
- Hrabe, Thomas, Yuxiang Chen, Stefan Pfeffer, Luis Kuhn Cuellar, Ann-Victoria Mangold, and Friedrich Förster (2012). “PyTom: a python-based toolbox for localization of macromolecules in cryo-electron tomograms and subtomogram analysis”. In: *Journal of structural biology* 178.2, pp. 177–188 (cit. on pp. 19, 91).

- Huiskonen, Juha T., Marie-Laure Parsy, Sai Li, David Bitto, Max Renner, and Thomas A. Bowden (2014). “Averaging of viral envelope glycoprotein spikes from electron cryotomography reconstructions using Jsubtomo”. In: *JoVE (Journal of Visualized Experiments)* 92, e51714 (cit. on pp. 19, 91).
- Hurt, Ed and Martin Beck (2015). “Towards understanding nuclear pore complex architecture and dynamics in the age of integrative structural analysis”. In: *Current opinion in cell biology* 34, pp. 31–38 (cit. on p. 17).
- Hutchings, Joshua, Viktoriya Stancheva, Elizabeth A. Miller, and Giulia Zanetti (2018). “Subtomogram averaging of COPII assemblies reveals how coat organization dictates membrane shape”. In: *Nature communications* 9.1, pp. 1–8 (cit. on pp. 17, 22, 29, 37, 40, 48, 51, 58, 91, 92, 136).
- Jensen, Grant J. and Roger D. Kornberg (2000). “Defocus-gradient corrected back-projection”. In: *Ultramicroscopy* 84.1, pp. 57–64 (cit. on p. 46).
- Kazantsev, Ivan G., Joanna Klukowska, Gabor T. Herman, and Laslo Cernetec (2010). “Fully three-dimensional defocus-gradient corrected backprojection in cryoelectron microscopy”. In: *Ultramicroscopy* 110.9, pp. 1128–1142 (cit. on p. 46).
- Khoshouei, Maryam, Stefan Pfeffer, Wolfgang Baumeister, Friedrich Förster, and Radoslin Danev (2017). “Subtomogram analysis using the Volta phase plate”. In: *Journal of structural biology* 197.2, pp. 94–101 (cit. on pp. 47, 91).
- Koharudin, Leonardus MI, William Furey, Hao Liu, Yong-Jian Liu, and Angela M. Gronenborn (2009). “The phox domain of sorting nexin 5 lacks phosphatidylinositol 3-phosphate (PtdIns (3) P) specificity and preferentially binds to phosphatidylinositol 4, 5-bisphosphate (PtdIns (4, 5) P2)”. In: *Journal of Biological Chemistry* 284.35, pp. 23697–23707 (cit. on p. 125).
- Kontziampasis, Dimitrios, David P Klebl, Matthew G Iadanza, Charlotte A Scarff, Florian Kopf, Frank Sobott, Diana CF Monteiro, Martin Trebbin, Stephen P Muench, and Howard D White (2019). “A cryo-EM grid preparation device for time-resolved structural studies”. In: *IUCrJ* 6.6 (cit. on p. 146).
- Kosinski, Jan, Shyamal Mosalaganti, Alexander von Appen, Roman Teimer, Amanda L DiGuilio, William Wan, Khanh Huy Bui, Wim J. H. Hagen, John A. G. Briggs, Joseph S. Glavy, Ed Hurt, and Martin Beck (Apr. 2016). “Molecular architecture of the inner ring scaffold of the human nuclear pore complex”. In: *Science* 352.6283, p. 363 (cit. on p. 30).
- Koumandou, V. Lila, Mary J. Klute, Emily K. Herman, Ricardo Nunez-Miguel, Joel B. Dacks, and Mark C. Field (2011). “Evolutionary reconstruction of the retromer complex and its function in *Trypanosoma brucei*”. In: *Journal of cell science* 124.9, pp. 1496–1509 (cit. on p. 117).
- Kovtun, Oleksiy, Natalya Leneva, Yury S. Bykov, Nicholas Ariotti, Rohan D. Teasdale, Miroslava Schaffer, Benjamin D. Engel, David J. Owen, John A. G. Briggs, and Brett M. Collins (2018). “Structure of the membrane-assembled retromer coat determined by cryo-electron tomography”. In: *Nature* 561.7724, pp. 561–564 (cit. on pp. 17, 22, 29, 37, 48, 58, 91, 92, 117, 128, 131).

- Kremer, James R., David N. Mastronarde, and J. Richard McIntosh (1996). “Computer Visualization of Three-Dimensional Image Data Using IMOD”. In: *Journal of Structural Biology* 116.1, pp. 71–76 (cit. on pp. 39, 135).
- Kudryashev, Mikhail (2018). “Resolution in electron tomography”. In: *Cellular Imaging: Electron Tomography and Related Techniques*. Ed. by Eric Hanssen. Springer International Publishing, pp. 261–282 (cit. on pp. 35, 43).
- Kudryashev, Mikhail, Daniel Castaño-Díez, Cédric Deluz, Gherici Hassaine, Luigino Grasso, Alexandra Graf-Meyer, Horst Vogel, and Henning Stahlberg (2016). “The structure of the mouse serotonin 5-HT₃ receptor in lipid vesicles”. In: *Structure* 24.1, pp. 165–170 (cit. on pp. 22, 48, 58).
- Kudryashev, Mikhail, Daniel Castaño-Díez, and Henning Stahlberg (2012). “Limiting factors in single particle cryo electron tomography”. In: *Computational and structural biotechnology journal* 1.2, e201207002 (cit. on p. 43).
- Kudryashev, Mikhail, Marco Stenta, Stefan Schmelz, Marlise Amstutz, Ulrich Wiesand, Daniel Castaño-Díez, Matteo T. Degiacomi, Stefan Münnich, Christopher K.E. Bleck, Julia Kowal, Andreas Diepold, Dirk W. Heinz, Matteo Dal Peraro, Guy R. Cornelis, and Henning Stahlberg (July 2013). “In situ structural analysis of the *Yersinia enterocolitica* injectisome”. In: *eLife* 2. Ed. by Volker Dötsch, e00792 (cit. on pp. 30, 56, 57).
- Kühlbrandt, Werner (Aug. 2014a). “Cryo-EM enters a new era”. In: *eLife* 3, e03678 (cit. on p. 11).
- (2014b). “The resolution revolution”. In: *Science* 343.6178, pp. 1443–1444 (cit. on p. 11).
- Kunz, Michael and Achilleas S. Frangakis (2014). “Super-sampling SART with ordered subsets”. In: *Journal of Structural Biology* 188.2, pp. 107–115 (cit. on p. 42).
- (2017). “Three-dimensional CTF correction improves the resolution of electron tomograms”. In: *Journal of Structural Biology* 197.2, pp. 114–122 (cit. on p. 46).
- Kurten, Richard C., Anthony D. Eddington, Parag Chowdhury, Richard D. Smith, April D. Davidson, and Brian B. Shank (2001). “Self-assembly and binding of a sorting nexin to sorting endosomes”. In: *Journal of Cell Science* 114.9, pp. 1743–1756 (cit. on p. 120).
- Kvainickas, Arunas, Ana Jimenez-Orgaz, Heike Nägele, Zehan Hu, Jörn Dengjel, and Florian Steinberg (2017). “Cargo-selective SNX-BAR proteins mediate retromer trimer independent retrograde transport”. In: *Journal of Cell Biology* 216.11, pp. 3677–3693 (cit. on p. 117).
- Lawrence, Michael C. (1992). “Least-squares method of alignment using markers”. In: *Electron tomography*. Springer, pp. 197–204 (cit. on pp. 36, 94).
- Leigh, Kendra E., Paula P. Navarro, Stefano Scaramuzza, Wenbo Chen, Yingyi Zhang, Daniel Castaño-Díez, and Misha Kudryashev (2019). “Subtomogram averaging from cryo-electron tomograms”. In: *Methods in Cell Biology*. Vol. 152. Elsevier, pp. 217–259 (cit. on p. 18).
- Li, Xueming, Paul Mooney, Shawn Zheng, Christopher R. Booth, Michael B. Braunfeld, Sander Gubbens, David A. Agard, and Yifan Cheng (May 2013). “Electron counting

- and beam-induced motion correction enable near-atomic-resolution single-particle cryo-EM". In: *Nature Methods* 10, p. 584 (cit. on pp. 35, 36).
- Liu, Hao, Zu-Qiang Liu, Carol X-Q Chen, Stephen Magill, Yu Jiang, and Yong-Jian Liu (2006). "Inhibitory regulation of EGF receptor degradation by sorting nexin 5". In: *Biochemical and biophysical research communications* 342.2, pp. 537–546 (cit. on p. 125).
- Lucas, María, David C. Gershlick, Ander Vidaurrazaga, Adriana L. Rojas, Juan S. Bonifacio, and Aitor Hierro (2016). "Structural mechanism for cargo recognition by the retromer complex". In: *Cell* 167.6, pp. 1623–1635 (cit. on p. 117).
- Lučić, Vladan, Alexander Rigort, and Wolfgang Baumeister (2013). "Cryo-electron tomography: the challenge of doing structural biology in situ". In: *Journal of Cell Biology* 202.3, pp. 407–419 (cit. on p. 91).
- Lyumkis, Dmitry, Axel F. Brilot, Douglas L. Theobald, and Nikolaus Grigorieff (2013). "Likelihood-based classification of cryo-EM images using FREALIGN". In: *Journal of structural biology* 183.3, pp. 377–388 (cit. on p. 13).
- Mahamid, Julia, Ruud Schampers, Hans Persoon, Anthony A. Hyman, Wolfgang Baumeister, and Jürgen M Plitzko (Nov. 2015). "A focused ion beam milling and lift-out approach for site-specific preparation of frozen-hydrated lamellas from multicellular organisms". en. In: *Journal of Structural Biology* 192.2, pp. 262–269 (cit. on p. 31).
- Marko, Michael, Chyongere Hsieh, Richard Schalek, Joachim Frank, and Carmen Mannella (Feb. 2007). "Focused-ion-beam thinning of frozen-hydrated biological specimens for cryo-electron microscopy". In: *Nature Methods* 4, p. 215 (cit. on p. 31).
- Mastronarde, David N. (2005). "Automated electron microscope tomography using robust prediction of specimen movements". In: *Journal of structural biology* 152.1, pp. 36–51 (cit. on pp. 92, 135).
- (2008). "Correction for non-perpendicularity of beam and tilt axis in tomographic reconstructions with the IMOD package". In: *Journal of microscopy* 230.2, pp. 212–217 (cit. on pp. 93, 94).
- Mastronarde, David N. and Susannah R. Held (2017). "Automated tilt series alignment and tomographic reconstruction in IMOD". In: *Journal of structural biology* 197.2, pp. 102–113 (cit. on pp. 21, 37, 67, 91, 92, 94, 96, 112).
- Matias, Valério R. F., Ashraf Al-Amoudi, Jacques Dubochet, and Terry J. Beveridge (2003). "Cryo-Transmission Electron Microscopy of Frozen-Hydrated Sections of *Escherichia coli* and *Pseudomonas aeruginosa*". In: *Journal of Bacteriology* 185.20, pp. 6112–6118 (cit. on p. 31).
- McMullan, G., S. Chen, R. Henderson, and A. R. Faruqi (2009). "Detective quantum efficiency of electron area detectors in electron microscopy". In: *Ultramicroscopy* 109.9, pp. 1126–1143 (cit. on p. 32).
- McNally, Kerrie E and Peter J Cullen (2018). "Endosomal retrieval of cargo: retromer is not alone". In: *Trends in cell biology* 28.10, pp. 807–822 (cit. on p. 116).
- Merino-Trigo, Ana, Markus C. Kerr, Fiona Houghton, Anna Lindberg, Christina Mitchell, Rohan D. Teasdale, and Paul A. Gleeson (2004). "Sorting nexin 5 is localized to a subdomain of the early endosomes and is recruited to the plasma membrane fol-

- lowing EGF stimulation”. In: *Journal of cell science* 117.26, pp. 6413–6424 (cit. on p. 125).
- Moor, Hans (1987). “Theory and Practice of High Pressure Freezing”. en. In: *Cryotechniques in Biological Electron Microscopy*. Ed. by Rudolf Alexander Steinbrecht and Karl Zierold. Berlin, Heidelberg: Springer Berlin Heidelberg, pp. 175–191 (cit. on p. 31).
- Morado, Dustin R., Bo Hu, and Jun Liu (2016). “Using Tomoauto: a protocol for high-throughput automated cryo-electron tomography”. In: *JoVE (Journal of Visualized Experiments)* 107, e53608 (cit. on p. 34).
- Muller-Reichert, Thomas and Gaia Pigino (2019). *Three-dimensional Electron Microscopy*. Academic Press (cit. on p. 25).
- Nakane, Takanori, Dari Kimanius, Erik Lindahl, and Sjors H. W. Scheres (June 2018). “Characterisation of molecular motions in cryo-EM single-particle data by multi-body refinement in RELION”. In: *eLife* 7. Ed. by Axel T Brunger, e36861 (cit. on p. 57).
- Nakane, Takanori, Abhay Kotecha, Andrija Sente, Greg McMullan, Simonas Masiulis, Patricia MGE Brown, Ioana T Grigoras, Lina Malinauskaite, Tomas Malinauskas, Jonas Miehling, et al. (2020). “Single-particle cryo-EM at atomic resolution”. In: *BioRxiv* (cit. on p. 145).
- Nans, Andrea, Mikhail Kudryashev, Helen R. Saibil, and Richard D. Hayward (Dec. 2015). “Structure of a bacterial type III secretion system in contact with a host membrane in situ”. In: *Nature Communications* 6, p. 10114 (cit. on pp. 30, 60).
- Navarro, Paula P., Henning Stahlberg, and Daniel Castaño-Díez (2018). “Protocols for subtomogram averaging of membrane proteins in the Dynamo software package”. In: *Frontiers in molecular biosciences* 5, p. 82 (cit. on pp. 58, 65).
- Naydenova, K., G. McMullan, M. J. Peet, Y. Lee, P. C. Edwards, S. Chen, E. Leahy, S. Scotcher, R. Henderson, and C. J. Russo (2019). “CryoEM at 100 keV: a demonstration and prospects”. In: *IUCrJ* 6.6 (cit. on p. 145).
- Nguyen, Thi Hoang Duong, Wojciech P. Galej, Xiao-chen Bai, Chris Oubridge, Andrew J. Newman, Sjors H. W. Scheres, and Kiyoshi Nagai (Feb. 2016). “Cryo-EM structure of the yeast U4/U6.U5 tri-snRNP at 3.7 Å resolution”. In: *Nature* 530, p. 298 (cit. on p. 57).
- Nicastro, Daniela, Cindi Schwartz, Jason Pierson, Richard Gaudette, Mary E. Porter, and J. Richard McIntosh (2006). “The molecular architecture of axonemes revealed by cryoelectron tomography”. In: *Science* 313.5789, pp. 944–948 (cit. on pp. 58, 60, 65).
- Nickell, Stephan, Friedrich Förster, Alexandros Linaroudis, William Del Net, Florian Beck, Reiner Hegerl, Wolfgang Baumeister, and Jürgen M. Plitzko (2005). “TOM software toolbox: acquisition and analysis for electron tomography”. In: *Journal of structural biology* 149.3, pp. 227–234 (cit. on pp. 58, 65, 92).
- Nisar, Shaista, Eamonn Kelly, Pete J. Cullen, and Stuart J. Mundell (2010). “Regulation of P2Y1 receptor traffic by sorting Nexin 1 is retromer independent”. In: *Traffic* 11.4, pp. 508–519 (cit. on p. 117).

- Noble, Alex J., Venkata P. Dandey, Hui Wei, Julia Brasch, Jillian Chase, Priyamvada Acharya, Yong Zi Tan, Zhening Zhang, Laura Y. Kim, Giovanna Scapin, Micah Rapp, Edward T Eng, William J. Rice, Anchi Cheng, Carl J. Negro, Lawrence Shapiro, Peter D. Kwong, David Jeruzalmi, Amedee des Georges, Clinton S. Potter, and Bridget Carragher (May 2018). “Routine single particle CryoEM sample and grid characterization by tomography”. In: *eLife* 7. Ed. by Axel T Brunger, e34257 (cit. on p. 30).
- Noble, Alex J. and Scott M. Stagg (2015). “Automated batch fiducial-less tilt-series alignment in Appion using Protomo”. In: *Journal of structural biology* 192.2, pp. 270–278 (cit. on pp. 92, 112).
- Noble, Alex J., Hui Wei, Venkata P. Dandey, Zhening Zhang, Yong Zi Tan, Clinton S. Potter, and Bridget Carragher (Oct. 2018). “Reducing effects of particle adsorption to the air–water interface in cryo-EM”. In: *Nature Methods* 15.10, pp. 793–795 (cit. on p. 30).
- Nogales, Eva (2016). “The development of cryo-EM into a mainstream structural biology technique”. In: *Nature methods* 13.1, pp. 24–27 (cit. on p. 11).
- Oikonomou, Catherine M., Yi-Wei Chang, and Grant J. Jensen (Feb. 2016). “A new view into prokaryotic cell biology from electron cryotomography”. In: *Nature Reviews Microbiology* 14, p. 205 (cit. on p. 28).
- Otsu, Nobuyuki (1979). “A threshold selection method from gray-level histograms”. In: *IEEE transactions on systems, man, and cybernetics* 9.1, pp. 62–66 (cit. on p. 96).
- Palovcak, Eugene, Daniel Asarnow, Melody G. Campbell, Zanlin Yu, and Yifan Cheng (2020). “Enhancing SNR and generating contrast for cryo-EM images with convolutional neural networks”. In: *bioRxiv* (cit. on p. 145).
- Peitsch, Camille Françoise, Sven Beckmann, and Benoît Zuber (2016). “iMEM: Isolation of Plasma Membrane for Cryoelectron Microscopy”. In: *Structure* 24.12, pp. 2198–2206 (cit. on pp. 145, 146).
- Penczek, Pawel A. (2010). “Resolution measures in molecular electron microscopy”. In: *Methods in enzymology*. Vol. 482. Elsevier, pp. 73–100 (cit. on p. 19).
- Penczek, Pawel A., Jia Fang, Xueming Li, Yifan Cheng, Justus Loerke, and Christian MT Spahn (2014). “CTER—Rapid estimation of CTF parameters with error assessment”. In: *Ultramicroscopy* 140, pp. 9–19 (cit. on pp. 15, 69).
- Penczek, Pawel A., Michael Marko, Karolyn Buttle, and Joachim Frank (1995). “Double-tilt electron tomography”. In: *Ultramicroscopy* 60.3, pp. 393–410 (cit. on p. 36).
- Pennycook, Stephen J., B. David, C. Barry Williams, et al. (2010). “Transmission electron microscopy: a textbook for materials science”. In: *Microscopy and Microanalysis* 16.1, p. 111 (cit. on p. 11).
- Peralta, Bibiana, David Gil-Carton, Daniel Castaño-Díez, Aurelie Bertin, Claire Boulogne, Hanna M Oksanen, Dennis H. Bamford, and Nicola G. A. Abrescia (2013). “Mechanism of Membranous Tunnelling Nanotube Formation in Viral Genome Delivery”. In: *PLOS Biology* 11.9, pp. 1–15 (cit. on pp. 52, 58).
- Pettersen, Eric F., Thomas D. Goddard, Conrad C. Huang, Gregory S. Couch, Daniel M. Greenblatt, Elaine C. Meng, and Thomas E. Ferrin (2004). “UCSF Chimera—a visu-

- alization system for exploratory research and analysis”. In: *Journal of computational chemistry* 25.13, pp. 1605–1612 (cit. on pp. 21, 68).
- Pfeffer, Stefan, Laura Burbaum, Pia Unverdorben, Markus Pech, Yuxiang Chen, Richard Zimmermann, Roland Beckmann, and Friedrich Förster (2015). “Structure of the native Sec61 protein-conducting channel”. In: *Nature communications* 6.1, pp. 1–7 (cit. on pp. 29, 33, 91).
- Prosser, Derek C., Duvinh Tran, Allana Schooley, Beverly Wendland, and Johnny K. Ngsee (2010). “A novel, retromer-independent role for sorting nexins 1 and 2 in RhoG-dependent membrane remodeling”. In: *Traffic* 11.10, pp. 1347–1362 (cit. on p. 117).
- Punjani, Ali, John L. Rubinstein, David J. Fleet, and Marcus A. Brubaker (2017). “cryoSPARC: algorithms for rapid unsupervised cryo-EM structure determination”. In: *Nature methods* 14.3, pp. 290–296 (cit. on p. 13).
- Purushothaman, Latha Kallur and Christian Ungermann (2018). “Cargo induces retromer-mediated membrane remodeling on membranes”. In: *Molecular biology of the cell* 29.22, pp. 2709–2719 (cit. on p. 126).
- Radermacher, Michael (2006). “Weighted Back-projection Methods”. en. In: *Electron Tomography*. Ed. by Joachim Frank. New York, NY: Springer New York, pp. 245–273 (cit. on p. 41).
- Ramachandran, G. N. and A. V. Lakshminarayanan (1971). “Three-dimensional Reconstruction from Radiographs and Electron Micrographs: Application of Convolutions instead of Fourier Transforms”. In: *Proceedings of the National Academy of Sciences* 68.9, pp. 2236–2240 (cit. on p. 41).
- Reimer, Ludwig (2013). *Transmission electron microscopy: physics of image formation and microanalysis*. Vol. 36. Springer (cit. on p. 11).
- Renaud, J. P. (2020). *Structural Biology in Drug Discovery: Methods, Techniques, and Practices*. Wiley (cit. on pp. 9, 10).
- Rice, William J., Anchi Cheng, Alex J. Noble, Edward T. Eng, Laura Y. Kim, Bridget Carragher, and Clinton S. Potter (2018). “Routine determination of ice thickness for cryo-EM grids”. In: *Journal of Structural Biology* 204.1, pp. 38–44 (cit. on p. 30).
- Righetto, Ricardo D., Nikhil Biyani, Julia Kowal, Mohamed Chami, and Henning Stahlberg (2019). “Retrieving high-resolution information from disordered 2D crystals by single-particle cryo-EM”. In: *Nature communications* 10.1, pp. 1–10 (cit. on p. 12).
- Rigort, Alexander and Jürgen M. Plitzko (2015). “Cryo-focused-ion-beam applications in structural biology”. In: *Archives of Biochemistry and Biophysics* 581, pp. 122–130 (cit. on p. 31).
- Rohou, Alexis and Nikolaus Grigorieff (2015). “CTFFIND4: Fast and accurate defocus estimation from electron micrographs”. In: *Journal of structural biology* 192.2, pp. 216–221 (cit. on pp. 45, 67, 108, 135).
- Romero-Durana, Miguel, Brian Jiménez-García, and Juan Fernández-Recio (Dec. 2019). “pyDockEneRes: per-residue decomposition of protein–protein docking energy”. In: *Bioinformatics* 36.7, pp. 2284–2285 (cit. on p. 122).
- Roseman, Alan M. (2003). “Particle finding in electron micrographs using a fast local correlation algorithm”. In: *Ultramicroscopy* 94.3-4, pp. 225–236 (cit. on p. 21).

- Rosenthal, Peter B. and Richard Henderson (2003). “Optimal determination of particle orientation, absolute hand, and contrast loss in single-particle electron cryomicroscopy”. In: *Journal of molecular biology* 333.4, pp. 721–745 (cit. on p. 19).
- Rout, Michael P. and Andrej Sali (2019). “Principles for integrative structural biology studies”. In: *Cell* 177.6, pp. 1384–1403 (cit. on pp. 10, 11).
- Russo, Christopher J. and Lori A. Passmore (2016). “Ultrastable gold substrates: Properties of a support for high-resolution electron cryomicroscopy of biological specimens”. In: *Journal of Structural Biology* 193.1, pp. 33–44 (cit. on p. 36).
- Ryabov, A, JW Thurner, D Nabben, MV Tsarev, and P Baum (2020). “Attosecond metrology in a continuous-beam transmission electron microscope”. In: *Science Advances* 6.46, eabb1393 (cit. on p. 145).
- Sandberg, Kristian (2007). “Methods for image segmentation in cellular tomography”. In: *Methods in cell biology* 79, pp. 769–798 (cit. on p. 15).
- Schaffer, Miroslava, Stefan Pfeffer, Julia Mahamid, Stephan Kleindiek, Tim Laugks, Sahratha Albert, Benjamin D Engel, Andreas Rummel, Andrew J Smith, Wolfgang Baumeister, et al. (2019). “A cryo-FIB lift-out technique enables molecular-resolution cryo-ET within native *Caenorhabditis elegans* tissue”. In: *Nature methods* 16.8, pp. 757–762 (cit. on p. 145).
- Schatz, Michael and Marin van Heel (1990). “Invariant classification of molecular views in electron micrographs”. In: *Ultramicroscopy* 32.3, pp. 255–264 (cit. on p. 56).
- Scheres, Sjors H. W. (2012). “A Bayesian view on cryo-EM structure determination”. In: *Journal of molecular biology* 415.2, pp. 406–418 (cit. on pp. 13, 142).
- Scheres, Sjors H. W. and Shaoxia Chen (July 2012). “Prevention of overfitting in cryo-EM structure determination”. In: *Nature Methods* 9, p. 853 (cit. on pp. 18, 49).
- Scheres, Sjors H. W., Roberto Melero, Mikel Valle, and Jose-Maria Carazo (2009). “Averaging of Electron Subtomograms and Random Conical Tilt Reconstructions through Likelihood Optimization”. In: *Structure* 17.12, pp. 1563–1572 (cit. on pp. 57, 59).
- Scheres, Sjors H. W., Mikel Valle, Rafael Nuñez, Carlos O. S. Sorzano, Roberto Marabini, Gabor T. Herman, and Jose-Maria Carazo (2005). “Maximum-likelihood multi-reference refinement for electron microscopy images”. In: *Journal of molecular biology* 348.1, pp. 139–149 (cit. on p. 13).
- Schmidli, Claudio, Stefan Albiez, Luca Rima, Ricardo Righetto, Inayatulla Mohammed, Paolo Oliva, Lubomir Kovacik, Henning Stahlberg, and Thomas Braun (2019). “Microfluidic protein isolation and sample preparation for high-resolution cryo-EM”. In: *Proceedings of the National Academy of Sciences* 116.30, pp. 15007–15012 (cit. on pp. 145, 146).
- Schur, Florian K. M. (2019). “Toward high-resolution in situ structural biology with cryo-electron tomography and subtomogram averaging”. In: *Current opinion in structural biology* 58, pp. 1–9 (cit. on p. 65).
- Schur, Florian K. M., Wim J. H. Hagen, Alex de Marco, and John A. G. Briggs (2013). “Determination of protein structure at 8.5Å resolution using cryo-electron tomography and sub-tomogram averaging”. In: *Journal of Structural Biology* 184.3, pp. 394–400 (cit. on p. 45).

- Schur, Florian K. M., Wim J. H. Hagen, Michaela Rumlová, Tomáš Ruml, Barbara Müller, Hans-Georg Kräusslich, and John A. G. Briggs (Jan. 2015). “Structure of the immature HIV-1 capsid in intact virus particles at 8.8 Å resolution”. In: *Nature* 517, pp. 505–508 (cit. on p. 28).
- Schur, Florian K. M., Martin Obr, Wim J. H. Hagen, William Wan, Arjen J. Jakobi, Joanna M. Kirkpatrick, Carsten Sachse, Hans-Georg Kräusslich, and John A. G. Briggs (2016). “An atomic model of HIV-1 capsid-SP1 reveals structures regulating assembly and maturation”. In: *Science* 353.6298, pp. 506–508 (cit. on pp. 17, 22, 28, 30, 37, 48, 58, 66, 68, 91, 92).
- Schwartz, Osip, Jeremy J Axelrod, Sara L. Campbell, Carter Turnbaugh, Robert M. Glaeser, and Holger Müller (2019). “Laser phase plate for transmission electron microscopy”. In: *Nature methods* 16.10, pp. 1016–1020 (cit. on p. 145).
- Seaman, Matthew N. J. (2012). “The retromer complex—endosomal protein recycling and beyond”. In: *Journal of cell science* 125.20, pp. 4693–4702 (cit. on p. 117).
- Seaman, Matthew N. J., J. Michael McCaffery, and Scott D. Emr (1998). “A membrane coat complex essential for endosome-to-Golgi retrograde transport in yeast”. In: *The Journal of cell biology* 142.3, pp. 665–681 (cit. on p. 116).
- Sierecki, Emma, Loes M. Stevers, Nichole Giles, Mark E. Polinkovsky, Mehdi Moustaqil, Sergey Mureev, Wayne A. Johnston, Mareike Dahmer-Heath, Dubravka Skalamera, Thomas J. Gonda, et al. (2014). “Rapid mapping of interactions between human SNX-BAR proteins measured in vitro by AlphaScreen and single-molecule spectroscopy”. In: *Molecular & Cellular Proteomics* 13.9, pp. 2233–2245 (cit. on p. 120).
- Sigworth, Fred J. (1998). “A Maximum-Likelihood Approach to Single-Particle Image Refinement”. In: *Journal of Structural Biology* 122.3, pp. 328–339 (cit. on p. 56).
- (2016). “Principles of cryo-EM single-particle image processing”. In: *Microscopy* 65.1, pp. 57–67 (cit. on p. 16).
- Sigworth, Fred J., Peter C. Doerschuk, Jose-Maria Carazo, and Sjors H. W. Scheres (2010). “An introduction to maximum-likelihood methods in cryo-EM”. In: *Methods in enzymology*. Vol. 482. Elsevier, pp. 263–294 (cit. on p. 13).
- Simonetti, Boris, Chris M. Danson, Kate J. Heesom, and Peter J. Cullen (2017). “Sequence-dependent cargo recognition by SNX-BARs mediates retromer-independent transport of CI-MPR”. In: *Journal of Cell Biology* 216.11, pp. 3695–3712 (cit. on p. 117).
- Simonetti, Boris, Blessy Paul, Karina Chaudhari, Saroja Weeratunga, Florian Steinberg, Madhavi Gorla, Kate J Heesom, Greg J. Bashaw, Brett M. Collins, and Peter J. Cullen (2019). “Molecular identification of a BAR domain-containing coat complex for endosomal recycling of transmembrane proteins”. In: *Nature Cell Biology* 21.10, pp. 1219–1233 (cit. on p. 126).
- Sindelar, Charles V. and Nikolaus Grigorieff (2012). “Optimal noise reduction in 3D reconstructions of single particles using a volume-normalized filter”. In: *Journal of structural biology* 180.1, pp. 26–38 (cit. on p. 11).
- Small, Scott A. and Gregory A. Petsko (2015). “Retromer in Alzheimer disease, Parkinson disease and other neurological disorders”. In: *Nature Reviews Neuroscience* 16.3, pp. 126–132 (cit. on p. 116).

- Song, Kangkang, Zhiguo Shang, Xiaofeng Fu, Xiaochu Lou, Nikolaus Grigorieff, and Daniela Nicastro (Jan. 2018). “Structure of the ciliary axoneme at nanometer resolution reconstructed by TYGRESS”. In: *bioRxiv*, p. 363317 (cit. on p. 33).
- Stahlberg, Henning, Nikhil Biyani, and Andreas Engel (2015). “3D reconstruction of two-dimensional crystals”. In: *Archives of biochemistry and biophysics* 581, pp. 68–77 (cit. on p. 12).
- Steinberg, Florian, Matthew Gallon, Mark Winfield, Elaine C. Thomas, Amanda J. Bell, Kate J. Heesom, Jeremy M. Tavaré, and Peter J. Cullen (2013). “A global analysis of SNX27–retromer assembly and cargo specificity reveals a function in glucose and metal ion transport”. In: *Nature cell biology* 15.5, pp. 461–471 (cit. on p. 117).
- Stölken, Michael, Florian Beck, Thomas Haller, Reiner Hegerl, Irina Gutsche, Jose-Maria Carazo, Wolfgang Baumeister, Sjors H. W. Scheres, and Stephan Nickell (2011). “Maximum likelihood based classification of electron tomographic data”. In: *Journal of structural biology* 173.1, pp. 77–85 (cit. on pp. 50, 57, 58, 65).
- Su, Min (2019). “goCTF: Geometrically optimized CTF determination for single-particle cryo-EM”. In: *Journal of Structural Biology* 205.1, pp. 22–29 (cit. on p. 45).
- Suloway, Christian, Jian Shi, Anchi Cheng, James Pulokas, Bridget Carragher, Clinton S. Potter, Shawn Q. Zheng, David A. Agard, and Grant J. Jensen (2009). “Fully automated, sequential tilt-series acquisition with Leginon”. In: *Journal of structural biology* 167.1, pp. 11–18 (cit. on p. 92).
- Sun, Dapeng, Natalia V. Varlakhanova, Bryan A. Tornabene, Rajesh Ramachandran, Peijun Zhang, and Marijn G. J. Ford (2020). “The cryo-EM structure of the SNX–BAR Mvp1 tetramer”. In: *Nature Communications* 11.1, pp. 1–10 (cit. on pp. 119, 120).
- Sun, Ming, Caleigh M Azumaya, Eric Tse, Adam Frost, Daniel Southworth, Kliment A Verba, Yifan Cheng, and David A Agard (2020). “Practical considerations for using K3 cameras in CDS mode for high-resolution and high-throughput single particle cryo-EM”. In: *bioRxiv* (cit. on p. 145).
- Swarbrick, James D, Daniel J Shaw, Sandeep Chhabra, Rajesh Ghai, Eugene Valkov, Suzanne J Norwood, Matthew NJ Seaman, and Brett M Collins (2011). “VPS29 is not an active metallo-phosphatase but is a rigid scaffold required for retromer interaction with accessory proteins”. In: *PLoS One* 6.5, e20420 (cit. on pp. 117, 131).
- Tabuchi, Mitsuaki, Izumi Yanatori, Yasuhiro Kawai, and Fumio Kishi (2010). “Retromer-mediated direct sorting is required for proper endosomal recycling of the mammalian iron transporter DMT1”. In: *Journal of cell science* 123.5, pp. 756–766 (cit. on p. 117).
- Tang, Guang, Liwei Peng, Philip R. Baldwin, Deepinder S. Mann, Wen Jiang, Ian Rees, and Steven J. Ludtke (2007). “EMAN2: an extensible image processing suite for electron microscopy”. In: *Journal of structural biology* 157.1, pp. 38–46 (cit. on p. 21).
- Tegunov, Dimitry and Patrick Cramer (2019). “Real-time cryo-electron microscopy data preprocessing with Warp”. In: *Nature methods* 16.11, pp. 1146–1152 (cit. on p. 16).

- Tegunov, Dimitry, Liang Xue, Christian Dienemann, Patrick Cramer, and Julia Mahamid (2020). “Multi-particle cryo-EM refinement with M visualizes ribosome-antibiotic complex at 3.7 Å inside cells”. In: *bioRxiv* (cit. on pp. 19, 65, 91, 112, 145).
- Thon, F. (1966). “Zur Defokussierungsabhängigkeit des Phasenkontrastes bei der elektronenmikroskopischen Abbildung”. In: *Zeitschrift für Naturforschung* 21a, pp. 476–478 (cit. on p. 43).
- Tocheva, Elitza I., Zhuo Li, and Grant J. Jensen (2010). “Electron cryotomography”. In: *Cold Spring Harbor perspectives in biology* 2.6, a003442 (cit. on p. 91).
- Turoňová, Beata, Florian K. M. Schur, William Wan, and John A. G. Briggs (2017). “Efficient 3D-CTF correction for cryo-electron tomography using NovaCTF improves subtomogram averaging resolution to 3.4 Å”. In: *Journal of structural biology* 199.3, pp. 187–195 (cit. on pp. 28, 46, 66, 83, 86, 87, 108).
- Van Heel, Marin and Michael Schatz (2005). “Fourier shell correlation threshold criteria”. In: *Journal of structural biology* 151.3, pp. 250–262 (cit. on p. 19).
- Van Weering, Jan R. T., Richard B. Sessions, Colin J. Traer, Daniel P. Klover, Vikram K. Bhatia, Dimitrios Stamou, Sven R. Carlsson, James H. Hurley, and Peter J. Cullen (2012). “Molecular basis for SNX-BAR-mediated assembly of distinct endosomal sorting tubules”. In: *The EMBO journal* 31.23, pp. 4466–4480 (cit. on pp. 120, 122, 125, 128).
- VandenBussche, Elisah J and David J Flannigan (2019). “Reducing radiation damage in soft matter with femtosecond-timed single-electron packets”. In: *Nano letters* 19.9, pp. 6687–6694 (cit. on p. 145).
- Villa, Elizabeth, Miroslava Schaffer, Jürgen M. Plitzko, and Wolfgang Baumeister (Oct. 2013). “Opening windows into the cell: focused-ion-beam milling for cryo-electron tomography”. en. In: *Current Opinion in Structural Biology* 23.5, pp. 771–777 (cit. on p. 30).
- Vulović, Miloš, Lenard M. Voortman, Lucas J. van Vliet, and Bernd Rieger (2014). “When to use the projection assumption and the weak-phase object approximation in phase contrast cryo-EM”. In: *Ultramicroscopy* 136, pp. 61–66 (cit. on p. 11).
- Wade, R. H. (1992). “A brief look at imaging and contrast transfer”. In: *Ultramicroscopy* 46.1, pp. 145–156 (cit. on p. 42).
- Walz, Jochen, Dieter Typke, Michael Nitsch, Abraham J. Koster, Reiner Hegerl, and Wolfgang Baumeister (1997). “Electron Tomography of Single Ice-Embedded Macromolecules: Three-Dimensional Alignment and Classification”. In: *Journal of Structural Biology* 120.3, pp. 387–395 (cit. on p. 60).
- Wan, William and John A. G. Briggs (2016). “Cryo-electron tomography and subtomogram averaging”. In: *Methods in enzymology*. Vol. 579. Elsevier, pp. 329–367 (cit. on pp. 18, 19, 37, 65, 91, 92, 94).
- Wan, William, Larissa Kolesnikova, Mairi Clarke, Alexander Koehler, Takeshi Noda, Stephan Becker, and John A. G. Briggs (Nov. 2017). “Structure and assembly of the Ebola virus nucleocapsid”. In: *Nature* 551, pp. 394–397 (cit. on pp. 28, 30).
- Wang, Jing, Maximilian Brackmann, Daniel Castaño-Díez, Mikhail Kudryashev, Kenneth N Goldie, Timm Maier, Henning Stahlberg, and Marek Basler (2017). “Cryo-

- EM structure of the extended type VI secretion system sheath–tube complex”. In: *Nature microbiology* 2.11, pp. 1507–1512 (cit. on pp. 22, 58).
- Ward, Andrew B., Andrej Sali, and Ian A. Wilson (2013). “Integrative structural biology”. In: *Science* 339.6122, pp. 913–915 (cit. on p. 10).
- Wassmer, Thomas, Naomi Attar, Miriam V. Bujny, Jacqueline Oakley, Colin J. Traer, and Peter J. Cullen (2007). “A loss-of-function screen reveals SNX5 and SNX6 as potential components of the mammalian retromer”. In: *Journal of cell science* 120.1, pp. 45–54 (cit. on p. 117).
- Winey, Mark, Janet B. Meehl, Eileen T. O’Toole, and Thomas H. Giddings Jr (2014). “Conventional transmission electron microscopy”. In: *Molecular biology of the cell* 25.3, pp. 319–323 (cit. on p. 12).
- Winkler, Hanspeter (2007). “3D reconstruction and processing of volumetric data in cryo-electron tomography”. In: *Journal of structural biology* 157.1, pp. 126–137 (cit. on p. 38).
- Winkler, Hanspeter and Kenneth A. Taylor (2003). “Focus gradient correction applied to tilt series image data used in electron tomography”. In: *Journal of Structural Biology* 143.1, pp. 24–32 (cit. on p. 45).
- (2006). “Accurate marker-free alignment with simultaneous geometry determination and reconstruction of tilt series in electron tomography”. In: *Ultramicroscopy* 106.3, pp. 240–254 (cit. on p. 39).
- Xiong, Quanren, Mary K. Morphew, Cindi L. Schwartz, Andreas H. Hoenger, and David N. Mastronarde (2009). “CTF determination and correction for low dose tomographic tilt series”. In: *Journal of structural biology* 168.3, pp. 378–387 (cit. on pp. 44, 45, 108, 135).
- Xu, Min, Martin Beck, and Frank Alber (2012). “High-throughput subtomogram alignment and classification by Fourier space constrained fast volumetric matching”. In: *Journal of Structural Biology* 178.2, pp. 152–164 (cit. on pp. 50, 55).
- Xu, Min, Ge Yang, Xiaoqi Chai, Hariank Muthakana, Eric P Xing, Xiaodan Liang, and Tzviya Zeev-Ben-Mordehai (July 2017). “Deep learning-based subdivision approach for large scale macromolecules structure recovery from electron cryo tomograms”. In: *Bioinformatics* 33.14, pp. i13–i22 (cit. on p. 57).
- Yao, Hangping, Yutong Song, Yong Chen, Nanping Wu, Jialu Xu, Chujie Sun, Jiaying Zhang, Tianhao Weng, Zheyuan Zhang, Zhigang Wu, et al. (2020). “Molecular architecture of the SARS-CoV-2 virus”. In: *Cell* (cit. on p. 145).
- Yong, Xin, Lin Zhao, Wankun Deng, Hongbin Sun, Xue Zhou, Lejiao Mao, Wenfeng Hu, Xiaofei Shen, Qingxiang Sun, Daniel D. Billadeau, et al. (2020). “Mechanism of cargo recognition by retromer-linked SNX-BAR proteins”. In: *PLoS biology* 18.3, e3000631 (cit. on pp. 117, 126, 131).
- Zanetti, Giulia, James D. Riches, Stephen D. Fuller, and John AG Briggs (2009). “Contrast transfer function correction applied to cryo-electron tomography and subtomogram averaging”. In: *Journal of Structural Biology* 168.2, pp. 305–312 (cit. on p. 43).
- Zhang, Kai (2016). “Gctf: Real-time CTF determination and correction”. In: *Journal of Structural Biology* 193.1, pp. 1–12 (cit. on p. 45).

- Zhang, Xing and Z. Hong Zhou (2011). “Limiting factors in atomic resolution cryo electron microscopy: No simple tricks”. In: *Journal of Structural Biology* 175.3, pp. 253–263 (cit. on pp. 43, 46).
- Zheng, Qingxiong S., Michael B. Braunfeld, John W. Sedat, and David A. Agard (2004). “An improved strategy for automated electron microscopic tomography”. In: *Journal of structural biology* 147.2, pp. 91–101 (cit. on p. 92).
- Zheng, Shawn Q., Bettina Keszthelyi, Eric Branlund, John M. Lyle, Michael B. Braunfeld, John W. Sedat, and David A. Agard (2007). “UCSF tomography: an integrated software suite for real-time electron microscopic tomographic data collection, alignment, and reconstruction”. In: *Journal of structural biology* 157.1, pp. 138–147 (cit. on p. 92).
- Zheng, Shawn Q., Eugene Palovcak, Jean-Paul Armache, Kliment A. Verba, Yifan Cheng, and David A. Agard (2017). “MotionCor2: anisotropic correction of beam-induced motion for improved cryo-electron microscopy”. In: *Nature methods* 14.4, pp. 331–332 (cit. on pp. 36, 67, 135).
- Zhong, Qi, Cheri S. Lazar, Hélène Tronchère, Trey Sato, Timo Meerloo, Michele Yeo, Zhou Songyang, Scott D. Emr, and Gordon N. Gill (2002). “Endosomal localization and function of sorting nexin 1”. In: *Proceedings of the National Academy of Sciences* 99.10, pp. 6767–6772 (cit. on p. 125).
- Zhu, Shiwei, Tatsuro Nishikino, Bo Hu, Seiji Kojima, Michio Homma, and Jun Liu (Oct. 2017). “Molecular architecture of the sheathed polar flagellum in *Vibrio alginolyticus*”. In: *Proceedings of the National Academy of Sciences* 114.41, p. 10966 (cit. on p. 60).
- Zivanov, Jasenko, Takanori Nakane, Björn O. Forsberg, Dari Kimanius, Wim J. H. Hagen, Erik Lindahl, and Sjors H. W. Scheres (2018). “New tools for automated high-resolution cryo-EM structure determination in RELION-3”. In: *Elife* 7, e42166 (cit. on p. 68).